

ABSTRACT

Title of dissertation: **DEGENERATE GASES OF STRONTIUM
FOR STUDIES OF
QUANTUM MAGNETISM**

**Daniel Schaefer Barker,
Doctor of Philosophy, 2016**

Dissertation directed by: **Dr. G.K. Campbell and Professor S.L. Rolston
Joint Quantum Institute,
National Institute of Standards and Technology
and
Department of Physics, University of Maryland**

We describe the construction and characterization of a new apparatus that can produce degenerate quantum gases of strontium. The realization of degenerate gases is an important first step toward future studies of quantum magnetism. Three of the four stable isotopes of strontium have been cooled into the degenerate regime. The experiment can make nearly pure Bose-Einstein condensates containing $\simeq 1 \times 10^4$ atoms, for ^{86}Sr , and $\simeq 4 \times 10^5$ atoms, for ^{84}Sr . We have also created degenerate Fermi gases of ^{87}Sr with a reduced temperature, $T/T_F \simeq 0.2$. The apparatus will be able to produce Bose-Einstein condensates of ^{88}Sr with straightforward modifications.

We also report the first experimental and theoretical results from the strontium project. We have developed a technique to accelerate the continuous loading of strontium atoms into a magnetic trap. By applying a laser addressing the $^3P_1 \rightarrow ^3S_1$ transition in our magneto-optical trap, the rate at which atoms populate the magnetically-trapped 3P_2 state can be increased by up to 65%. Quantum degenerate gases of atoms in the metastable 3P_0 and 3P_2 states are a promising platform for quantum simulation of systems with long-range interactions. We have performed an initial numerical study of a method to transfer the

ground state degenerate gases that we can currently produce into one of the metastable states via a three-photon transition. Numerical simulations of the Optical Bloch equations governing the three-photon transition indicate that $\gtrsim 90\%$ of a ground state degenerate gas can be transferred into a metastable state.

DEGENERATE GASES OF STRONTIUM
FOR STUDIES OF QUANTUM MAGNETISM

by

Daniel Schaefer Barker

Dissertation submitted to the Faculty of the Graduate School of the
University of Maryland, College Park in partial fulfillment
of the requirements for the degree of
Doctor of Philosophy
2016

Advisory Committee:

Dr. Gretchen K. Campbell, Advisor

Professor Steven L. Rolston, Chair

Professor John T. Fourkas, Dean's Representative

Professor Luis A. Orozco

Dr. Eite Tiesinga

© Copyright by
Daniel Schaefer Barker
2016

Foreword

Several of the figures in this thesis will only properly display in, and print from, Adobe Acrobat or Adobe Reader.

Acknowledgments

When I joined Team Strontium in January of 2010, our lab was about halfway through its conversion from conference room to usable research space. Building the lab from usable space to functioning apparatus has been a journey of both intense frustration and incredible satisfaction. My part in this process was enabled by the support of my collaborators, mentors, friends, and family members.

Many undergraduates, graduate students and postdocs contributed to the construction of the apparatus. Undergraduates Patrick McKenna and Eliot Bohr were preternaturally capable of tackling any task we could throw at them. Guil Miranda designed the vacuum system. Avinash Kumar and Erin Marshall built many of the analog and digital buffers for the computer control system. Swarnav Banik made the prestabilization cavity for our forthcoming clock laser. Post-doc Joe Pechkis set up the computer control and much of the 1064-nm laser system. He also brought an essential outside viewpoint to the experiment and taught me how to make a dipole trap. Neal Piseni has become our resident master of laser electronics. The experiment would not function without the circuits that he developed. Ben Reschovsky has been my partner on the apparatus since construction began in earnest in the summer of 2010. His contributions to the apparatus are innumerable and I am continually impressed with his ability to get all the red lasers working simultaneously. I would not have arrived at this juncture without Neal and Ben, and I am happy to be leaving the experiment in such capable hands.

I could not have asked for an advisor better than Gretchen. The depth and breadth of her knowledge astounds me and I am very appreciative of her tolerance for my silliest questions. Gretchen somehow manages to be available whenever we really needed her advice and absent whenever we needed time to solve a problem on our own. I am inspired by her optimism and enthusiasm, even in the face of experimental adversity. She believed that the experiment would work back in the early days of 2012, when I certainly didn't think that such an outcome was possible.

The Joint Quantum Institute is an excellent environment and has given me the opportunity to interact with a host of great scientists. Steve Rolston and Trey Porto invited the strontium team into their group meetings and have served as secondary advisors throughout the construction process. Alessandro Restelli has exponentially improved all our electronics. It has been my pleasure to collaborate with other members of the Campbell group: Anand Ramanathan, Kevin Wright, Brad Blakestad, Jeff Lee, Avinash Kumar, Steve Eckel, Fred Jendrzejewski, Swarnav Banik, Neil Anderson, and Monica Gutierrez Galan. I would particularly like to acknowledge Steve and Fred, for all their insight on BEC physics, image processing tricks, and DMD programming. I want to thank all our fellow 2nd floor denizens, who generously loaned us tools and experimental expertise: Subhadeep De, Dan Campbell, Dan Schwartz, Varun Vaidya, Ryan Price, Andika Putra, Sean Li, Joe Tiamsuphat, Ana Valdes Curiel, Erin Marshall, Dimitrios Trypogeorgos, and, especially, Creston Herold, who was the senior graduate student the strontium project didn't have. Thanks also to "CPR" members Matt Beeler, Kevin Twedt, Jenn Robinson, Matt Reed, Zach Smith, Aftaab Dewan, Dalia Ornelas, Sandy Craddock, Mary Lyon, and Elizabeth Goldschmidt.

The JQI and physics department staff makes our science possible. Cindy Dooley, Melissa Britton, Kelly Hickman, Kate Sickles, Anh La, Cheryl Ekstrom, Jesse Anderson, Al Godinez, Claudia Key, Brylan Lonon, Jessica Crosby, Paulina Alejandro, Lorraine DeSalvo, and Doug Bensen all made important contributions to the experiment and my experience at UMD. Machinists Dave Cogswell, Bruce Rowley, Thomas Tamarkin, and Edd Cole do exemplary work and bailed us out by rushing jobs on several occasions.

My early scientific development was greatly influenced by several members of the Goucher College physics department. Sasha Dukan shared her love of science and, perhaps inadvertently, convinced me to stick with the physics major during my sophomore year. Marin Pichler introduced me to atomic physics and let me play with the lasers in his lab. Ben Sugerman turned the homework up to 11 (in all the classes since he also bought the

department espresso machine).

My family and friends have kept me sane through it all. I got necessary doses of pancakes, video games and comisseration from my long-time roommates Zach Smith, Trystan Koch, John Biddle, and Steve Lynam. The Lake crew can always be counted on for stimulating conversations on just about any topic. The friendship of David Bulkley, the brother I don't have, has sustained my curiosity and optimism. All my Goucher pals remind me that science isn't everything, and I especially want to thank Jon Rubin for dragging me out of the apartment during first year. My parents, Patti and Rick, my sisters, Molly and Cailin, and our neighbor, Viki, have all been consistent positive forces in my life. Jenn reminds me to come home in the evening, keeps me organized, and so much more. I cannot imagine my life without her.

Table of Contents

Foreword	ii
Acknowledgements	iii
List of Tables	viii
List of Figures	ix
List of Abbreviations	xi
1 Introduction	1
1.1 Alkaline-Earth Atoms	1
1.2 Quantum Magnetism	5
1.3 Ultracold Gas Theory	11
1.3.1 Thermal Atoms	12
1.3.2 Bose-Einstein Condensates	13
1.3.3 Degenerate Fermi Gases	17
1.4 Thesis Outline	19
2 Production of Degenerate Gases	20
2.1 The bMOT and the Metastable Reservoir	20
2.2 The rMOT	25
2.3 The Optical Dipole Trap	32
2.4 Strontium Bose-Einstein Condensates	38
2.4.1 ^{86}Sr BEC	38
2.4.2 ^{84}Sr BEC	40
2.4.2.1 Trap Frequency Measurement	42
2.5 Degenerate Fermi Gas of ^{87}Sr	43
3 Experimental Apparatus	51
3.1 Laser Systems	51
3.1.1 461-nm Laser System	52
3.1.2 689-nm Laser System	58

3.1.3	Repump Lasers	63
3.1.4	Optical Dipole Traps	67
3.1.4.1	1064-nm Laser System	67
3.1.4.2	445-nm Laser System	70
3.2	Imaging Systems	76
3.3	Vacuum System	83
3.4	Magnetic Field Coils	87
3.5	Computer Control	94
4	Enhanced Magnetic Trap Loading	98
4.1	Publication: Enhanced magnetic trap loading for atomic strontium	99
4.1.1	Abstract	99
4.1.2	Introduction	99
4.1.3	Apparatus	102
4.1.4	Results	106
4.1.5	Simulation	110
4.1.6	Conclusions	114
4.2	Additional Work	116
5	Three-Photon Process	117
5.1	Publication: Three-photon process for producing a degenerate gas of metastable alkaline-earth-metal atoms	117
5.1.1	Abstract	117
5.1.2	Introduction	118
5.1.3	3-Photon Dynamics	120
5.1.4	Experimental Considerations	125
5.1.5	Conclusions	132
5.2	STIRAP	133
A	Fermionic Absorption Cross Section	139
A.1	Absorption for Bosonic Isotopes	139
A.2	Relative Cross Section Calculation	140
	Bibliography	147

List of Tables

1.1	Properties of Alkaline-Earth Atoms	4
2.1	bMOT Isotope Shifts	22
2.2	rMOT Isotope Shifts	26
2.3	Dipole Trap Waists	35
3.1	bMOT Beatnote Frequencies	57
3.2	Imaging System Lenses	76
3.3	Imaging System Resolutions	81
5.1	Rabi Simulation Parameters	124
5.2	Single Photon Transition Linewidths	127
5.3	Magic Wavelengths	131
5.4	STIRAP Simulation Parameters	136

List of Figures

1	Optics Legend	xiv
1.1	Strontium Energy Level Diagram	3
1.2	Lattice Quantum Magnetism	7
1.3	Box Trap Quantum Magnetism	9
1.4	Density Distributions	13
2.1	bMOT Parameter Ramps	24
2.2	Fermionic rMOT Hyperfine Levels	28
2.3	rMOT Parameter Ramps	30
2.4	ODT Power Ramps	37
2.5	^{86}Sr Bose-Einstein Condensation	39
2.6	^{84}Sr Bose-Einstein Condensation	41
2.7	Three-Beam Cross Vertical Trap Frequency	42
2.8	Three-Beam Cross Horizontal Trap Frequencies	44
2.9	^{87}Sr Degenerate Fermi Gas	45
2.10	Degenerate Fermi Gas Azimuthal Profile	47
2.11	Evaporation Time Dependence of T/T_F	49
3.1	461-nm Master Laser	53
3.2	461-nm Slave Laser	55
3.3	689-nm Master Laser	59
3.4	689-nm Slave Lasers	61
3.5	Repump Lasers	65
3.6	1064-nm Dipole Trap Laser	68
3.7	Interference-Induced Loss	69
3.8	Vertical Chamber-side Optics	71
3.9	Horizontal Chamber-side Optics	72
3.10	DMD Imaging System Test	73
3.11	Imaging System Resolution Tests	79
3.12	Vacuum Chamber	83
3.13	Zeeman Slower Design	88
3.14	MOT and Shim Coils	90

3.15	Cooling Manifold and MOSFETs	92
3.16	SetList v1.6.0	94
3.17	Computer Control Hardware	96
4.1	Depumping Spectroscopy Level Diagram	101
4.2	Depumping Transition Spectroscopy	102
4.3	Repumping Transition Spectroscopy	104
4.4	Atom Number Enhancement vs. Depump Beam Parameters	106
4.5	Atom Number Enhancement vs. Depumping Power	108
4.6	Depumping Enhancement and Atom Number Saturation	110
4.7	Comparison of Depumping Spectroscopy to Simulation	112
4.8	Simulations of Alternative Depumping Schemes	115
5.1	3-Photon Transition Schematic	119
5.2	3-Photon Transition Level Diagram	121
5.3	Rabi Dynamics Simulation	123
5.4	3-Photon Linewidths	126
5.5	Differential Polarizability of Relevant Levels	130
5.6	STIRAP Simulation	134
5.7	STIRAP Linewidths	137
A.1	Fermionic Optical Pumping	140
A.2	Cross Section Time Dependence	141
A.3	Steady State Cross Section	142
A.4	Cross Section Spin Dependence	144
A.5	Fermionic OBE Simulation	145
A.6	OBE Cross Section	146

List of Abbreviations

a_0	Bohr radius
c	Speed of light
ϵ_0	Vacuum permittivity
\hbar	Planck's constant, reduced
k_B	Boltzmann's constant
μ_B	Bohr magneton divided by \hbar
AC	Alternating Current
ACD	Achromatic Doublet
AE	Alkaline-Earth-like
AI	Analog Input
AO	Analog Output
AOM	Acousto-Optic Modulator
AR	Anti-Reflection
ASE	Amplified Spontaneous Emission
AWG	American Wire Gauge
BEC	Bose-Einstein Condensate
BJT	Bipolar Junction Transistor
bMOT	blue Magneto-Optical Trap
CCD	Charge-Coupled Device
CG	Clebsch-Gordan
CMOS	Complementary Metal-Oxide-Semiconductor
COM	Center of Mass
DAC	Digital to Analog Converter
DAQ	Data Acquisition
DC	Direct Current
DDE	Dynamic Data Exchange
DDS	Direct Digital Synthesis
DFG	Degenerate Fermi Gas
DL	Diode Laser
DMD	Digital Micromirror Device
DO	Digital Output
ECDL	External Cavity Diode Laser
EIT	Electromagnetically-Induced Transparency
EOM	Electro-Optic Modulator
FALC	Fast Analog Linewidth Control
FET	Field-Effect Transistor

FFT	Fast Fourier Transform
FWHM	Full Width at Half Maximum
HCL	Hollow Cathode Lamp
HEPA	High-Efficiency Particulate Arrestance
HWP	Half-Wave Plate
InGaAs	Indium Gallium Arsenide
IR	Infrared
JILA	JILA
JQI	Joint Quantum Institute
LD	Laser Diode
LMA	Large Mode Area
LTRF	Loading Time Reduction Factor
LWP	Long Wave Pass
MOSFET	Metal-Oxide-Semiconductor Field-Effect Transistor
MOT	Magneto-Optical Trap
NA	Numerical Aperture
NI	National Instruments
NIR	Near Infrared
NIST	National Institute of Standards and Technology
OBEs	Optical Bloch Equations
OD	Optical Depth
ODT	Optical Dipole Trap
OFR	Optical Feshbach Resonance
OSG	Optical Stern-Gerlach
PBS	Polarizing Beamsplitter
PD	Photodiode
PDH	Pound Drever Hall
PCI	Peripheral Component Interconnect
PCIe	PCI Express
PID	Proportional Integral Differential
PI	Proportional Integral
PLL	Phase-Locked Loop
PM	Polarization Maintaining
PSC	Physical Sciences Complex
PSF	Point Spread Function
PZT	Piezoelectric Transducer

QWP	Quarter-Wave Plate
RF	Radiofrequency
RGA	Residual Gas Analyzer
rMOT	red Magneto-Optical Trap
ROI	Region Of Interest
SHG	Second Harmonic Generation
SM	Single Mode
S/N	Signal to Noise
SRS	Stanford Research Systems
STIRAP	Stimulated Raman Adiabatic Passage
SWP	Short Wave Pass
TA	Tapered Amplifier
TOF	Time Of Flight
TSP	Titanium Sublimation Pump
ULE	Ultra-Low Expansion glass
UMD	University of Maryland
USAF	U.S. Air Force
USB	Universal Serial Bus
VCO	Voltage Controlled Oscillator
VI	Virtual Instrument


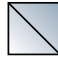















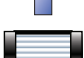






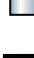

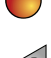

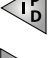




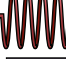
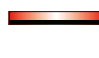
Flat Mirror:		Polarizing Beamsplitter Cube:	
Curved Mirror:		Glan Laser Polarizer:	
Diffraction Grating:		Optical Isolator:	
Mirror w/ PZT:		Faraday Rotator:	
Grating w/ PZT:		Half-Wave Plate:	
Lenses:		Quarter-Wave Plate:	
Beam Dump:		Bichromatic Wave Plate:	
Iris:		Non-Linear Crystal:	
Flipper Mirror:		Acousto-Optic Modulator:	
Solenoid Shutter:		Electro-Optic Modulator:	
SRS Shutter:		Fiber Electro-Optic Modulator:	
Laser Diode:		Liquid Crystal Variable Waveplate:	
Photo Diode:		Digital Micromirror Device:	
PID Controller:		Single Mode Fiber:	
PDH Module:		Polarization Maintaining Fiber:	
FALC Module:		Large Mode Area Fiber:	
SWP Dichroic:		Tapered Amplifier:	
LWP Dichroic:			

Figure 1: List of optical components and associated symbols. These symbols are taken or adapted from Alexander Franzen's *ComponentLibrary* (version 3, available at <http://www.gwoptics.org/ComponentLibrary/>), which is licensed under the Creative Commons Attribution-NonCommercial 3.0 Unported License (<http://creativecommons.org/licenses/by-nc/3.0/>).

Chapter 1: Introduction

1.1 Alkaline-Earth Atoms

The advent of laser cooling and the advancement of atom trapping techniques have enabled unprecedented control over atomic motion [1–6]. These developments have led to the use of laser-cooled atoms in a range of applications from precision measurements to studies of many-body quantum mechanics [7–14]. Among the early results was the observation of Bose-Einstein condensation [15–17] and Fermi degeneracy [18–21] in dilute gases of alkali atoms. A Bose-Einstein condensate (BEC) or degenerate Fermi gas (DFG) is the many-body ground state for a confined, three-dimensional gas of bosons or fermions, respectively. The trapping potential and the inter-atom interactions can be controlled externally [9, 11, 22–27], so a quantum degenerate gas can be forced to emulate a variety of physical systems [9]. If the changes to the potential and interactions are made adiabatically, the atomic gas will remain in its ground state and can be used to explore the low energy phase diagram of the simulated physical system [7, 9, 14]. This process is one example of quantum simulation, which we will examine further in Section 1.2.

The first efforts to laser cool alkaline-earth-metal (AE) atoms [28–38] were motivated by their application to frequency metrology [8, 39–47].¹ The valence shell of alkaline-earth atoms contains two electrons, which can pair their spins in either a singlet or triplet configuration (with the caveat that the pairing and orbital occupation must be consistent with the Pauli exclusion principle). In the electric dipole approximation, op-

¹For the purposes of this thesis, ytterbium is an alkaline-earth because it also has two valence electrons.

tical fields do not couple to the atomic magnetic moment, so we expect the singlet and triplet pairings to give rise to two completely independent level structures [48, 49]. The nuclear charge of the atom mixes the electronic spin and orbital angular momentum [48]. This mixing allows optical transitions between singlet and triplet levels to proceed, but with substantially smaller linewidths than dipole-allowed transitions (see Table 1.1 and Figure 1.1). Two of these transitions ($^1S_0 \rightarrow ^3P_0$ and $^1S_0 \rightarrow ^3P_2$) violate an additional transition selection rule,

$$J - J' = 0, \pm 1 \ (J = 0 \nrightarrow J' = 0), \quad (1.1)$$

where J (J') is the total electronic angular momentum of the lower (upper) state of the transition [48, 50]. These *doubly-forbidden* transitions to $|^3P_0\rangle$ and $|^3P_2\rangle$ only have non-zero linewidths because there are higher-order effects, such as magnetic quadrupole transitions (for $|^3P_2\rangle$) and mixing among the 3P_J states (for $|^3P_0\rangle$) [51–55].² The $^1S_0 \rightarrow ^3P_0$ transition has been of particular interest to the atomic clock community because, in addition to its narrow linewidth and optical frequency, it is insensitive to first-order Zeeman shifts [56–59].

Degenerate gases of alkaline-earth atoms are primarily interesting because, in the 1S_0 and 3P_0 states, they are insensitive to magnetic fields and because they can be probed with unprecedented precision using the dipole-forbidden singlet-to-triplet transitions (see Figure 1.1). The $^1S_0 \rightarrow ^3P_1$ transition allows laser cooling to temperatures of $\lesssim 20 \mu\text{K}$ [33–38] and even, for Sr, to quantum degeneracy [65]. This transition has also been used to tune atomic interactions [27, 66–68], generate spin-orbit coupling in a DFG [69], produce homonuclear molecules [70–73], and aid excitation to Rydberg states (which have large principal quantum numbers) [74–76]. The doubly-forbidden transitions have enabled the observation of coherent nuclear spin exchange between electronic

²For example, the $^1S_0 \rightarrow ^3P_0$ transition in ^{87}Sr is predicted to have a linewidth $\simeq 1 \text{ mHz}$.

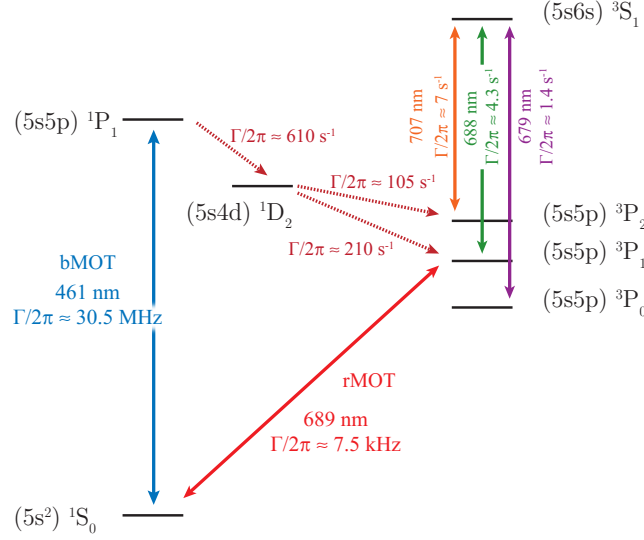


Figure 1.1: The lowest-lying energy levels of strontium that are relevant to this thesis (not to scale). Linewidths and decay rates (denoted here by Γ) are taken from [60–64]. Cooling on the strong $^1S_0 \rightarrow ^1P_1$ transition can reduce the atomic temperature to ≈ 1 mK. This transition has a slow leak (1 in 50,000 scattering events) that populates states in the 3P_J manifold. Atoms are returned to the ground state by optically pumping them to $|^3P_1\rangle$ via $|^3S_1\rangle$. The weaker $^1S_0 \rightarrow ^3P_1$ transition allows cooling to temperatures ≈ 1 μ K. Doubly-forbidden transitions from the ground state to either $|^3P_0\rangle$ ($\lambda = 698$ nm) or $|^3P_2\rangle$ ($\lambda \approx 671$ nm) will allow high precision spectroscopy and manipulation of quantum degenerate gases.

states [77, 78], the control of which is a prerequisite for quantum computation schemes in AE atoms [79–81]. These doubly-forbidden transitions can also probe BECs [55, 82] and be used to study many-body dynamics in optical lattices [83–85]. Stray magnetic fields are an important noise source in precision measurements, so using ultracold or degenerate gases that are insensitive to such fields is advantageous [86–89]. Fermionic AE isotopes have a small magnetic moment due to their nuclear spin, I (all bosonic AE atoms have nuclear spin, $I = 0$, see Table 1.1). However, because the nuclear magnetic moment is so small, the nuclear spin state is not perturbed by collisions between the fermionic atoms [90]. The collisions conserve not only the total nuclear angular momentum, but also its projection onto the quantization axis. This extra conservation law is the manifestation (by Noether’s theorem) of an underlying $SU(2I + 1)$ symmetry obeyed by the collisions.³ There are several interesting condensed matter systems that have $SU(N)$ -

³The literature typically denotes this symmetry as $SU(N)$, where $N = 2I + 1$, and I shall refer to it

Table 1.1: Scattering lengths (a_s) [108–112], transition linewidths [62,63,113], nuclear spin (I), and natural abundances [114,115] for the alkaline-earth(-like) elements that have been cooled to degeneracy. Alkaline-earth atoms have an even number of electrons and an even number of protons. Thus, the bosonic isotopes also possess an even number of neutrons. In nuclei with an even number of both protons and neutrons, the nucleons pair their spins in a singlet configuration and so all alkaline-earth bosons have nuclear spin $I = 0$.

Isotope	a_s	$\Gamma_{1S_0 \rightarrow 1P_1}$	$\lambda_{1S_0 \rightarrow 1P_1}$	$\Gamma_{1S_0 \rightarrow 3P_1}$	$\lambda_{1S_0 \rightarrow 3P_1}$	I	Abundance
^{40}Ca	$440 a_0$	34.7 MHz	423 nm	370 Hz	657 nm	0	96.94%
^{43}Ca	$\approx 65 a_0$					7/2	0.13%
^{84}Sr	$123 a_0$	30.5 MHz	461 nm	7.5 kHz	689 nm	0	0.56%
^{86}Sr	$823 a_0$					0	9.86%
^{87}Sr	$96 a_0$					9/2	7.00%
^{88}Sr	$-2 a_0$					0	82.58%
^{168}Yb	$252 a_0$	30.6 MHz	399 nm	182 kHz	556 nm	0	0.12%
^{170}Yb	$64 a_0$					0	2.98%
^{171}Yb	$-3 a_0$					1/2	14.08%
^{172}Yb	$-699 a_0$					0	21.69%
^{173}Yb	$199 a_0$					5/2	16.10%
^{174}Yb	$105 a_0$					0	32.02%
^{176}Yb	$-24 a_0$					0	13.00%

symmetric Hamiltonians [90–101] and these Hamiltonians could be simulated using an AE atom DFG [69, 102–104].⁴

The creation of degenerate gases of AE atoms is technically challenging. Many cooling and trapping techniques can only be applied to magnetic elements [3, 6, 15–18, 50], such as alkali atoms. Temperatures less than $\approx 100 \mu\text{K}$ have only been reached in atomic gases of AE atoms by laser cooling on the dipole-forbidden $1S_0 \rightarrow 3P_1$ transition [33–38]. Laser systems capable of efficiently exciting this transition are complicated and, for Sr and Ca, were not commercially available until recently. In addition, the wavelength of the $1S_0 \rightarrow 1P_1$ transition is $< 560 \text{ nm}$ for all AE elements [113]. Lasers that produce light at such short wavelengths have low power output or incorporate frequency doubling. As

as such. Note that $SU(N)$ is the special unitary group of order N .

⁴Many Hamiltonians in high-energy physics also exhibit $SU(N)$ -symmetry and so there have been proposals to simulate lattice gauge theories using AE atoms [105–107].

such, these laser systems are typically very expensive and can be difficult to maintain.

The first AE isotope to be cooled to degeneracy was ^{174}Yb [116]. The poor collisional properties of the most abundant isotopes hampered progress toward degeneracy in calcium and strontium (see Table 1.1). Bose-Einstein condensation was achieved in both elements in 2009 [111, 117, 118]. All the AE isotopes in Table 1.1 (save ^{172}Yb and ^{43}Ca) have been brought to degeneracy [119–124] and research is proceeding at several additional institutions [77, 78, 125–128]. Calcium is difficult to work with due to the very narrow linewidth of its $^1S_0 \rightarrow ^3P_1$ transition. The low natural abundance of the only stable fermionic isotope, ^{43}Ca , also restricts the study of $SU(N)$ -symmetric Hamiltonians. Ytterbium is the easiest AE element to cool to degeneracy due to the favorable scattering properties of several of its naturally abundant isotopes and its comparatively broad $^1S_0 \rightarrow ^3P_1$ transition. However, the 182 kHz width of this transition is a disadvantage in many applications [66, 68, 69], and the related higher temperatures in the ytterbium narrow-line MOT limited the degenerate gas atom number until recently [128, 129]. The 7.5 kHz wide $^1S_0 \rightarrow ^3P_1$ transition in strontium (see Figure 1.1) allows laser cooling to temperatures lower than 1 μK [65, 130], and consequently enables the production of large degenerate gases [131]. The fermionic isotope of strontium, ^{87}Sr , has the largest nuclear spin of the AE atoms and it can be used to implement $SU(N)$ -symmetric Hamiltonians for N as large as 10. For these reasons, we have chosen to work with strontium rather than ytterbium or calcium.

1.2 Quantum Magnetism

In crystalline solids, the electron dynamics can often be described using a tight-binding model [7, 132–136]. The nuclei of the crystal can be thought of as lattice *sites* that the electrons *hop* among. When two electrons reside on the same site, they interact via the Coulomb potential. The Hamiltonian for such a system, restricted to its lowest energy

band, is called the Fermi-Hubbard Hamiltonian (see Figure 1.2),

$$H = -J \sum_{\langle i,j \rangle} \sum_{m_F} (c_{i,m_F}^\dagger c_{j,m_F} + h.c.) + U \sum_i \sum_{m_F > m_{F'}} n_{i,m_F} n_{i,m_{F'}} + \sum_i \sum_{m_F} \epsilon_i n_{i,m_F}. \quad (1.2)$$

The first sum represents electron hopping among sites, the second sum encapsulates the on-site interaction between electrons, and the last sum describes site-dependent energy offsets (of size ϵ_i). In anticipation of the rest of this section, We are neglecting any possible spin dependence in the interaction and using m_F to indicate the spin projection onto the quantization axis. Sites of the crystal lattice are indexed by i and j . The fermionic operator, c_{i,m_F}^\dagger , creates an electron on site i with spin projection m_F (*i.e.* it creates an electron in state $|i, m_F\rangle$). We take the sum on $\langle i, j \rangle$ over the set of all nearest neighbors i and j . There are $n_{i,m_F} = c_{i,m_F}^\dagger c_{i,m_F}$ electrons with spin projection m_F on the lattice site i . The parameters, J and U , can be calculated using the Wannier basis functions, $w(\vec{x}) = \langle \vec{x} | i, m_F \rangle$,

$$\begin{aligned} J &= - \int d\vec{x} w(\vec{x}) \left(-\frac{\hbar^2 \nabla^2}{2m} + V(\vec{x}) \right) w(\vec{x} - \vec{x}_0), \\ U &= g_0 \int d\vec{x} d\vec{x}' w^2(\vec{x}) \delta(\vec{x} - \vec{x}') w^2(\vec{x}'), \end{aligned} \quad (1.3)$$

where m is the mass, $V(\vec{x})$ is the lattice potential, \vec{x}_0 is the lattice period, $g_0 \delta(\vec{x} - \vec{x}')$ is the interaction potential,⁵ $\delta(\vec{x})$ is the Dirac delta function, and $\vec{x} - \vec{x}'$ is the interparticle distance [9, 79, 90, 137, 138]. For repulsive interactions ($g_0 > 0$) and $\epsilon_i = 0$, the Hamiltonian 1.2 exhibits a quantum phase transition from a metallic phase, when $J \gg U$, to a Mott insulating phase, when $U \gg J$ [7, 9, 133, 137, 138]. The Hamiltonian 1.2 has also been proposed as a model for high- T_c superconductivity [135]. The extent to which the Fermi-Hubbard Hamiltonian 1.2 captures the interesting behavior of condensed matter systems such as high- T_c superconductors is not yet clear [135, 139, 140]. Efforts in this direction

⁵This approximation for the interaction potential is valid under the assumption that the positively charged nuclei screen the Coulomb interaction at long range.

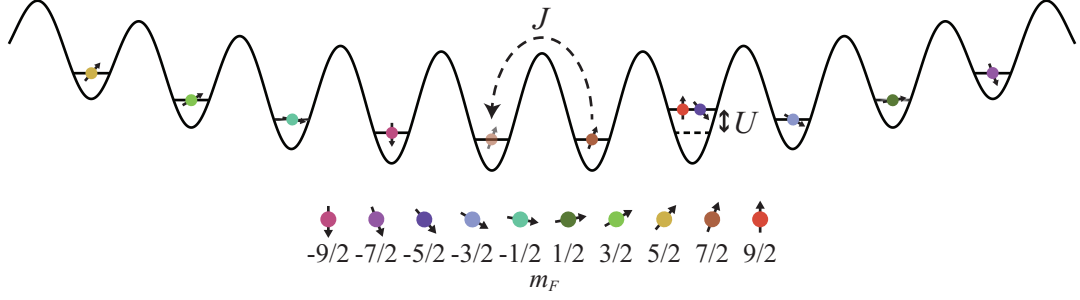


Figure 1.2: Proposed realization of $SU(N)$ -symmetric Hamiltonians in an optical lattice. Atoms can hop between lattice sites and reduce their energy by J . If two atoms occupy the same lattice site, there is an energy cost U . The figure shows two technical issues that are not discussed in the text. An external harmonic trapping potential causes the atomic density to vary across the lattice and the Gaussian profile of the lattice beams causes the lattice depth to vary as well.

are hampered because the ϵ_i are typically not well controlled in condensed matter systems and because a theoretical, or computational, description of the strongly-interacting regime of the Fermi-Hubbard model is challenging [135, 139–142].

The dynamics of fermionic atoms confined in the nodes (or anti-nodes) of an optical standing wave, an *optical lattice*, are also governed by the Fermi-Hubbard Hamiltonian 1.2 (see Figure 1.2) [9, 90, 137, 138]. In alkali atoms, U depends on the atomic spin projection, m_F , due to the magnetic moment of the unpaired valence electron [9]. However, in AE atoms, U is independent of atomic spin state because the collisions are $SU(N)$ -symmetric [90].⁶ When $U \gg J$, a Mott insulating state forms and the number of atoms on each lattice site is restricted to integer values that are determined by the local chemical potential [9, 90, 137, 138]. Deep in the Mott insulating regime, we can perform a perturbative expansion on the Hamiltonian 1.2 using J as the small parameter. The development and study of such an expansion is generically non-trivial, so I refer the interested reader to the literature [90, 143–153]. However, if we restrict ourselves to uniform filling of the lattice,⁷ the perturbative Hamiltonian takes on a particularly simple

⁶Note that, because both the 1S_0 and 3P_0 states obey $SU(N)$ symmetry, alkaline-earth atoms can be used to study a more generic two-orbital $SU(N)$ -symmetric Fermi-Hubbard Hamiltonian, which I will not discuss here [90, 95].

⁷This means that we are neglecting the last term in Equation 1.2.

form that illustrates the essential physics [90],

$$H = \frac{2J^2}{U} \sum_{\langle i,j \rangle} S_{ij}^2, \quad (1.4)$$

where $S_{ij}^2 = \sum_{m_F, m_F'} S_{m_F'}^{m_F}(i) S_{m_F}^{m_F'}(j) = \sum_{m_F, m_F'} c_{i, m_F'}^\dagger c_{i, m_F} c_{j, m_F}^\dagger c_{j, m_F'}$, swaps the atomic spin state between sites i and j .⁸ Even the comparatively simple Hamiltonian of Equation 1.4 is predicted to display exotic phases, depending on the number of atoms per site and the number of populated spin states [90, 92, 93, 96–101, 154].

The perturbative expansion that leads to Equation 1.4 is only valid when the thermal energy, $k_B T$, is smaller than the spin exchange energy, which is on the order of J^2/U . Since the atoms are typically confined in a lattice formed by several retroreflected lasers with wavenumber, k , the natural energy scale is the photon recoil energy, $E_R = \hbar^2 k^2 / 2m$. When the lattice depth, V_0 , is much larger than E_R , J and U are given by

$$\begin{aligned} J &= \frac{4}{\sqrt{\pi}} E_R \left(\frac{V_0}{E_R} \right)^{3/4} e^{-2\sqrt{V_0/E_R}}, \\ U &= \sqrt{\frac{8}{\pi}} k a_s E_R \left(\frac{V_0}{E_R} \right)^{3/4}, \end{aligned} \quad (1.5)$$

where a_s is the s -wave scattering length and $g_0 = 4\pi\hbar^2 a_s / m$ for cold atoms (see Equation 1.3) [155–158].⁹ For a simple, cubic, three-dimensional optical lattice, the Mott transition occurs when $U \approx 36J$ [138]. If we use a_s for ^{87}Sr (see Table 1.1) and assume a 1064-nm lattice laser wavelength, then the Mott transition occurs when $V_0 \approx 14E_R$. At this lattice depth, $J^2/k_B U \approx 20$ pK, which is extraordinarily small (even in the context of an ultracold atom experiment). To my knowledge, only two experiments have succeeded in reaching equilibrium temperatures similar to J^2/U [159, 160].¹⁰

⁸Because I've written the Hamiltonian in terms of S_{ij}^2 instead of $\vec{S}_i \cdot \vec{S}_j$, the numerical prefactor is 2 and not 4 [9, 49, 90].

⁹The scattering length is the radial intercept of the long-range scattering wavefunction [49]. In the absence of $SU(N)$ symmetry of the collisions, we would replace a_s with the interspecies scattering length.

¹⁰Other groups have observed spin exchange interactions with systems prepared out of equilibrium [161–

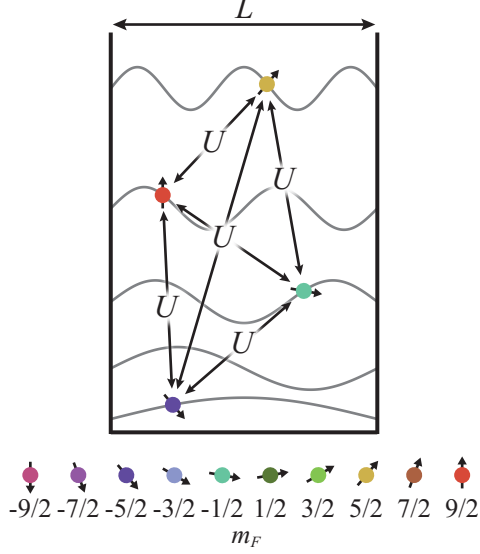


Figure 1.3: Proposed realization of $SU(N)$ -symmetric spin Hamiltonians in a one-dimensional uniform potential. In the limit of weak interactions, U , atoms cannot jump between energy levels of the box potential during a collision. Atoms can only exchange their spin state. The energy levels of the square well potential act like sites in an optical lattice, but the effective spin-spin interaction has infinite range.

Because there are significant challenges to achieving $k_B T \lesssim J^2/U$, we would like to develop a way to study spin dynamics at higher temperatures. Figure 1.3 shows an alternative method for realizing spin Hamiltonians with cold atoms [165]. An ultracold gas can be made effectively one-dimensional by imposing a strong transverse confining potential. When the energy quantum of the harmonic transverse confinement, $\hbar\omega_x = \hbar\omega_y = \hbar\omega_\perp$, exceeds the chemical potential, the gas enters the thermodynamically one-dimensional regime.¹¹ The interactions of atoms in a one-dimensional regime can be described by a contact potential, $g_{1D}\delta(z - z')$, where $g_{1D} = 2\hbar\omega_\perp a_s$ and z is the axial coordinate [9, 157]. If the axial trapping potential is a one-dimensional infinite square well with length L , then the interaction energy, U , is

$$U = g_{1D} \int_0^L dz \phi_j(z) \phi_k(z) \phi_{j'}(z) \phi_{k'}(z) \quad (1.6)$$

[164].

¹¹Note that the collisions between the atoms are still three-dimensional because the transverse harmonic oscillator length $a_\perp = \sqrt{\hbar/m\omega_\perp}$ is much larger than a_s .

where $\phi_j(z) = \sqrt{2/L} \sin(j\pi z/L)$ is the wavefunction of an atom in a square well with energy, $E_j = (\hbar j\pi)^2/2mL^2$. The initial states of the colliding atoms are indexed by (j, k) and the final states are indexed by (j', k') . The integral in Equation 1.6 is non-zero only when $j \pm k = \pm(j' \pm k')$ and, for sufficiently weak interactions, conservation of energy requires that $j^2 + k^2 = j'^2 + k'^2$. Together, these two conditions imply that either $(j, k) = (j', k')$ or $(j, k) = (k', j')$, and so $U = 2\hbar\omega_\perp a_s/L$ [165]. Assuming that there is at most one atom per energy level,¹² the Hamiltonian for the system of particles in the box potential is then

$$H = -U \sum_{j < k} S_{jk}^2, \quad (1.7)$$

where S_{jk}^2 has the same form as in Equation 1.4 (the fermionic operator, c_{j,m_F}^\dagger , now creates an atom in the square well energy level j in the spin state $|m_F\rangle$) [165]. The Hamiltonians of Equation 1.4 and Equation 1.7 both describe spin exchange processes on a lattice. However, the interactions in Equation 1.7 are infinite range because the "lattice" sites are the energy levels of the one-dimensional box potential. Importantly, the Hamiltonian 1.7 is valid provided that $|E_j - E_k| > U$ for all occupied energy levels j and k . The lowest two energy levels have the smallest splitting, so we require

$$\frac{|E_2 - E_1|}{U} = \frac{3\hbar\pi^2}{4m\omega_\perp a_s L} > 1, \quad (1.8)$$

which is independent of the atomic temperature and can be satisfied by tuning the product $\omega_\perp L$. For ^{87}Sr , $U/2\pi\hbar = 10$ Hz satisfies Equation 1.8 for $L = 10 \mu\text{m}$ and $\omega_\perp/2\pi = 10$ kHz [165]. Degenerate gases have recently been produced in uniform (*i.e.* box-like) trapping potentials with length scales $\approx 10 \mu\text{m}$ [166–168]. This method for realizing $SU(N)$ -symmetric spin dynamics in a cold atom system is a viable path forward that does

¹²By loading a spin-polarized degenerate Fermi gas into the one-dimensional square well, we can ensure that there are no doubly-occupied energy levels. A laser addressing a doubly-forbidden transition could then initialize spin dynamics by changing the spin states of the atoms. This laser can also control the number of spin states that are populated, and so control the order, N , of the $SU(N)$ symmetry group.

not necessitate cooling to $\lesssim 100$ pK temperatures. We are currently working to extend the capabilities of our apparatus so that we can study degenerate gases in one-dimensional square-well potentials. As it is impossible to make an infinitely deep trap, we still need to produce the strontium gases with temperatures, and chemical potentials, $\lesssim 100$ nK to observe interesting dynamics (see Section 3.1.4.2).

1.3 Ultracold Gas Theory

We must prepare strontium degenerate gases to access the temperature regime where the spin physics discussed in Section 1.2 becomes observable. An ultracold gas becomes quantum degenerate when the spatial extent of a single particle wavefunction becomes comparable to the mean interparticle spacing. This condition is conveniently expressed in terms of the phase-space density,

$$\rho = n\lambda_T^3 = n\left(\frac{2\pi\hbar^2}{mk_BT}\right)^{3/2}, \quad (1.9)$$

where λ_T is the thermal de Broglie wavelength, n is the atomic density, m is the atomic mass, and T is the temperature of the ultracold gas. Quantum degeneracy occurs in a harmonically trapped gas when $\rho \gtrsim 1$.

We can detect a degenerate gas using an absorption image taken after the atoms have been released from our optical dipole trap (ODT, see Section 2.3) for a variable time-of-flight (TOF). The absorption image measures the optical depth of the strontium gas (see Section 3.2), from which we can extract the column density, $\tilde{n}(x, y) = \int dz n(\vec{x})$ (and we have taken \hat{z} to be the imaging axis) [169]. Near the trap center, the optical dipole trap produces a harmonic trapping potential,

$$V(\vec{x}) \approx V_0 + \frac{1}{2}m\omega_x^2x^2 + \frac{1}{2}m\omega_y^2y^2 + \frac{1}{2}m\omega_z^2z^2, \quad (1.10)$$

where the trap frequencies are $\omega_{x,y,z}$ and trap depth is V_0 (see Section 2.3). To distinguish a degenerate gas from a gas of thermal atoms, we must first understand the characteristics of a thermal gas expanding out of the ODT.

1.3.1 Thermal Atoms

For thermal gases (*i.e.* gases with $\rho \ll 1$), the Bose-Einstein and Fermi-Dirac distribution functions (f_{BE} and f_{FD} , respectively) can be approximated using Maxwell-Boltzmann statistics. The mean occupation of the single-particle state ℓ , with energy E_ℓ , is then given by the Maxwell-Boltzmann distribution function,

$$f_{MB}(E_\ell) = e^{-(E_\ell - \mu)/k_B T}, \quad (1.11)$$

where μ is the chemical potential. In the semiclassical approximation, Equation 1.11 becomes

$$f_{MB}(\vec{x}, \vec{p}) = e^{-(H(\vec{x}, \vec{p}) - \mu)/k_B T}. \quad (1.12)$$

The Hamiltonian, $H(\vec{x}, \vec{p})$, for our harmonically trapped gas is

$$H(\vec{x}, \vec{p}) = \frac{p^2}{2m} + [V(\vec{x}) - V_0], \quad (1.13)$$

where $V(\vec{x})$ and V_0 are defined in Equation 1.10. The density of thermal atoms in a harmonic trap is given by

$$n_{\text{th}}(\vec{x}) = \int d\vec{p} \frac{f_{MB}(\vec{x}, \vec{p})}{(2\pi\hbar)^3} = \frac{N_{\text{th}}}{\pi^{3/2} r_x r_y r_z} e^{-x^2/r_x^2 - y^2/r_y^2 - z^2/r_z^2}, \quad (1.14)$$

where $r_{x,y,z} = \sqrt{2k_B T / m\omega_{x,y,z}^2}$, $N_{\text{th}} = \int d\vec{x} n_{\text{th}}(\vec{x})$ is the atom number, and our assumption that $\rho \ll 1$ allows us to neglect the chemical potential [157]. When the cloud is released in TOF, it expands freely and so an atom initially at position \vec{x}_i with momentum \vec{p} can be

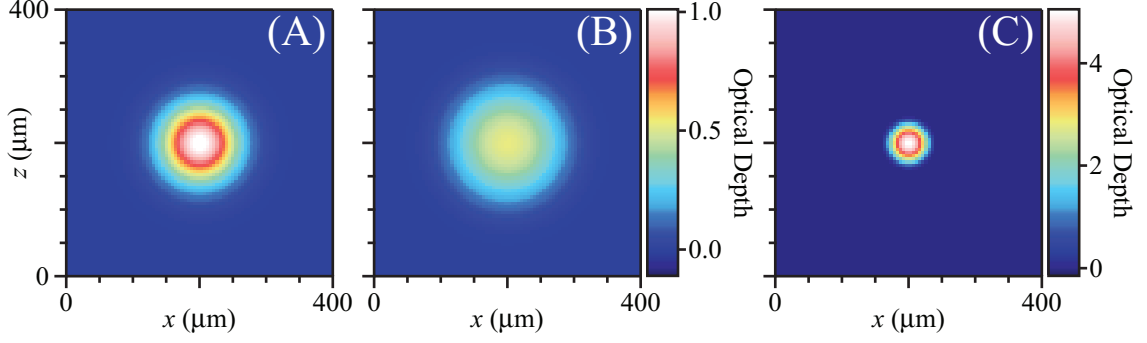


Figure 1.4: Ideal column density distributions for an ultracold gas that has expanded out of a harmonic trap for a long time-of-flight. A thermal gas (A), a degenerate Fermi gas (B), and a Bose-Einstein condensate (C). The distributions contain the same number of atoms and have the same characteristic widths. The fugacity, $\zeta = e^{\mu/k_B T}$, of the DFG is 100. (A) and (B) share the same color scale. The distributions were created using Equations 1.16 (A), 1.34 (B), and 1.24 (C).

found at a position

$$\vec{x}(t) = \vec{x}_i + \vec{p}t/m, \quad (1.15)$$

where t is the time of flight. We can use Equation 1.15 and Liouville's theorem to show that the semiclassical distribution of the atomic cloud after the time-of-flight is given by Equation 1.12 provided we replace \vec{x} with $\vec{x}(t) - \vec{p}t/m$. The density distribution in TOF can then be found by following the same procedure as we used to arrive at Equation 1.14. The result of this calculation, after an additional integration over the imaging axis, is [157]

$$\tilde{n}_{\text{th}}(x, y, t) = \frac{N_{\text{th}}}{\pi r_x(t) r_y(t)} e^{-x^2/r_x(t)^2 - y^2/r_y(t)^2}, \quad (1.16)$$

where $r_{x,y}(t) = r_{x,y} \sqrt{1 + \omega_{x,y}^2 t^2}$. For $t \gg \omega_{x,y}^{-1}$, the atomic cloud is isotropic with $r_{x,y}(t) = t\sqrt{2k_B T/m}$ (see Figure 1.4(A)).

1.3.2 Bose-Einstein Condensates

Bose-Einstein condensation occurs in an ideal gas when a macroscopic fraction of the constituent atoms occupies the ground state [48, 157, 169]. This macroscopic occupancy is possible only when the atoms obey Bose-Einstein statistics (*i.e.* the many-particle

wavefunction is symmetric under particle permutation). We will now show, following the derivation in [157], that a BEC will form in the three-dimensional Bose gas trapped in the ODT at a temperature, T_c , above absolute zero. In an ideal Bose gas, the mean occupation of the single-particle state ℓ , with energy E_ℓ , is given by

$$f_{BE}(E_\ell) = \frac{1}{e^{(E_\ell - \mu)/k_B T} - 1}. \quad (1.17)$$

On physical grounds, we expect $f_{BE}(E_\ell) > 0$, so the chemical potential must always be smaller than the energy of the ground state, E_0 . It can be shown that the number of atoms in excited states, N_{ex} , is

$$\begin{aligned} N_{\text{ex}} &= \sum_{\ell \neq 0} f_{BE}(E_\ell) \\ &\approx \int_{E_0}^{\infty} dE \frac{g(E)}{e^{(E - \mu)/k_B T} - 1} \\ &\leq \int_0^{\infty} dE' \frac{g(E')}{e^{E'/k_B T} - 1}, \end{aligned} \quad (1.18)$$

where $g(E)$ is the density of states, $E' = E - E_0$, and we have taken $\mu = 0$ on the last line of Equation 1.18. In the three-dimensional harmonic potential of our ODT (see Equation 1.10), $g(E) = E^2/(2\hbar^3\omega_x\omega_y\omega_z)$ and therefore

$$N_{\text{ex}} \leq (k_B T)^3 \int_0^{\infty} d\varepsilon \frac{\varepsilon^2}{e^\varepsilon - 1}, \quad (1.19)$$

where $\varepsilon = E'/k_B T$. The integral in Equation 1.19 is finite, so $N_{\text{ex}} \propto (k_B T)^3$. At T_c , we expect

$$N = N_{\text{ex}} = C(k_B T_c)^3, \quad (1.20)$$

where C is a constant.¹³ Equation 1.20 shows us that a BEC will form in a harmonically trapped, three-dimensional Bose gas at $T_c > 0$.¹⁴ Although we have assumed an ideal gas, the conclusion that $T_c > 0$ still holds for the interacting Bose gases present in the experiment [157].

Unlike the thermal cloud, the density of a condensate is given by

$$n_c(\vec{x}) = |\psi(\vec{x})|^2, \quad (1.21)$$

where $\psi(\vec{x})$ is the ground state many-body wavefunction and $\int d\vec{x} |\psi(\vec{x})|^2 = N_c$. We can calculate $\psi(\vec{x})$ using the time-independent Gross-Pitaevskii equation [157, 169–171]

$$-\frac{\hbar^2 \nabla^2}{2m} \psi(\vec{x}) + (V(\vec{x}) - V_0) \psi(\vec{x}) + g_0 |\psi(\vec{x})|^2 \psi(\vec{x}) = \mu \psi(\vec{x}). \quad (1.22)$$

The mean-field interaction between the atoms in the BEC is characterized by $g_0 = 4\pi\hbar^2 a_s/m$. In typical BECs (and certainly in those that we can produce), the mean-field term in Equation 1.22 dominates the kinetic energy term. The Gross-Pitaevskii equation can then be simplified by making the Thomas-Fermi approximation (where we completely neglect the kinetic term). After taking the approximation and combining Equations 1.21, 1.22, and 1.10, we find the Thomas-Fermi expression for the condensate density,

$$n_c(\vec{x}) = \frac{15N_c}{8\pi r_x^c r_y^c r_z^c} \max \left[1 - (x/r_x^c)^2 - (y/r_y^c)^2 - (z/r_z^c)^2, 0 \right], \quad (1.23)$$

where the $r_{x,y,z}^c = \sqrt{2\mu/m\omega_{x,y,z}^2}$ are the Thomas-Fermi radii. We can proceed as we did for a thermal gas (see Equation 1.16) to find the BEC column density after the time of

¹³Note that we've switched from a grand-canonical to a canonical description of the gas.

¹⁴This did not have to be the case. For example, it is well known that $T_c = 0$ for a homogeneous, two-dimensional Bose gas [157].

flight (see Figure 1.4(C)),

$$\tilde{n}_c(x, y, t) = \frac{5N_c}{2\pi r_x^c(t)r_y^c(t)} \max\left[\left(1 - \left(\frac{x}{r_x^c(t)}\right)^2 - \left(\frac{y}{r_y^c(t)}\right)^2\right)^{3/2}, 0\right], \quad (1.24)$$

The relationship between $r_{x,y}^c(t)$ and $r_{x,y}^c$ for our totally asymmetric ODT (*i.e.* $\omega_x \neq \omega_y \neq \omega_z$, see Table 2.3) must be measured or computed numerically [172]. However, for a radially-symmetric tube-shaped trap ($\omega_x = \omega_z \gg \omega_y$), the relationship between the time-of-flight and *in situ* Thomas-Fermi radii is [169, 172]

$$\begin{aligned} r_x^c(t) &= r_x^c \sqrt{1 + \omega_x^2 t^2}, \\ r_y^c(t) &= \frac{\omega_x}{\omega_y} r_x^c \left(1 + \frac{\omega_y^2}{\omega_x^2} \left[\omega_x t \arctan \omega_x t - \ln \sqrt{1 + \omega_x^2 t^2}\right]\right), \end{aligned} \quad (1.25)$$

and we have used $r_y^c/r_x^c = \omega_x/\omega_y$ (see Equation 1.23). For a long TOF ($t \gg \omega_{x,y,z}^{-1}$), the ratio of the Equations 1.25 is $r_y^c(t)/r_x^c(t) = (\pi/2)(\omega_y/\omega_x)^2$. The aspect ratio of an asymmetric BEC inverts after a sufficiently long time of flight.

We have two ways to distinguish a BEC from a thermal gas in our TOF absorption images. First, when $T \lesssim T_c$, the density distribution of the ultracold gas after TOF,

$$\tilde{n}_{\text{tot}}(x, y) = \tilde{n}_{\text{th}}(x, y) + \tilde{n}_c(x, y), \quad (1.26)$$

is bimodal and the time-dependence is now implicit (see Equation 1.16 and Equation 1.24). For $T \ll T_c$, $\tilde{n}_{\text{tot}}(x, y) \rightarrow \tilde{n}_c(x, y)$. Second, the aspect ratio of the BEC inverts in time of flight (see Equation 1.25). The inversion of the aspect ratio occurs because the momentum-space density of the BEC, $n_c(\vec{p})$, is related to the condensate's position-space density, $n_c(\vec{x})$, through a Fourier transform. In contrast, the aspect ratio of a thermal gas never inverts and a thermal cloud is asymptotically isotropic (see Equation 1.16). Our ODT is totally asymmetric and the tightest confinement is along the vertical axis. Observing that the vertical width is greater than the horizontal width of an ultracold gas is the least

ambiguous way to distinguish a BEC from a thermal gas in our trapping configuration.

1.3.3 Degenerate Fermi Gases

Neutral strontium has a single stable fermionic isotope, ^{87}Sr . Fermions obey Fermi-Dirac statistics and so the mean occupation of a single-particle state ℓ , with energy E_ℓ , is

$$f_{FD}(E_\ell) = \frac{1}{e^{(E_\ell - \mu)/k_B T} + 1}. \quad (1.27)$$

The Fermi-Dirac distribution is similar to the Bose-Einstein distribution (Equation 1.17), but the sign of the constant in the denominator has flipped. The change of sign is significant because it means that, in contrast with Equation 1.17,

$$f_{FD}(E_\ell) \leq 1. \quad (1.28)$$

We can see from Equation 1.27 that in the $T \rightarrow 0$ limit all states ℓ with $E_\ell < \mu_{T \rightarrow 0}$ will have unit occupancy and all states ℓ with $E_\ell > \mu_{T \rightarrow 0}$ will be empty. The chemical potential at $T \rightarrow 0$, $\mu_{T \rightarrow 0}$, defines a temperature scale,

$$k_B T_F = \mu_{T \rightarrow 0}, \quad (1.29)$$

where T_F is the Fermi temperature. The number of atoms in a harmonically trapped, three-dimensional, gas when $T \rightarrow 0$ is given by

$$\begin{aligned} N &= M \int_0^\infty dE g(E) f_{FD}(E) \\ &= \frac{M}{2\hbar^3 \bar{\omega}^3} \int_0^{\mu_{T \rightarrow 0}} dE E^2 \\ &= \frac{M \mu_{T \rightarrow 0}^3}{6\hbar^3 \bar{\omega}^3}, \end{aligned} \quad (1.30)$$

where M is the number of populated spin states, $\bar{\omega} = (\omega_x \omega_y \omega_z)^{1/3}$, and we are assuming equal occupation of each populated spin state [157]. By combining Equation 1.29 and Equation 1.30, we find the functional dependence of T_F on N ,

$$k_B T_F = \hbar \bar{\omega} \left(\frac{6N}{M} \right)^{1/3}. \quad (1.31)$$

For $T < T_F$ occupation of states with $E > k_B T_F$ is exponentially suppressed, while for $T > T_F$ the gas will be governed by Maxwell-Boltzmann statistics. A Fermi gas, such as an ultracold cloud of ^{87}Sr , is called a degenerate Fermi gas (DFG) when its temperature is less than the Fermi temperature (*i.e.* $T/T_F < 1$). The crossover into the quantum degenerate regime is smooth for a Fermi gas, while for a Bose gas there is a phase transition at the onset of degeneracy (see Section 1.3.2). This smooth crossover makes detection of a DFG substantially more difficult than detection of a BEC.

The density distribution of a Fermi gas can be found, in a semiclassical approximation, by integrating the Fermi-Dirac distribution (Equation 1.27) over momentum, \vec{p} ,

$$n_{FD}(\vec{x}) = \frac{1}{(2\pi\hbar)^3} \int \frac{d\vec{p}}{\zeta^{-1} e^{H(\vec{x}, \vec{p})/k_B T} + 1} \quad (1.32)$$

where $\zeta = e^{\mu/k_B T}$ is the fugacity [173–177]. After carrying out the integral in Equation 1.32, we find,

$$\begin{aligned} n_{FD}(\vec{x}) &= - \left(\frac{mk_B T}{2\pi\hbar^2} \right)^{3/2} \text{Li}_{3/2} \left(- \zeta e^{-x^2/r_x^2 - y^2/r_y^2 - z^2/r_z^2} \right) \\ &= - \lambda_T^{-3} \text{Li}_{3/2} \left(- \zeta e^{-x^2/r_x^2 - y^2/r_y^2 - z^2/r_z^2} \right) \end{aligned} \quad (1.33)$$

where $r_{x,y,z} = \sqrt{2k_B T / m\omega_{x,y,z}^2}$ and $\text{Li}_s(\nu)$ is the polylogarithm of order s [173, 175–177]. A free expansion of duration t and integration along the imaging axis yields the column

density distribution,

$$\tilde{n}_{FD}(x, y, t) = -\frac{m(k_B T)^2}{2\pi\omega_z\hbar^3\sqrt{1+\omega_x^2 t^2}\sqrt{1+\omega_y^2 t^2}} \text{Li}_2\left(-\zeta e^{-x^2/r_x(t)^2-y^2/r_y(t)^2}\right), \quad (1.34)$$

where $r_{x,y}(t) = r_{x,y}\sqrt{1+\omega_{x,y}^2 t^2}$ [174–177]. The column density of a degenerate Fermi gas (Equation 1.34) is flatter, near the center, and broader, in the wings, than the equivalent distribution for a thermal gas (Equation 1.16) at the same temperature that contains the same number of atoms (see Figure 1.4(B)).

1.4 Thesis Outline

My thesis describes the construction and initial characterization of a new apparatus that is capable of producing degenerate quantum gases of strontium. In this chapter, I have discussed why such gases are of scientific interest, the theoretical tools that can be used to study them, and the application that we’re currently pursuing in the Campbell group.¹⁵ Chapter 2 contains the main result of the thesis: the realization, in our apparatus, of degenerate quantum gases of three isotopes of strontium. In Chapter 3, I detail the technical features of the experiment. The first experimental and theoretical results of the strontium project are presented in Chapters 4 and 5, respectively. Appendix A describes some technical aspects of the image processing for the fermionic isotope, ⁸⁷Sr. I hope that this thesis will be useful to future researchers on the Sr project and to others building toward strontium degeneracy. Remember, if you’re bored, build more red lasers!

¹⁵For a more general (and historical) background on ultracold strontium gases, I suggest (in chronological order) the theses of K. Vogel [178], M. Boyd [53], S. Nagel [179], A. Ludlow [180], P. Mickelson [181], and S. Stellmer [182].

Chapter 2: Production of Degenerate Gases

We have built an apparatus that can produce degenerate quantum gases of strontium. In this chapter, I discuss the creation of degenerate quantum gases of three of the stable isotopes of strontium (^{84}Sr , ^{86}Sr , and ^{87}Sr). The technical details of the apparatus are described in Chapter 3. Strontium experiments typically require three (or four) sequential cooling and trapping stages in a UHV chamber to increase the phase-space density of the atomic gas to the degenerate regime [117, 118, 121–123, 181–184] and ours is no different. The first trap is a Magneto-Optical Trap that operates on the blue, 461-nm, $^1S_0 \rightarrow ^1P_1$ transition (the bMOT). The bMOT captures strontium atoms from a Zeeman-slowed atomic beam and cools them to temperatures of $\simeq 1$ mK (see Section 2.1). These precooled atoms can be transferred to a second Magneto-Optical Trap (the rMOT), operating on the red, 689-nm, $^1S_0 \rightarrow ^3P_1$ transition, where the temperature is reduced to $\simeq 1$ μK (see Section 2.2). In some of our procedures, the bMOT-to-rMOT transfer is mediated by a magnetic quadrupole trap, the *metastable reservoir*, that can aid in the accumulation of the lower abundance strontium isotopes (see Section 2.1 and Chapter 4). The fourth trap is a 1064-nm crossed-beam Optical Dipole Trap (ODT) that allows us to perform forced evaporation on the ultracold gas, and so achieve quantum degeneracy (see Sections 2.3, 2.4, and 2.5).

2.1 The bMOT and the Metastable Reservoir

The bMOT provides the initial confinement and cooling of atomic strontium gases in the experiment. It is a standard, three-beam, retroreflected magneto-optical trap operating

on the broad ($\Gamma_{bl}/2\pi \simeq 30.5$ MHz [62, 63]), $^1S_0 \rightarrow ^1P_1$ transition at 461 nm [5, 28, 30, 31, 178, 185–188]. Due to the simple hyperfine structure of the 1S_0 state and the broad transition linewidth, the behavior of the bMOT can be described by Doppler-cooling theory. For simplicity, I will consider the case of two cooling beams that counter-propagate along the z -axis, so that atoms move freely along the transverse dimensions. An atom at position $\vec{x} = x\hat{x} + y\hat{y} + z\hat{z}$ and moving with velocity $\vec{v} = v_x\hat{x} + v_y\hat{y} + v_z\hat{z}$ within the bMOT volume then experiences an average scattering force [50]

$$\langle \vec{F}_s(\vec{x}, \vec{v}) \rangle = \hbar k_{bl} \frac{\Gamma_{bl}}{2} \left(\frac{s_+ \hat{z}}{1 + s_+ + 4(\Delta - \vec{k}_+ \cdot \vec{v} + g_{J'} \mu_B d\vec{B} \cdot \vec{x})^2 / \Gamma_{bl}^2} - \frac{s_- \hat{z}}{1 + s_- + 4(\Delta - \vec{k}_- \cdot \vec{v} - g_{J'} \mu_B d\vec{B} \cdot \vec{x})^2 / \Gamma_{bl}^2} \right), \quad (2.1)$$

where $k_{bl} = 2\pi/\lambda_{bl} = 2\pi/(461 \text{ nm})$ is the bMOT transition wavenumber, $d\vec{B} = dB\hat{z}$ is the magnetic field gradient, $g_{J'} = 1$ is the Landé g -factor for $|^1P_1\rangle$, Δ is the laser detuning, $\vec{k}_\pm = \pm k_{bl}\hat{z}$ is the wavevector of the upward (+) or downward (−) propagating beam, and s_\pm is the associated saturation parameter (here, and throughout the thesis, the z -axis is vertical and the x -axis is parallel to the atomic beam). The beam propagating along \vec{k}_\pm is circularly polarized in the σ^\pm state with respect to the quantization axis defined by \hat{z} . Equation 2.1 neglects the force due to gravity,¹ but implicitly includes factors that dependent on Clebsch-Gordan coefficients and the atomic angular momentum projection on to the quantization axis. These factors are all equal to unity for bosonic isotopes and need only be addressed explicitly when trapping ^{87}Sr (see Section 2.2 or [186]).

For sufficiently small displacements and velocities, the force in Equation 2.1 produces damped harmonic motion, so we would naively expect the temperature of the atomic gas confined in the bMOT to reach absolute zero. However, the discrete stochastic nature of the scattering force imposes two important restrictions on the physically realizable

¹In this section, this is reasonable because $\vec{F}_g \simeq 10^{-24}$ N is approximately $10^5\times$ smaller than the maximum scattering force.

Table 2.1: The isotope shifts of the 461-nm transition referenced to the transition frequency in ^{88}Sr , ω_{88} [189, 190]. For ^{87}Sr , the bMOT operates on the $F = 9/2 \rightarrow F' = 11/2$ transition. The g -factors for the fermionic excited states, $g_{F'}$, are also shown.

Isotope	Transition	$(\omega - \omega_{88})/2\pi$	$g_{F'}$
^{88}Sr	$^1S_0 \rightarrow ^1P_1$	0 MHz	
^{87}Sr	$^1S_0, F = 9/2 \rightarrow ^1P_1, F' = 7/2$	-9 MHz	-2/9
^{87}Sr	$^1S_0, F = 9/2 \rightarrow ^1P_1, F' = 11/2$	-52 MHz	4/99
^{87}Sr	$^1S_0, F = 9/2 \rightarrow ^1P_1, F' = 9/2$	-69 MHz	2/11
^{86}Sr	$^1S_0 \rightarrow ^1P_1$	-125 MHz	
^{84}Sr	$^1S_0 \rightarrow ^1P_1$	-270 MHz	

temperature [48, 50]. The scattering force is caused by discrete photon absorption events, each imparting a momentum of $\hbar k_{bl}$ to the atom. If the atomic cloud reaches the recoil temperature, $T_{\text{recoil}} = \hbar^2 k_{bl}^2 / mk_B$, further cooling cannot occur.² Each atom absorbs and re-emits photons randomly. Although the average force due to emission events is zero, the fluctuations in both the absorption and emission processes prevent the strontium gas temperature from lowering below [178, 191]

$$T = T_{\text{Doppler}} \frac{1 + s_+ + s_- + 4(\Delta/\Gamma_{bl})^2}{4|\Delta/\Gamma_{bl}|}. \quad (2.2)$$

The Doppler temperature, $T_{\text{Doppler}} = \hbar\Gamma_{bl}/2k_B$, is the lowest temperature that can be reached in Doppler-cooling theory. For the $^1S_0 \rightarrow ^1P_1$ transition, $T_{\text{recoil}} \simeq 1 \mu\text{K}$ and $T_{\text{Doppler}} \simeq 720 \mu\text{K}$, so the bMOT temperature is Doppler limited. MOTs with alkali atoms, which have complex hyperfine structure, can cool below the Doppler limit, but T_{Doppler} is the fundamental temperature limit in the bMOT.

The absence of sub-Doppler cooling in the bMOT also allows an additional heating mechanism, which can typically be neglected in alkali atom experiments, to adversely affect the sample temperature [192]. Local intensity imbalances, $s_+(x, y) \neq s_-(x, y)$,

²There are clever methods to surpass this limitation (see, *e.g.*, [50]), but they are not relevant to this thesis.

arising from imperfections in the transverse profile of the bMOT beams add a component to the low-velocity expansion of the scattering force that is proportional to $s_+(x, y) - s_-(x, y)$ and independent of \vec{v} . If we expand the scattering force in a series about $(\vec{x}, \vec{v}) = (0, 0)$, then

$$\langle \vec{F}_s(\vec{x}, \vec{v}) \rangle = - \left[C_z z + C_v v_z - C_s (s_+(x, y) - s_-(x, y)) \right] \hat{z}, \quad (2.3)$$

where C_z , C_v , and C_s are constants that depend on all the parameters in Equation 2.1 [48, 50, 192]. The last term in Equation 2.3 implies that the atomic motion damps toward a finite, imbalance-dependent velocity.³ Imperfections in the MOT beam optics cause $s_+(x, y) - s_-(x, y)$ to vary about its mean value across the transverse extent of the MOT with an approximately Gaussian distribution. The width of the distribution of transverse intensity fluctuations adds an additional width to the bMOT velocity distribution and so limits the temperature of the atomic gas.⁴ The magnitude of the heating effect depends on the MOT beam saturations, s_{\pm} , so a bMOT operating with total saturation $s_{\text{tot}} > 1$ to increase its atom loading rate is heavily penalized in achievable temperature. Note that sub-Doppler cooling and recoil heating both add terms to Equation 2.3 that are independent of s_{\pm} .⁵ When either of these processes significantly affects the MOT dynamics, as is the case in alkali MOTs, the additional heating term in Equation 2.3 can be reduced to a negligible level by reducing the cooling beam intensities.

We load our bMOT from a Zeeman-slowed atomic beam [1, 193] (the details of which I give in Chapter 3), which supplies a high flux of strontium atoms moving at velocities $\lesssim 100$ m/s to the bMOT capture region.⁶ The bMOT beams have a $1/e^2$ radius

³Because the motion is harmonic, this effect can also be viewed as a local offset to the bMOT center position.

⁴There are also density-dependent heating mechanisms, but the high achievable temperatures in the bMOT limit the density and so reduce their importance.

⁵The hyperfine structure of ^{87}Sr allows sub-Doppler cooling, but the achievable temperature is much higher than in the rMOT [186].

⁶Chirp slowing is ruled out by the technical details of the 461-nm slave laser (see Section 3.1.1) and strontium 2D MOTs with sufficiently high flux have not yet been demonstrated [194].

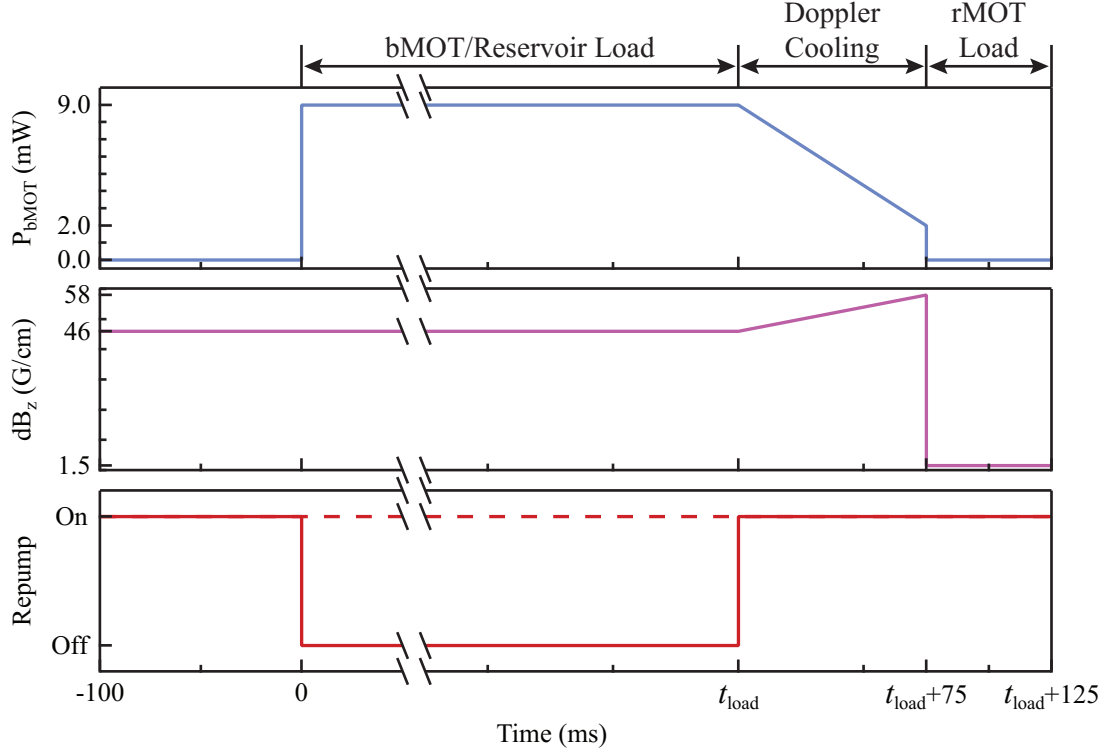


Figure 2.1: The intensity and field gradient ramps during the bMOT. We load either the bMOT (dashed red repumping line in the bottom panel) or the metastable reservoir (solid red line in the same panel) for a time, t_{load} . A 75 ms Doppler-cooling stage commences at the end of the loading time to reduce the temperature of the ultracold gas. When $t = t_{\text{load}} + 75$ ms, we extinguish the bMOT cooling light and change the magnetic field gradient to 1.5 G/cm to begin transfer of the strontium gas into the rMOT.

of ≈ 8 mm and a detuning of $\Delta/2\pi = -45$ MHz $\simeq -1.5\Gamma_{bl}/2\pi$. The sum of the saturation parameters of all six bMOT beams is $s_{\text{tot}} \approx 1.3$ and the magnetic field gradient, along the symmetry axis of the MOT quadrupole coil, during atom loading is $dB_z \approx 46$ G/cm. If we assume that each bMOT beam uniformly illuminates a 1.6 cm diameter circular region with an intensity given by $s_{\text{tot}}/2$ and that beams opposing the atomic velocity scatter photons at the maximum rate, then the bMOT will capture all atoms moving with velocity less than $v_c \simeq 80$ m/s.⁷ A slow leak (≈ 1 in 5×10^4 photon scattering events [61]) from the 1P_1 state shelves atoms in the metastable 3P_2 state, which is dark to the bMOT cooling light (see Figure 1.1). Shelved atoms can be returned to the bMOT cooling cycle using repumping lasers that pump these atoms into the comparatively short-lived 3P_1 state (see

⁷The approximation for the intensity preserves the total beam power.

Chapter 3 for details of the repumping scheme). Atoms that are shelved in low-field-seeking Zeeman sublevels of $|^3P_2\rangle$ are magnetically trapped by the quadrupole field of the bMOT [195] (the Landé g -factor for $|^3P_2\rangle$ is $g_J = 3/2$). If we opt to remove the repumping light, the bMOT will continuously load atoms into this metastable reservoir.

The experimental sequence for loading the bMOT is shown in Figure 2.1. The Zeeman slower loads the bMOT (corresponding to the dashed line in the Repump panel of Figure 2.1) or the metastable reservoir (corresponding to the solid line in the same panel) for a loading time, t_{load} . We set the loading time so that the atom number at the end of the broadband stage of the rMOT (see Section 2.2) is $\gtrsim 1 \times 10^7$. Our atom number requirement means that t_{load} is typically between 0.1 s and 10 s depending of the abundance of the loaded strontium isotope (see Table 2.1 for a list of the 461-nm transition isotope shifts and isotopic abundances). Once loading is complete, we use a Doppler-cooling stage in the bMOT to reduce the temperature of the ultracold gas (if atoms were loaded into the metastable reservoir, the repump lasers are turned on at this point). The power in each bMOT beam is ramped from its peak (≈ 9 mW) to ≈ 2 mW in 75 ms. Simultaneously, the magnetic field gradient is ramped from ≈ 46 G/cm to ≈ 58 G/cm, which alleviates the decompression induced by the intensity ramp. The atomic cloud temperature at this point is typically on the order of the Doppler temperature (*i.e.* $T \simeq 1$ mK). The final values of the bMOT power and field gradient, and the ramp duration, were chosen to maximize the atom transfer into the rMOT. After the Doppler-cooling stage, we extinguish the bMOT beams and snap the magnetic field gradient to 1.5 G/cm to begin atom transfer into the rMOT.

2.2 The rMOT

The rMOT cools the ultracold gas into the μK regime. It operates on the narrow, 689-nm, $^1S_0 \rightarrow ^3P_1$ intercombination transition ($\Gamma_r/2\pi \simeq 7.5$ kHz) and has a retrore-

Table 2.2: The isotope shifts of the 689-nm transition referenced to the transition frequency in ^{88}Sr , ω_{88} [196–198]. For ^{87}Sr , the rMOT requires light addressing both the $F = 9/2 \rightarrow F' = 11/2$ and the $F = 9/2 \rightarrow F' = 9/2$ transitions. The g -factors for the fermionic excited states, $g_{F'}$, are also shown.

Isotope	Transition	$(\omega - \omega_{88})/2\pi$	$g_{F'}$
^{87}Sr	$^1S_0, F = 9/2 \rightarrow ^3P_1, F' = 7/2$	1352 MHz	$-1/3$
^{87}Sr	$^1S_0, F = 9/2 \rightarrow ^3P_1, F' = 9/2$	222 MHz	$2/33$
^{88}Sr	$^1S_0 \rightarrow ^3P_1$	0 MHz	
^{86}Sr	$^1S_0 \rightarrow ^3P_1$	-164 MHz	
^{84}Sr	$^1S_0 \rightarrow ^3P_1$	-352 MHz	
^{87}Sr	$^1S_0, F = 9/2 \rightarrow ^3P_1, F' = 11/2$	-1241 MHz	$3/11$

flected, three-beam configuration.⁸ The simple, ground-state hyperfine structure for the bosonic isotopes means that Equation 2.1, with appropriate parameter replacements, still accurately describes the cooling force. For the rMOT, $T_{\text{Doppler}} = \hbar\Gamma_r/2k_B \simeq 180$ nK and $T_{\text{recoil}} = \hbar^2 k_r^2 / mk_B \simeq 460$ nK, so we expect an ultracold gas confined by the rMOT to reach temperatures $\lesssim 1$ μK [130, 199].⁹ However, several important complications arise because the rMOT cooling transition is $\approx 4000\times$ narrower than the bMOT cooling transition [33, 36, 130, 200, 201] (see Section 3.1.2 for a discussion of the technical challenge of addressing such a narrow transition). First, even if we make generous assumptions about the rMOT scattering force, the rMOT capture velocity, v_c , is $\lesssim 1$ m/s (see below for more details on the rMOT beam parameters). Because the rMOT has such a small v_c , the rMOT cannot efficiently capture atoms from the Zeeman-slowed atomic beam, necessitating the use of the bMOT for initial cooling. Second, appreciable photon scattering occurs only when

$$4(\Delta - \vec{k}_{\pm} \cdot \vec{v} \pm g_{J'}\mu_B d\vec{B} \cdot \vec{x})^2 \lesssim \Gamma_r^2, \quad (2.4)$$

⁸The laser beams for the rMOT and bMOT are combined before the vacuum chamber using dichroic mirrors, so the two traps share most of their optics.

⁹The rMOT is recoil limited, so the extra heating mechanism described in Section 2.1 is insignificant.

where $\vec{k}_\pm = \pm k_r \hat{z}$, $g_{J'} = 3/2$ is the Landé g -factor for $|^3P_1\rangle$, and Δ is the detuning from the $^1S_0 \rightarrow ^3P_1$ transition (other symbols have already been defined in Section 2.1). Because $\Gamma_r/2\pi = 7.5$ kHz, the condition of Equation 2.4 is only satisfied inside a small phase-space shell. The characteristic widths of this shell are $w_z = \Gamma_r/(g_{J'}\mu_B dB) \simeq 20 \mu\text{m}$ and $w_{v_z} = \Gamma_r/k_{bl} \simeq 5$ mm/s when $s_\pm \simeq 1$. Even if we assume the maximum available saturation, $s_\pm \simeq 2,400$, the widths of the shell only increase to $w_z \simeq 800 \mu\text{m}$ and $w_{v_z} \simeq 18$ cm/s. Both of these widths are smaller than the position and velocity distribution of the bMOT. By frequency modulating the rMOT beams, we can simultaneously cool atoms in many overlapping phase-space shells. Given our frequency modulation parameters and beam powers (see below), atoms in the phase-space region defined by $|\vec{x}| \lesssim 6$ mm, $|\vec{v}| \lesssim 1.4$ m/s will scatter photons rapidly.¹⁰ Third, the gravitational force is only $\simeq 16\times$ weaker than the maximum rMOT scattering force and so is an important perturbation to the rMOT dynamics.

Stable operation of the rMOT is even more complicated for ^{87}Sr due to its nuclear spin [36, 53, 182]. The 3P_1 state has electronic spin angular momentum while the 1S_0 state does not, which causes a large mismatch in the Landé g -factors. The g -factors, $g_{F'}$, for $|^3P_1\rangle$ are listed in Table 2.2 and the nuclear g -factor, g_I , for $|^1S_0\rangle$ is negligible compared to the transition linewidth (the ground-state magnetic moment is given by $\mu_I \times m_F \simeq 2\pi \times 200$ Hz/G $\times m_F$, where m_F is the projection of the total angular momentum along the quantization axis [53]). We illustrate the issue created by the g -factor mismatch in Figure 2.2. An atom experiences a restoring force at position z provided that the sign of

$$((m_F \pm 1)g_{F'}\mu_B - m_F\mu_I)dB_z z \quad (2.5)$$

is independent of m_F , where m_F is the projection of the total angular momentum along the quantization axis. Stable MOT operation occurs when the sign of Expression 2.5 is

¹⁰This overestimates the capture volume and capture velocity of the rMOT because I've neglected the Gaussian intensity profile of the rMOT beams.

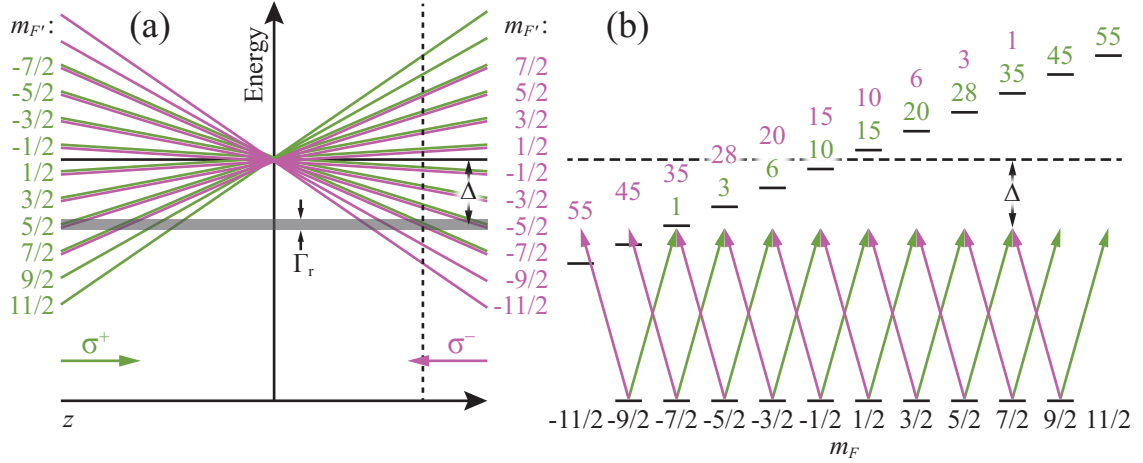


Figure 2.2: (a) The shift in the ^{87}Sr Zeeman levels of $|^1S_0, F = 9/2\rangle$ and $|^3P_1, F' = 11/2\rangle$ with position z in the magnetic field of the rMOT (note that the Zeeman shifts for $|^1S_0, F = 9/2\rangle$ are negligible on the energy scale of the figure). The ground (excited) state Zeeman levels are labeled using m_F ($m_{F'}$). The transparent grey band indicates the transition linewidth, Γ_r , and the laser detuning $|\Delta| \gg \Gamma_r$. The energy of the excited-state Zeeman level $|m_{F'}\rangle$ is shown in green (purple) if a σ^+ (σ^-) photon can cause a transition to it from the ground-state Zeeman level $|m_F = m_{F'} - 1\rangle$ ($|m_F = m_{F'} + 1\rangle$). Due to the mismatch in the ground- and excited-state Landé g -factors, ground-state atoms in Zeeman states with $m_F > 0$ ($m_F < 0$) only scatter photons on the left (right) side of the rMOT. (b) shows the Zeeman shifts and laser detunings at the position marked by the dotted vertical line in (a). (a) and (b) share the same vertical scale, so the spectral width of the excited-state Zeeman levels in (b) is the same as the width of the transparent grey band in (a). The green (purple) numbers in (b) are the square of the Clebsch-Gordan coefficients, normalized so the smallest coefficient is unity, for σ^+ (σ^-) transitions. The 55 : 1 of the squared Clebsch-Gordan coefficients for $\sigma^\pm : \sigma^\mp$ transitions favors trapping for $|m_F = \pm 9/2\rangle$ on the $\mp z$ side of the rMOT. Therefore, we can stabilize the fermionic rMOT by rapidly pumping the ground-state population toward the local stretched state ($|m_F = \pm 9/2\rangle$). See the text for a more detailed explanation.

independent of m_F for all positions z , which requires that [36]

$$\begin{aligned} \frac{F}{F+1} &< \frac{g_{F'}\mu_B}{\mu_I} < \frac{F}{F-1} \text{ for } F \rightarrow F+1, \\ \frac{F-1}{F} &< \frac{g_{F'}\mu_B}{\mu_I} < \frac{F}{F-1} \text{ for } F \rightarrow F. \end{aligned} \quad (2.6)$$

Confinement in the ^{87}Sr rMOT is provided by a *trapping* laser near-resonant with the $F = 9/2 \rightarrow F' = 11/2$ transition, which violates Equations 2.6. However, stable trapping is still possible because the $m_F = \pm 9/2$ states preferentially scatter photons that provide restoring momentum on the $\mp z$ -side of the MOT (which is also the case for some other $\pm m_F$ level pairs, see Figure 2.2). To realize a stable rMOT in this way, ^{87}Sr atoms in the $\mp z$ region must be optically pumped into $|m_F = \pm 9/2\rangle$, so that they feel a restoring force.

A second, *stirring*, laser that is near-resonant with the $F = 9/2 \rightarrow F' = 9/2$ transition can perform the optical pumping because the g -factor for $|F' = 9/2\rangle$ is substantially smaller than the $|F' = 11/2\rangle$ g -factor (see Table 2.2). The trapping laser, addressing $|F = 9/2\rangle \rightarrow |F' = 11/2\rangle$, confines ^{87}Sr atoms that are in locally trappable m_F levels and the stirring laser, addressing $|F = 9/2\rangle \rightarrow |F' = 9/2\rangle$, rapidly randomizes the ground-state spin populations to prevent atoms from accumulating in untrapped m_F levels.¹¹ Both the stirring and trapping lasers cool the ^{87}Sr , but the achievable rMOT temperature is limited because more optical power (as compared to the bosonic rMOT) is needed to maintain stable operation. We observe ^{87}Sr rMOT temperatures that are approximately 50% higher than temperature of a ^{84}Sr rMOT.

Here, I will discuss the rMOT trapping sequence for ^{87}Sr . The trapping sequence for bosonic isotopes is identical except that we need only one cooling laser to operate the rMOT. We have chosen to use the ^{87}Sr stirring laser for the $^{88,86,84}\text{Sr}$ rMOT because its laser locking setup is more flexible (see Section 3.1.2). Atom transfer into the rMOT commences at the end of the bMOT Doppler-cooling stage, $t = t_{\text{load}} + 75$ ms (see Figure 2.1 and Figure 2.3, which show the rMOT portion of the experimental sequence). The rMOT beams have a $1/e^2$ radius of 2.5 mm and the initial magnetic field gradient is 1.5 G/cm. The stirring and trapping beams are overlapped, with identical polarization helicity, using a polarization-maintaining fiber beamsplitter (see Section 3.1.2). Each stirring (trapping) beam initially contains 0.7 mW (3.25 mW) of power, which corresponds to $s_{\pm} \simeq 2,400$ (11,000). We increase the capture velocity of the rMOT by frequency modulating both lasers at 30 kHz with a modulation depth of 2 MHz. The near-resonant edge of the laser frequency spectrum has a detuning of ≈ -15 kHz for both lasers.¹² We operate the rMOT at these initial conditions for 50 ms to recapture atoms from the

¹¹The trapping instability discussed here also applies to the bMOT, but the large bMOT transition linewidth and small hyperfine splitting between $|F' = 11/2\rangle$ and $|F' = 9/2\rangle$ mean that the bMOT stirs itself (see Table 2.1).

¹²Note that, because we do not lock our 689-nm lasers to an atomic reference (see Section 3.1.2), there is an uncertainty, $\simeq \Gamma_r$, in the quoted laser detunings.

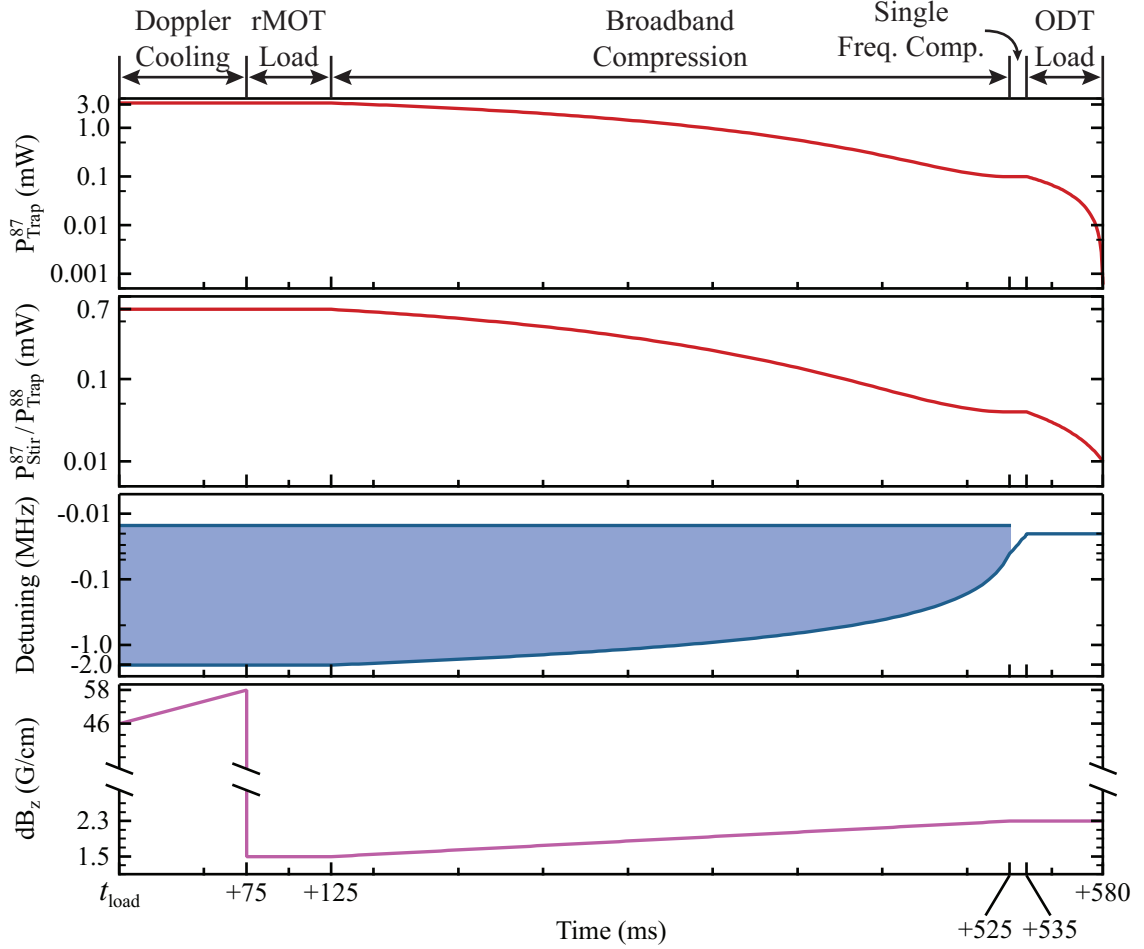


Figure 2.3: The temporal profiles of the rMOT trapping laser intensity (top), stirring laser intensity (upper middle), detuning (lower middle), and field gradient (bottom). The shaded region in the detuning graph indicates the spectral width of the laser frequency modulation. Atoms are recaptured from the bMOT for 50 ms. The rMOT is then cooled, by lowering the laser intensities, and compressed, by reducing the frequency modulation depth and increasing the magnetic field gradient, for 400 ms. The laser frequency modulation is then switched off and the detuning is further reduced to ≈ -20 kHz over 10 ms. During the final 45 ms of the rMOT, atoms are loaded into an optical dipole trap (see Section 2.3) while the stirring (trapping) laser power is ramped to $10 \mu\text{W}$ (600 nW). For experiments with bosonic isotopes, the ^{87}Sr stirring laser acts as the trapping laser and the ^{87}Sr trapping laser is unused. In all other ways, the experimental sequences for the bosonic rMOT and fermionic rMOT are identical.

bMOT. The atom transfer into the rMOT is only $\approx 15\%$ efficient, which is the primary limitation on the final atom number in our degenerate gases.¹³ We then compress the rMOT by linearly increasing the magnetic field gradient to 2.3 G/cm and linearly reducing the frequency modulation depth to 25 kHz over a period of 400 ms (see Figure 2.3 and note the logarithmic scale on several of the vertical axes). The powers in the stirring (trapping) beams are simultaneously reduced to 40 μ W (100 μ W) with a half-Gaussian temporal profile, $P(t) \propto P_{\text{init}} e^{-(t/t_{\text{ramp}})^2}$, with $t_{\text{ramp}} = 400$ ms. At the end of this broadband cooling period, the ultracold gas typically contains $\gtrsim 1 \times 10^7$ atoms (set by t_{load} , see Section 2.1) at a temperature $\lesssim 2$ μ K. As the cooling beam power is reduced during the broadband rMOT compression, the gravitational force causes the atoms to sag against the upward propagating rMOT beams, giving the rMOT a characteristic pancake shape [53, 180, 182]. The rMOT sits at a vertical position z_0 where the Zeeman shift and laser detuning adjust the scattering force such that it balances the gravitational force, which causes the sample temperature to decouple from the laser detuning.¹⁴ In this condition, we expect the strontium gas to reach a temperature

$$T \simeq \frac{\hbar \Gamma_r \sqrt{s_+ + 1}}{2k_B}, \quad (2.7)$$

which, with suitable substitutions for s_+ , is in reasonable agreement with our measurements (see [180] for further discussion and a derivation of Equation 2.7). To cool and compress the rMOT further, we turn off the frequency modulation, setting the single frequency detuning $\Delta \approx -40$ kHz, and then linearly ramp Δ to ≈ -20 kHz in 10 ms while the laser intensities are held constant. The rMOT overlaps with the optical dipole trap during the single frequency compression and dipole trap loading begins (see Section 2.3).¹⁵ At the

¹³The small size of the rMOT beams probably limits the transfer. Higher power trapping lasers would allow us to expand the beams and we've purchased a 689-nm tapered amplifier toward this end.

¹⁴The gravitational sag effect is more pronounced for the bosonic isotopes for two reasons: we use less optical power in the bosonic rMOT, and, in the ^{87}Sr rMOT, the equilibrium position, z_0 , varies with $|m_F\rangle$.

¹⁵We use magnetic bias fields to set the final rMOT position to coincide with the ODT. These fields are

end of the single frequency compression (and in the absence of the ODT), the rMOT retains $\approx 90\%$ of the atoms present at the end of the broadband compression. The rMOT temperature for $\{^{88}\text{Sr}, ^{87}\text{Sr}, ^{86}\text{Sr}, ^{84}\text{Sr}\}$ is approximately $\{600 \text{ nK}, 1.5 \text{ } \mu\text{K}, 1.3 \text{ } \mu\text{K}, 1.0 \text{ } \mu\text{K}\}$ and $\rho \gtrsim 10^{-2}$.¹⁶ We have found that increasing the single frequency compression time is detrimental to the atom number and does not reduce the final temperature. The ODT is loaded from the rMOT for 45 ms while the stirring (trapping) beam power is linearly reduced to 10 μW (600 nW). We turn off the rMOT beams and the magnetic quadrupole field at the end of the ODT loading time.

2.3 The Optical Dipole Trap

A 1064-nm, crossed-beam optical dipole trap confines the atoms during the final cooling to quantum degeneracy. The tightly-focused ODT beams induce an AC Stark shift on the energy levels of strontium atoms in the rMOT. The 1064-nm beams are red-detuned from the $^1S_0 \rightarrow ^1P_1$ and $^3P_J \rightarrow ^3S_1$ transitions, so the maximum 1064-nm laser intensity locally minimizes the energies of $|^1S_0\rangle$ and $|^3P_J\rangle$ [202]. That is to say, an atom experiences a potential, $V(\vec{x})$, proportional to the laser intensity, $I(\vec{x})$, due to the interaction of its induced electric dipole moment with the oscillating electric field of the 1064-nm laser:

$$V(\vec{x}) = -\frac{\text{Re}(\alpha(\lambda))I(\vec{x})}{2\epsilon_0 c}. \quad (2.8)$$

where $\alpha(\lambda)$ is the electric polarizability of the atom and λ is the ODT laser wavelength. The semiclassical expression for $\alpha(\lambda)$, with $\omega = 2\pi c/\lambda$, is

$$\alpha(\lambda) = 6\pi\epsilon_0 c \sum_j \frac{\Gamma_j/\omega_j^2}{\omega_j^2 - \omega^2 - i\Gamma_j \omega^3/\omega_j^2}, \quad (2.9)$$

supplied by several pairs of Helmholtz coils (see Section 3.4).

¹⁶Because ^{88}Sr is nearly non-interacting, it can be cooled to much lower temperatures than the other isotopes (see Table 1.1).

where $i = \sqrt{-1}$ and the j th atomic resonance occurs at a frequency ω_j with a natural decay rate Γ_j [202]. All the 1064-nm ODT beams are Gaussian, so, for a radially-symmetric single beam trap, $V(\vec{x})$ is characterized by two length scales: the Gaussian $1/e^2$ radius (*i.e.* the Gaussian waist), w , and the Rayleigh range, $R = \pi w^2/\lambda$. Near the focus of the Gaussian beam, we can expand the potential in a Taylor series and find that, to second order,

$$V(\vec{x}) \approx V_0 + \frac{1}{2}m\omega_x^2x^2 + \frac{1}{2}m\omega_y^2y^2 + \frac{1}{2}m\omega_z^2z^2, \quad (2.10)$$

where the m is the atomic mass and the origin coincides with the trap center. The trap frequencies, $\omega_{x,y,z}$, and trap depth, V_0 , can be computed from the Gaussian beam parameters and the polarizability of the atomic state, $\alpha(\lambda)$, at the wavelength of the ODT laser (1064 nm in this case) [53, 202] using

$$\begin{aligned} \omega_{x,y,z} &= \sqrt{\frac{\text{Re}(\alpha(\lambda))}{2m\epsilon_0 c} \left[\partial_{x,y,z}^2 I(\vec{x}) \right]_{\vec{x}=0}}, \\ V_0 &= -\frac{\text{Re}(\alpha(\lambda))I(0)}{2\epsilon_0 c}. \end{aligned} \quad (2.11)$$

When the force of gravity can be neglected, $V_0 \propto P$ and $\omega_{x,y,z} \propto \sqrt{P}$, where P is the optical power in the ODT beam. Far-detuned dipole traps are nearly conservative, but trapped atoms still scatter photons out of the ODT beam. In contrast to photon scattering in a MOT, scattering events in an ODT cause heating because the scattering rate does not depend on the atomic velocity. The maximum photon scattering rate occurs at the trap center and it is given by

$$\gamma_{scatt} = \frac{\text{Im}(\alpha(\lambda))I(0)}{\hbar\epsilon_0 c}. \quad (2.12)$$

For the dipole traps used in our experiment, $\gamma_{scatt} \lesssim 5 \times 10^{-3} \text{ s}^{-1}$. The associated heating rate is given by

$$\gamma_{heat} \leq 2E_R\gamma_{scatt} \lesssim 2 \text{ nK/s}, \quad (2.13)$$

where E_R is the recoil energy for the 1064-nm ODT laser and we have used our upper bound for γ_{scatt} .

An atomic gas in an optical dipole trap can be cooled using forced evaporation [21, 203–207]. The elastic collision rate, γ_{el} , between atoms is

$$\gamma_{el} = n_0 \sigma_e \bar{v}, \quad (2.14)$$

where n_0 is the peak atomic density, σ_e is the elastic scattering cross section, and $\bar{v} = \sqrt{16k_B T / \pi m}$ is the mean relative velocity [157]. For sufficiently small collision energies, the elastic cross section is approximately $\sigma_e = 8\pi a_s^2$ (for bosons) or $\sigma_e = 4\pi a_s^2$ (for fermions in distinct spin states), where a_s is the s -wave scattering length (see Table 1.1).¹⁷ The elastic collisions redistribute energy among the atoms and so allow some atoms to acquire an energy $E > V_0$. These atoms subsequently escape the trap and, because they necessarily carry away more than the average energy per particle, the atoms remaining in the trap will re-equilibrate to a lower temperature. Assuming that the ultracold gas obeys Maxwell-Boltzmann statistics and that $V_0 \gg k_B T$,¹⁸ the rate at which atoms with $E > V_0$ are created is [157, 208]

$$\gamma_{evap} = \gamma_{el} \frac{V_0}{\sqrt{2} k_B T} e^{-V_0/k_B T}. \quad (2.15)$$

The exponential term in Equation 2.15 quickly suppresses evaporation when V_0 is fixed. By continuously reducing the trap depth, we can maintain a favorable ratio of V_0 to $k_B T$ and force evaporative cooling to nK temperatures. Evaporative cooling will increase the phase-space density of our strontium gas provided that γ_{evap} exceeds the background gas collision rate and the 3-body molecule formation rate [208–213]. The background loss rate, $\Gamma_1 \simeq 0.1 \text{ s}^{-1}$, is constant, but the 3-body loss rate $\Gamma_3 \propto n_0^2 \sigma_e^2$.¹⁹ So, efficient

¹⁷It should be noted that this constant σ_e approximation is not very good for several strontium isotopes [109].

¹⁸This is not typically true for our dipole traps.

¹⁹I am distinguishing between the 3-body loss constant, K_3 and the 3-body loss rate, $\Gamma_3 \propto K_3 n_0^2$.

Table 2.3: The Gaussian $1/e^2$ radii for all the dipole traps. The horizontal lattice waist is calculated, but all other waists were extracted from parametric heating measurements [214]. To prevent crosstalk, all heating measurements were conducted in single beam traps (the vertical beams had to be setup in an optical lattice configuration to allow this). We estimate that the uncertainty is $\approx 10\%$ for most of the waist measurements. A thermal effect complicates the data for the cross pancake trap and so the extracted waists, reported here, are systematically larger than the actual beam waists.

Trapping Beam	w_x	w_y	w_z
Main Pancake	310 μm	–	31 μm
Cross Pancake	–	270 μm	16 μm
Vertical Cross/Lattice	105 μm	105 μm	–
Horizontal Lattice	–	100 μm	100 μm
Loose Vertical Cross	230 μm	230 μm	–

evaporation requires an intermediate n_0 that permits $\gamma_{\text{evap}} > \Gamma_1, \Gamma_3$.

Our optical dipole trap is formed by the intersection of three Gaussian beams and its design was heavily influenced by the work of the Rice and Innsbruck groups [131, 182, 215]. The Gaussian waists for all the beams implemented on the apparatus are listed in Table 2.3. The *main pancake* and *cross pancake* beams propagate in the horizontal plane and intersect at an angle of 45° . Both pancake beams were designed to have a $\approx 10:1$ aspect ratio with the tight waist aligned along the vertical axis (the cross pancake has a significantly different aspect ratio due to astigmatism). We chose this *crossed-pancake* trapping configuration to mimic the pancake shape of the rMOT. The *vertical cross/lattice* beam propagates along the z -axis and is aligned to the center of the crossed-pancake trap. Although the vertical beam does not support the atoms against gravity, it increases the horizontal trapping frequencies. The tighter horizontal confinement provided by the vertical beam is crucial to our realization of a degenerate Fermi gas (see Section 2.5). The vertical beam passes through a liquid crystal variable waveplate on the far side of the vacuum

chamber. Together, the variable waveplate and a polarizing beam cube act as a switch that can change vertical dipole beam into a vertical optical lattice. Each of the three ODT beams is linearly polarized along an axis that is perpendicular to the polarization vector of the other two beams (for more details, see Section 3.1.4.1).

Two additional dipole beam paths are installed on the apparatus. These are the *loose vertical cross* beam and the *horizontal lattice* beam (see Table 2.3).²⁰ The loose cross beam was used in conjunction with the main dipole beam to produce our first ⁸⁶Sr Bose-Einstein condensates (see Section 2.4.1). The confinement this beam produces is too weak to significantly assist in the evaporation of other strontium isotopes, and so we have discontinued its use. The horizontal lattice beam copropagates with the cross pancake beam and creates an optical lattice along the y-axis. In combination with the vertical cross/lattice beam, the horizontal lattice beam generates two-dimensional optical lattices. Atoms trapped in such lattices can form a thermodynamically one-dimensional system, which is a prerequisite for several of the theoretical proposals discussed in Section 1.2.

The ODT loading and forced evaporation sections of the experimental sequence for producing degenerate Fermi gases are shown in Figure 2.4. The evaporation ramps for producing Bose-Einstein condensates are similar and their differences from Figure 2.4 will be discussed in Section 2.4. We turn on the ODT beams at the beginning of the experimental cycle and hold them at the initial powers ($\{P_{\text{main}}, P_{\text{cross}}, P_{\text{vert}}\} = \{1.6 \text{ W}, 0.8 \text{ W}, 0.1 \text{ W}\}$) until loading from the rMOT is complete. The crossed-pancake ODT captures $\simeq 80\%$ ($\simeq 30\%$) of bosons (fermions) from the compressed, single-frequency rMOT.²¹ We make no effort to spin-polarize fermionic gases after loading into the dipole trap. All ODT beam powers are adiabatically increased to $\{P_{\text{main}}, P_{\text{cross}}, P_{\text{vert}}\} = \{3.2 \text{ W}, 1.6 \text{ W}, 0.6 \text{ W}\}$ in 200 ms with a sinusoidal ramp.²² These ramps compress the strontium gas and increase

²⁰These beams are not necessary for the results in this thesis, but I discuss them for completeness.

²¹The difference in transfer efficiencies is due to the differing rMOT gravitational sag for bosons and fermions (see Section 2.2).

²² $P(t) = \frac{P_f + P_i}{2} - \frac{P_f - P_i}{2} \cos(\pi t / t_{\text{ramp}})$, with $t_{\text{ramp}} = 200 \text{ ms}$.

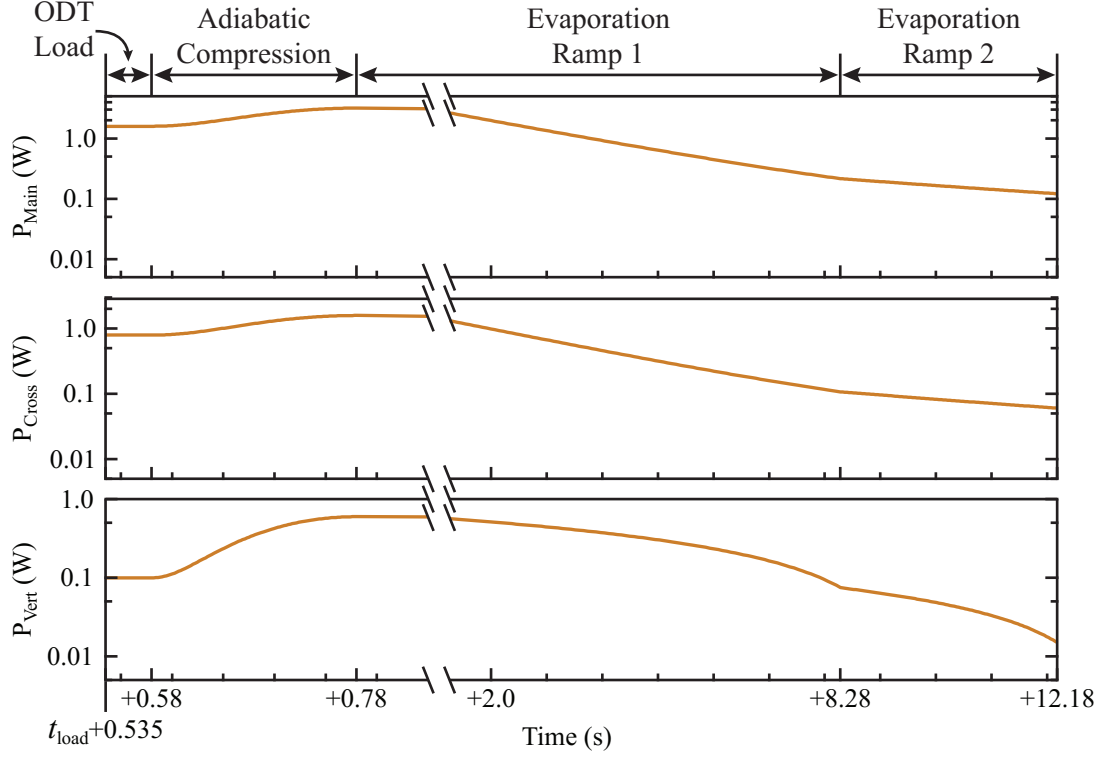


Figure 2.4: The power in the various ODT beams during trap loading and forced evaporation for ^{87}Sr . We load the ODT from the rMOT for 45 ms and then adiabatically compress the trap over a period of 200 ms. There are two exponential evaporation ramps with time constants of 2.5 s and 5.5 s, respectively. The vertical beam power is reduced linearly during both evaporation stages. The ramps are similar for experiments with the bosonic isotopes and the differences will be explained in Section 2.4.

the elastic scattering rate [169] (see Equation 2.14). Forced evaporation proceeds in two exponential ramp steps. The first ramp has a time constant of 2.5 s and a duration of 7.5 s for experiments with ^{87}Sr . These two parameters are varied depending on the strontium isotope (see Section 2.4). The second ramp has a time constant of 5.5 s and a variable duration. It is necessary only for achieving degeneracy in ^{87}Sr . Ramps for the vertical beam are linear rather than exponential. The vertical beam power after the first (second) evaporation ramp is 75 mW (15 mW). After the strontium atoms have been cooled to degeneracy, we snap off all ODT beams and allow the atomic cloud to expand for a variable time of flight (TOF). We then measure the momentum distribution of the gas using resonant absorption imaging on the $^1S_0 \rightarrow ^1P_1$ transition (see Section 3.2).

2.4 Strontium Bose-Einstein Condensates

2.4.1 ^{86}Sr BEC

The first degenerate gases we were able to produce were BECs of ^{86}Sr . The large scattering length of ^{86}Sr leads to a large 3-body loss rate, which limits the evaporation efficiency and final condensate atom number [121]. To overcome the large 3-body loss rate, Γ_3 , evaporation must proceed at a peak density $n_0 \simeq 10^{12} \text{ cm}^{-3}$ [131, 210]. Originally, we made ^{86}Sr BECs in an ODT consisting of the main pancake and loose vertical cross beams. We loaded the ODT with $P_{\text{main}} = 3 \text{ W}$ and $P_{\text{loose vert}} = 10 \text{ mW}$. After holding at the initial powers for 100 ms, the ODT contained $\simeq 3 \times 10^6$ ^{86}Sr atoms at $\simeq 600 \text{ nK}$. We exponentially reduced the power in the main beam for 2.5 s with a time constant of 1 s.²³ The loose vertical beam power was simultaneously increased linearly to $P_{\text{loose vert}} = 75 \text{ mW}$. At the end of the ramp, we had made nearly pure condensates containing $\simeq 3 \times 10^4$ atoms. The transition temperature was $\simeq 50 \text{ nK}$.

We have recently made ^{86}Sr BECs in the crossed-pancake ODT. Trap loading proceeds at the initial main and cross beam powers as described in Section 2.3. Neither vertical beam is used and we omit the adiabatic compression. Again, we hold at the initial powers for 100 ms and at the end of this time there are $\simeq 3 \times 10^6$ atoms remaining in the trap at $\simeq 900 \text{ nK}$. We exponentially ramp down the cross and main beam powers toward powers of 30 mW and 300 mW, respectively (these powers are the horizontal asymptotes of the ramps). The ramp duration is still 2.5 s and the time constant remains 1 s. Images of BECs produced in the cross-pancake trap are shown in Figure 2.5. By reducing the evaporation time, we produce partially condensed clouds that show the characteristic bimodal density distribution (Figure 2.5(A)). If we evaporate for the full 2.5 s, the ^{86}Sr BEC is nearly pure and contains $\simeq 1 \times 10^4$ atoms (Figure 2.5(B)). Both absorption images

²³The horizontal asymptote of the exponential ramp is the power at which gravity causes the trap depth to vanish.

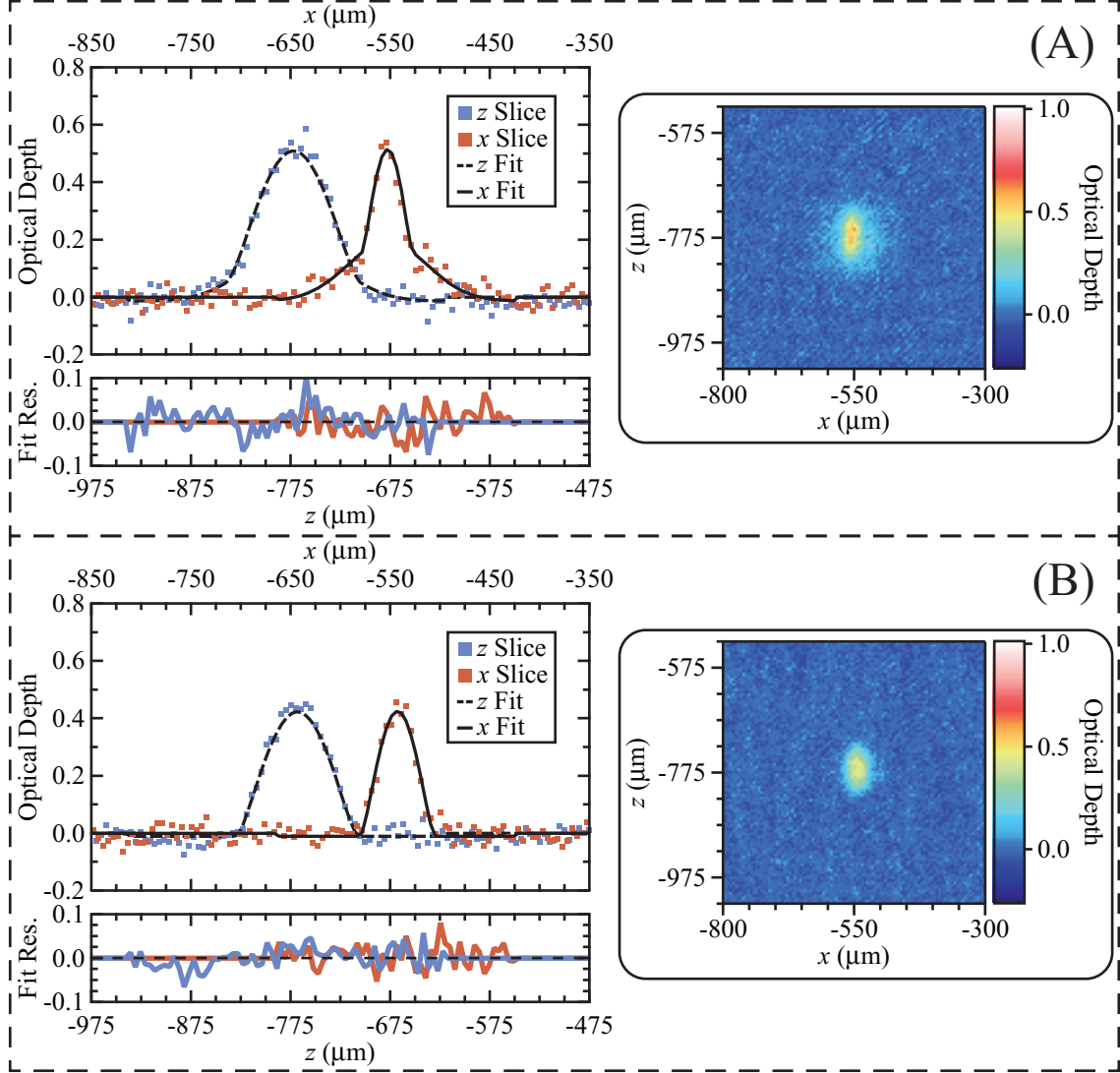


Figure 2.5: The first ^{86}Sr Bose-Einstein condensates produced in the crossed-pancake trap and observed using the horizontal imaging system (see Section 3.2). (A) A partially Bose-condensed cloud of ^{86}Sr atoms after a TOF of 25 ms (right). The left plot in (A) shows slices (averaged over 2 pixels) through the cloud and a two-dimensional fit to Equation 1.26. The temperature of the thermal component of the cloud in (A) is ≈ 30 nK. (B) The corresponding plots for a nearly pure ^{86}Sr BEC containing $\approx 1 \times 10^4$ atoms. Because the thermal fraction of the gas is small, we fit the image in (B) with Equation 1.24. The inversion of the aspect ratio can be seen clearly in both images.

in Figure 2.5 have inverted aspect ratios, which confirms the presence of a BEC. With further optimization of the trap loading and evaporation, the ^{86}Sr BEC atom number in the crossed-pancake could probably be increased to match the number we achieved in our original realization.

2.4.2 ^{84}Sr BEC

We have also succeeded in creating Bose-Einstein condensates of ^{84}Sr . The evaporation ramps for ^{84}Sr are identical to the ramps for ^{87}Sr (see Figure 2.4) except that the time constant for the first ramp is 0.75 s. Only the first ramp is necessary to reach quantum degeneracy, and in this section we do not use the second ramp. In Section 2.4.2.1, we create ^{84}Sr BECs using both evaporation stages to measure the ODT frequencies at the trapping conditions where we achieve Fermi degeneracy.

Figure 2.6 shows absorption images and fits for some of the first ^{84}Sr BECs that were produced with our apparatus. If we truncate the evaporation, we can produce clouds with both a clear bimodal density distribution and an inverted aspect ratio in the BEC component (Figure 2.6(A)). When the evaporation continues for 2.25 s, the resulting condensate is nearly pure and contains $\approx 4 \times 10^5$ atoms (Figure 2.6(B)). Systematic offsets in the optical depth, or "flat-topping", due to technical noise are visible in both parts of the figure. These systematics make fitting and accurate atom number counting difficult. The fitted Thomas-Fermi radii are less sensitive to the systematic offsets and, in combination with the trapping frequencies (see Section 2.4.2.1), we can use them to compute N_c and μ with

$$\begin{aligned} N_c &= \frac{\bar{a}}{15a_s} \left(\frac{\bar{r}}{\bar{a}} \right)^5, \\ \mu &= \frac{\hbar\bar{\omega}}{2} \left(\frac{\bar{r}}{\bar{a}} \right)^2, \end{aligned} \tag{2.16}$$

where $\bar{\omega} = (\omega_x\omega_y\omega_z)^{1/3}$, $\bar{r} = (r_x r_y r_z)^{1/3}$, and $\bar{a} = \sqrt{\hbar/m\bar{\omega}}$ [157]. Note that \bar{r} is

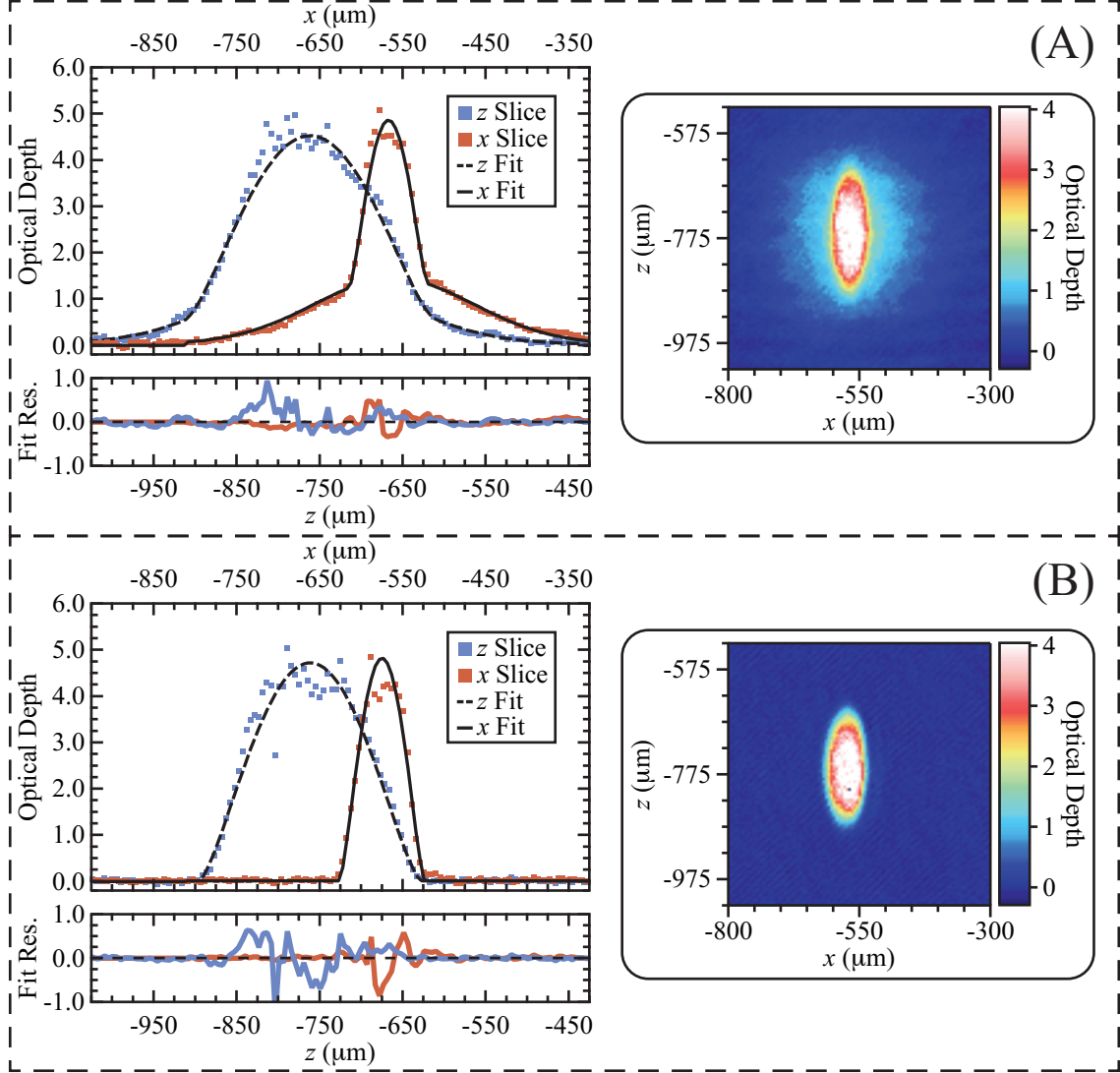


Figure 2.6: Bose-Einstein condensation of ^{84}Sr the three-beam cross trap observed using the horizontal imaging system (see Section 3.2). (A) A partially Bose-condensed cloud of ^{84}Sr atoms after a TOF of 25 ms (right). The left plot in (A) shows slices (averaged over 4 pixels) through the cloud and a two-dimensional fit to Equation 1.26. The temperature of the thermal component of the cloud in (A) is ≈ 170 nK. (B) The corresponding plots for a nearly pure ^{84}Sr BEC containing $\approx 4 \times 10^5$ atoms. Because the thermal fraction of the gas is small, we fit the image in (B) with Equation 1.24. The inversion of the aspect ratio can be seen clearly in both images.

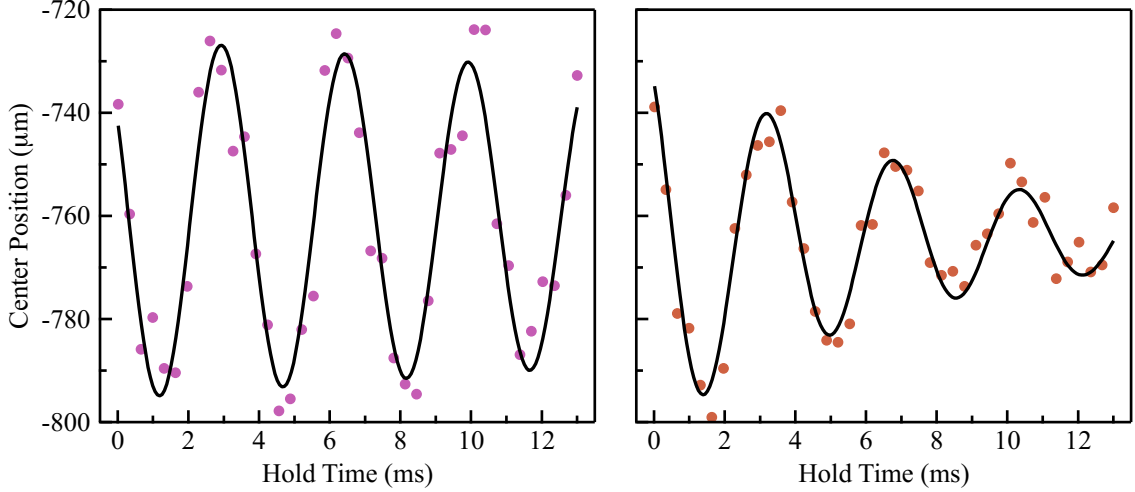


Figure 2.7: Measurement of the vertical trap frequency of the three-beam cross trap using center-of-mass (COM) oscillations of a partially Bose-condensed cloud of ^{84}Sr . COM oscillations of the BEC fraction (thermal fraction) are shown on the left (right). Solid lines are fits with an exponentially decaying sine function. The extracted trap frequency, $\omega_z/2\pi$, from the left (right) plot is 286 Hz (279 Hz) and the average of the two frequencies is $\omega_z/2\pi = 283$ Hz. We use the spectral width and S/N of the feature at $\omega_z/2\pi$ in the FFT of each data series to estimate that the uncertainty in the vertical trap frequency is $\lesssim 10\%$.

defined in terms of the *in-situ* Thomas-Fermi radii, so using Equation 2.16 requires numeric integration of the equations from [172] (see Section 1.3.2). For ^{84}Sr BECs created using the two-stage evaporation sequence (where we can use the trap frequency measurements from Section 2.4.2.1), the Thomas-Fermi radii indicate that $N_c \simeq 5 \times 10^5$ and $\mu/2\pi\hbar \simeq 1$ kHz.

2.4.2.1 Trap Frequency Measurement

We measured the trap frequencies in the three-beam cross trap at the end of the second evaporation stage. To do this, we prepared a ^{84}Sr BEC using the same evaporation profile as we use for the fermions. The ^{84}Sr cloud still contains a significant thermal component at the end of the evaporation.²⁴ We held the trap at the final parameters for 10 ms and then excited the cloud by pulsing either the vertical dipole beam or the main dipole beam to a high power. When we pulse the main beam to 300 mW, we excite center-

²⁴We did not try to purify the BEC because we wanted to replicate the ^{87}Sr evaporation procedure in order to reduce any systematic errors (*e.g.* thermal lensing of the ODT optics).

of-mass (COM) oscillations along the vertical, z -axis in both the condensate and thermal components of the ^{84}Sr cloud [172, 216–218]. A decaying sine fit to these oscillations yields the vertical trap frequency, $\omega_z/2\pi = 283$ Hz (see Figure 2.7). Pulsing the vertical beam to 100 mW excites both center-of-mass and breathing mode oscillations along both horizontal axes. Anharmonicity of the ODT couples the oscillations along the x - and y -axes, so we fit the oscillations with the sum of two exponentially decaying sine functions. Figure 2.8 shows the breathing oscillations of the ^{84}Sr condensate and fits to the data, which yield trap frequencies of $\omega_x/2\pi = 9.8$ Hz and $\omega_y/2\pi = 20$ Hz. Although the data are not shown, we also observe COM oscillations of the BEC and breathing oscillations of the thermal component in this series of images. Fitting these additional oscillations allows us to estimate, from the spread in the fit results, that the uncertainty in the horizontal trap frequencies is $\simeq 10\%$. We also took an FFT of each data series in Figure 2.7 and Figure 2.8. The ratio of the spectral width to the S/N of the feature at $\omega_{x,y,z}/2\pi$ in the FFT gives the uncertainty in the trap frequency $\omega_{x,y,z}/2\pi$.²⁵ The uncertainties derived from the FFTs indicate that the uncertainty in each trap frequency is $\lesssim 15\%$.

2.5 Degenerate Fermi Gas of ^{87}Sr

The experimental sequence for producing a ^{87}Sr DFG has been described in Sections 2.1, 2.2, and 2.3. Evaporation efficiency in Fermi gases drops precipitously with temperature (faster than the prediction of Equation 2.15) because the antisymmetry of the wavefunction prevents fermions in the same internal state from colliding in the s -wave channel [18, 49, 175, 219].²⁶ The large number (10) of nuclear spin states in ^{87}Sr reduces this Pauli blocking effect and has allowed other groups to efficiently evaporate to degeneracy in a completely depolarized ^{87}Sr gas [123, 131, 182]. We pursued this approach to

²⁵We symmetrize the data in Figure 2.8 about $t_{\text{hold}} = 0$ before taking the FFT to increase the spectral resolution.

²⁶Collisions in the p -wave channel in strontium typically are frozen out for $T \lesssim 100$ μK [109].

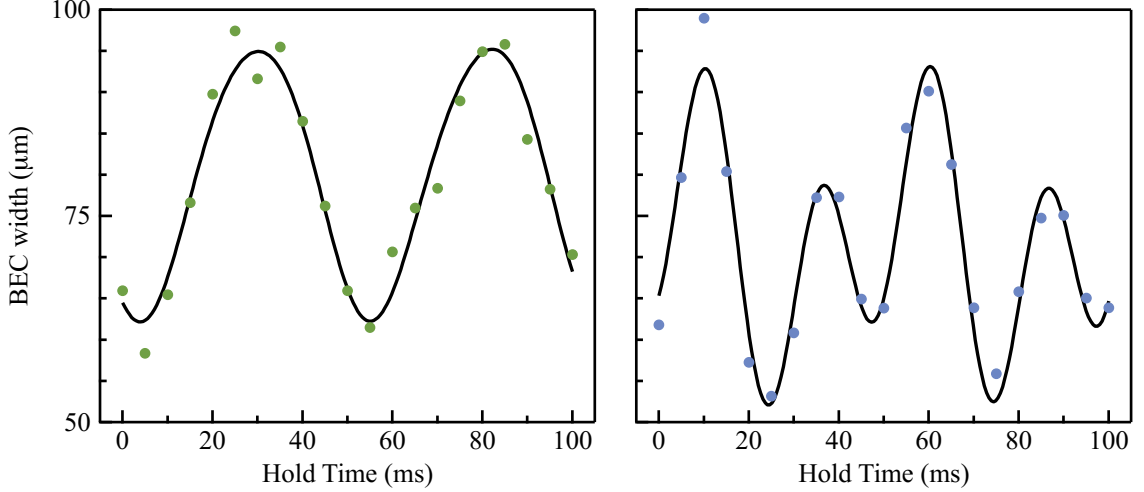


Figure 2.8: Measurement of the horizontal trap frequencies of the three-beam cross trap using breathing-mode oscillations of a partially Bose-condensed cloud of ^{84}Sr . Breathing oscillations along the x -axis (y-axis) are shown on the left (right). Anharmonicity of the trap couples the two oscillations. Solid lines are fits to the sum of two exponentially decaying sine functions. The resulting trap frequencies are $\omega_x/2\pi = 9.8$ Hz and $\omega_y/2\pi = 20$ Hz. We estimate that the uncertainty in the frequencies is $\approx 15\%$ (see text). FFTs of both plots exhibit a peaks near each trap frequency, which supports our analysis.

degeneracy because it is both the least technically challenging method and it has, thus far, yielded the most degenerate ^{87}Sr DFGs, $T/T_F \approx 0.1$ [123, 131, 220]. The ^{87}Sr rMOT is spin-depolarized by necessity (see Section 2.2), so we expect that the portion of the cloud that we transfer into the ODT will also be depolarized.²⁷ The imaging techniques that are currently implemented on the apparatus cannot resolve the nuclear spin states of ^{87}Sr , so we cannot confirm that the Fermi gas in our ODT is a balanced mixture of all 10 states. However, our ability to produce DFGs is strong evidence that a large fraction of the nuclear spin states are significantly populated.

Fitting the TOF absorption images of our Fermi gases with Equation 1.34 is undesirable because the fugacity, $\zeta = e^{\mu/k_B T}$, affects both the amplitude and shape of $\tilde{n}_{FD}(x, y, t)$ [177]. We instead fit the processed optical depth, D_{rs} , of the absorption

²⁷During his visit to the JQI in the fall of 2015, Dr. Jun Ye told us that his group has found that Stark-shifts to the rMOT cooling transition due to the 1064-nm ODT cause the rMOT to partially spin-polarize as it is loaded into the ODT. The initial trap depth in the JILA experiment is substantially larger than ours, which would exacerbate any spin polarization [184].

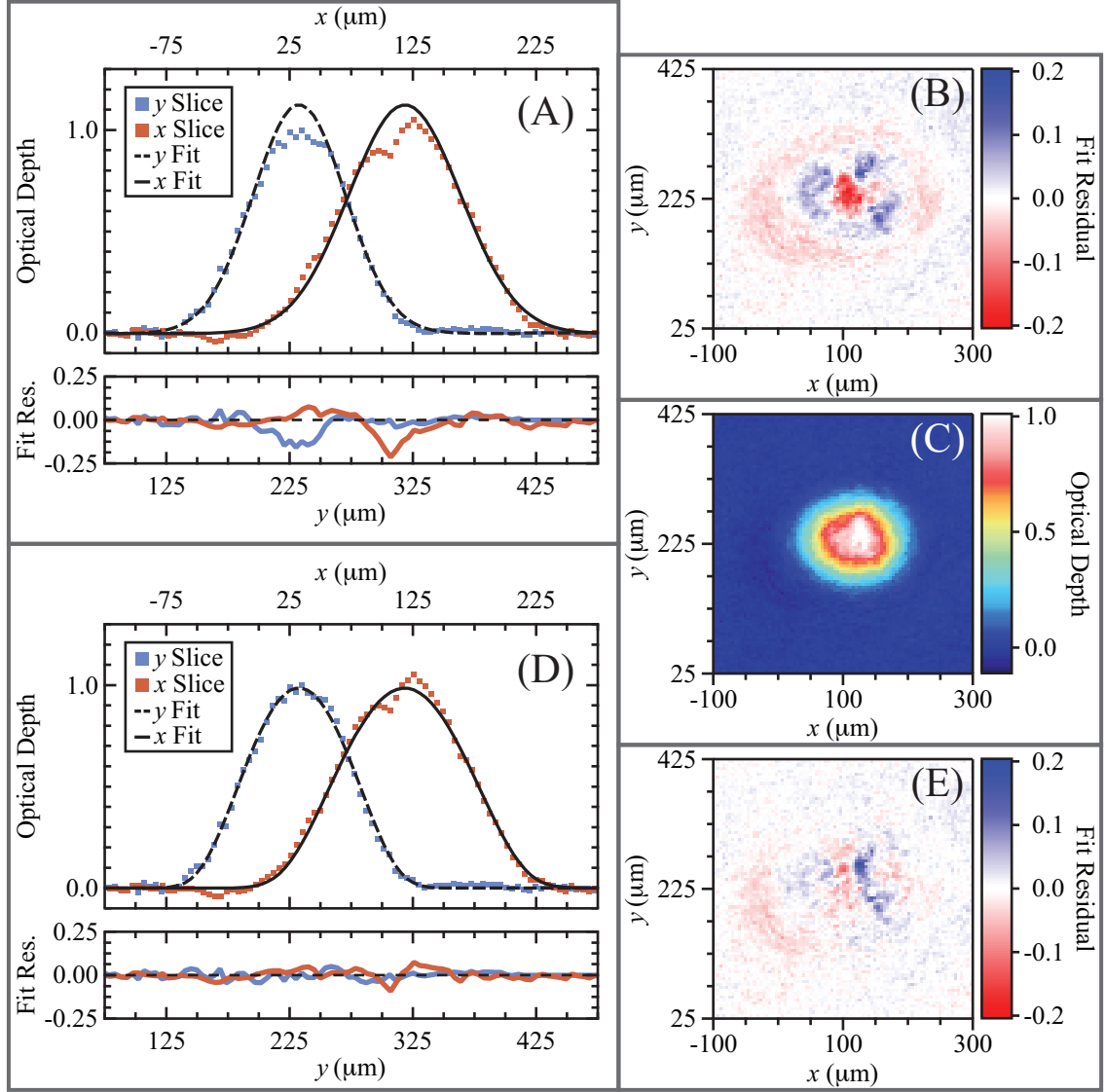


Figure 2.9: A degenerate Fermi gas of ^{87}Sr expanding from the three-beam cross trap, (C), and observed using the vertical imaging system (see Section 3.2). Single-pixel wide slices through the image and either a two-dimensional Gaussian fit (A) or a two-dimensional Fermi-Dirac fit (D). The associated two-dimensional residuals are shown in (B) or (E). The temperature given by the Fermi-Dirac fit is ≈ 15 nK.

images using²⁸

$$D_{FD}^{\text{fit}}(x, y) = A \frac{\text{Li}_2\left(-\zeta e^{-(x-x_0)^2/r_x(t)^2 - (y-y_0)^2/r_y(t)^2}\right)}{\text{Li}_2(-\zeta)} + B, \quad (2.17)$$

in which ζ only affects the shape of the density distribution [177].²⁹ We weight the fit with the uncertainty in the optical depth, $\delta D_{rs}(x, y)$, which we compute using

$$\delta D_{rs}(x, y) \approx \delta_{bg} e^{D_{rs}(x, y)}, \quad (2.18)$$

where δ_{bg} is the measured background noise level (see Section 3.2). Equation 2.17 contains seven fitting parameters: A , B , x_0 , y_0 , $r_x(t)$, $r_y(t)$, and ζ . Initial guesses for these parameters, except for ζ , are generated from a Gaussian fit to the absorption image. To avoid biasing our fits toward higher fugacities, and thus lower T/T_F , we always initialize the fit to Equation 2.17 with $\zeta = 1$. We can extract T , N , and T/T_F from the parameters with [175–177]

$$\begin{aligned} T/T_F &= (-6 \text{Li}_3(-\zeta))^{-1/3}, \\ N &= \frac{\pi A r_x(t) r_y(t) \text{Li}_3(-\zeta)}{\sigma_{88} \text{Li}_2(-\zeta)}, \\ T &\approx \frac{m}{4k_B} \left[\left(\frac{r_x(t)}{t} \right)^2 + \left(\frac{r_y(t)}{t} \right)^2 \right]. \end{aligned} \quad (2.19)$$

Note that the bosonic scattering cross section, σ_{88} , appears in the expansion for N due to technical details of the image processing (see Appendix A), and that we are computing T using a long TOF approximation.

Figure 2.9 shows an absorption image of a ^{87}Sr Fermi gas taken at 25 ms TOF, (Fig-

²⁸We compute $\text{Li}_2(\nu)$ using the approximation method developed in [221–223]. Methods for approximating $\text{Li}_s(\nu)$ can be found in [224–226], but these approaches are slower than [221] for $\text{Li}_2(\nu)$. The NIST Digital Library of Mathematical Functions [227] is another useful resource.

²⁹The column density, \tilde{n}_{FD} , and the processed optical depth, D_{rs} , are related to each other by the scattering cross section σ_{88} (see Section 3.2 and Appendix A).

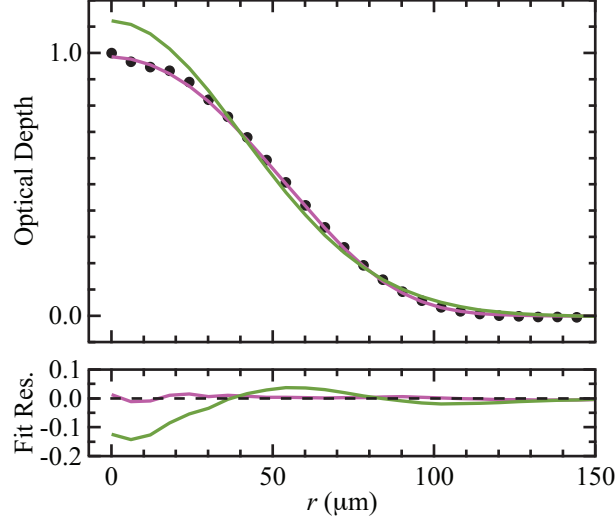


Figure 2.10: Azimuthally averaged profiles of the degenerate Fermi gas and fits shown in Figure 2.9. The azimuthally averaged {optical depth, thermal fit, Fermi-Dirac fit} is shown using the {black dots, green line, purple line} (top). Azimuthally averaged fit residuals in colors corresponding to the fit (bottom).

ure 2.9(C)), and two-dimensional fits to the image assuming either Maxwell-Boltzmann statistics, Equation 1.16 (Figure 2.9(A), (B)), or Fermi-Dirac statistics, Equation 2.17 (Figure 2.9(D), (E)). The duration of the second evaporation ramp for this experimental run was 3.7 s. The fit to the thermal distribution overshoots in both the center and the wings as we expect for a Fermi gas with $T/T_F < 1$ (Figure 2.9(A)). The residuals for this fit have a "bullseye" structure, which suggests that the density distribution cannot be fully described with Maxwell Boltzmann statistics (Figure 2.9(B)). In Figure 2.9(D), we see that a fit with Equation 2.17 yields substantially better agreement with the measured column density. There is no clear pattern in the residuals for the Fermi-Dirac fit, as we would expect if the fit correctly captured the essential features of the data (Figure 2.9(E)). The difference in quality between the thermal and Fermi-Dirac fits is more apparent when we azimuthally average the image and fits (Figure 2.10). Combining Equation 2.19 with the parameters from the Fermi-Dirac fit yields $T/T_F = 0.17$.

Care must be taken when fitting an absorption image with Equation 2.17. When $T/T_F \lesssim 0.2$, the variations in the density distribution with temperature are restricted to the edges of the cloud because lower energy states are fully occupied [177]. The signal-

to-noise ratio for absorption imaging in this region of the cloud is necessarily low, which makes thermometry difficult. For this reason, we use the experiment's vertical imaging system, which employs a low-noise PIXIS camera from Princeton Instruments, to acquire all the ^{87}Sr DFG images. We also remove fringing in the absorption image by projecting it onto a basis constructed using the Gram-Schmidt method (see Section 3.2). When $T/T_F \gtrsim 1$, the Fermi-Dirac distribution is indistinguishable from a thermal distribution. Because ζ enters Equation 2.17 as a shape parameter, a fit to an image with low peak optical depth (*i.e.* with low S/N) can easily return $T/T_F < 1$ even when the gas is not degenerate.

We confirm that our fits accurately report the degeneracy by computing T/T_F with an independent method. We can find N by numerically integrating over the image ROI and can find T using the last line in Equation 2.19.³⁰ The Fermi temperature is related to N by

$$T_F = \frac{\hbar\bar{\omega}}{k_B} \left(\frac{6N}{M} \right)^{1/3}, \quad (2.20)$$

where M is the number of populated spin states (we assume that $M = 10$) [175–177]. Together, Equation 2.20 and T give us T/T_F provided that we know the trap frequencies since $\bar{\omega} = (\omega_x\omega_y\omega_z)^{1/3}$. We measured the trap frequencies in Section 2.4.2.1, so we can calculate T/T_F at the end of the second evaporation ramp.

Figure 2.11 shows T/T_F as a function of the duration of the second evaporation stage. We calculate T/T_F from both the fitted ζ (Equation 2.19, purple circles) and the numerically integrated N (Equation 2.20, green triangles). Because we have not yet measured the spin state populations, both methods for computing T/T_F have substantial uncertainty. Spin states with lower population are less degenerate (see Equation 2.20) and so contribute predominantly to the wings of the density distribution. The opposite is true for the spin states with higher than average population. The fitted fugacity, ζ ,

³⁰It would be better to get T by fitting the time-dependence of $r_{x,y}(t)$ in a series of images taken at distinct TOF, t . However, we have found that the method we employ here catches all images that fit degenerate, but in actuality are not.

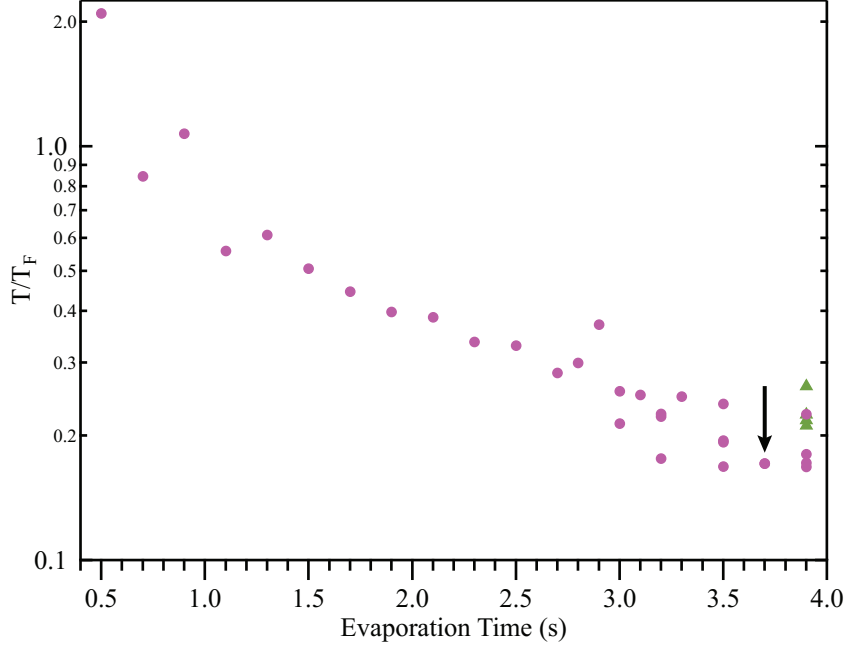


Figure 2.11: T/T_F as a function of the duration of the second evaporation ramp in the three-beam cross trap. Purple circles indicate T/T_F calculated from the fitted ζ using Equation 2.19. Green Triangles show T/T_F determined using Equation 2.20. The black arrow signifies the data point that is displayed in Figure 2.9 and Figure 2.10. All data were taken with a 25 ms time-of-flight.

is a measure of the average degeneracy of the DFG, so it gives an upper bound on T/T_F (Equation 2.19) for the most populated spin state [123]. The T/T_F determined by computing T_F (Equation 2.20) and T is also an upper bound on the degeneracy of the most populated spin state. However, the bound produced with this method is looser because Equation 2.20 requires an explicit assumption about the spin distribution. The offset of T/T_F between the two procedures might be caused by finite spin polarization of the ^{87}Sr DFG. However, the more likely culprit is the long TOF approximation that we used to get the temperature (Equation 2.19). The measured trap frequencies indicate that this approximation is only valid for $t > 100$ ms and such a long TOF is not possible in our apparatus.³¹ Both measurements of T/T_F indicate that we have produced ^{87}Sr DFGs with $T/T_F \simeq 0.2$ and $T_F \simeq 56$ nK. This temperature range is certainly sufficient for

³¹We could use the relationship between $r_{x,y}(t)$ and $r_{x,y}$ from Section 1.3.3 to get a better temperature measurement. We have not done so here because the long TOF approximation gives a more conservative bound on T/T_F .

initial quantum magnetism experiments, although temperatures that are at least an order of magnitude lower will be necessary for many proposals [\[90\]](#).

Chapter 3: Experimental Apparatus

Every laser cooling experiment has three essential components: a vacuum chamber, a set of magnetic field coils, and a laser system. Computer control of these systems facilitates the creation of quantum degenerate samples. To characterize the ultracold gases, we image the momentum- or position-space distribution of the samples onto CCD or CMOS cameras. In this chapter, I describe the realization of all of these systems in our apparatus.

3.1 Laser Systems

Laser cooling and trapping of alkaline-earth atoms requires a complicated system of multiple lasers. The non-magnetic ground state prevents sub-Doppler cooling and RF-assisted evaporation (as described in Chapter 2). In combination with the low capture velocity of the $^1S_0 \rightarrow ^3P_1$ transition, the technical challenges associated with the non-magnetic ground state mean that high phase-space densities can only be produced using a two-color laser cooling sequence. A 461-nm laser system provides initial cooling to mK temperatures, so that our 689-nm lasers can capture the strontium atoms and further cool them to the μK regime. Several repumping lasers return atoms that leak from the 1P_1 state into metastable 3P states to the ground state. These lasers allow accumulation of sufficient atoms for a final stage of evaporative cooling, which proceeds in a 1064-nm optical dipole trap. A blue-detuned optical dipole trap, at 445 nm, and red-detuned optical lattices, at 1064 nm, control the final potential experienced by our quantum degenerate samples.

3.1.1 461-nm Laser System

The experiment uses two 461-nm lasers. The first is a Littman-Metcalf configuration master oscillator that we constructed with an Anti-Reflection-coated (AR-coated) laser diode (Nichia NDBA116T) and a holographic grating (Thorlabs GH13-18V). We lock this laser to the $^1S_0 \rightarrow ^1P_1$ transition in ^{88}Sr via polarization rotation spectroscopy. The second laser is a Toptica TA-SHG pro slaved to the master oscillator with a low bandwidth beatnote lock.

The Littman-Metcalf optomechanics of the master oscillator are based on a design from JILA (we also use these optomechanics for our repump lasers, see 3.1.3). The high quality of the laser diode AR-coating combined with the strong feedback from the reflective grating have allowed the laser to operate in the same mode without realignment of the optomechanics on a timescale of one year. The proximity of the master oscillator to the 1064-nm optical setup initially caused the laser diode temperature to be unstable, resulting in a rapid drift in the lasing frequency.¹ This drift limited the period over which the lock to spectroscopy could be maintained to $\simeq 30$ minutes. We overcame this limitation by implementing a two-stage temperature stabilization scheme. By maintaining the optomechanics baseplate temperature at 29 °C, we decouple the laser diode temperature from the lab environment and increase the laser locking time to $\gtrsim 4$ hours.²

Figure 3.1 shows the optics layout for the 461-nm master oscillator and polarization rotation spectroscopy. After the light from the master oscillator passes through an optical isolator (ConOptics 711C-3, return loss > 28 dB), approximately 15 mW of power is available for spectroscopy and beatnote locking of the 461-nm slave laser. A polarizing beamsplitter picks off several hundred μW of this power and sends it into a 50/50 single mode fiber beamsplitter (Thorlabs FC488-50B-APC), where it is combined with light

¹The AOMs used in the 1064-nm optical setup get hot during operation.

²B. Reschovsky designed the temperature controller that stabilizes all the diode lasers that we constructed. The design is available on the JQI Github repository: <https://github.com/JQIamo/Linear-Temperature-Controller>.

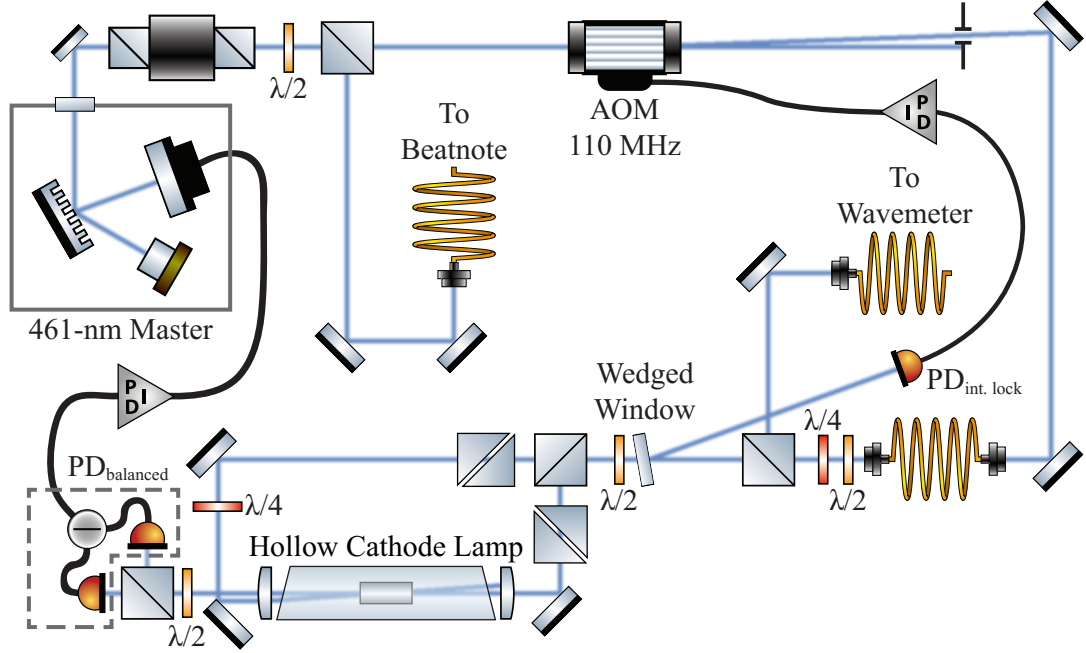


Figure 3.1: The 461-nm master oscillator optics setup. The output of the laser splits at a PBS into a path to the slave laser beatnote lock and a path to the spectroscopy lock optics. An intensity lock to the RF drive of the frequency offset AOM stabilizes the optical power for spectroscopy. A hollow cathode lamp creates a strontium sample for the polarization spectrometer, which locks the master laser frequency using feedback to the laser’s PZT.

from the slave laser to generate an optical beatnote. Typically, the unused output port of the fiber splitter has $\gtrsim 100 \mu\text{W}$ of light from the master oscillator. The remaining power from the laser transmits the polarizing beamsplitter and is blueshifted 110 MHz by an AOM (IntraAction AOM-1101GA1). A single mode optical fiber guides the beam to a polarization rotation spectroscopy setup (which [228] inspired us to implement). The spectroscopy light is polarized with a PBS and intensity stabilized using feedback to the RF drive of the 110-MHz AOM. The small amount of light that is rejected by the PBS is fiber coupled and sent to a wavemeter (HighFinesse WS-7). A second PBS divides the beam into a weak probe and strong pump, each of which are transmitted through a Glan-Laser polarizer (Thorlabs GL5-A) to increase the polarization purity. The pump and probe counter-propagate through a hollow cathode lamp (Hamamatsu L2783-38NE-SR)³ that is

³Hamamatsu has discontinued its line of see-through HCLs. Similar lamps can be bought from Photron Pty. Ltd. as a custom order. However, initial work with these lamps in the ErNa lab suggests that they

placed at the focus of a 1:1 telescope to increase saturation of the optical resonance. The HCL is magnetically shielded with MuMetal to reduce Zeeman shifts due to stray fields.⁴ A $\lambda/4$ waveplate circularly polarizes the pump beam before it enters the hollow cathode to induce a differential saturation of the σ^+ and σ^- transitions of the 461-nm resonance. The differential saturation causes a rotation of the probe beam polarization, which we detect using a balanced polarimeter consisting of a PBS and a balanced photodetector (Thorlabs PDB210A). The quality of the polarimeter could be increased by replacing the PBS with a Wollaston polarizer, but we have not found the PBS to be detrimental to experimental stability.⁵ The output of the polarimeter is fed into a JQI PID 2.5.2 (designed by J. Tiamsuphat) that controls the position of the Littman-Metcalf cavity mirror with a PZT. We have found that the large linewidth of the 461-nm transition renders feedback to the laser diode current of the master oscillator unnecessary. However, a feedforward of the PZT voltage to the current should be implemented in the next generation of the experiment to increase the laser locking time. We always lock the laser to the $^1S_0 \rightarrow ^1P_1$ resonance of ^{88}Sr due its high natural abundance and because the isotope shifts for the other reasonably abundant isotopes (^{87}Sr and ^{86}Sr) are smaller than the width of the ^{88}Sr feature.

We use a Toptica TA-SHG pro to generate sufficient power at 461-nm to load and operate the bMOT. The TA-SHG pro consists of an IR Littrow-configuration seed laser operating at 922 nm, a tapered amplifier, and a SHG crystal inside a bow-tie optical cavity. The frequency-doubled output of the laser is initially split into two arms (see Figure 3.2). A high-power arm supplies cooling and trapping light to the apparatus. A low-power arm that generates the beatnote and provides a second probe beam. During normal operation,

provide lower optical depth than the Hamamatsu lamps.

⁴The shift in the laser lock point due to a refrigerator magnet positioned next to the HCL is about 10 MHz (2 MHz) without (with) the MuMetal shield in place. A better shield should be built into the spectroscopy setup when the experiment moves into the PSC.

⁵We have observed lab-temperature dependent drifts in the laser lock point that are $\simeq 1$ MHz peak-to-peak. However, it is not clear whether these drifts are caused by temperature sensitivity of the PBS in the polarimeter, since the wavemeter readout is also temperature sensitive.

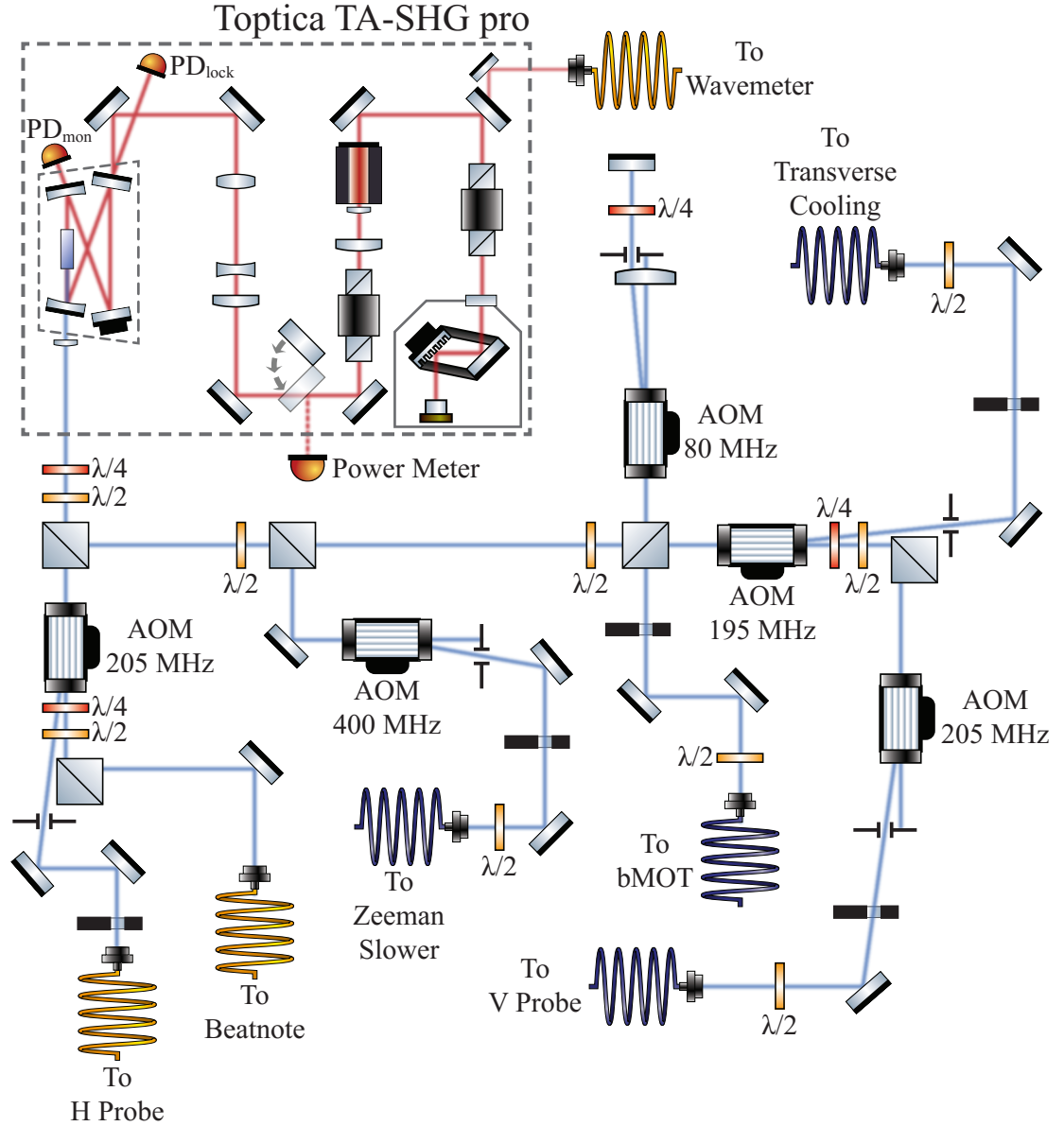


Figure 3.2: The 461-nm slave laser and optics for initial cooling of strontium gases. The innards of the Toptica TA-SHG pro and the fiber link to the wavemeter are shown top left. The bottom left section contains the horizontal probe optics and the beatnote lock fiber launch. The right side diagrams the high-power arm, which supplies all cooling light and the vertical probe beam.

there should be 400 to 500 mW of 461-nm light in the high-power arm. If the power falls below 400 mW when the Toptica's TA is being run at 2.2 A drive current, then realignment of the internal optics of the TA-SHG pro may be required. In the low-power arm, an AOM operating at 205 MHz blueshifts light for the horizontal imaging system. The 0th-order output of this AOM goes to the 2nd input port of the beatnote lock fiber beamsplitter. We align 0th-order light into the fiber splitter with the AOM on to ensure that changes to the 0th-order beam mode due to diffraction into the 1st order do not degrade the fiber coupling efficiency. The unused output port of the fiber splitter typically contains $\gtrsim 400 \mu\text{W}$ ($\gtrsim 1 \text{ mW}$) of power from the slave laser with (without) the RF drive applied to the AOM. We observe no power dependent offset to the beatnote locking frequency over this range. A high-speed fiber-coupled photodiode (Thorlabs DET02AFC) detects the beatnote between the two 461-nm lasers and sends it to a JQI PLL beatnote locking circuit (implemented by N. Pisenti based on the design in [229]).⁶ The beatnote circuit stabilizes the frequency offset of the slave from master such that the slave detuning is -205 MHz from the Sr isotope of interest. By changing the reference frequency to the beatnote PLL, we can rapidly switch the slave laser frequency to trap any Sr isotope (see Table 3.1). Because locking the SHG cavity requires all the fast feedback inputs to the seed laser, only PZT feedback is available for the beatnote lock. The high gain and slow response of the PZT input combined with the fast bandwidth of the PLL chip make stable frequency locking impossible to achieve unless we limit the feedback time constant to $\approx 1 \text{ Hz}$.⁷ This low bandwidth is sufficient for stable operation of the bMOT and for spectroscopy on the 461-nm transition since the lock to the SHG cavity eliminates higher frequency noise.

The light entering the high-power arm of the slave laser setup is split into three paths (see Figure 3.2). In the first path, a 400-MHz AOM (Brimrose TEM-400-100-

⁶The JQI beatnote circuit can be found on Github: <https://github.com/JQIamo/beatnote-pll>.

⁷As a result, we cannot currently perform isotopic mixture experiments since the slave laser frequency takes several seconds to change by $\approx 50 \text{ MHz}$, the smallest isotope shift. We have designed a circuit to feedforward the PZT voltage to overcome this challenge, but it has not yet been incorporated into the locking electronics.

Table 3.1: The PLL reference frequencies for trapping each Sr isotope. Because the ^{88}Sr beatnote frequency is not 90 MHz, we can deduce that the zero crossing of the polarization rotation spectroscopy is offset from the resonance by about one linewidth. The offset is likely due to a combination of imperfect laser polarization, DC electromagnetic energy shifts in the excited state, and perturbations due to the unresolved isotope shifts. The lock offset is stable on the timescale of several days, so it does not adversely affect short-term experimental performance and we recalibrate the beatnote frequencies daily.

Isotope	PLL Frequency
^{88}Sr	$\approx 129 \text{ MHz}$
^{87}Sr	$\approx 181 \text{ MHz}$
^{86}Sr	$\approx 254 \text{ MHz}$
^{84}Sr	$\approx 400 \text{ MHz}$

461) redshifts the light, which is then launched into a SM PM optical fiber (Coastal Connections P-FAnsFAnskx-3.8c/125/3-7). This fiber delivers light to the Zeeman slower and typically provides $\gtrsim 50 \text{ mW}$ of power with a detuning of -605 MHz . A telescope expands the Zeeman slower beam to a $1/e^2$ radius $\approx 6 \text{ mm}$ before the beam enters the vacuum chamber and is focused onto the nozzle of the Sr oven. The second path supplies power to the bMOT. A double-passed 80-MHz AOM (IntraAction ATM-801A1) blueshifts light by 160 MHz to set the bMOT detuning to -45 MHz . This light is coupled into a custom 1×3 SM PM fiber beamsplitter (Evanescence Optics Inc.) that connects to each arm of the bMOT. The horizontal MOT beams contain $\approx 9 \text{ mW}$ while the vertical beam contains $\approx 11 \text{ mW}$.⁸ The bMOT beams have a $1/e^2$ radius of $\approx 8 \text{ mm}$, which corresponds to a total peak saturation, $s_{\text{tot}} = I/I_{\text{sat}}, \approx 1.3$. We lock the intensity of the bMOT beams to allow repeatable intensity sweeps at the end of the bMOT loading stage.⁹ A wedged window picks off light from one of the horizontal bMOT beams and directs it to a PD (Thorlabs DET36A). The PD signal is amplified (with an SRS SR570), filtered (Newport LB1005 PI), and fed back to the 80-MHz AOM's RF drive power. The third path couples

⁸The measured splitting ratio of the fibersplitter is 31% : 37% : 31%.

⁹We implemented these sweeps based on a tip from the group of Dr. T.C. Killian and have found that they increase the rMOT atom number by $\approx 50\%$.

blue light to the transverse-cooling stage and the vertical imaging system. An AOM operating at 195 MHz (Brimrose TEM-200-50-461) blueshifts light to set the transverse-cooling detuning to -10 MHz. The 1st order output of this AOM is coupled through an SM PM optical fiber to the transverse-cooling stage while the 0th order output is deflected into another AOM, which sets the vertical probe beam detuning. After the fiber, a PBS divides the ≈ 20 mW of transverse-cooling light into two beams for vertical and horizontal Doppler cooling. A cylindrical telescope expands each beam to a $1/e^2$ radius of 9 mm (3 mm) along the direction parallel (perpendicular) to the propagation axis of the atomic beam. The second AOM operates at 205 MHz (IntraAction ATM-2001A1) to shift its 1st order beam into resonance with the $^1S_0 \rightarrow ^1P_1$ transition. The resonant light is fiber coupled to the vertical imaging system during normal operation, but can be switched to a second horizontal imaging system by plugging the fiber into a different output port at the experiment.

3.1.2 689-nm Laser System

Cooling strontium to μK temperatures requires a laser addressing the $^1S_0 \rightarrow ^3P_1$ intercombination transition.¹⁰ This transition has a linewidth of only 7.5 kHz. Such a narrow linewidth could not be achieved with commercially available diode lasers when we began constructing the apparatus. To obtain the necessary combination of narrow linewidth, reasonable power, and frequency flexibility, we reference a set of slave lasers to a cavity-stabilized master laser via injection locks or beatnote locks. This configuration lets us easily change the laser frequency to trap any strontium isotope in the rMOT or to perform spectroscopy on the 689-nm transition.

Our 689-nm master oscillator is a Toptica DL pro that we phase stabilize to a high finesse ULE optical cavity (ATFilms ATF-6010-4) using the Pound-Drever-Hall

¹⁰In principle, μK temperatures could also be reached using a $5s5p\ ^3P_2 \rightarrow 5s4d\ ^3D_3$ MOT, but no group has attempted this to my knowledge.

AOM to offset the master laser frequency from the ULE cavity resonance such that the DL pro output is detuned by -80 MHz from the $F = 9/2 \rightarrow F' = 11/2$ resonance of ^{87}Sr . The 0th order diffraction from the GHz AOM is coupled into a network of 99 : 1 and 50 : 50 fiber beamsplitters (the *beatnote network*) that sends light to a wavemeter (HighFinesse GmbH WS-7) and mixes in light from the slave lasers to generate optical beatnotes. Typically, $100\text{ }\mu\text{W}$ of light from the master laser is available at the ULE cavity breadboard. A 20-MHz EOM (Thorlabs EO-PM-R-20-C1), powered by an amplified Toptica PDH 110 module, phase modulates this light, which then passes through some mode-matching optics and enters the optical cavity. An amplified Si PD measures the light rejected by the ULE cavity. The PDH 110 demodulates the photodiode signal to create the PDH error signal, which has a spectral width on the order of the cavity linewidth. A Toptica FALC module uses the PDH error signal to narrow the DL pro linewidth below the cavity linewidth. By observing the Fourier transform of the locked PDH error signal, we can see that the FALC servo bandwidth is $\gtrsim 1$ MHz. A second PD measures the power transmitted by the optical cavity and serves as a useful diagnostic of the quality of the lock. We have tested the master laser linewidth using three methods. First, we used self-heterodyne through a 2 km fiber delay line to set a conservative upper bound on the laser linewidth of 48 kHz [231–234].¹¹ Second, the ^{88}Sr rMOT temperature can be as low as 600 nK, so we can use the Doppler-cooling limit (see Section 2.2) to bound the convolution of the natural and laser linewidths at 25 kHz. Because 600 nK is similar to the recoil limit for the 689-nm transition (see Section 2.2), we suspect that the locked laser linewidth is actually < 7.5 kHz. Finally, the power transmitted by the ULE cavity is stable when the master laser is locked, so the laser linewidth is on the order of the cavity linewidth (≈ 6 kHz). We have found (unsurprisingly) that the number of atoms confined by the rMOT depends strongly on the exact performance of the PDH lock. Degradation of

¹¹The delay time of the fiber is $t_d \approx 10\text{ }\mu\text{s}$, which corresponds to a linewidth, $f = 1/2\pi t_d \approx 16$ kHz. The observed self-heterodyne signal shows clearly that t_d is not large enough for an accurate measurement, which indicates that the laser coherence time is $\gtrsim t_d/3$.

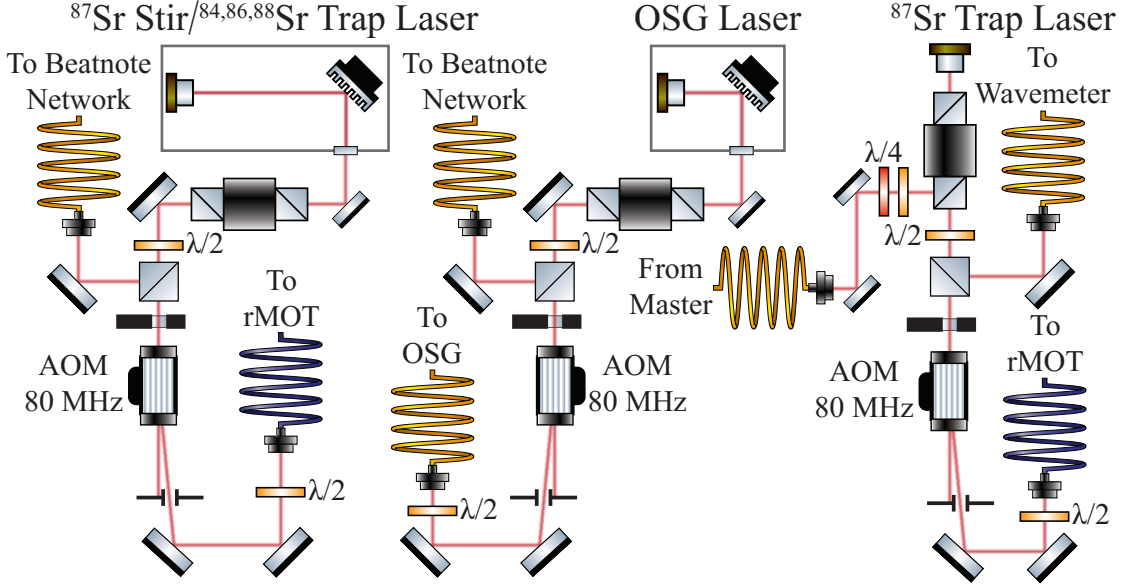


Figure 3.4: The 689-nm slave laser system. Right: an injection-locked laser diode provides trapping light close to resonance with the $F = 9/2 \rightarrow F' = 11/2$ transition for the fermionic rMOT. Left: a beatnote-locked laser makes the bosonic rMOT or stirs the ^{87}Sr spin population to stabilize the fermionic rMOT. Center: a second beatnote-locked laser for optical Stern-Gerlach spin readout or optical Feshbach Resonance spectroscopy.

the PDH lock does not strongly affect the rMOT temperature; providing further evidence that the rMOT temperature is not laser linewidth limited. When the low atom number condition occurs, the atom number can typically be recovered by tuning the gain of the PDH 110 or by adjusting the PID gains of the FALC.

We currently have three 689-nm slave lasers integrated into the experiment (see Figure 3.4). The ^{87}Sr trapping slave is an injection locked LD (OptNext HL6750MG) that addresses the $F = 9/2 \rightarrow F' = 11/2$ hyperfine transition [36, 196]. The other two lasers are long-cavity (10 cm) and short-cavity (2.2 cm) Littrow configuration ECDLs that we constructed based on the designs in [235]. Both Littrow ECDLs contain AR-coated LDs: the long-cavity laser uses a Sacher SAL-690-025 LD and the short-cavity laser uses an OptNext HL6738MG that we AR-coated in the UMD Nanocenter’s FabLab.¹² The long-

¹²The anti-reflection coating is comprised of two layers, as suggested in [236]: one layer of Al_2O_3 to bring the facet coating to $\lambda/2$, and a final $\lambda/4$ layer of HfO_2 . The deposition was done via electron beam evaporation, and monitored in-situ by scanning the diode current across the lasing threshold.

cavity laser (the *stirring* laser henceforth) provides trapping light for experiments with bosonic isotopes and $F = 9/2 \rightarrow F' = 9/2$ stirring light for experiments with fermionic strontium (see Section 2.2 or [36, 196]). The short-cavity laser will be used for optical Stern-Gerlach (OSG) separation of the spin states of ^{87}Sr in future experiments. All the slave laser control electronics were constructed at JQI - by B. Reschovsky, N. Pisenti, and me - using designs by N. Pisenti, B. Reschovsky, and A. Restelli (Some of these designs are based on [237, 238]).¹³ Beatnote locks to the 689-nm master laser stabilize and narrow the frequencies of the OSG and stirring lasers. The beatnote signals are detected by fiber coupled PDs (Thorlabs DET025AFC) and JQI PLL beatnote locking circuits compare the beatnote frequency to a reference frequency from a JQI DDS v4.0 (designed by S. Olmshenk) to transfer the master laser coherence to the slave lasers. Unlike the beatnote lock described in Section 3.1.1, the implementation here combines fast feedback to each slave's LD current with slow feedback to its PZT. The beatnote locking bandwidth for both Littrow configuration slaves is typically $\gtrsim 1$ MHz and we can achieve locking bandwidths up to 2 MHz with careful optimization of the grating feedback into the slave laser LD.

All three slave lasers have similar optical setups. Approximately 100 μW of each laser's output goes to the beatnote network (for the stirring laser and OSG laser) or to the wavemeter (for the ^{87}Sr trapping laser). An 80-MHz AOM (IntraAction ATM-801A1) blueshifts the remaining power from each laser before coupling to the experiment through an optical fiber. All laser beams can be extinguished with 100% contrast with SRS laser shutters. For the stirring and trapping lasers, the RF drive frequency of the AOM can set the laser detuning within $\approx \pm 3$ MHz of the relevant hyperfine transition without significantly degrading the fiber coupling efficiency. We are therefore able to frequency broaden the lasers by modulating the frequency of the AOM's RF drive in the power efficient, single-pass configuration without unwanted amplitude modulation (see also [182]). To enable

¹³The Github repositories for control circuits that I did not reference in 3.1.1 are: <https://github.com/JQIamo/current-controller>, <https://github.com/JQIamo/hv-piezo-driver>.

both simple frequency broadening and accurate detuning in single frequency operation, the drive electronics for the AOMs can rapidly switch the RF source between a VCO and a DDS.¹⁴ Two inputs of a custom 4×4 fiber beamsplitter (from Evanescence Optics Inc.) transmit $\approx 700 \mu\text{W}/\text{output}$ ($\approx 3 \text{ mW}/\text{output}$) of AOM-shifted light from the stirring (trapping) laser to the rMOT.¹⁵ The fibersplitter facilitates the combination of multiple laser frequencies into the rMOT and the integration of new slave lasers that will be necessary for experiments with isotopic mixtures.¹⁶ In the current retroreflected rMOT configuration we use only three outputs of the fibersplitter, so the power in 4th output is wasted, but we will use this output to power the upward and downward propagating rMOT beams separately in the next generation of the experiment [65, 182, 239]. The OSG laser optics includes an AOM to preserve experimental flexibility and achieve fast optical switching (the beatnote lock reference frequency is sufficient to set the OSG detuning since only single frequency operation is necessary). Optical power for OSG separation is guided to the experiment through a SM optical fiber. The experiment-side optics for optical Stern-Gerlach have not been completed, but the planned entrance point for the OSG beams is indicated in Figure 3.9.

3.1.3 Repump Lasers

Due to the $^1P_1 \rightarrow ^1D_2$ leak out of the bMOT, accumulation of sufficient atoms for degenerate gas production is impossible without the assistance of repumping lasers. There exists an infinite ladder of 3S , 3P , and 3D states above the metastable $5s5p\ ^3P$ manifold. In principle, the existence of this ladder implies that there are an infinite number of possible

¹⁴We are currently working to improve our AOM drive electronics and the new design is available on Github: <https://github.com/JQIamo/aom-driver>.

¹⁵If we couple OSG laser light through the fiber splitter, $\approx 2 \text{ mW}/\text{output}$ is available for the rMOT. However, we observed no increase in atom number for either bosons or fermions when using the OSG laser for the rMOT. This suggests that the transfer efficiency from the bMOT to the rMOT is not power limited for the current rMOT beam radii.

¹⁶We have two spare long-cavity laser bodies and a 689-nm Toptica BoostA awaiting their addition to the 689-nm laser system.

repumping transitions, but most of these transitions are impractical due to either their resonant frequency or linewidth. To this point, five repumping methods have been used in strontium quantum degenerate gas experiments [178, 240–242]. Our technique was initially developed by the optical clock community. It utilizes two lasers addressing the $^3P_0 \rightarrow ^3S_1$, 679-nm transition and the $^3P_2 \rightarrow ^3S_1$, 707-nm transition. This approach is advantageous because it rigorously returns all atoms to the ground state and inexpensive laser diodes can produce the necessary wavelengths. The alternative strategies typically require only a single laser, which reduces experimental complexity, but at a less convenient wavelength.¹⁷

We currently use four repumping lasers in the experiment (see Figure 3.5). The single 679-nm laser and two of the three 707-nm lasers (A and B) are Littman-Metcalf configuration ECDLs based on the JILA design (for additional discussion see Section 3.1.1). These two 707-nm lasers use AR-coated laser diodes (Toptica LD-0705-0040-AR-1) and the 679-nm laser uses an uncoated laser diode (similar to SDL7311). All the Littman-Metcalf repumps were constructed using Thorlabs holographic gratings (either GH13-18V or GH25-18V). Two-stage temperature control (as described in Section 3.1.1) improves the frequency stability of the Littman-Metcalf repumps. The PZT voltage of the 707-nm lasers feeds forward to the LD current to increase the mode-hop free tuning range. Typically, the free-running wavelength of the lasers drifts slowly enough that we can efficiently recover atoms from the metastable reservoir for $\simeq 1$ hour without adjusting the PZT voltage or diode current. The last 707-nm laser (C) is an OptNext HL7001MG laser diode that we injection lock using 707-nm laser B as a master oscillator. We fiber couple the 679-nm laser and 707-nm laser A to the experiment using the same SM fiber, which delivers 2.5 mW (5 mW) of power at 679-nm (707-nm). 707-nm laser C is coupled to the experiment through a fiber EOM (Jenoptik PM705) and can supply as much as 5.5 mW.

¹⁷We are currently considering a switch to a $5s5p\ ^3P_2 \rightarrow 5s6d\ ^3D_2$, 403-nm transition repumper because laser diodes with significantly higher power output compared to typical 707-nm laser diodes are available.

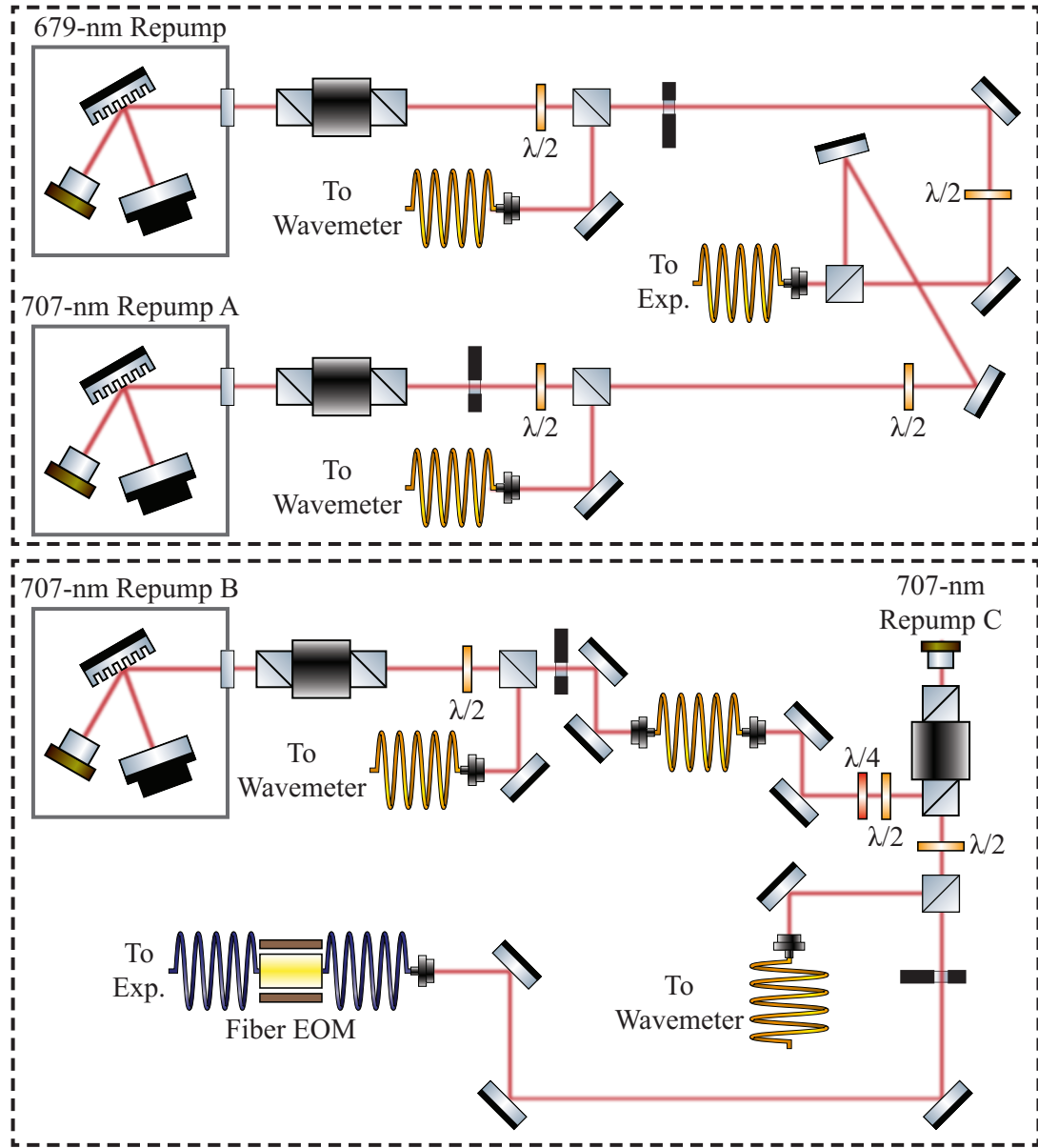


Figure 3.5: A sketch of the two repump laser optical breadboards. Top: the 679-nm laser and 707-nm laser A reach the experiment through the same SM optical fiber. Bottom: 707-nm laser B injection locks 707-nm laser C so that the fiber EOM can supply enough power for repumping ^{87}Sr . SRS shutters provide digital control of the laser intensity and the lasers are individually coupled to a wavemeter that stabilizes their frequency. The 688-nm depumping laser that we use in Chapter 4 is not shown, but the layout of its breadboard is similar to those in the top panel.

All the lasers can be extinguished using SRS shutters. Repumping in strontium does not require laser switching faster than ≈ 1 ms, so we do not use AOMs with these lasers.

For experiments with bosonic isotopes, we use only the 679-nm laser and 707-nm laser A. Each laser is coupled to the WS-7 wavemeter through a multimode fiber switch, which allows us to readout the operating frequency of all the repump lasers rapidly. A Labview program (written by B. Reschovsky) compares the measured frequency to a setpoint and adjusts the laser's PZT voltage with a low-speed DAC. We routinely stabilize the frequency of each laser to within ± 5 MHz, which is substantially narrower than the observed width of the bosonic repumping spectrum. Repumping the fermionic isotope, ^{87}Sr , is more complicated than repumping bosonic isotopes due to the presence of hyperfine structure. Using the known hyperfine A and B coefficients [243], we can see that the 707-nm repumping spectrum is broadened to ≈ 6 GHz.¹⁸ We have used several methods to increase our 707-nm laser linewidths from $\lesssim 1$ MHz to ≈ 6 GHz. Initially, we emulated several atomic clock groups and modulated the PZT of lasers A and B (which was fiber coupled directly to the experiment during this time, see Section 4.1.3). For the results presented in Chapter 2, we had successfully injection locked laser C, but did not have an RF source for the fiber EOM. We modulated the frequency of laser A at 750 Hz and stabilized laser C by locking laser B using the wavemeter. The repumping efficiency can be moderately increased by tuning the drive current of laser C to make it slightly multimode. The combination of a modulated laser and a single frequency (or slightly multimode) laser allowed us to load enough ^{87}Sr atoms to produce degenerate Fermi gases. However, we have found that this repumping method is not repeatable from day to day because it depends sensitively on the tuning of the grating feedback to 707-nm laser A and the injection feedback to 707-nm laser C. A recently constructed RF source for the fiber EOM allows more repeatable broadening of laser C. This source may eliminate the need for

¹⁸The 679-nm repumping spectrum is also broadened by hyperfine structure, but addressing a single hyperfine transition allows efficient repumping.

frequency modulation of laser A, which would reduce experimental complexity and make production of Bose-Fermi isotopic mixtures possible. Repumping with the fiber EOM has not yet been fully implemented, but the initial repumping tests have been promising.

3.1.4 Optical Dipole Traps

Atomic strontium is non-magnetic in its ground state, so optical confinement is necessary for the production of quantum degenerate gases. Our experiment currently has two laser systems for optical dipole trapping: a 30-W, 1064-nm fiber laser that produces attractive potentials and a 1-W, 445-nm diode laser that generates repulsive potentials. Only the 1064-nm system is necessary for the production of degenerate gases. The 445-nm laser will be used in future experiments to create arbitrary and dynamically tunable potentials to manipulate the degenerate samples.

3.1.4.1 1064-nm Laser System

A 30-W IPG fiber laser (YLR-30-1064-LP-SF) provides 1064-nm light for optical dipole trapping. We split the output of the fiber laser into four paths to supply power to the main pancake trap, cross pancake trap, vertical cross/lattice, and the horizontal lattice (see Figure 3.6). Each path contains an AOM (IntraAction AOM-402AF4 or AOM-302AF4) and a solenoid shutter. We built the solenoid shutters using computer speaker voice coils using the design from [244]. The voice coils actuate mirrors that deflect the 1064-nm light into beam blocks and give full extinction of the ODTs. We drive the AOMs at RF frequencies offset from each other by 5 MHz and alternate between using the +1 or -1 diffraction order to minimize interference effects between the ODT beams. An amplified JQI DDS v4.0 is the RF source for each AOM. Each trapping beam is separated in frequency from all the others by at least 10 MHz and the polarizations of the main pancake, cross pancake, and vertical cross are set to be mutually orthogonal at

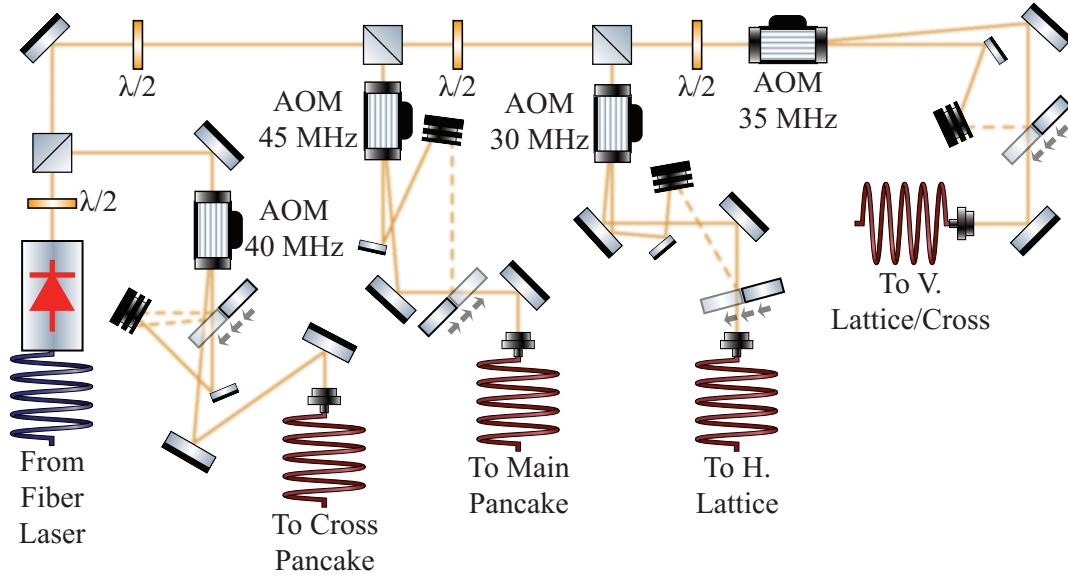


Figure 3.6: The 1064-nm laser breakout breadboard. The IPG fiber laser output (left) is split into four arms to supply power to each of the main pancake trap, cross pancake trap, vertical lattice, and horizontal lattice. AOMs offset the laser frequency between the traps to prevent heating of the atomic samples due to interference effects.

the experiment to further minimize interference.¹⁹ Despite an angle-cleaved AO crystal, the AOM-AF series AOMs generate a back-reflected acoustic wave during operation. The back-reflection mixes a 50-dB suppressed ∓ 1 order beam into the ± 1 order output of each AOM. The unwanted order can interfere with other ODT beams at the experiment and drastically reduce the lifetime in a crossed dipole trap (see Figure 3.7). By offsetting each AOM's RF drive by 5 MHz, we ensure that the atomic sample cannot respond to the any interference patterns created by the opposite order light.

We fiber couple the dipole trap light to the experiment with SM LMA optical fibers (Coastal Connections S-FAMkFAMk-10nx/130/3-7.6). These fibers are significantly less expensive than the photonic crystal fibers used elsewhere in the JQI and can withstand up to 10 W of power in their core. The primary disadvantage of the LMA fibers is that the fiber cladding alone is a multimode wave guide, so finding the core-guided mode

¹⁹We have used polarizing beamsplitters on the far side of the chamber to estimate that the polarization extinction ratio of the ODT beams is ≈ 20 dB.

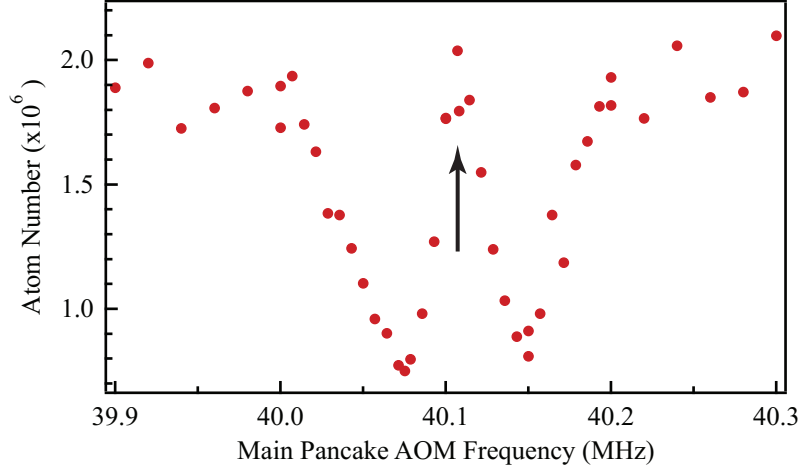


Figure 3.7: Atom number after a 2 s hold in the crossed dipole trap as a function of main pancake AOM drive frequency. The black arrow indicates the cross pancake AOM drive frequency. The main and cross pancake beams are nominally detuned from each other by 80 MHz. The data suggest that a back-reflected acoustic wave couples a small amount of opposite diffraction order light from each AOM to the experiment. We confirmed this hypothesis by heterodyning the fiber-coupled light for the dipole beams.

during initial alignment can be challenging. The IPG laser output has $M^2 \simeq 1$, so we routinely achieve fiber coupling efficiencies $\simeq 80\%$. At the LMA fiber output, each dipole beam is polarized with a Glan laser polarizer (Thorlabs GL10-C26). With the IPG power set to 15 W, the {main pancake, cross pancake, vertical cross, horizontal lattice} beam contains {4 W, 2.5 W, 1 W, 1 W} after the polarizer. The vacuum chamber optics for all the dipole beams can be seen in Figure 3.8 and Figure 3.9. We pick off a fraction of each dipole beam with either a backside-polished laser line mirror (Thorlabs NB1-K14-SP) or an AR-coated wedged window (Thorlabs WW11050-C14) and focus it onto an InGaAs PD (Thorlabs DET10C). Assuming the beam sampler’s Jones matrix is proportional to the identity (*i.e.* the beam sampler’s reflectivity is polarization independent), then the PD current is a measure of the full beam power. We convert the PD current to a voltage (with either a 1-k Ω or a 5-k Ω resistor) and use it to stabilize the dipole beam power via feedback to the AOM RF power from a PID 2.5.2. The typical amplitude of short-term intensity fluctuations is $\lesssim 1\%$ when the dipole beams are intensity locked.²⁰ However,

²⁰We have not yet performed a spectrum analysis of these fluctuations, but the locking bandwidth is typically $\simeq 20$ kHz. Out-of-loop PDs have only recently been installed on all the ODT beam paths. Analysis

the long-term fluctuations (timescales $\simeq 1$ day) in the intensity lockpoint are $\simeq 10\%$. We investigated several potential sources of these drifts related to the intensity locking optics and PDs, but none of these appear to be responsible. The most likely culprit is temperature instability in either current-to-voltage conversion resistor or the input offset trimpot in the PID. Although the long timescale drifts in laser intensity have not yet been an impediment to experimental progress, the resistors and trimpots should be replaced when the next version of the JQI PID is finished.

3.1.4.2 445-nm Laser System

The current goal of the strontium experiment is the realization of a uniform potential for alkaline-earth-metal atoms. We have added a dynamically-shapable, blue-detuned ODT to the apparatus in order to achieve this goal and increase experimental flexibility. The light source for the blue-detuned trap is a multimode, high-power, 445-nm laser diode (Casio M140). A DMD evaluation board (Texas Instruments DLP Lightcrafter 3000) provides dynamic shaping of the potential. The DMD is a 608×684 array of $7.6 \mu\text{m}$ pitch aluminum mirrors that is controlled by a Linux processor embedded on the Lightcrafter evaluation board. Each mirror's tilt can be switched between $+12^\circ$ and -12° relative to the DMD chip normal. The Lightcrafter memory can store up to 96 1-bit depth BMP images, which we create using Matlab.²¹ The "new" SetList v1.6.0 cycle control software (see Section 3.5) loads the image patterns to the DMD and controls image display timing with a TTL trigger.²² The maximum frame rate of the DMD depends of the number of images in the pattern sequence. Sequences with ≤ 24 images fit inside a single buffer on the DMD, allowing frame rates up to 4 kHz. Longer sequences require multiple buffers, limiting the frame rate to 1.6 kHz. Once the ultracold gases have reached degeneracy, the

of fast intensity fluctuations will proceed when we can borrow a low-frequency spectrum analyzer.

²¹The image bit depth is not a limitation because we are using monochromatic illumination.

²²The forthcoming version of Setlist will use a Matlab, rather than a Lua, function parser. This will allow us to integrate image creation directly into Setlist.

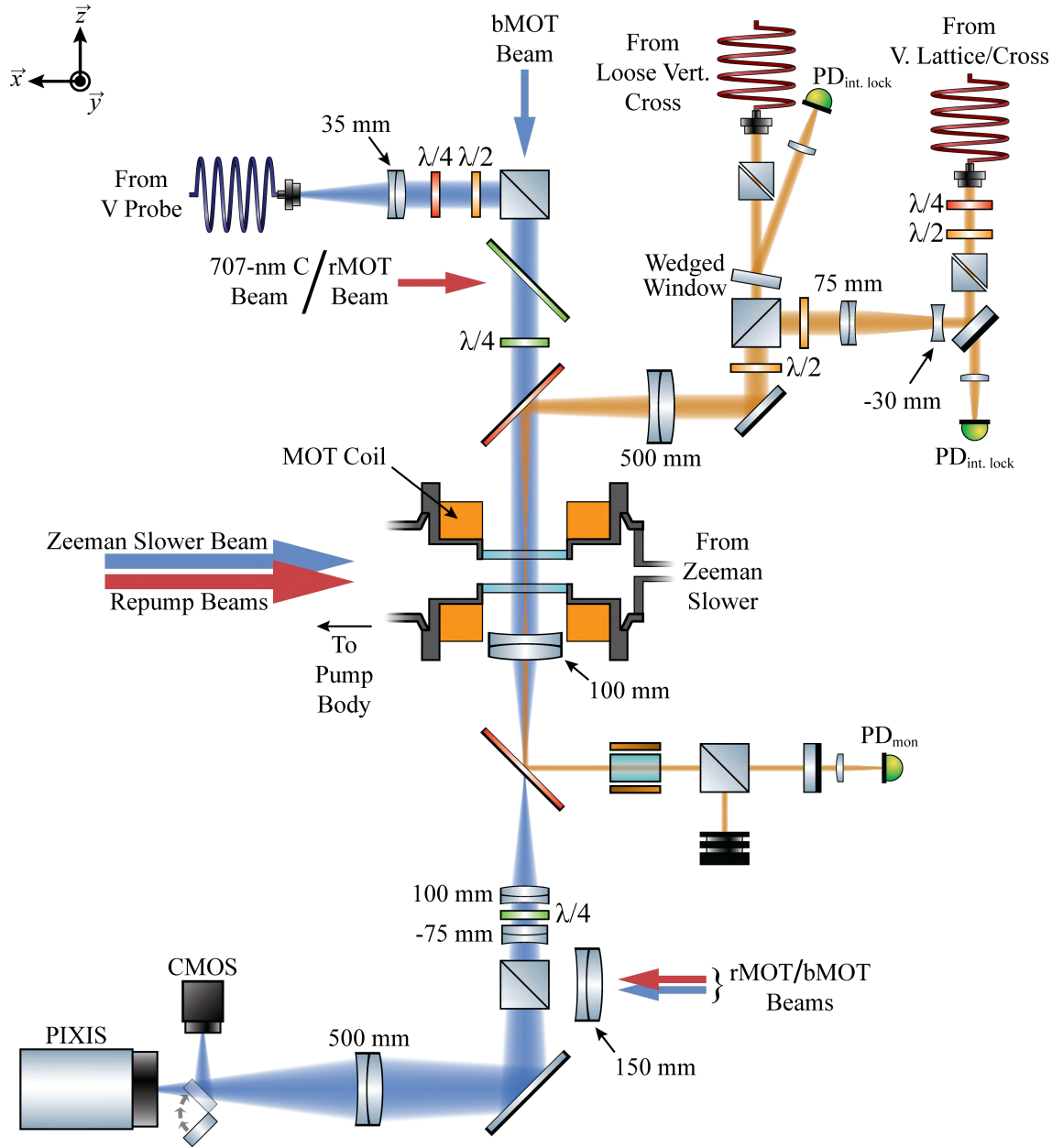


Figure 3.8: The vertical dipole trapping and imaging optics. The vertical MOT beams, a 707-nm repump beam, two 1064-nm dipole trapping beams, and the vertical probe beam are combined above the chamber using polarizing and dichroic beamsplitters. The laser beams are separated underneath the chamber in a similar manner and the MOT beams are retroreflected (by optics that are not shown). The loose vertical cross helped to produce our first ^{86}Sr BECs, but we discontinued its use once the horizontal cross pancake beam was added to the apparatus and its input fiber is currently disconnected on the laser side. A liquid crystal variable waveplate (Meadowlark Optics SRC-200-IR2) allows either of the vertical cross beams to be adiabatically deformed into an optical lattice.

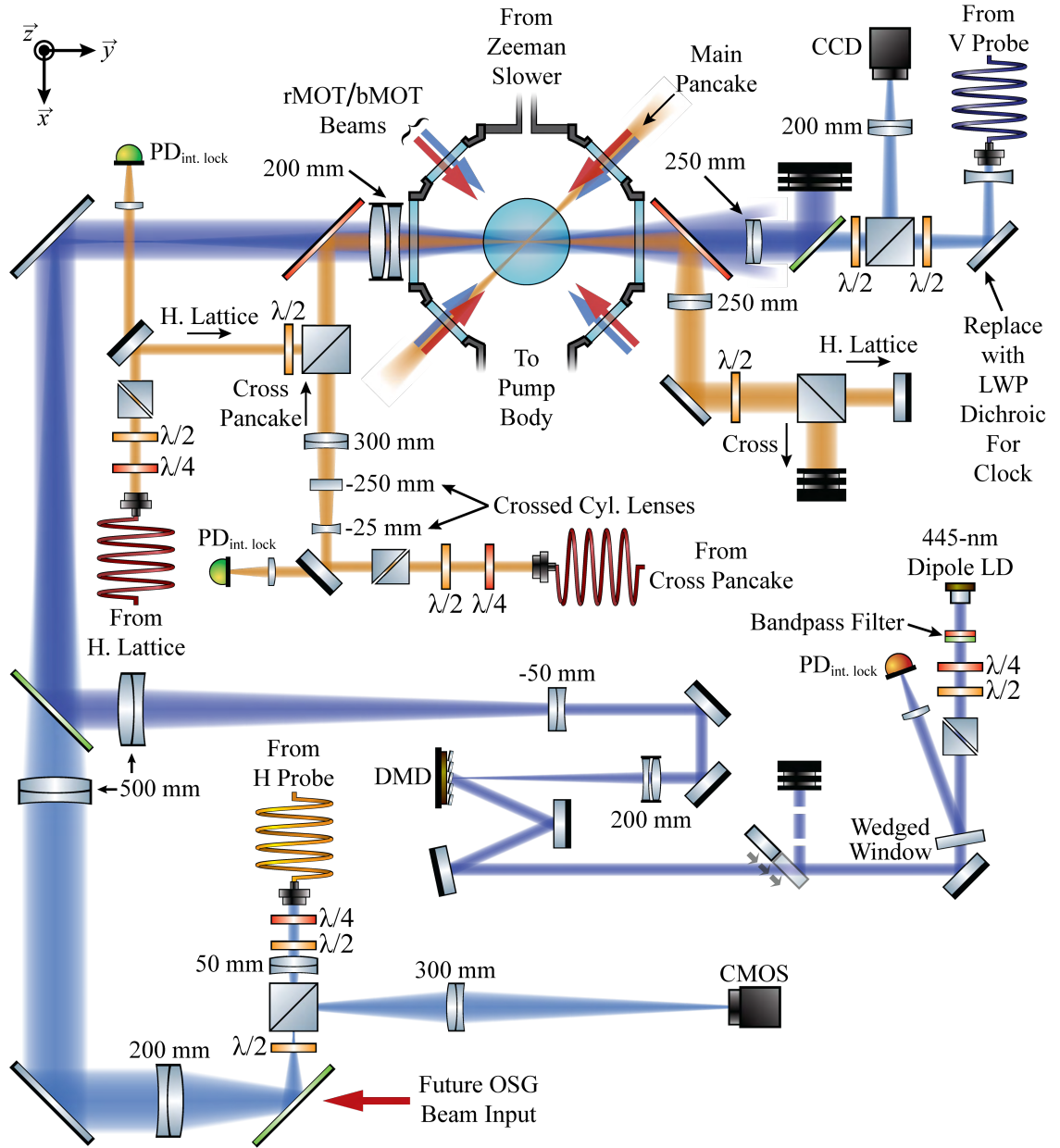


Figure 3.9: The horizontal dipole trapping and imaging optics. Dichroic beamsplitters combine 445-nm, 461-nm, and 1064-nm beams on the left side of the chamber to overlap dipole trapping beams and probe light at the atoms. Future input points for OSG beams and a clock laser are indicated. The 445-nm laser system optics and the DMD are shown lower right.

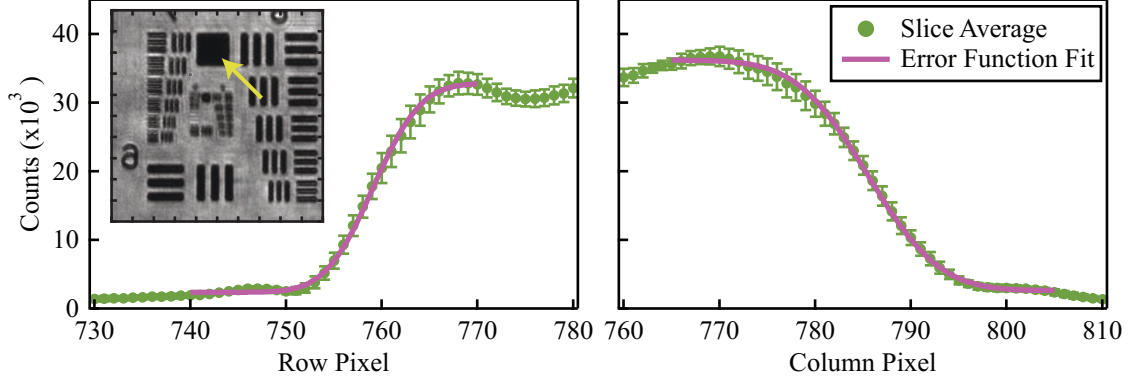


Figure 3.10: The USAF 1951 test pattern imaged with the DMD relay imaging system and error function fits to 50-pixel wide slices through the indicated pattern feature in the inset (see Section 3.2). Error bars represent the standard deviation of the pixels within the slice. By counting the width in pixels of group 7, element 1 (inset, top left), we estimate the magnification, in this test setup, to be 10.87(32). The uncertainty in the magnification represents a 1 pixel uncertainty in the separation of a line pair.

trap frequencies of the 1064-nm dipole traps are $\lesssim 100$ Hz, so even the lower of the DMD frame rates enables adiabatic deformation of the potential.²³

Quasi-uniform trapping potentials require rapid spatial changes in the magnitude of the confining potential near the trap edge (and the minimization of such changes near the trap center) [226, 245, 246]. In our case, the strength of the trapping potential is proportional to the optical intensity. Sufficiently large intensity gradients are attainable with the complementary approaches of high optical resolution and intensity. When cooled to 14 °C, the Casio LD supplies up to 1 W of power at 443.5 nm with a spectral width ≈ 1 nm.²⁴ The optics for the blue-detuned ODT can be seen in Figure 3.9. To prevent any resonant ASE (near 461 nm) from reaching the degenerate gas, we send the blue dipole beam through an optical bandpass filter (Chroma Technology ZET436/20x, cutoff $\lambda \approx 446$ nm). A wedged window (Thorlabs WW41050-C6) at near normal incidence samples the beam after polarization by a Glan Laser polarizer (Thorlabs GLB10). We

²³Assuming that suitable grayscale control of the potential has been implemented on the DMD via half-toning or holography. If instead the DMD has only binary control of the potential, we would require the trap frequencies to be much larger than this frame rate.

²⁴With the laser at full output power, the Thorlabs TCLDM9 LD mount and ITC4005 temperature controller can only maintain this temperature if the LD turns off for several seconds during bMOT loading or between experimental cycles.

detect the sampled power with a Si PD (Thorlabs DET36A) and use the PD signal to lock the laser intensity using feedback to the LD current from a Newport LB1005 PI controller. A solenoid shutter gives us slow digital control of the blue-detuned beam and displaying a black image on the DMD extinguishes the light at the atomic sample on a time scale similar to the DMD frame rate. Two mirrors align the dipole light onto the DMD at an angle of incidence of 24° so that the $+12^\circ$ tilted micromirrors reflect the beam at normal incidence. Due to the small spatial extent of the micromirrors, the DMD is a diffractive optical element, so the reflected (0th-order) beam typically contains only $\lesssim 25\%$ of the incident power.²⁵ We initially planned to fiber couple light from the LD to the DMD with an SM fiber to improve spatial mode of the 445-nm beam incident to the DMD. However, the multispatial mode of the LD output prevented efficient fiber coupling, which forced us to transmit light to the DMD in free space.

To make a blue-detuned dipole trap, we relay-image the DMD onto the atomic sample (see Table 3.2 for a list of lenses used in the *forward blue dipole* system).²⁶ The relay imaging system was designed to have a $10\times$ demagnification and a diffraction-limited Airy PSF radius of $2.5\ \mu\text{m}$. The large demagnification increases the intensity of the ODT beam by $\sim 100\times$ and means that each resolution-limited spot contains light from approximately 51 micromirrors, so we can achieve nearly continuous grayscale control of the trap shape (at fixed depth) via half-toning [247]. We characterized the relay system by using it to image a USAF 1951 test target onto a CCD camera with $2.5\ \mu\text{m}$ pixels (Point Grey FL3-U3-32S2M-CS). Figure 3.10 shows the results of this test. We can estimate the resolution and magnification of the imaging system from the number of line pairs per mm of the largest unresolved feature group and by counting the pixel width of a line pair, respectively. However, this method for determining the resolution

²⁵Even when the 445-nm LD is operating at low power, there can be appreciable light anywhere in the 2π steradians that have a line of sight to the face of the DMD chip. Beware!

²⁶This imaging system was named to distinguish it from the *reverse blue dipole* imaging system, which uses some of the same optics for a different purpose.

is inherently subjective, and better results can be achieved by fitting the edge of a test pattern feature with a Heaviside theta function convolved with a Gaussian approximation to the PSF – *i.e.* a Gaussian error function (see Table 3.3 for a summary of the results and Section 3.2 for a more detailed explanation of the analysis). The Airy radius along the \vec{x} (\vec{z}) axis of Figure 3.9 is $2.6(2) \mu\text{m}$ ($3.9(2) \mu\text{m}$). The difference in resolution between the two directions is due to astigmatism.²⁷ Dynamically-shapeable traps have a variety of uses, but in order to study $SU(N)$ -symmetric Hamiltonians, a box-like potential with the smallest possible spatial extent is desirable (see Section 1.2). The current relay system’s resolution will likely restrict the size of a uniform potential to be $\gtrsim 10 \mu\text{m}$. If this line of research is still active when the experiment moves to its new home in the PSC, a higher resolution system should be implemented (perhaps using the method of [248]).

A useful dynamically-shapable trap must be substantially deeper than the chemical potential of the degenerate gas that it is intended to confine. The intensity of the dipole trapping beam at the atoms and the real part of the AC polarizability of strontium at 443.5 nm set the trap depth. Assuming uniform illumination of the DMD, the average intensity inside a resolution limited spot is

$$I_{avg} \gtrsim f M^2 \frac{P}{A} \approx \frac{1}{8} \times 11.9^2 \times \frac{1 \text{ W}}{608 \times 684 \times (7.64 \mu\text{m})^2} \approx 0.7 \text{ W/mm}^2. \quad (3.1)$$

An optical power, P , reflects off a DMD with area, A , and propagates through an imaging system with magnification $1/M$ (see Section 3.2 for discussion of the magnification measurement). The diffractive nature of the DMD and losses in the imaging system allow only a fraction, f , of P to reach the degenerate gas. Only 25% of P diffracts into the 0th order and a further 50% is lost before the power can be measured on the far side of the vacuum chamber, so we can conservatively estimate that $f \approx 1/8$. The AC polarizability of the 1S_0 ground state, $\alpha_{^1S_0}$, can be found using the method of [53, 202] and the data

²⁷A deformed mirror is likely the cause of the aberration. Most of the mirrors have been changed between the test setup and the experimental configuration.

Table 3.2: The component lenses, data acquisition cameras, and magnification for each imaging system. The *forward blue dipole* system images the DMD onto the atoms and the *reverse blue dipole* system allows *forward* system’s objective lens to be used for high resolution imaging of ultracold samples.

Lens	Horizontal	Vertical	Blue Dipole	
			Forward	Reverse
Objective	Thorlabs AC254-250-A	Edmund Optics 49-390	CVI LAP-200.0-40.0-SLMF-450-PM	
Relay 1	–	OptoSigma 026-1170	Thorlabs AC508-500-A	
Relay 2	–	Thorlabs ACN254-075-A	Thorlabs ACN254-050-A	Thorlabs AC508-200-A
Eye Piece	Thorlabs AC254-200-A	Thorlabs AC508-400-A	Thorlabs ACA254-200-A	Thorlabs AC254-300-A
Camera	Point Grey FL3-FW-20S4M-C	Princeton Instruments PIXIS Excelon 1024B	–	Point Grey FL3-U3-32S2M-CS
Measured Magnification	.898	5.48	11.86	3.85

from [113]. The maximum trap depth of the blue-detuned ODT is then ≈ 400 nK, which is about $\{8\times, 40\times, 7\times\}$ larger than the chemical potential of the largest $\{^{84}\text{Sr}, ^{86}\text{Sr}, ^{87}\text{Sr}\}$ degenerate gases created by the apparatus.

3.2 Imaging Systems

The quantities of interest in ultracold gas experiments are typically the momentum, position, and internal state (spin) distributions of the atomic cloud. These distributions and their time dependence can be measured with a variety of spectroscopy and imaging techniques [17, 169, 218, 249–252]. We have chosen to use near-resonance absorption imaging on the 461-nm, $^1S_0 \rightarrow ^1P_1$ transition for data collection. Absorption imaging on this transition has the advantage of simplicity, high signal to noise, and high spatial resolution for a given NA. The downside of using the 32-MHz wide line is that the hyperfine transitions in ^{87}Sr are not resolved, which complicates image analysis (see Appendix A) and prevents simple spectroscopic readout of the nuclear spin state.

During each experimental run, we acquire three images: an absorption image, F_1 , with both probe light and the atomic sample; a bright-field image, F_2 , with probe light only; and a dark-field image, F_3 , that characterizes background light pollution. From these three images, we can extract the optical depth of the ultracold gas, which can give us access to all the distributions that we want to measure. Here I will discuss the absorption technique following the approach of [169]. The images measure the optical depth of the atomic cloud, D_a , and the normalized probe intensity in the object plane, P , but are effected by several noise sources: S represents scattering of the probe after the object plane, A is the fluctuating probe amplitude, and B is the noise from all other sources. The contribution from each noise source, Z , to the signal measured by a camera pixel at position (x, y) can be treated as an independent random variable, $z(x, y)$. The distribution function for $z(x, y)$ is $Z(z, x, y)$. Without loss of generality, we can represent $z(x, y)$ using

$$z(x, y) = \bar{z}(x, y) + \delta z(x, y), \quad (3.2)$$

where $\bar{z}(x, y)$ is the mean value of $z(x, y)$ and $\delta z(x, y)$ is another random variable with distribution function $Z(\delta z, x, y) = Z(z - \bar{z}, x, y)$. The counts recorded by the camera pixel at (x, y) , in the image F_i , can be expressed in terms of the optical depth, probe intensity, and noise terms as

$$\begin{aligned} F_1(x, y) &= a_1(P(x, y)e^{-D_a(x, y)} + s_1(x, y)) + b_1(x, y), \\ F_2(x, y) &= a_2(P(x, y) + s_2(x, y)) + b_2(x, y), \\ F_3(x, y) &= b_3(x, y), \end{aligned} \quad (3.3)$$

where $D_a(x, y)$ is the optical depth of the ultracold gas at (x, y) , $P(x, y)$ is the probe intensity (normalized such that $\int P(x, y)dx dy = 1$). $s_i(x, y)$, $b_i(x, y)$, and a_i are sampled from their underlying distribution functions ($S(s, x, y)$, $B(b, x, y)$, and $A(a)$, respectively). Note that we are neglecting fluctuations in P that could occur between F_1 and F_2 . The

optical depth of the atomic cloud measured by the pixel at (x, y) , $D_m(x, y)$, is

$$\begin{aligned} D_m(x, y) &= -\ln \left[\frac{F_1(x, y) - F_3(x, y)}{F_2(x, y) - F_3(x, y)} \right] \\ &= -\ln \left[\frac{a_1(P(x, y)e^{-D_a(x, y)} + \bar{s}(x, y) + \delta s_1(x, y)) + \delta b_{12}(x, y)}{a_2(P(x, y) + \bar{s}(x, y) + \delta s_2(x, y)) + \delta b_{23}(x, y)} \right]. \end{aligned} \quad (3.4)$$

In deriving Equation 3.4, we have used Equation 3.2 and taken $\delta b_{ij}(x, y) = \delta b_i(x, y) - \delta b_j(x, y)$. The technical noise terms are small for our imaging systems, so $D_m(x, y) \approx D_a(x, y)$. We can find the leading-order correction to $D_m(x, y)$ by expanding the argument of the logarithm of Equation 3.4 in a Taylor series,

$$D_m(x, y) = -\ln \left[e^{-D_a(x, y)} + \left(1 - e^{-D_a(x, y)}\right) \frac{\bar{s}(x, y) + \delta s(x, y) + \delta b(x, y)/a}{P(x, y)} \right], \quad (3.5)$$

where, for simplicity, we take $a = a_1 \approx a_2$, $\delta b(x, y) = \delta b_{12}(x, y) \approx \delta b_{23}(x, y)$, and $\delta s(x, y) = \delta s_1(x, y) \approx \delta s_2(x, y)$. The approximations for the random variables are valid because the images, F_i , are taken in rapid succession and therefore the random variables are correlated. Equation 3.5 shows that the sensitivity of absorption imaging to D_a rolls off exponentially with D_a due to the imperfections of the imaging system. Formally, the response, dD_m , of measured optical depth to a change, dD_a , in the actual optical depth is given by

$$dD_m(x, y) = dD_a(x, y) \left(1 - K(x, y)e^{D_a(x, y)}\right), \quad (3.6)$$

where $K(x, y)$ represents the fraction in the argument of the logarithm in Equation 3.5.

There are three imaging systems currently implemented on the apparatus: a low-resolution, horizontal system that we use for TOF imaging of the MOTs and high temperature gases in the ODT; a high-resolution, vertical system that we use for both TOF and *in-situ* imaging of optically trapped samples; and a high-resolution, horizontal imaging system (the *reverse blue dipole* path) that will eventually be used to measure spin state populations of ^{87}Sr degenerate Fermi gases. Table 3.2 shows the lenses and data acquisi-

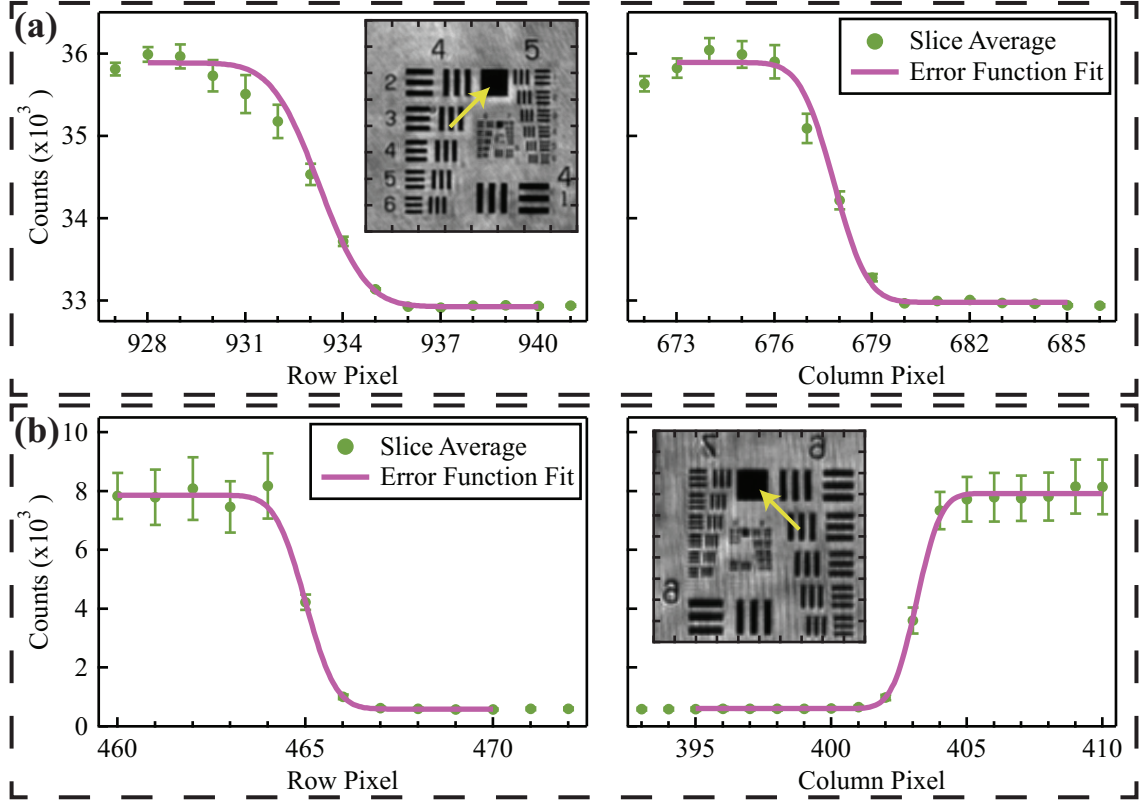


Figure 3.11: Imaging resolution tests for the horizontal, (a), and vertical, (b), imaging systems using the USAF 1951 test pattern. The left and right graph in (a), (b), show error function fits to 10-pixel, 50-pixel, wide slices through the pattern feature indicated in the inset.

tion camera for each imaging system. Flea cameras from Point Grey have a small form factor with reasonable quantum efficiency (from 30% to 50%, depending on the sensor) and dark counts (typically ≤ 30 counts for a 12-bit DAC). The Flea cameras can also be dropped-in for temporary imaging or alignment tasks. The PIXIS provides high quantum efficiency (for high-magnification imaging), low dark counts, and low readout noise. We find the imaging magnification by observing the effect of gravity on the rMOT, or ODT, in TOF (horizontal and reverse blue dipole) and measuring the TOF separation of a BEC diffracted by an optical lattice (vertical). The forward blue dipole imaging magnification was measured *in situ* by observing, with the vertical imaging system, the size at the atoms of a known pattern on the DMD.

The key performance metrics for the imaging systems in our experiment are the

resolution and point-spread function (PSF). There are two criteria, due to Rayleigh and Sparrow, for assessing the resolving power of an optical system [253–255]. The Rayleigh criterion says that two point-like objects are resolvable if the second object’s Airy diffraction pattern in the image plane is centered on the first null in the Airy pattern of the first object. The Sparrow criterion posits that the two objects can be resolved when the distance between them is equal to the FWHM of the central peak of the imaging system’s PSF. We evaluate the resolution of each imaging system using a USAF 1951 test target (see Figures 3.10 and 3.11). An imaging system’s PSF can be approximated as a Gaussian with $1/e^2$ width w , $g(x, w)$, and the change in optical intensity in the object plane across the edge of a test pattern feature is proportional to the Heaviside theta function, $\Theta(x)$. The resulting optical intensity in the image plane is

$$A_1 + A_2(g * \Theta)(x) = A_1 + A_2 \int_{-\infty}^{\infty} g(x', w)\Theta(x - x')dx' = A_3 + A_4 \operatorname{erf}(x, w) \quad (3.7)$$

where $\{A_1, A_2, A_3, A_4\}$ are constants and $\operatorname{erf}(x, w)$ is the Gaussian error function. By fitting slices through a square pattern in the test images with Equation 3.7, we can find the Gaussian approximation to the PSF of each imaging system. The FWHM of the Gaussian PSF gives a Sparrow resolution for the imaging system. The width of the Gaussian approximate PSF and the position of the first null, x_0 , in the Airy PSF of an imaging system are related by

$$x_0 \approx 0.529 \times 3.8317 \times w. \quad (3.8)$$

The first numerical factor in Equation 3.8 converts the Gaussian width to the characteristic width of the Airy function and the second factor relates the Airy width to the location of the first null. The Rayleigh and Sparrow resolutions for all the tested imaging systems can be found in Table 3.3. Because the objective for the blue dipole imaging system was already installed on the apparatus, the reverse blue dipole imaging system resolution has not been tested.

Table 3.3: The Rayleigh (for an Airy PSF) and Sparrow (for a Gaussian PSF) resolutions for all three imaging systems. I extracted the resolutions using the error function fits to the USAF test patterns in Figure 3.10 and Figure 3.11. The quoted resolution uncertainties were calculated using the 1σ uncertainty in the fitted error function width. The horizontal and vertical systems were tested with 461-nm light, while the blue dipole system was tested at 445 nm. The resolution tests did not include a viewport, but simulations of the higher resolution systems in Zemax suggest that the vacuum chamber viewport should marginally improve the imaging resolution.

Imaging System	Rayleigh		Sparrow	
	Row	Column	Row	Column
Horizontal	16.0(8) μm	11.3(9) μm	13.1(7) μm	9.3(7) μm
Vertical	4.3(4) μm	4.8(6) μm	3.6(3) μm	4.0(5) μm
Blue Dipole	2.6(2) μm	3.9(2) μm	2.1(2) μm	3.2(2) μm

There are several potential technical issues that can affect the imaging performance. The first is image blurring during the integration time, Δt , due to the 461-nm photon recoil velocity, $v_{rec} \approx 9.8$ mm/s. Given that the transition decay rate, Γ_{bl} , sets an upper limit on the photon scattering rate, the root-mean-square blur is $r_{rms} = v_{rec} \sqrt{\Gamma_{bl} \Delta t^3 / 3} \approx 0.08 \times (\Delta t / \mu\text{s})^{3/2} \mu\text{m}$, which suggests that we restrict the imaging time to $\lesssim 10 \mu\text{s}$ for $\approx \mu\text{m}$ resolution imaging. The second potential issue is saturation of the atomic transition by the probe beam, which causes bleaching of the ultracold gas and can reduce S/N . We can relate the measured optical depth, $D_m(x, y)$, to the resonant, unsaturated optical depth, $D_{rs}(x, y) = \tilde{n}(x, y) / \sigma_{88}$ (see Appendix A), through the susceptibility [256, 257] and find

$$D_{rs}(x, y) = D_m(x, y)(1 + 4\Delta^2 + s(x, y)). \quad (3.9)$$

Δ is the laser detuning in units of Γ_{bl} and $s(x, y)$ is the local saturation parameter, $I(x, y) / I_{sat}$. The bright-field image contains $I(x, y)$ in units of counts per pixel, which we can convert into units of I_{sat} with knowledge of two quantities: the imaging-system magnification, and the system's detection efficiency in mW/count (*i.e.* the total quantum

efficiency of the imaging system).²⁸ We can obtain the latter by iris-ing the probe beam until it is fully collected onto the camera and then measuring the probe power as it enters the chamber with a trusted power meter. A third issue is differential mechanical vibration of the optomechanical elements of an imaging system. If the relative motion has a characteristic frequency that is incommensurate with the imaging frame rate, fringes can appear in the processed absorption image. The best ways to eliminate this issue are to increase the mechanical stability of the system, increase the frame rate, or decrease the level of background vibration.²⁹ For a sufficiently large data series, the associated bright-field images are a representative sample of the space of all possible probe beam images (for the given configuration of the apparatus). We take a random subset of the bright-field images (usually 20 – 30) and create an orthonormal (albeit incomplete) basis for the space of probe images using a Gram-Schmidt process.³⁰ The probe beam intensity profile in the absorption image can be reconstructed by projecting the atom-free region of the image onto the orthonormal basis. This method removes most high-amplitude or low-frequency fringes from the processed absorption image. Fitting to the basis is slow and making the basis from a time-ordered subset of bright-field images can create fringing in the processed image, so we only use an orthonormal basis in post-processing and not during live data acquisition.

We use a multistep procedure to fit our absorption images with Equations 1.26 and 2.17. We begin by calculating the background noise level, δ_{bg} , using a region of the image that contains no atoms. The uncertainty, $\delta D_{rs}(x, y)$, in the extracted optical depth, $D_{rs}(x, y)$, of the strontium gas grows exponentially with $D_{rs}(x, y)$ (see Equations 3.5

²⁸ $I(x, y)$ is given by $a_2(P(x, y) + s_2(x, y))$ (see Equation 3.3), so this correction is accurate only when $s_2(x, y) \ll P(x, y)$.

²⁹For our apparatus, the dominant source of mechanical noise is airflow from the HEPA filters above the vacuum chamber, some of which have a line of sight to the optics. In the new PSC lab space, the approximation to laminar flow is substantially better.

³⁰The experience of the ErNa (née Na) experiment suggests that a complete basis requires $\simeq 500$ bright-field images. This number is substantially less than the number of pixels because the space of all possible bright-field images is much smaller than the space of all possible images.

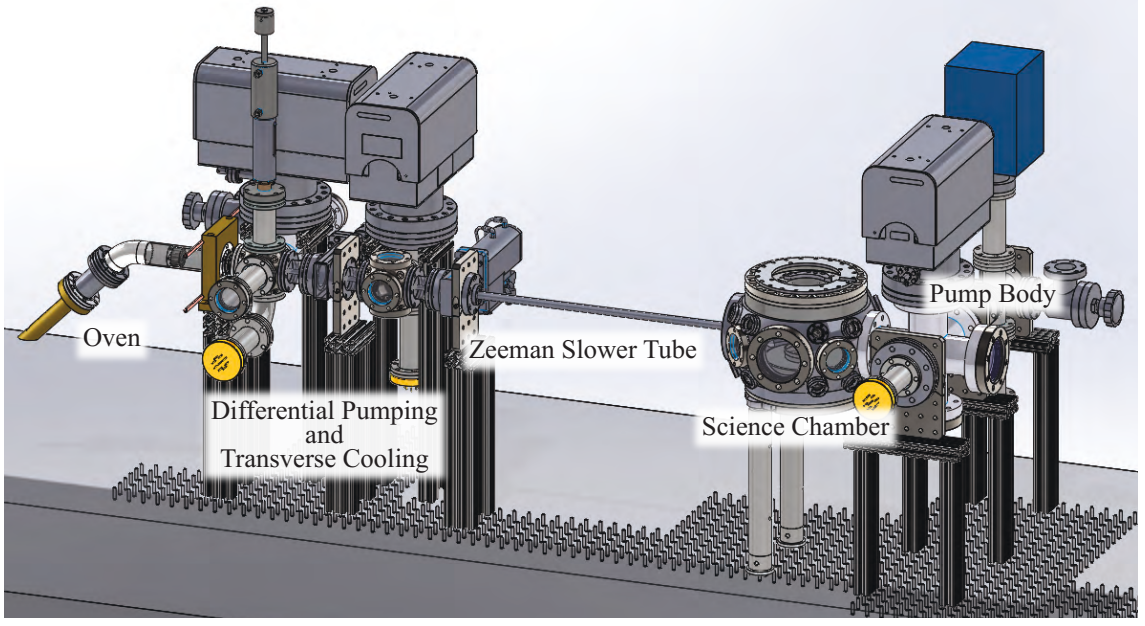


Figure 3.12: A 3D model of the vacuum chamber for the experiment with the major sections indicated. The \vec{B} field generating coils, plumbing connections, elevated optical breadboards, and oven supports are not shown.

and 3.6), so

$$\delta D_{rs}(x, y) \approx \delta_{bg} e^{D_{rs}(x, y)/C_D}, \quad (3.10)$$

where C_D is an empirically estimated cutoff. For images with a maximum optical depth $\lesssim 2$, we take $C_D = 1$. Optical depths > 2 are systematically underestimated due to technical noise and we take $C_D \approx 3$ when we want to fit to these high optical depths (see Equations 3.5 and 3.6). We use Equation 3.10 to weight our fits to the absorption image. We fit Gaussians to the gas to create initial guesses for the column density $\tilde{n}(x, y)$. The guesses for the distribution of the cloud are then used to generate initial parameters for a fit to Equation 1.26 or Equation 2.17.

3.3 Vacuum System

Ultracold neutral atom samples are extraordinarily delicate due to their low temperature and the shallow depth of typical confining potentials. As such, quantum degenerate

gases can only be produced in UHV or XHV environments. Because strontium only begins to have appreciable vapor pressure when it is heated above 300 °C, the design of a vacuum chamber that contains both a high-flux atomic source and a UHV region is nontrivial. Our vacuum chamber achieves these conflicting goals by separating the atomic beam source from the science chamber with several stages of differential pumping. The differential pumping tubes divide the chamber (shown in Figure 3.12) into three sections: the atomic-beam source, the transverse-cooling stage, and the science chamber.

An oven with a microcapillary array nozzle, based on the design in [258],³¹ is our atomic beam source. Two custom *ex vacuo* heaters (Mellen Company Inc. 11C-2403.5-TC and 11C-1302-TC) stabilize the nozzle and atomic reservoir temperatures to 650 °C and 600 °C, respectively, during experimental operation. We reduce the nozzle and reservoir temperatures to 250 °C and 100 °C, respectively, when the experiment is idle. Water-cooled brass blocks dissipate excess heat from the oven and keep the remainder of the vacuum system at a reasonable temperature. Because these blocks are cooled by house water, which has an effectively infinite reservoir, a flow switch (Proteus 0100C110) interlocks both the heaters and two electronic water valves to reduce the severity of any floods.³² A pneumatically-actuated flag can shutter the atomic beam during an experimental cycle, to reduce collisions with the ultracold gas and prevent strontium buildup on the Zeeman slower viewport. A 75 L/s ion pump (Gamma Vacuum 75S-CVX-6S-SC-220-N)³³ maintains a pressure $\simeq 6 \times 10^{-8}$ Torr when the oven is hot and $\simeq 4 \times 10^{-10}$ Torr when it is idling. These pressures are measured with a Varian UHV-24 ion gauge and they are typically one order of magnitude lower than the pressure implied by the ion pump current. The beam source section of the chamber can be isolated with

³¹This nozzle was installed on Christmas eve, 2015. The prior nozzle was also a microtube array, but the capillaries were secured with a high-temperature vacuum-compatible metallic epoxy. As we should have expected, the epoxy was unequal to the 650 °C temperature of the nozzle and its outgassing may have caused the slow poisoning of the oven section ion pump.

³²We seek to prevent a repeat of the great RbYb flood of 2010.

³³All our ion pumps accidentally have 220 V heaters.

a manual gate valve, which allows us to vent and open this section to replenish strontium or replace the ion pump while maintaining UHV in the remainder of the chamber. The atomic beam exits this region of the chamber through a pair of 0.25" diameter, 3" long differential pumping tubes.

A transverse-cooling stage increases the atomic flux into the science chamber. A small, 6-way cross gives us optical access along the directions perpendicular to the atomic beam. By inserting light detuned to the red of the $^1S_0 \rightarrow ^1P_1$ resonance, we can reduce the divergence of the atomic beam with 2D Doppler cooling. This decreased divergence increases the atom number in the bMOT by a factor of three. The distance between the oven nozzle and the two-dimensional-cooling zone is $d \approx 35$ cm. Other strontium degenerate gas experiments place the Doppler-cooling region much closer ($d \approx 10$ cm) to the atomic beam source [53, 182]. We added several viewports to the atom source during the oven changeover in the winter of 2015 because we suspected that the position of our transverse-cooling stage might adversely affect the atomic flux. The full, two-dimensional, Doppler-cooling stage could not be moved into the atom source section of the chamber due to the position of the atomic beam shutter. We split the Doppler-cooling stage so that horizontal atomic beam collimation occurs in the atom source section of the chamber and vertical collimation occurs in the transverse-cooling stage. The split-cooling configuration marginally improved the atom number compared to the original two-dimensional-cooling setup (the rMOT atom number was increased by $\approx 15\%$). The horizontal Doppler-cooling beams cause heating in the vertical direction, which may be sufficient for atoms to be skimmed from the atomic beam by the differential pumping tubes before the excess heat can be removed by the vertical cooling beams. Switching the position of the beam shutter and the vertical cooling would eliminate this issue and potentially further increase the atomic flux.³⁴ The transverse-cooling stage is pumped by a 75 L/s ion pump (75S-CVX-

³⁴We do not plan to test this hypothesis, since the next generation of the experiment will use a commercial strontium source from AOSense, Inc.

6S-SC-220-N), which sustains a pressure of $\approx 6 \times 10^{-10}$ Torr when the oven is hot and $\approx 1.5 \times 10^{-10}$ Torr when the oven is idling. A single differential pumping tube and a pneumatic gate valve isolate the transverse-cooling stage from the science chamber. The gate valve closes automatically in the event of a power outage.³⁵

The science chamber is a Kimball Physics spherical square attached to a 6-way cross pump body. The pump body incorporates a 75 L/s ion pump (75S-CVX-6S-SC-220-N), a titanium sublimation pump (VGScienta ST22 controlled by SPC8), a RGA (MKS Instruments e-Vision2), and an ion gauge (Varian UHV-24P). The presence of the pneumatic gate valve at the far end of the Zeeman slower tube enables independent venting of the science chamber.³⁶ Custom reentrant viewports on the top and bottom flanges of the spherical square allow coils to be placed close to the atomic samples.³⁷ All viewports have a custom AR-coating from Spectrum Thin Films (laser line at 461 nm and 689 nm plus broadband NIR).³⁸ The 2.75" and 4.5" viewports were installed with custom washers that allow Thorlabs cage system components to attach directly to the vacuum chamber. A band heater (TEMPCO MBH00162) keeps the Zeeman slower beam's sapphire entrance viewport at 150 °C to reduce strontium deposition. Even when the viewport is hot, the pressure in the science chamber is $\lesssim 5 \times 10^{-11}$ Torr (the measurement is limited by local heating of the chamber by the ion gauge). The ion pump is capable of maintaining this pressure without the assistance of the TSP (multiple TSP firings were necessary to initially lower the pressure from $\approx 1 \times 10^{-10}$ Torr). However, we run the TSP about once every year to ensure that the controller is still operating. This yearly TSP firing usually affects the pressure at the level of 1×10^{-12} Torr, which is similar to the background variation in

³⁵These are more frequent than one would expect. The ion pumps are all connect to a UPS with a ≈ 9 hour battery life. A pressurized air bladder, which is periodically refilled by a compressor, actuates the gate valve and beam shutter.

³⁶Fortunately, this feature has not been necessary.

³⁷Due to a fabrication error, the reentrant viewports block optical access from the 1.33" flange viewports. We have replacement viewports on hand that will be installed on the next generation of the apparatus.

³⁸We do not think this coating is very high quality and are now using a wider band custom coating from Cascade Optical Corporation on all new viewports.

the ion gauge reading.

3.4 Magnetic Field Coils

The initial confinement and cooling stages of ultracold alkaline-earth-metal atom experiments require spatially varying magnetic fields with magnitudes $\simeq 100$ gauss. For our experiment, the stages that require magnetic fields are a Zeeman slower, the bMOT, the metastable reservoir, and the rMOT. In principle, the necessary magnetic fields for some [259–263] of these steps could be provided by permanent magnets, but we generate all fields with electromagnetic coils for greater flexibility.

The Zeeman slower is a multilayer, variable-pitch "spin-flip" design with three coils: a positive slower coil, a negative slower coil, and a compensation coil [1, 193, 264].³⁹ A laser beam detuned from the 461-nm transition by -605 MHz counter-propagates with the atomic beam and slows the constituent atoms when the Doppler shift brings the laser into resonance. An ideal slower coil produces a Zeeman shift that exactly compensates the Doppler shift along its length to maintain a constant average scattering force, $\langle \vec{F}_s \rangle$, from the 461-nm beam. The magnetic field profile that produces this compensation is

$$\vec{B}_{\text{targ}}(x) = (B_{\text{sqr}} \sqrt{x/x_0 - 1} + B_0) \hat{x}, \quad (3.11)$$

where x_0 is the slower exit position, B_{sqr} is the magnetic field scale factor, B_0 is the magnetic field offset, and the origin for x is located at the bMOT center position (see Figure 3.13). The linewidth, Γ_{bl} , and wavevector, \vec{k}_{bl} , of the $^1S_0 \rightarrow ^1P_1$ transition set an upper limit on the achievable force,

$$\langle \vec{F}_s \rangle_{\text{max}} = \frac{\hbar \vec{k}_{bl} \Gamma_{bl}}{2} = m \vec{a}_{\text{max}}, \quad (3.12)$$

³⁹Note that strontium has no spin flip due to its nonmagnetic ground state.

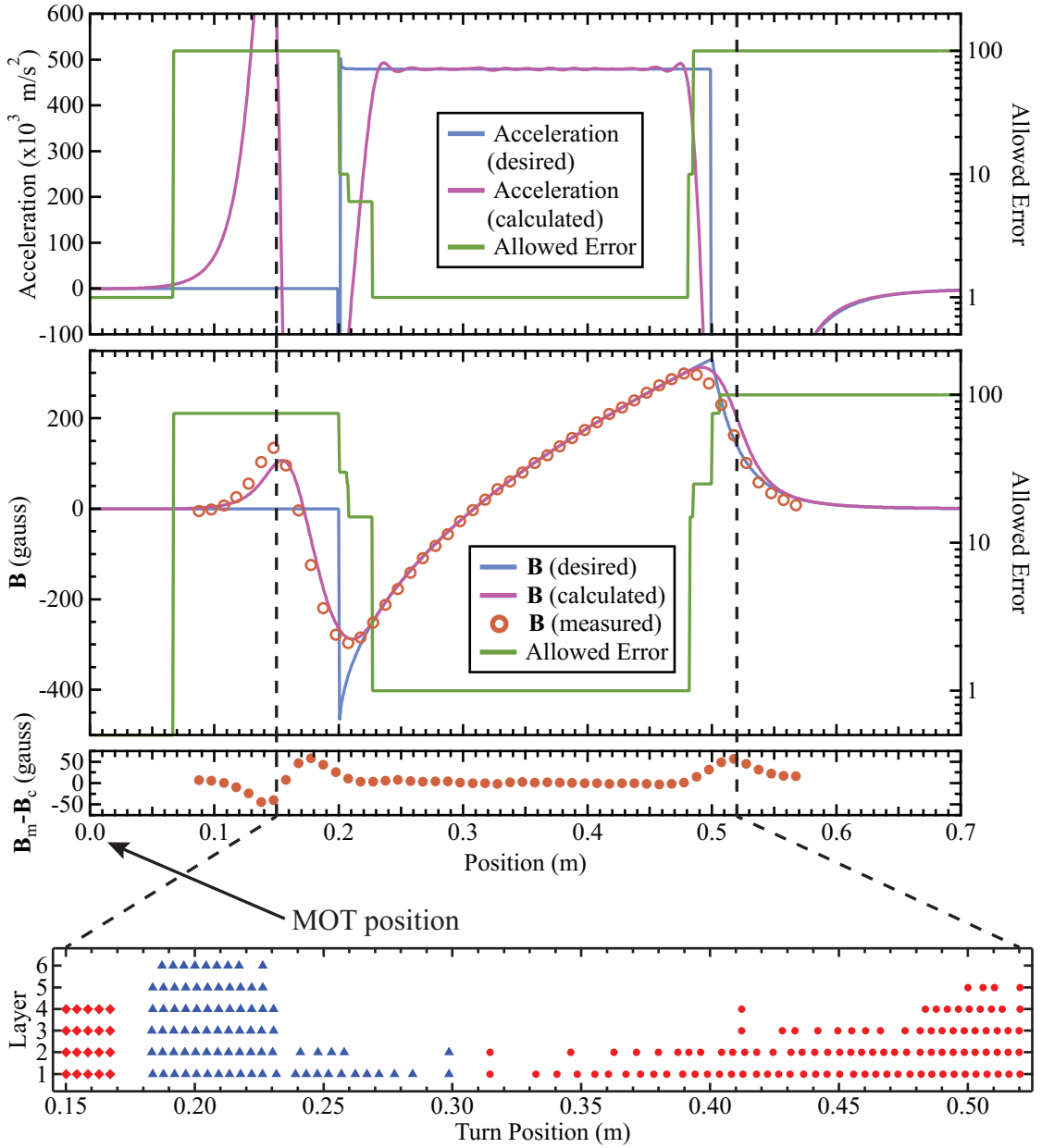


Figure 3.13: Calculation and measurement of the Zeeman slower field profile. Top: The calculated and desired acceleration profiles for the Zeeman slower (left axis). Middle: Calculated, desired and measured magnetic field profiles for the slower (left axis) with the difference between calculated and measured fields shown below. The measured profile had to be scaled by a factor of $62.5\times$, rather than the expected factor of $50\times$, to achieve good agreement with the calculated profile. We believe that the discrepancy is due to poor calibration of the gauss meter (see text). Top and Middle: The residuals at each step in the calculation are divided by the allowed error (right axis). Bottom: the position of each turn in the positive (red circles), negative (blue triangles), and compensation (red diamonds) coils as it crosses the xz -plane (see Figure 3.9) above the slower axis.

with m the atomic mass and

$$\vec{a}_{max} = \frac{\hbar \vec{k}_{bl} \Gamma_{bl}}{2m}. \quad (3.13)$$

In practice, the available laser intensity, I , limits the maximum atomic deceleration below \vec{a}_{max} because, on resonance, $\langle F_s \rangle \propto s/(1+s)$, where $s = I/I_{sat}$ is the saturation parameter of the 461-nm transition and $I_{sat} \approx 40.3 \text{ mW/cm}^2$. Our Zeeman slower is designed to achieve a constant deceleration of $\vec{a}_{target}(x) = 0.4a_{max}\hat{x}$, corresponding to $s = 2/3$, over a length $\approx 25 \text{ cm}$.

An iterative procedure, written in Igor pro by C. Herold and I. Spielman for Rb experiments, optimizes the design of the slower. I extended the program to handle a more generic coil configuration and to permit easy "by-hand" manipulation of the coils for making initial guesses. The iterative optimizer stretches and compresses four random turns from the positive or negative current coils for better replication of an ideal slower profile (it also adjusts the current in each coil section). Because we ultimately care about the consistency of the acceleration, the optimizer alternately compares the configuration's field profile, $B(x)\hat{x}$, and acceleration profile,

$$\vec{a}(x) = \left(\frac{\mu_B}{\hbar k_{bl}} \right)^2 \frac{dB}{dx} (B_0 + B(x)) \hat{x}, \quad (3.14)$$

to their target forms. The square deviation of the calculated and target fields is calculated at each point ($\approx 15 \text{ samples/cm}$) and is divided by the square of the position-dependent allowed error (see Figure 3.13), which prevents unphysical changes in the field profile from spoiling fit convergence.⁴⁰ If the new coil configuration has a lower total deviation than the old coil configuration, the optimizer retains the new configuration and updates the residuals. With a reasonable initial guess for the coils, the program produced an acceptable set of coil positions after about 1000 iterations and calculated the drive currents in the

⁴⁰Note that the allowed error is determined empirically. I adjusted its value in the wings to improve the convergence in the slowing region.

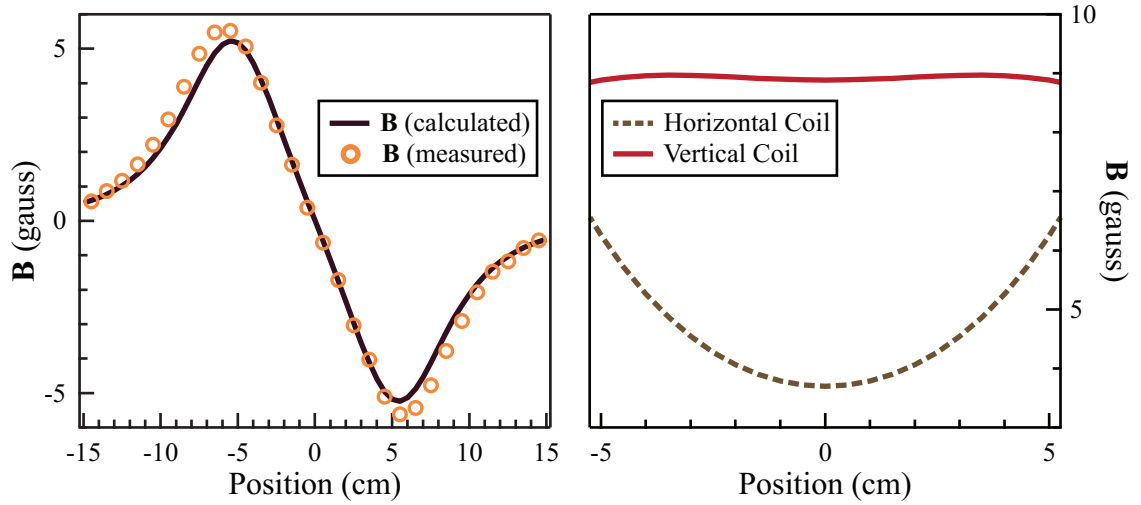


Figure 3.14: Left: the calculated (solid line) and measured (open circles) axial magnetic field profiles for the MOT coils at a drive current of 1 A. The spacing between the MOT coils was 7.925 cm. The measured profile had to be scaled by 1.25 to achieve quantitative agreement with the calculation (see text). Right: The calculated magnetic field profiles for the vertical shim coil (solid red) and the horizontal shim coils (dashed olive) at the maximum drive current of 6 A.

{*positive, negative, compensator*} coils to be $\{I_+, I_-, I_c\} = \{35.8 \text{ A}, -29.0 \text{ A}, 61.4 \text{ A}\}$.⁴¹

The calculated acceleration and field profiles, as well as the associated coil positions, are shown in Figure 3.13. We constructed the slower by wrapping 0.427 cm wide, kapton-coated, square tubing (from Small Tube Products with coating provided by S&W Wire Co.) onto a 1.51" diameter aluminum form. I then measured the field profile at 2% of the design current with a Hall probe. There is qualitative agreement between the calculation and measurement, but quantitative agreement was only obtained with a 62.5 \times scale factor (rather than 50 \times as expected, see Figure 3.13). Three sources of the discrepancy immediately present themselves: imperfect wrapping of the slower coils, inaccurate currents from the test supplies, and poor calibration of the Hall probe. The currents from the bench supplies that I used are only accurate at the 10% level. This inaccuracy in the supply currents can account for some small kinks that are visible in the plot of the magnetic field residuals (near the changeover from the positive to the

⁴¹Experimental optimization of the bMOT, and the transfer into the rMOT, yielded somewhat different currents: $\{I_+, I_-, I_c\} = \{39.5 \text{ A}, -32.0 \text{ A}, 32.1 \text{ A}\}$

negative coil) in Figure 3.13, but not for the overall difference in scale. There are three reasons I believe that the Hall-probe calibration is the primary culprit (and not errors in the calculation or winding of the slower). First, the Hall probe is old and I did not test it against a known reference. Second, the MOT coils were designed using an independent method and their axial field was measured, using a current source with higher precision, by the experiment's first undergraduate researcher, P. McKenna (see Figure 3.14). The only commonality between the MOT coil and Zeeman slower procedures was the Hall probe, but the measurements both required rescaling by $1.25\times$ for quantitative agreement with the relevant calculation. Third, although the experimentally optimized drive currents are distinct from the calculated values, the difference does not match the $1.25\times$ factor that we would expect if there were flaws in the coils.

The quadrupole and shimming fields for the MOTs are all simple paired coil designs. We generate these designs by modeling each turn of a coil as a current-carrying loop and then summing the magnetic fields from all the loops. The MOT coils were made from the same tubing as the Zeeman slower, each consisting of 6 layers of 8 turns. The coils were designed to induce magnetic field gradients of 1.15 gauss/cm/A in the quadrupole configuration. As I discussed above, the measured field gradient only qualitatively agrees with the calculation, which is likely due to poor calibration of the Hall probe (see the left pane of Figure 3.14).⁴² The installed spacing (9.18 cm) between the MOT coils is slightly larger than the designed spacing (7.925 cm), so the coils actually produce field gradients of 0.96 gauss/cm/A. The shim coils each consist of 26 turns of 16 AWG wire. The x - and y -axis shims have two layers and were wrapped directly onto the science chamber's 4.5" Conflat viewports. The z -axis shims have only a single layer wrapped onto the 8" flange of the reentrant viewports. We have not measured the shim coil fields because the coils were installed after the chamber was under vacuum. The calculated axial fields for the

⁴²Because we have over-specified power supplies and for the reasons already discussed, we did not immediately check the Hall probe's calibration. The probe is shared throughout the JQI and its location is currently unknown.

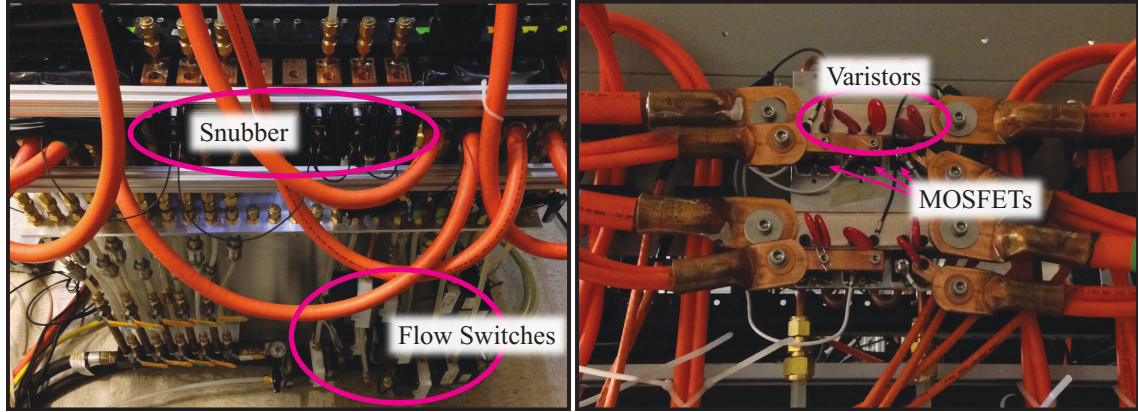


Figure 3.15: The water cooling breakout manifold (left) and the bank of MOSFET current regulators (right).

horizontal and vertical shim coils can be seen in the right pane of Figure 3.14. The vertical shims create a more uniform field because they are nearer to the Helmholtz configuration than the horizontal shims.

Commercial power supplies provide the base current source for all coil sets. An Agilent E3614A drives each shim coil pair. Ramps of the shim current are implemented via analog voltage control of each Agilent supply’s current output. A Sorensen XG 8-100 or XG 12-70 powers each Zeeman coil and a TDK-Lambda GEN40-125 powers the MOT coils. The currents for the Zeeman and MOT coils are regulated by PI feedback from a hall sensor (F.W. Bell CSLM-50LA or CSLM-100LA). The PI control circuit was developed at the JQI by I. Spielman, S. De, and K. Nelson based on the ideas in the Ph.D. thesis of K. White [265].⁴³ In our apparatus, each PI controller drives the gate voltages of a bank of one or two N-type power MOSFETs (STMicroelectronics STE250NS10),⁴⁴ which are connected in series with the regulated coil (see Figure 3.15). The MOSFETs act as variable resistors and restrict the current flow from the power supply. Several varistors are connected across each MOSFET to clamp the drain-source voltage at 36 V during current switching. Efficient transfer of atoms from the bMOT to the rMOT necessitates a rapid

⁴³The circuit schematic can be found in [264] and an updated version, by Z. Smith, suitable for driving shim coils is available at <https://github.com/JQIamo/bipolar-mosfet-board>.

⁴⁴These MOSFETs have been discontinued, but comparable parts are available from IXYS.

change ($t_{switch} \approx 1$ ms) in the MOT coil current from ≈ 50 A to ≈ 1 A. The measured inductance, $L = 375 \mu\text{H}$, of the MOT coils limits the switching speed. This limitation is particularly important near the end of the current sweep because interaction of the coil inductance with the PI control loop can lead to ringing. We decrease the switching time by connecting a snubbing circuit, which consists of a freewheeling Schottky diode and a 5Ω resistance, across the MOT coils, forming an LR circuit. When the reverse voltage across the coil drops to ≈ 5 V, the snubber exponentially reduces the current with a time constant $\approx 75 \mu\text{s}$. After installation of the snubber, the coils switch 96% of the way from the bMOT to rMOT operating current in $\lesssim 250 \mu\text{s}$. Some small-amplitude ringing persists at the end of the current switch, but it is not clear whether the effect is real or due to the overshoot issues of the F.W. Bell sensors.⁴⁵

The Zeeman slower, the MOT coils, and the MOSFETs require active cooling to prevent overheating. We flow chilled water through the square tubing of the coils or through the aluminum cooling block to which the MOSFET banks are bolted. The current and water are combined at a manifold positioned next to the vacuum chamber's optical table (see Figure 3.15). I modified the current-water breakout tabs to suit our needs from the design of R. Brown [266]. Because the chilled building water is dirty and has a low input-to-return pressure differential, we built a closed chilled water loop in the lab. A Neslab System *III* heat exchanger (P/N: 327004090100) uses the building water to cool a mixture of distilled water and OptiShield anti-corrosive to 15°C . The System *III* supplies water from its reservoir to the manifold at 80 psi. Particulate filters (Swagelok 6S-FF-440) on the input side of each manifold channel prevent the coils from clogging. Flow switches on the output side (Proteus 0100C110) interlock the outputs of each coil's power supply. The heat exchanger includes a temperature sensor that shuts off its pump when the water reservoir temperature exceeds 35°C . This functionality provides an indirect temperature interlock mediated by the flow switches. Our implementation of the current interlocks is

⁴⁵These sensors will be replaced with LEM Ultrastab sensors when the experiment moves to the PSC.

The screenshot displays the SetList v1.6.0 software interface. At the top, there are buttons for 'QUIT', 'Launch Viewer', and 'Run'. Below these are tabs for 'Cycle?', 'Staging List', 'Variables', 'User Functions', 'Save/Load Procedures', 'Errors', 'Diagnostics', 'About SetList', and 'Preferences'. A 'SetList Table' section contains buttons for 'To End Table Editing', 'Undo', 'Select Layout', 'Configure Layouts', 'Fit Columns to Text', and 'Manage Devices'. The main table lists 41 experimental steps, each with a 'Comment', 'Mode', 'Group', 'Delay', and a series of columns for different device channels (H La, DMC, Vert, BL, BI, H, H, P, Blue, Cros, Vari, X OC, SRS, SRS, SRS, SRS, Posil, Run, Num, Patti, Disp, Prog). The 'Group' column is highlighted in purple, indicating it is used for tagging rows in and out of the active procedure. The 'ODT channels' layout is visible, showing various channels like ODT, SinR, SinL, ExpF, ExpL, ExpH, ExpV, ExpW, ExpD, ExpA, ExpG, ExpI, ExpJ, ExpK, ExpL, ExpM, ExpN, ExpO, ExpP, ExpQ, ExpR, ExpS, ExpT, ExpU, ExpV, ExpW, ExpX, ExpY, ExpZ, ExpAA, ExpAB, ExpAC, ExpAD, ExpAE, ExpAF, ExpAG, ExpAH, ExpAI, ExpAJ, ExpAK, ExpAL, ExpAM, ExpAN, ExpAO, ExpAP, ExpAQ, ExpAR, ExpAS, ExpAT, ExpAU, ExpAV, ExpAW, ExpAX, ExpAY, ExpAZ, ExpBA, ExpBB, ExpBC, ExpBD, ExpBE, ExpBF, ExpBG, ExpBH, ExpBI, ExpBJ, ExpBK, ExpBL, ExpBM, ExpBN, ExpBO, ExpBP, ExpBQ, ExpBR, ExpBS, ExpBT, ExpBU, ExpBV, ExpBW, ExpBX, ExpBY, ExpBZ, ExpCA, ExpCB, ExpCC, ExpCD, ExpCE, ExpCF, ExpCG, ExpCH, ExpCI, ExpCJ, ExpCK, ExpCL, ExpCM, ExpCN, ExpCO, ExpCP, ExpCQ, ExpCR, ExpCS, ExpCT, ExpCU, ExpCV, ExpCW, ExpCX, ExpCY, ExpCZ, ExpDA, ExpDB, ExpDC, ExpDD, ExpDE, ExpDF, ExpDG, ExpDH, ExpDI, ExpDJ, ExpDK, ExpDL, ExpDM, ExpDN, ExpDO, ExpDP, ExpDQ, ExpDR, ExpDS, ExpDT, ExpDU, ExpDV, ExpDW, ExpDX, ExpDY, ExpDZ, ExpEA, ExpEB, ExpEC, ExpED, ExpEE, ExpEF, ExpEG, ExpEH, ExpEI, ExpEJ, ExpEK, ExpEL, ExpEM, ExpEN, ExpEO, ExpEP, ExpEQ, ExpER, ExpES, ExpET, ExpEU, ExpEV, ExpEW, ExpEX, ExpEY, ExpEZ, ExpFA, ExpFB, ExpFC, ExpFD, ExpFE, ExpFF, ExpFG, ExpFH, ExpFI, ExpFJ, ExpFK, ExpFL, ExpFM, ExpFN, ExpFO, ExpFP, ExpFQ, ExpFR, ExpFS, ExpFT, ExpFU, ExpFV, ExpFW, ExpFX, ExpFY, ExpFZ, ExpGA, ExpGB, ExpGC, ExpGD, ExpGE, ExpGF, ExpGG, ExpGH, ExpGI, ExpGJ, ExpGK, ExpGL, ExpGM, ExpGN, ExpGO, ExpGP, ExpGQ, ExpGR, ExpGS, ExpGT, ExpGU, ExpGV, ExpGW, ExpGX, ExpGY, ExpGZ, ExpHA, ExpHB, ExpHC, ExpHD, ExpHE, ExpHF, ExpHG, ExpHH, ExpHI, ExpHJ, ExpHK, ExpHL, ExpHM, ExpHN, ExpHO, ExpHP, ExpHQ, ExpHR, ExpHS, ExpHT, ExpHU, ExpHV, ExpHW, ExpHX, ExpHY, ExpHZ, ExpIA, ExpIB, ExpIC, ExpID, ExpIE, ExpIF, ExpIG, ExpIH, ExpII, ExpIJ, ExpIK, ExpIL, ExpIM, ExpIN, ExpIO, ExpIP, ExpIQ, ExpIR, ExpIS, ExpIT, ExpIU, ExpIV, ExpIW, ExpIX, ExpIY, ExpIZ, ExpJA, ExpJB, ExpJC, ExpJD, ExpJE, ExpJF, ExpJG, ExpJH, ExpJI, ExpJJ, ExpJK, ExpJL, ExpJM, ExpJN, ExpJO, ExpJP, ExpJQ, ExpJR, ExpJS, ExpJT, ExpJU, ExpJV, ExpJW, ExpJX, ExpJY, ExpJZ, ExpKA, ExpKB, ExpKC, ExpKD, ExpKE, ExpKF, ExpKG, ExpKH, ExpKI, ExpKJ, ExpKK, ExpKL, ExpKM, ExpKN, ExpKO, ExpKP, ExpKQ, ExpKR, ExpKS, ExpKT, ExpKU, ExpKV, ExpKW, ExpKX, ExpKY, ExpKZ, ExpLA, ExpLB, ExpLC, ExpLD, ExpLE, ExpLF, ExpLG, ExpLH, ExpLI, ExpLJ, ExpLK, ExpLL, ExpLM, ExpLN, ExpLO, ExpLP, ExpLQ, ExpLR, ExpLS, ExpLT, ExpLU, ExpLV, ExpLW, ExpLX, ExpLY, ExpLZ, ExpMA, ExpMB, ExpMC, ExpMD, ExpME, ExpMF, ExpMG, ExpMH, ExpMI, ExpMJ, ExpMK, ExpML, ExpMN, ExpMO, ExpMP, ExpMQ, ExpMR, ExpMS, ExpMT, ExpMU, ExpMV, ExpMW, ExpMX, ExpMY, ExpMZ, ExpNA, ExpNB, ExpNC, ExpND, ExpNE, ExpNF, ExpNG, ExpNH, ExpNI, ExpNJ, ExpNK, ExpNL, ExpNM, ExpNO, ExpNP, ExpNQ, ExpNR, ExpNS, ExpNT, ExpNU, ExpNV, ExpNW, ExpNX, ExpNY, ExpNZ, ExpOA, ExpOB, ExpOC, ExpOD, ExpOE, ExpOF, ExpOG, ExpOH, ExpOI, ExpOJ, ExpOK, ExpOL, ExpOM, ExpON, ExpOO, ExpOP, ExpOQ, ExpOR, ExpOS, ExpOT, ExpOU, ExpOV, ExpOW, ExpOX, ExpOY, ExpOZ, ExpPA, ExpPB, ExpPC, ExpPD, ExpPE, ExpPF, ExpPG, ExpPH, ExpPI, ExpPJ, ExpPK, ExpPL, ExpPM, ExpPN, ExpPO, ExpPP, ExpPQ, ExpPR, ExpPS, ExpPT, ExpPU, ExpPV, ExpPW, ExpPX, ExpPY, ExpPZ, ExpQA, ExpQB, ExpQC, ExpQD, ExpQE, ExpQF, ExpQG, ExpQH, ExpQI, ExpQJ, ExpQK, ExpQL, ExpQM, ExpQN, ExpQO, ExpQP, ExpQQ, ExpQR, ExpQS, ExpQT, ExpQU, ExpQV, ExpQW, ExpQX, ExpQY, ExpQZ, ExpRA, ExpRB, ExpRC, ExpRD, ExpRE, ExpRF, ExpRG, ExpRH, ExpRI, ExpRJ, ExpRK, ExpRL, ExpRM, ExpRN, ExpRO, ExpRP, ExpRQ, ExpRR, ExpRS, ExpRT, ExpRU, ExpRV, ExpRW, ExpRX, ExpRY, ExpRZ, ExpSA, ExpSB, ExpSC, ExpSD, ExpSE, ExpSF, ExpSG, ExpSH, ExpSI, ExpSJ, ExpSK, ExpSL, ExpSM, ExpSN, ExpSO, ExpSP, ExpSQ, ExpSR, ExpSS, ExpST, ExpSU, ExpSV, ExpSW, ExpSX, ExpSY, ExpSZ, ExpTA, ExpTB, ExpTC, ExpTD, ExpTE, ExpTF, ExpTG, ExpTH, ExpTI, ExpTJ, ExpTK, ExpTL, ExpTM, ExpTN, ExpTO, ExpTP, ExpTQ, ExpTR, ExpTS, ExpTT, ExpTU, ExpTV, ExpTW, ExpTX, ExpTY, ExpTZ, ExpUA, ExpUB, ExpUC, ExpUD, ExpUE, ExpUF, ExpUG, ExpUH, ExpUI, ExpUJ, ExpUK, ExpUL, ExpUM, ExpUN, ExpUO, ExpUP, ExpUQ, ExpUR, ExpUS, ExpUT, ExpUU, ExpUV, ExpUW, ExpUX, ExpUY, ExpUZ, ExpVA, ExpVB, ExpVC, ExpVD, ExpVE, ExpVF, ExpVG, ExpVH, ExpVI, ExpVJ, ExpVK, ExpVL, ExpVM, ExpVN, ExpVO, ExpVP, ExpVQ, ExpVR, ExpVS, ExpVT, ExpVU, ExpVV, ExpVW, ExpVX, ExpVY, ExpVZ, ExpWA, ExpWB, ExpWC, ExpWD, ExpWE, ExpWF, ExpWG, ExpWH, ExpWI, ExpWJ, ExpWK, ExpWL, ExpWM, ExpWN, ExpWO, ExpWP, ExpWQ, ExpWR, ExpWS, ExpWT, ExpWU, ExpWV, ExpWW, ExpWX, ExpWY, ExpWZ, ExpXA, ExpXB, ExpXC, ExpXD, ExpXE, ExpXF, ExpXG, ExpXH, ExpXI, ExpXJ, ExpXK, ExpXL, ExpXM, ExpXN, ExpXO, ExpXP, ExpXQ, ExpXR, ExpXS, ExpXT, ExpXU, ExpXV, ExpXW, ExpXX, ExpXY, ExpXZ, ExpYA, ExpYB, ExpYC, ExpYD, ExpYE, ExpYF, ExpYG, ExpYH, ExpYI, ExpYJ, ExpYK, ExpYL, ExpYM, ExpYN, ExpYO, ExpYP, ExpYQ, ExpYR, ExpYS, ExpYT, ExpYU, ExpYV, ExpYW, ExpYX, ExpYY, ExpYZ, ExpZA, ExpZB, ExpZC, ExpZD, ExpZE, ExpZF, ExpZG, ExpZH, ExpZI, ExpZJ, ExpZK, ExpZL, ExpZM, ExpZN, ExpZO, ExpZP, ExpZQ, ExpZR, ExpZS, ExpZT, ExpZU, ExpZV, ExpZW, ExpZX, ExpZY, ExpZZ.

Figure 3.16: Screen capture of a typical experimental procedure as it appears in SetList v1.6.0. The group column (purple) allows rows to be tagged in and out of the active procedure. User configurable layouts allow device channels to be hidden or shown in groups based on experimental usage (the *ODT channels* layout is visible above).

robust to power cycles (of either the flow switches, power supplies, or heat exchanger) and loss of house water flow to the heat exchanger.

3.5 Computer Control

Two computers (creatively named *Acquisition* and *Control*) govern the experimental procedure and data acquisition. *Control* runs the JQI "new" SetList v1.6.0 cycle control software, which controls a host of commercial and custom hardware peripherals. *Acquisition* acquires images in Labview or Lightfield and analyzes them in Igor. Figure 3.16 shows a typical SetList procedure (in this case for creating ^{84}Sr Bose-Einstein condensates) and Figure 3.17 shows the connections between the computers and the peripherals.

The "new" SetList⁴⁶ is an object-oriented Labview application that was initially written by C. Herold, J. Tiamsuphat, and Z. Siegel.⁴⁷ SetList has been significantly extended by N. Pisenti, Z. Smith, B. Reschovsky and me since its v1.0.0 release. SetList has two key advantages compared to its older cousin, both of which result in increased portability between Labview releases. First, the move to object-oriented Labview allows for accessible and transparent implementation of controls for new devices. Second, we switched from standard Labview controls to an interactive text table (the *setlist*) for procedure definition. All channels in the table can be grouped and colored to increase readability. Also, the text format is easily version controlled with a local Git repository.

The *setlist* is a programming interface for a master device and a theoretically unlimited number of slave devices (see Figure 3.16). At runtime, SetList loads each device with its own hardware image table of the *setlist*. The master device, in our case a SpinCore Technologies Inc. PulseBlasterUSB, controls experimental timing. Several of its digital output channels function as variable frequency clocks for the slave devices, commanding them to step through their own hardware images. The slave devices in use on the experiment include National Instruments multifunction DAQ cards, Arduino microprocessors, SRS function generators (DS345), a Newport linear actuator, and the DMD (see Figure 3.17). The NI cards provide AO, DO, and AI channels that control a host of analog and digital devices (*e.g.* AOM RF drivers, camera shutters, \vec{B} -field coil electronics). All AO and DO channels are buffered to drive 50 Ω loads and the digital channels are opto-isolated as well. The Arduino microprocessors give us tabled control over all the JQI DDS v4.0 boards in the experiment (and will be used to control other devices in the future). We use the SRS function generators for frequency and amplitude modulation of the RF drive to AOMs. The linear actuator automatically sets the PIXIS camera position to keep the atomic cloud in focus and the DMD generates arbitrary trapping potentials (see Section 3.1.4.2).

⁴⁶So named because it is based on the NIST Laser Cooling and Trapping Group's "old" SetList.

⁴⁷The most recent SetList code is available on Github: <https://github.com/JQIamo/SetList>.

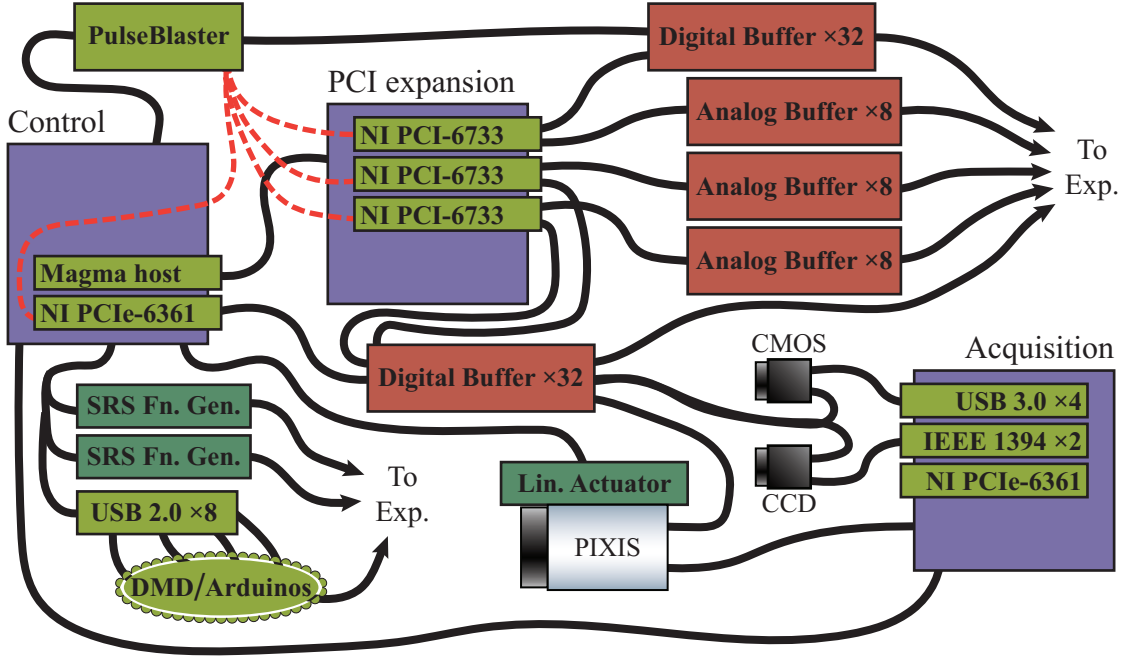


Figure 3.17: Schematic of the AO/DO cards and peripherals that we use to control the experiment. We increased the number of PCI slots in *Control* with a PE3R PCI expansion from Magma. Red dashed lines indicated clock connections, some of which are omitted for clarity.

The tasks of image acquisition and analysis are split between several programs. Like many of the JQI ultracold atom groups, we use Igor pro for image analysis. The analysis scripts were initially written for the RbI, RbII, and RbYb experiments. I modified these scripts to analyze strontium gases correctly and to be more user friendly.⁴⁸ I also added a Gram-Schmidt basis constructor and, in collaboration with B. Reschovsky, several new fitting routines. Point Grey’s Flea cameras are easily controlled with a Labview VI that saves raw images to a dedicated disk in Igor binary format. During live image processing, this VI also controls the Igor scripts via DDE. We use Princeton Instruments’s Lightfield software to store images from their PIXIS camera. However, Lightfield can only store data in the proprietary .spe file format, which cannot be read by Igor, and does not natively acquire data in a manner compatible with the workflow of our typical data runs.⁴⁹ I

⁴⁸For example, data series are easily sortable; fit uncertainties are tracked; ROIs can be copied between series; and data can be automatically reprocessed while allowing user supervision.

⁴⁹D. Trypogeorgos has informed me that Princeton Instruments now bundles Lightfield with external

alleviated the first problem by adding a .spe parser to the Labview Flea camera control VI so that the PIXIS images could be converted to Igor binary. For the second issue, I wrote a C# plug-in for Lightfield that allows for quasi-continuous, shot-based image readout.⁵⁰ The interface between SetList, Lightfield, Igor, and the camera control VI is for the most part harmonious, but short cycle times or complicated fitting routines can desynchronize *Acquisition* and *Control*. The difficulty is the DDE connection between Labview and Igor, which does not permit the camera control VI to grab new images until Igor finishes its fitting routine. Our current workaround is to offset fitting from acquisition by one parameter scan, so that we fit the previous data sequence while we acquire the next. In the future, it would be useful to implement truly asynchronous data analysis.

libraries and Labview VIs. The workaround I developed would not have been necessary if the external libraries had been included with our copy of Lightfield.

⁵⁰All acquisition and analysis scripts are on Github: <https://github.com/JQIamo/sr-scripts>, <https://github.com/JQIamo/LightField-Loop-Acquisition>, <https://github.com/JQIamo/FleaAcquisition>.

Chapter 4: Enhanced Magnetic Trap Loading

Our work to improve the atomic flux in order to produce degenerate gases of ^{84}Sr and ^{87}Sr included the investigation of a technique to increase the loading rate of the metastable reservoir. While we have recently switched our initial trap from a continuously loaded magnetic trap to a repumped bMOT, the loading rate enhancement that we measured may be useful to other groups (especially those working with isotopic mixtures). Simulations of the trap loading dynamics also show that groups that work with atomic calcium should see greater improvements than we measured in strontium. Our measurements also resulted in the first publication from the apparatus [267], the submitted ArXiv version of which I reproduce, with some additional editing, in Section 4.1. The published work was a collaboration between Ben Reschovsky, Neal Pienti, Gretchen Campbell and me. Ben and I conceived the measurement procedure (see Sections 4.1.3 and 4.1.4) and I built the depumping laser optical setup, using a laser diode that was prepared by Ben and Neal (see Section 4.1.3). Ben, Neal and I collectively acquired all the experimental data presented in Section 4.1.4 and I developed the rate equation model in Section 4.1.5. All authors discussed the results and contributed to the editing of my original manuscript. At the end of the chapter, I discuss several blind alleys that we explored early in the data collection effort.

4.1 Publication: Enhanced magnetic trap loading for atomic strontium

4.1.1 Abstract

We report on a technique to improve the continuous loading of atomic strontium into a magnetic trap from a Magneto-Optical Trap (MOT). This loading enhancement is achieved by adding a depumping laser tuned to the $^3P_1 \rightarrow ^3S_1$ (688-nm) transition. The depumping laser increases atom number in the magnetic trap and subsequent cooling stages by up to 65 % for the bosonic isotopes and up to 30 % for the fermionic isotope of strontium. We optimize this trap loading strategy with respect to the 688-nm laser detuning, intensity, and beam size. To understand the results, we develop a one-dimensional rate equation model of the system, which is in good agreement with the data. We discuss the use of other transitions in strontium for accelerated trap loading and the application of the technique to other alkaline-earth-like atoms.

4.1.2 Introduction

Alkaline-earth-like (AE) atoms have received a great deal of recent interest due to the distinctive properties of their level structure [64, 113]. The largely disconnected singlet and triplet states in these atoms give rise to forbidden optical transitions, which could form the basis for an improved time standard [56, 57]. These transitions are also advantageous in a wide variety of other applications. For example, their low photon-scattering rates allow for the production of highly-excited Rydberg atoms with reduced decoherence compared to alkali metals [74]. Magnetic-field-insensitive singlet and triplet levels make AE atoms attractive for precision measurement and quantum sensing applications [86, 88]. In fermionic isotopes, these states manifest $SU(2I+1)$ spin symmetry, where I is the nuclear angular momentum, allowing quantum simulation of Hamiltonians that are inaccessible with alkali atoms [90, 146, 165]. All of these applications require or benefit from a

combination of large atom number and short experimental cycle times.

Recent advances in cooling and trapping techniques enabled production of the first strontium degenerate gases [117, 118, 121–123]. The small negative s-wave scattering length of the most abundant isotope, ^{88}Sr , hampered initial efforts to create Bose-Einstein condensates [109, 210, 268–270]. While the other stable isotopes (^{87}Sr , ^{86}Sr , and ^{84}Sr) possess favorable scattering lengths, their low natural abundance initially prevented Magneto-Optical Traps (MOT) from collecting enough atoms to reach degeneracy. Fortunately, laser cooling of strontium on the 461-nm line populates a magnetically-confined, metastable reservoir of atoms in the 3P_2 state (see Figure 4.1) [195]. The long lifetime of this reservoir (typically $\gtrsim 10$ s) compared to the MOT allows for the accumulation of sufficient populations of ^{87}Sr , ^{86}Sr , or ^{84}Sr for forced evaporation or sympathetic cooling of ^{88}Sr [117, 118, 121–123]. The ≈ 1 μK temperatures attainable with laser cooling on the 689-nm, intercombination transition (Figure 4.1) lead to short evaporation times to reach degeneracy. Given the low abundance of the interacting isotopes, the short evaporation time means that the reservoir loading time usually dominates the experimental cycle [118, 122, 123, 131].

Typical Sr degenerate gas experiments first use a MOT operating on the $^1S_0 \rightarrow ^1P_1$, 461-nm transition (bMOT) to capture atoms from a Zeeman-slowed atomic beam and cool them to ≈ 1 mK. Atoms slowly leak out of the bMOT cooling cycle (1:50,000 branching ratio) and into the metastable 3P manifold, where they populate the 3P_2 and 3P_1 states in a 1:2 ratio [60, 61]. The bMOT quadrupole field can magnetically trap atoms in the 3P_2 state (the Landé g -factor is $g_J = 3/2$ for bosonic isotopes, where J is the electronic angular momentum). Repumping lasers return 3P_2 atoms to the ground state once magnetic trap loading is complete, which, depending on the isotope, can take 30 s or more [118, 123, 131]. Loading times are also long for experiments with isotopic mixtures, since the isotope shifts of the 461-nm transition are on the same order of magnitude as the linewidth [122, 131]. Such small isotope shifts prohibit efficient simultaneous loading of the magnetic trap.

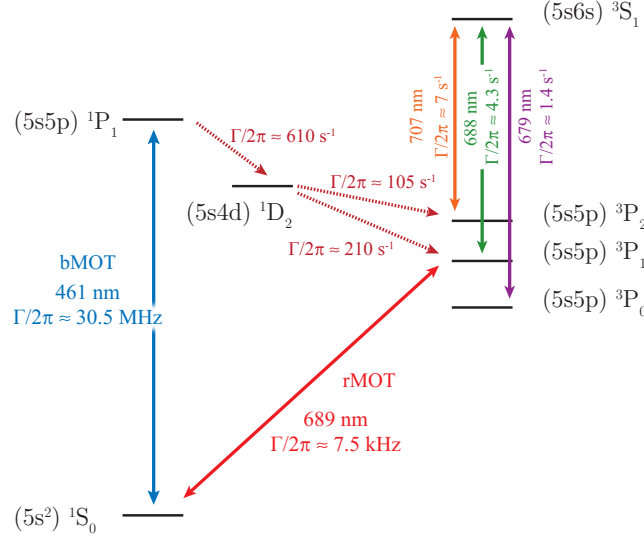


Figure 4.1: The low-lying energy levels of bosonic strontium with linewidths and natural decay rates taken from [60–64]. A Magneto-Optical Trap operating on the blue, 461-nm transition (bMOT) captures atoms from a Zeeman-slowed beam. Atoms in the bMOT continuously leak into the long-lived 3P_2 state, which is magnetically trapped by the bMOT quadrupole field. Two lasers at 688 nm and 679 nm increase the magnetic trap loading rate by pumping atoms that populate 3P_1 into 3P_2 . The 679-nm laser and a 707-nm laser return atoms to the ground state via the 3P_1 state once magnetic trap loading is complete. A Magneto-Optical Trap operating on the red, 689-nm transition (rMOT) then cools the sample to $\approx 1 \mu\text{K}$.

A second stage Magneto-Optical Trap using the 689-nm, intercombination line (rMOT) cools these atoms to $\approx 1 \mu\text{K}$ and facilitates loading into an optical dipole trap. Evaporation proceeds quickly due to the low initial temperature and degeneracy can be reached in $\approx 1 \text{ s}$ for most isotopes [131].

Here we present a technique to reduce the reservoir loading time or, equivalently, increase the atom number for experiments with strontium, as first suggested in [182]. The method relies on continuous optical pumping of atoms from the short-lived 3P_1 state into the magnetically trapped 3P_2 reservoir using the $^3P_1 \rightarrow ^3S_1$, 688-nm transition. This optical pumping greatly reduces the steady-state atom number in the bMOT, but increases the flux of low-field seeking atoms into the metastable reservoir. Although the $^3P_2: ^3P_1$ branching ratio from the 1D_2 state suggests that atom number should be enhanced by a factor of three (see Figure 4.1), we show that this estimate is incorrect since it does not consider the reduction in bMOT atom number caused by the 688-nm laser.

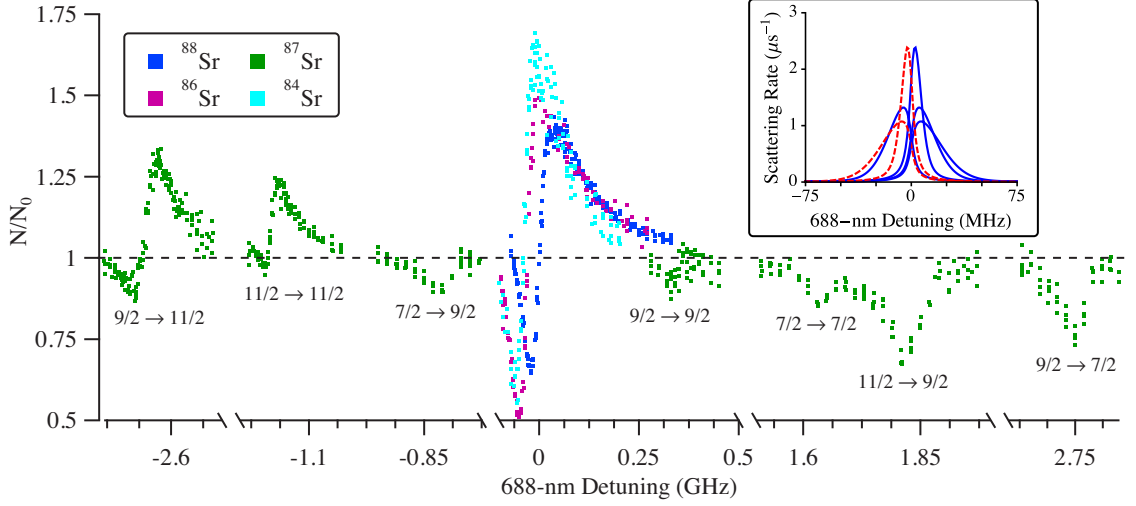


Figure 4.2: Measured atom number enhancement as a function of 688-nm laser detuning, Δ_{688} , for all strontium isotopes. The detuning zero is referenced to ^{88}Sr . For the data shown, the rMOT recaptures the less abundant isotopes and the bMOT recaptures ^{88}Sr . The depumper saturation parameter was $s_{688} \approx 35$ (≈ 50) for ^{88}Sr (^{87}Sr , ^{86}Sr , ^{84}Sr) and the 679-nm laser detuning, Δ_{679} , was set to maximize bMOT fluorescence. We label the fermionic hyperfine transitions with $F \rightarrow F'$, where F is the total angular momentum quantum number for 3P_1 and F' the corresponding quantum number for 3S_1 . Inset: The detuning-dependent scattering rate for each transition between 3P_1 and 3S_1 Zeeman levels, averaged over the volume of a one-dimensional bMOT with $s_{688} = 1$ (see Section 4.1.5). Solid blue curves pump to a 3S_1 Zeeman level that can decay to a magnetically trappable 3P_2 Zeeman state, but dashed red curves do not. Asymmetric lineshapes arise in the atom number enhancement because the dashed red scattering rate curves dominate at negative detuning.

We describe our experimental apparatus in Section 4.1.3 with an emphasis on the details relevant for the accelerated loading scheme. Section 4.1.4 explains the measurement procedure and results. In Section 4.1.5, we develop a rate equation model and demonstrate that our data is in agreement with expectations. We also simulate the trap loading enhancement for several other transitions in strontium and two in calcium. Section 4.1.6 is a summary of our results and give an outlook for future advances.

4.1.3 Apparatus

Our experimental setup is similar to other strontium apparatuses designed for optical clock and degenerate gas experiments [53, 180–182]. An oven with a microtubule array nozzle, heated to 600 °C, creates an atomic strontium beam. Two stages of differential pumping prevent the pressure in the experiment chamber (6×10^{-11} Torr) from rising while the oven is in operation. The atomic beam passes through a transverse cooling

stage, which consists of two orthogonal, retroreflected 461-nm laser beams. Each beam has ≈ 10 mW of power, a 1:3 aspect ratio ($1/e^2$ radius of 9 mm along the atomic beam axis), and -10 MHz detuning from the $^1S_0 \rightarrow ^1P_1$ transition. The Zeeman slower is a 35-cm long, multilayer, variable-pitch coil located immediately after the transverse cooling stage. The Zeeman slower is pumped with ≈ 48 mW of -600 MHz detuned 461-nm light, which is focused onto the oven nozzle with an initial $1/e^2$ radius of 5 mm.

The bMOT has a standard retroreflected, three-beam configuration. Each beam has a $1/e^2$ radius of 8 mm, a detuning $\Delta_{461} = -45$ MHz, and contains either ≈ 7 mW (for bosonic isotope data) or ≈ 9 mW (for ^{87}Sr data) of power. These parameters give $s_{461} = I/I_{\text{sat}} \approx 0.16$ per beam for the bosons and $s_{461} \approx 0.21$ per beam for the fermion. The quadrupole coil has a vertical axis of symmetry and produces a magnetic field gradient of 6 mT/cm along that axis during bMOT operation. The bMOT field gradient is sufficient for magnetically trapping of 3P_2 atoms in the low-field-seeking $|m_J = 1\rangle$ and $|m_J = 2\rangle$ Zeeman sublevels. In our vacuum chamber, the position of two recessed viewports along the symmetry axis of the coils limits the trap depth for the $|m_J = 1\rangle$ state to ≈ 5 mK. This limitation is unimportant for us since our bMOT loads ≈ 1 mK atoms into the magnetic trap, but it suggests that experiments with larger vacuum chambers may find that a higher temperature bMOT optimizes magnetic trap loading [182].

Two repumping lasers addressing the 679-nm, $^3P_0 \rightarrow ^3S_1$ and the 707-nm, $^3P_2 \rightarrow ^3S_1$ transitions are used to return 3P_2 atoms in the magnetic trap to the ground state. The two beams co-propagate with the Zeeman slower beam, share a $1/e^2$ radius of ≈ 1 cm, and contain ≈ 2.5 mW (679 nm) and ≈ 4.5 mW (707 nm) of power. For experiments with the bosonic isotopes, we lock the repump laser frequencies using slow feedback from a HighFinesse WS7 wavemeter.¹ The locking stability is ± 5 MHz, which is much narrower than the observed bosonic repumping linewidth.² The presence of hyperfine structure in

¹The identification of commercial products is for information only and does not imply recommendation or endorsement by the National Institute of Standards and Technology.

²The WS7 wavemeter resolution is specified to be 10 MHz, but we find that it can reliably detect 1 MHz

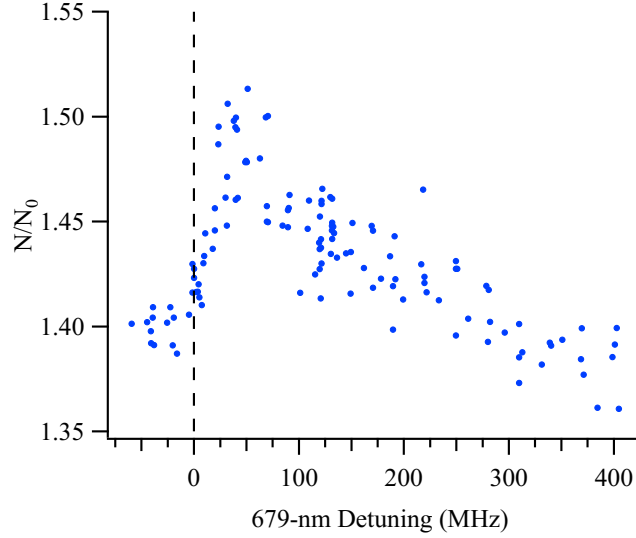


Figure 4.3: N/N_0 for ^{88}Sr recaptured in the bMOT as a function of Δ_{679} . The 688-nm laser has $s_{688} \approx 35$ and $\Delta_{688} \approx 30$ MHz. We reference the 679-nm detuning to the bMOT fluorescence maximum, indicated by the dashed vertical line. As shown in the inset to Figure 4.2, the asymmetry arises from detuning-dependent scattering rates. Transitions to 3S_1 Zeeman levels that can decay into the magnetic trap are predominately blue detuned, whereas red detuned transitions populate levels that decay to high-field seeking 3P_2 Zeeman states.

the fermion complicates repumping on the $^3P_2 \rightarrow ^3S_1$ transition. In order to cover as much of the ≈ 5.5 GHz hyperfine spectrum of the transition as possible, we modulate the 707-nm laser frequency at ≈ 700 Hz. To increase coverage of the hyperfine spectrum further, we use a second 707-nm laser that we modulate at ≈ 600 Hz. When optimized, application of the second laser to the experiment increases the ^{87}Sr atom number by about 10 %. For the fermionic data, the 679-nm laser is locked to the $|^3P_0, F = 9/2\rangle \rightarrow |^3S_1, F = 11/2\rangle$ transition (where $F = I + J$) using the wavemeter.

The linewidth of our 689-nm master oscillator is stabilized below the natural linewidth of the $^1S_0 \rightarrow ^3P_1$ resonance using a Pound-Drever-Hall lock to an optical cavity (finesse $\approx 240,000$) [230]. We injection lock a slave laser diode to the master to obtain sufficient power for trapping (for the fermion, this laser pumps the $|^1S_0, F = 9/2\rangle \rightarrow |^3P_1, F = 11/2\rangle$ transition). Dichroic beamsplitters overlap the 689-nm light for the rMOT with the bMOT beams. In each rMOT arm, the power is ≈ 3.5 mW

frequency offsets.

and the $1/e^2$ radius is 2.5 mm. The quadrupole field gradient switches to 0.16 mT/cm for rMOT operation. For the first 100 ms of rMOT operation, we frequency modulate the trapping laser at 30 kHz with a modulation depth of 1 MHz to increase the capture velocity of the rMOT. Over the next 400 ms, we linearly reduce the modulation depth to 100 kHz while simultaneously ramping the optical power to 100 μ W with a half-Gaussian temporal profile. In this work, we terminate rMOT operation at this stage ($T \approx 2$ μ K), but we can cool further by turning off the frequency modulation and reducing the intensity. The hyperfine structure of the fermion requires the use of a second slave laser to make a stable rMOT [36]. A beatnote lock to the master stabilizes the second laser to the $|^1S_0, F = 9/2\rangle \rightarrow |^3P_1, F = 9/2\rangle$ line [229]. The second slave laser provides ≈ 800 μ W of light per rMOT beam to the experiment. Aside from the reduction in initial power, the intensity and modulation ramps are identical to those for the trapping laser. We also linearly increase the rMOT magnetic field gradient to 0.24 mT/cm during the final 400 ms of the rMOT when trapping ^{87}Sr to increase the atomic density.

To enhance magnetic trap loading, a 688-nm laser resonant with the $^3P_1 \rightarrow ^3S_1$ transition pumps atoms that decay to 3P_1 out of the bMOT cycle and into 3P_2 . We call this laser the depumper because it makes the bMOT transition less closed. The depumper is a Littman-Metcalf configuration laser that we built using a laser diode (model HL6738MG¹) that was AR-coated in-house.³ The laser provides up to 2.8 mW of light to the experiment, which corresponds to $s_{688} = I/I_{\text{sat}} \approx 50$. The 688-nm beam enters the chamber horizontally and perpendicular to the Zeeman slower axis. This beam has a $1/e^2$ radius $w_{688} = 1.35$ mm except where otherwise noted. We stabilize the 688-nm laser detuning, Δ_{688} , to within ± 3 MHz by locking to the wavemeter.

We measure the magnetic trap loading enhancement by interleaving shots with the 688-nm laser on and off. The 679-nm repumping laser closes the $^3S_1 \rightarrow ^3P_0$ leak to

³The anti-reflection coating is comprised of two layers, as suggested in [236]: one layer of Al_2O_3 to bring the facet coating to $\lambda/2$, and a final $\lambda/4$ layer of HfO_2 . The deposition was done via electron beam evaporation, and monitored in-situ by scanning the diode current across the lasing threshold.

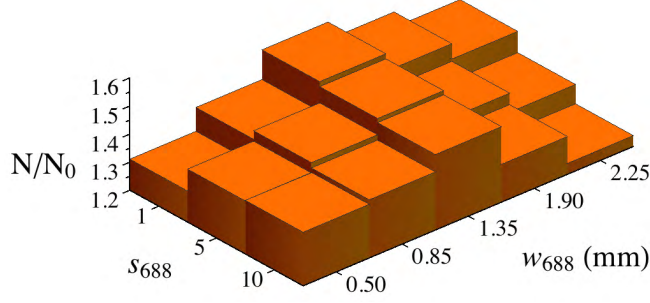


Figure 4.4: N/N_0 for ^{88}Sr recaptured in the bMOT versus s_{688} and w_{688} , where w_{688} is the $1/e^2$ radius of the depump beam. The standard errors are omitted for clarity, but are $\lesssim 0.03$. The optimal trap enhancement occurs when w_{688} roughly matches the $1/e$ radius of the bMOT and $s_{688} \approx 1$. Δ_{688} and Δ_{679} are both ≈ 30 MHz (corresponding to the maxima in Figures 4.2 and 4.3).

increase the depumper's effect. This repumping laser remains on during both shots of a depumper on/off pair of experimental runs, but does not affect trap loading when the 688-nm laser is off since the bMOT does not populate 3P_0 . After 0.5 s to 30 s of reservoir loading, an acousto-optic modulator extinguishes the 688-nm beam and optical shutters open to allow 707-nm light to reach the experiment. Either the bMOT or the rMOT can recapture atoms from the magnetic trap for detection and imaging. However, rMOT recapture greatly improves signal-to-noise for ^{87}Sr , ^{86}Sr , and ^{84}Sr , so we use the rMOT exclusively for recapture of these isotopes. The bMOT recapture stage lasts 100 ms and rMOT recapture consists of the full rMOT cycle described above. We take an absorption image after a 1 ms (25 ms) ballistic expansion for bMOT (rMOT) recapture using a resonant, 10 μs pulse of 461-nm light with $I/I_{\text{sat}} \approx 0.04$. Numerical integration of the image yields the atom number for each shot.

4.1.4 Results

We study the magnetic trap loading enhancement as a function of isotope, power, detuning, and beam size. The enhancement is measured by comparing the atom number recaptured in the rMOT or bMOT with and without the 688-nm laser. We find that the depumper's effect is independent of which MOT we use for atom recapture. The magnetic

trap loading enhancement is given by the normalized atom number, N/N_0 , where N is the atom number with the depumper on and N_0 the number with it off.

We investigate the loading enhancement as we scan the depumper across the 688-nm transition. For this data set, we set $s_{688} \approx 35$ for ^{88}Sr and $s_{688} \approx 50$ for all other isotopes. The repump laser frequencies are locked to maximize bMOT fluorescence. The magnetic trap loading time, t_{load} , for $\{^{88}\text{Sr}, ^{87}\text{Sr}, ^{86}\text{Sr}, ^{84}\text{Sr}\}$ is $\{1.5 \text{ s}, 10 \text{ s}, 6 \text{ s}, 7.5 \text{ s}\}$ resulting in typical N_0 of $\{2 \times 10^7, 5 \times 10^6, 1 \times 10^7, 8 \times 10^5\}$ in the rMOT. Adjustment of the wavemeter lockpoint allows us to scan Δ_{688} . Figure 4.2 shows the depumping spectrum for all isotopes and hyperfine transitions, the locations of which are in good agreement with [271]. On average, we observe trap loading improvements of $\approx 50\%$ for bosonic isotopes and $\approx 25\%$ for the fermionic isotope even without detailed optimization of the depumping parameters. The peak enhancement for each isotope occurs when $\Delta_{688} \approx 30 \text{ MHz}$ from resonance. In Figure 4.2 we also see that the choice of hyperfine transition is crucial for atom number gains in ^{87}Sr . Pumping to $|^3S_1, F=7/2\rangle$ and $|^3S_1, F=9/2\rangle$ is always detrimental because these manifolds decay with $\geq 60\%$ probability to $|^3P_2, F=7/2\rangle$ and $|^3P_2, F=9/2\rangle$, which have Landé g -factors too small for magnetic trapping at the bMOT field gradient. Pumping to $|^3S_1, F=11/2\rangle$ yields a lineshape similar to that of bosonic isotopes, but with reduced amplitude.

The asymmetric lineshapes observed in Figure 4.2 are due to the non-uniform magnetic fields in the bMOT. Quadrupole fields shift low-field-seeking states to higher energy and high-field-seeking states to lower energy. Because the Landé g -factor for 3S_1 is larger than for 3P_1 , this effect causes a blueshift for most transitions to 3S_1 states that can decay to $|^3P_2, m_J=1\rangle$ or $|^3P_2, m_J=2\rangle$ (see inset to Figure 4.2). For the same reason, transitions to 3S_1 states that can only populate untrapped 3P_2 Zeeman states are redshifted. As a result, trap loading is enhanced to the blue of resonance and reduced to the red of resonance.

For this depumping scheme, application of the 679-nm laser during the bMOT

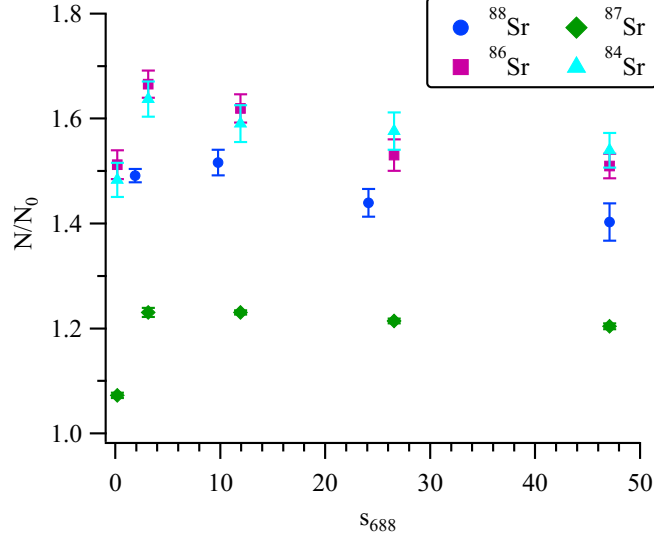


Figure 4.5: Atom number enhancement versus s_{688} with $w_{688} = 1.35$ mm. ^{87}Sr data are for the $F = 11/2 \rightarrow F' = 11/2$ transition and all isotopes are recaptured in the rMOT. Error bars represent the standard error in the mean for ≥ 10 measurements. The 688-nm and 679-nm laser detunings are set to ≈ 30 MHz.

is crucial; removing the 679-nm laser results in ≈ 50 % reduction of the enhancement. The effect of the 679-nm laser was studied by varying its detuning, Δ_{679} . As shown in Figure 4.3, setting $\Delta_{679} \approx 30$ MHz (relative to the detuning that maximizes the bMOT fluorescence) adds an additional ≈ 10 % to the enhancement. The asymmetric lineshape is caused by the same mechanism discussed above for the 688-nm transition.

With Δ_{688} and Δ_{679} stabilized at their optimized values, we study the trap loading enhancement for ^{88}Sr as a function of s_{688} and w_{688} . Slight focusing/defocusing of the 688-nm beam changes the waist at the location of the bMOT, but the Rayleigh range is always larger than the bMOT $1/e$ radius, r_{bMOT} , for the parameter range we study. Figure 4.4 shows that trap loading enhancement increases with s_{688} provided $w_{688} \lesssim r_{\text{bMOT}}$, with the optimal enhancement occurring when $w_{688} \approx r_{\text{bMOT}}$. High s_{688} increasingly reduces N/N_0 for larger beam waists. The data suggest that, for our bMOT parameters, a substantial number of atoms populate the 3P manifold before being fully captured by the bMOT. These atoms exist outside the bMOT radius and are too hot for magnetic confinement, but they are cold enough that they do not leave the bMOT capture volume during the ≈ 1 ms

decay time for the $^1P_1 \rightarrow ^1D_2 \rightarrow ^3P_1 \rightarrow ^1S_0$ path. The effect of varying s_{688} and w_{688} in the other isotopes was similar to the ^{88}Sr results. In Figure 4.5, we plot N/N_0 for a wider range of the saturation parameter at the optimum w_{688} . All isotopes exhibit a steep rise in trap loading enhancement for $s_{688} \lesssim 1$, followed by a shallow rolloff for $s_{688} > 1$. We find that the enhancement is sensitive to the 688-nm beam alignment and that the peak at $s_{688} \approx 1$ is present only when the beam traverses the center of the bMOT.

Before recapturing atoms from the magnetic trap, we do not first discard ground-state atoms remaining in the bMOT. Keeping the ground-state atoms increases both N and N_0 , but decreases their ratio. This choice biases our results toward lower enhancement values, particularly for short load times and for ^{88}Sr . However, the reduced N/N_0 is the appropriate metric for evaluating the loading enhancement in most experiments, since the cycle time is typically limited by N . In experiments with isotopic mixtures, in which bMOT atoms are lost before recapturing from the magnetic trap, the depumping technique is even more useful. If we remove the bMOT atoms before imaging, N/N_0 increases by up to 15 %.

Our technique reduces the trap loading time necessary to achieve a given atom number. For short trap loading times, N/N_0 is a measure of the increased loading rate achieved with the depumping laser. This regime is shown in Figure 4.2. For longer trap loading times, the atom number will saturate. Experiments requiring atom numbers close to the saturation limit can expect even greater reductions in loading time than suggested by the initial loading rate. We demonstrate this effect by fitting $N(t)$ and $N_0(t)$ with $N(t) = N^{\max}(1 - e^{-\alpha t})$, where α is the loading time constant and N^{\max} is the saturated atom number (see inset to Figure 4.6). Inverting the fitted function yields the loading time necessary to reach a given atom number with the depumper on, $t(N)$, or with the depumper off, $t_0(N_0)$. We plot the loading time reduction factor, $\text{LTRF}(N/N_0^{\max}) = t_0(N_0=N)/t(N)$, for ^{88}Sr and ^{84}Sr in Figure 4.6. The loading time reduction diverges as $N \rightarrow N_0^{\max}$ since $N^{\max} > N_0^{\max}$. For example, to reach an atom number of $\approx N_0^{\max}$, the depumping technique

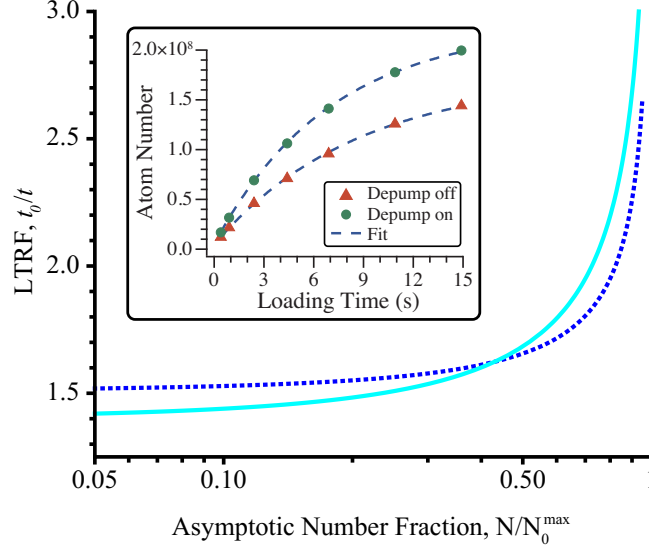


Figure 4.6: The Loading Time Reduction Factor (LTRF) for ^{88}Sr (dotted blue line) and ^{84}Sr (solid cyan line). The saturated atom number, N_0^{\max} , is the asymptote of the trap loading curve with the 688-nm laser off (for ^{88}Sr , red triangles, inset). The loading time necessary to transfer N atoms into the rMOT with the depump laser on (off) is given by t (t_0). Inset: The raw data and fits associated with the ^{88}Sr (dotted blue) LTRF curve. The standard error is smaller than the data points. We find t and t_0 by inverting the appropriate fit function (see text).

can reduce the loading time by a factor of ≈ 3 .

4.1.5 Simulation

To understand the enhancement better, we develop a one-dimensional rate equation model to simulate the bMOT depumping process. This was motivated by two features of our data: the asymmetric lineshapes depicted in Figure 4.2, and the discrepancy between the observed performance and the $3\times$ initial estimate given by the $^3P_2: ^3P_1$ branching ratio. A simple calculation, based on analysis of the cascade of Clebsch-Gordan (CG) coefficients connecting 1P_1 to 3P_1 and 3P_2 , suggests that $3\times$ trap loading enhancement is unlikely. However, this CG calculation depends sensitively on the relative populations of the 1P_1 Zeeman sublevels, which are position dependent, and the steady-state atom number in the bMOT. Both of these complications prevent analysis of experimental performance by this method. A full simulation of the optical pumping dynamics resolves both of these

issues, allowing direct comparison of data with theory. Straightforward modifications of the rate equation model allow us to compare our technique to alternative depumping transitions.

In the rate equation model, we track the population, P_{i,m_i} , in each magnetic sublevel of $i \in \{^1S_0, ^1P_1, \dots, ^3S_1\}$, with m_i the spin projection along the axis of a one-dimensional bMOT. Each level decays at a rate given by the appropriate linewidth, γ_{ij} , from Figure 4.1,

$$\Gamma_{|i,m_i\rangle \rightarrow |j,m_j; m_\gamma\rangle}^{decay} = \gamma_{ij} \left| \langle j, m_j; 1, m_\gamma | i, m_i \rangle \right|^2, \quad (4.1)$$

where $\langle i, m_i; 1, m_\gamma | j, m_j \rangle$ is the CG coefficient. In addition to the transitions shown in Figure 4.1, we also include the $^1D_2 \rightarrow ^1S_0$ quadrupole decay because its linewidth is non-negligible compared to decay rates into the 3P states [60]. Since we are not interested in individual atom trajectories, we average the driven excitation rate for $|i, m_i\rangle \rightarrow |j, m_j\rangle$, $\Gamma_{|i,m_i; m_\gamma\rangle \rightarrow |j,m_j\rangle}^{exc}$, over the position and velocity distribution of the MOT,

$$\rho(x, v) = \frac{e^{-mv^2/2k_B T} e^{-(x/r_{\text{bMOT}})^2}}{\pi r_{\text{bMOT}}^2 \sqrt{2\pi k_B T/m}}. \quad (4.2)$$

For the $^3P_0 \rightarrow ^3S_1$ and $^3P_1 \rightarrow ^3S_1$ transitions, we arrive at

$$\begin{aligned} \Gamma_{|i,m_i; m_\gamma\rangle \rightarrow |j,m_j\rangle}^{exc} = & \int_0^{x_{\max}} \int_{-v_{\max}}^{v_{\max}} \rho(x, v) \frac{s_{ij} \gamma_{ij} \sigma(m_\gamma) \left| \langle i, m_i; 1, m_\gamma | j, m_j \rangle \right|^2}{1 + s_{ij} + 4(\Delta_{m_i m_j} / \gamma_{ij})^2} dx dv, \end{aligned} \quad (4.3)$$

where s_{ij} is the saturation parameter, $\sigma(m_\gamma)$ is the fraction of s_{ij} with polarization $m_\gamma \in \{-1, 0, 1\}$, and the effective detuning between $|i, m_i\rangle$ and $|j, m_j\rangle$, $\Delta_{m_i m_j}$, includes Doppler and Zeeman shifts. We choose x_{\max}, v_{\max} to be much larger than the characteristic scale of $\rho(x, v)$. The symmetry of a one-dimensional MOT permits us to model only the $x > 0$ region with all scattering rates then multiplied by two. This choice simplifies the

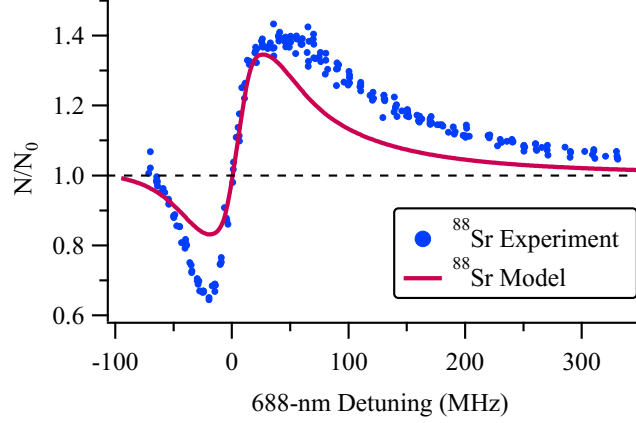


Figure 4.7: The ^{88}Sr curve from Figure 4.2 (blue circles) plotted with simulation results (magenta line) from the one-dimensional rate equation model described in Section 4.1.5. Parameters for the simulation are identical to experimental conditions (see Section 4.1.3). The model reproduces the qualitative lineshape and the peak enhancement of the data. The difference in the amplitude and width between the curves implies that our one-dimensional model does not accurately capture the full three-dimensional nature of our experiment.

tracking of magnetically trapped atoms because the magnetic field does not change sign in the simulation volume. Taking the transformation $s_{ij} \rightarrow 2s_{ij}$ in Equation (4.3) while maintaining $\Sigma_{m_\gamma} \sigma(m_\gamma) = 1$ gives the correct scattering rate for the two bMOT beams. We assume a pure circular polarization for both bMOT beams and a random polarization for the repumper and depumper.

We describe the evolution of the populations, $\{P_{i,m_i}\}$, with a system of coupled differential equations,

$$\begin{aligned}
 \dot{P}_{i,m_i} = & \mathcal{F}_{1S_0} \delta_{i,1S_0} - \beta(\delta_{i,1S_0} + \delta_{i,3P_2}) P_{i,m_i} \\
 & + \sum_{j,m_j,m_\gamma} \left(\Gamma_{|j,m_j; m_\gamma\rangle \rightarrow |i,m_i\rangle}^{exc} P_{j,m_j} - \Gamma_{|i,m_i; m_\gamma\rangle \rightarrow |j,m_j\rangle}^{exc} P_{i,m_i} \right. \\
 & \left. + \Gamma_{|j,m_j\rangle \rightarrow |i,m_i; m_\gamma\rangle}^{decay} P_{j,m_j} - \Gamma_{|i,m_i\rangle \rightarrow |j,m_j; m_\gamma\rangle}^{decay} P_{i,m_i} \right),
 \end{aligned} \tag{4.4}$$

where $\delta_{i,j}$ is the Kronecker delta, \mathcal{F}_{1S_0} is the atomic flux from the Zeeman slower, and $\beta \approx 0.1 \text{ s}^{-1}$ is the experimentally measured 1-body loss rate (the effect of which is negligible for states with short lifetimes). Without repumping, the bMOT loading time ($\lesssim 100 \text{ ms}$) is short compared to the magnetic trap loading time, so we take $\dot{P}_{i,m_i} = 0$ for

all $i \neq {}^3P_2$. We solve algebraically for $\{\dot{P}_{3P_2,-2}, \dots, \dot{P}_{3P_2,2}\}$ and numerically integrate the resulting first-order equations from $t = 0$ to $t = t_{\text{load}}$. The sum $(P_{3P_2,2} + P_{3P_2,1} + P_{1S_0,0})$ gives the total atom number at $t = t_{\text{load}}$ (the population of other states is negligible), which we equate with N or N_0 depending on whether the 688-nm laser is on or off. A fit of the model to the ${}^{88}\text{Sr}$, N_0 versus t_{load} data, with $s_{3P_1^3S_1} \equiv s_{688} = 0$ and \mathcal{F}_{1S_0} as the only free parameter, matches the experiment to better than 4 % for all reservoir loading times (all other parameters are taken from Section 4.1.3). We use the extracted value of \mathcal{F}_{1S_0} for all subsequent simulations, but we find that the results are independent of \mathcal{F}_{1S_0} and β .

We plot the simulated and measured N/N_0 for ${}^{88}\text{Sr}$ in Figure 4.7. Parameters for the simulation are taken from Section 4.1.3 except for s_{688} and Δ_{679} , which are the same as given in Figure 4.2. The simulation agrees reasonably well with experiment given the simplicity of the model and the absence of free parameters. The simulation approximately reproduces the asymmetric lineshape and the magnitude of the peak trap loading enhancement. The one-dimensional model also qualitatively replicates the behavior of N/N_0 as a function of s_{688} and Δ_{679} . The difference in dimensionality between the 1D simulation and 3D experiment likely causes the mismatch in both the width and amplitude of the lineshapes in Figure 4.7. The three-dimensional MOT beam configuration and magnetic quadrupole field complicate the optical pumping dynamics.

The choice of a $J = 1 \rightarrow J' = 1$ transition as our depumping line potentially limits the trap loading enhancement, since the 688-nm line has position-dependent dark states and small CG overlap with $|{}^3P_2, m_J = 2\rangle$. Furthermore, this transition requires a secondary laser to depopulate the 3P_0 state. Many repumping strategies exist for strontium and each of these possesses a nearby depumping resonance [182, 240–242]. We assess the relative merit of the various schemes by simulating them with optimum parameters (Figure 4.8). The $5s5p\ {}^3P_1 \rightarrow 5s5d\ {}^3D_2$ line at 487 nm and the $5s5p\ {}^3P_1 \rightarrow 5s6d\ {}^3D_2$ line at 397 nm have similar performance to the 688-nm line. All other transitions for which linewidth data are available give less enhancement. For the $5s5p\ {}^3P_1 \rightarrow 5p^2\ {}^3P_2$ transition, unfavorable

relative Landé g -factors between the excited state and 3P_1 marginally reduce the trap loading improvement. The linewidth of the $5s5p\ ^3P_1 \rightarrow 5s4d\ ^3D_2$ transition is too narrow for efficient optical pumping at bMOT temperatures.

We investigate the utility of the depumping scheme for other AE atoms. For Cd, Hg, Yb, Be, and Mg, the 1D_2 state lies above the 1P_1 state, so efficient continuous loading of the metastable reservoir does not occur [113, 182]. Direct pumping to the magnetically trapped state is possible for these atoms [272]. The $^1D_2: ^1S_0$ branching ratio in Ba and Ra is very large, which means that cooling to temperatures below the magnetic trap depth may not be possible without repumping [273, 274]. The level structure of calcium combines several features that make depumping more effective than in strontium (see Figure 4.8). The $^3P_2: ^3P_1$ branching ratio is $\approx 1:3$ and, more importantly, the $^1D_2 \rightarrow ^1S_0$ quadrupole transition linewidth is comparable to $^1D_2 \rightarrow ^3P_J$ decay rates. Ca can be trapped in a MOT operating on $^3P_2 \rightarrow ^3D_3$ transition [275], the loading of which could also benefit from this depumping technique. The loading enhancement for MOTs does not benefit from the detuning-dependent asymmetry seen for magnetic trap loading, which limits the simulated improvement in Ca to $\approx 50\%$.

4.1.6 Conclusions

We have demonstrated that the 688-nm transition can be used to reduce cycle time and increase atom number in ultracold strontium experiments. For the bosonic isotopes, applying both a 688-nm and a 679-nm laser to the bMOT increases atom number in the metastable reservoir by up to 65 % regardless of loading time. If an experiment requires large atom number relative to experimental limits, the trap loading time can be reduced by a factor of three or better. The enhancement is less for ^{87}Sr due to complications arising from hyperfine structure and smaller Landé g -factors for the 3P_2 state. If a second frequency component to simultaneously pump $|F = 11/2\rangle \rightarrow |F' = 11/2\rangle$ and $|F = 9/2\rangle \rightarrow |F' = 11/2\rangle$ were added to the depumping beam, we believe performance

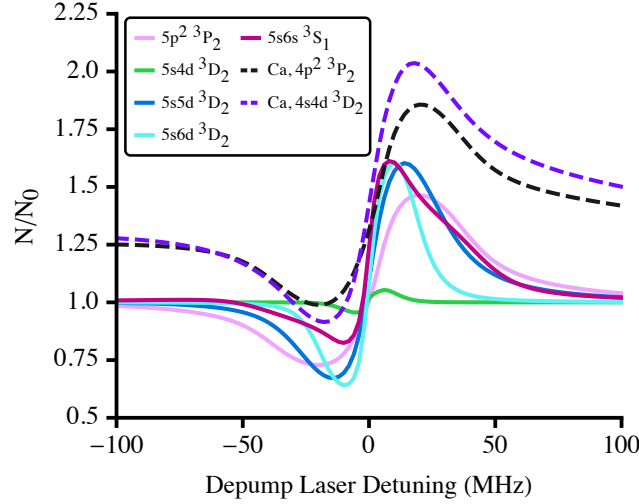


Figure 4.8: Simulations of several depumping schemes for bosonic strontium (solid lines) and calcium (dashed lines), which we label with the depumping transition excited state (the lower state is always $5s5p\ ^3P_1$ for Sr and $4s4p\ ^3P_1$ for Ca). In all simulations, we use our ^{88}Sr values for r_{bMOT} , t_{load} , s_{461} , Δ_{461} , \mathcal{F}_{1S_0} , and β . The depumper saturation parameter is $s_{\text{depump}} = 1$ except for the simulation of $5s4d\ ^3D_2$, where $s_{\text{depump}} = 2000$, which requires much higher saturation due to the narrow transition linewidth. For the simulation of $5s6s\ ^3S_1$, Δ_{679} is set to its optimal value. The Sr $5s5d\ ^3D_2$, Sr $5s6d\ ^3D_2$, Sr $5p^2\ ^3P_2$, Ca $4p^2\ ^3P_2$, and Ca $4s4d\ ^3D_2$ states may indirectly decay to 3P_0 via intermediate states outside of the 3P manifold. The model ignores these processes, but atoms decaying into 3P_0 can be recovered using *e.g.* a 679-nm laser (for Sr). The apparent offset of the enhancement for Ca is a Gaussian pedestal with a full width at half maximum of approximately 500 MHz. The linewidths necessary for these simulations can be found in [64, 113, 242, 276].

comparable to the bosonic isotopes would be achievable. This improvement might make the depumping technique a useful method to reduce dead time in ^{87}Sr atomic clocks [58].

Comparison with a one-dimensional rate equation model shows that our results for the bosons are consistent with expectations. The initial prediction of $3\times$ increased atom number, based on the branching ratio from 1D_2 into 3P_2 and 3P_1 , is not feasible. Simulations of alternative enhancement schemes indicate that pumping on either the $5s5p\ ^3P_1 \rightarrow 5s5d\ ^3D_2$ transition or the $5s5p\ ^3P_1 \rightarrow 5s6d\ ^3D_2$ transition, which are also accessible with diode lasers, offers similar performance to the approach pursued in this work. Regardless of the exact implementation, the trap loading enhancement scheme can substantially increase atom number independent of the bMOT loading rate or vacuum lifetime. We expect that this method will be helpful for experiments benefitting from high

atom number or faster cycle times.

The authors thank J.A. Pechkis for his work on the experimental apparatus. D.S. Barker acknowledges support from the NIST-ARRA Fellowship Program. This work was partially supported by ONR and the NSF through the PFC at the JQI.

4.2 Additional Work

We eventually settled on continuous interrogation of the bMOT with the 688-nm laser as the best depumping method. However, we explored several other approaches to try to alleviate the suppression of the bMOT atom number while preserving the enhanced magnetic trap loading. First, we chopped the 688-nm laser intensity at 10 Hz with a 50/50 duty cycle. Because the bMOT loading time was ≈ 100 ms, we thought this might increase the average bMOT atom number and preserve the depumping enhancement. We instead observed a 50% reduction in the 688-nm laser's effect, as one might expect from the duty cycle.⁴ Second, we tried to create a dark spot bMOT by masking out the center of the 707-nm repumping laser. By depumping the MOT region where atoms accumulate and repumping the region outside the MOT where atoms have not been fully captured, it seemed that the advantages of repumping and depumping could be combined. This laser configuration resulted in no magnetic trap loading whatsoever. Either the dark spot was not sufficiently dark or, as other groups have observed, the metastable reservoir has a very large spatial extent [182]. Finally, we varied the 688-nm laser polarization from σ^+ to linear to σ^- . The quadrupole field of the MOT effectively scrambles the laser polarization due to the spatial dependence of the quantization axis, so we expected that the trap loading enhancement would have no dependence on the laser polarization. However, we were able to measure a small polarization dependent change in the depumping enhancement (on the order of several percentage points), which suggests that our bMOT is not perfectly aligned to the quadrupole field zero.

⁴It may be the case that more asymmetric duty cycles are advantageous.

Chapter 5: Three-Photon Process

Once we abandoned continuously loading the magnetic trap as a route toward quantum degeneracy, we began to search for alternative uses for the 688-nm laser. One of our ideas resulted in a theory publication [277] and I have again included the submitted ArXiv version, with a few additional edits, here (see Section 5.1). The published work was a collaboration between Neal Piseni, Ben Reschovsky, Gretchen Campbell and me. I constructed the optical Bloch equations for the system and performed the numerical simulations (see Section 5.1.3). Neal calculated the AC Stark shifts for Section 5.1.4. All authors discussed and developed the rest of the work in Section 5.1.4. I wrote the paper and it was edited by all authors. After the paper was accepted, we realized that stimulated Raman adiabatic passage could be used to realize the three-photon transfer. I discuss the results of my efforts to explore the utility of such a protocol in Section 5.2.

5.1 Publication: Three-photon process for producing a degenerate gas of metastable alkaline-earth-metal atoms

5.1.1 Abstract

We propose a method for creating a quantum degenerate gas of metastable alkaline-earth atoms. Such degenerate gases have yet to be achieved due to inelastic collisions that limit evaporative cooling in the metastable states. Quantum degenerate samples prepared in the 1S_0 ground state can be rapidly transferred to either the 3P_2 or 3P_0 state via a coherent 3-photon process. Numerical integration of the density matrix evolution for the

fine structure of bosonic alkaline-earth atoms shows that transfer efficiencies of $\approx 90\%$ can be achieved with experimentally feasible laser parameters in both Sr and Yb. Importantly, the 3-photon process can be set up to impart no net momentum to the degenerate gas during the excitation, which will allow for studies of metastable samples outside the Lamb-Dicke regime. We discuss several experimental challenges to the successful realization of our scheme, including the minimization of differential AC Stark shifts between the four states connected by the 3-photon transition.

5.1.2 Introduction

Alkaline-earth-like (AE) atoms have attracted experimental and theoretical interest due to their narrow optical resonances and non-magnetic ground state. Recent experiments have exploited these properties to study atom interferometry [86, 88, 89], atomic clocks [56, 57], superradiant lasers [278], quantum simulation [104, 279, 280], and molecular physics [70, 71, 281, 282]. An outstanding experimental challenge is the realization of quantum degenerate samples of AE atoms in the metastable 3P_2 and 3P_0 states. These samples would be useful in a wide variety of applications. For example, the 3P_2 state has a permanent electric quadrupole moment, and 3P_2 degenerate gases are a potential platform for quantum simulation [283] or for studies of anisotropic collisions [284, 285]. Degenerate samples of 3P_0 atoms could help to advance atomic structure calculations [286–288], increase the accuracy of atomic clocks [58], or generate highly entangled states [289]. Simultaneous coherent manipulation of atoms in both 3P_2 and 3P_0 is required for several proposed quantum computing schemes [80, 81].

Inelastic collisional losses, which are on the order of $10^{-10} - 10^{-11} \text{ cm}^3/\text{s}$, prevent direct evaporation of metastable AE atoms to quantum degeneracy [269, 290–294]. Previous experiments used either incoherent excitation [269, 290, 292, 294, 295] or coherent excitation of a doubly-forbidden transition [293, 296, 297] to transfer pre-cooled AE atoms to a metastable state. These single-photon techniques necessarily impart momentum to the

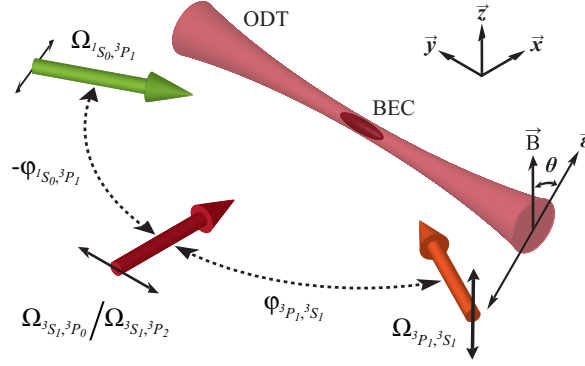


Figure 5.1: Laser configuration for the 3-photon excitation scheme. A Bose-Einstein Condensate (BEC) sits in an Optical Dipole Trap (ODT) in a region with a uniform magnetic field, $\vec{B} = B \hat{z}$. Three lasers cross at the BEC and drive the transition to the metastable state. These lasers address the $^1S_0 \rightarrow ^3P_1$, $^3P_1 \rightarrow ^3S_1$, and $^3S_1 \rightarrow ^3P_{0(2)}$ transitions with Rabi frequencies of $\Omega_{1S_0, 3P_1}$, $\Omega_{3P_1, 3S_1}$, and $\Omega_{3S_1, 3P_{0(2)}}$, respectively. The angles of incidence, $\varphi_{3P_1, 3S_1}$ and $\varphi_{1S_0, 3P_1}$, between the excitation laser beams and the x -axis can be chosen so as to eliminate the net momentum transfer to the condensate during the excitation process. The double headed black arrows indicate the polarization of the optical fields, which decomposes to either $|\sigma = 1\rangle + |\sigma = -1\rangle$ or $|\sigma = 0\rangle$ in the circular basis, depending on whether the laser is polarized parallel or perpendicular to the magnetic field. The angle between the ODT polarization vector and the magnetic field, θ , can be tuned to control dephasing due to differential AC Stark shifts between the four atomic states (see Section 5.1.4).

sample during excitation, limiting their application to either thermal atoms or the Lamb-Dicke regime. Additionally, addressing a doubly-forbidden transition is challenging due to the stringent requirements on the excitation laser's linewidth and the need for accurate spectroscopy of the $^1S_0 \rightarrow ^3P_{0(2)}$ transitions, which has only been performed on a few isotopes of AE atoms [44, 55, 59, 82, 298].

We propose a 3-photon excitation scheme for the creation of degenerate gases in metastable states by transferring the atoms through the $^1S_0 \rightarrow ^3P_1 \rightarrow ^3S_1 \rightarrow ^3P_{0(2)}$ path. During the 3-photon process each atom absorbs two photons and emits one, so an appropriate laser arrangement can eliminate the net momentum transfer to the atomic sample (see Figure 5.1). All the transitions addressed in this scheme are much broader than the doubly-forbidden transitions in AE atoms (the smallest single-photon linewidth is ≈ 370 Hz for Ca, ≈ 7.5 kHz for Sr, and ≈ 180 kHz for Yb), which substantially relaxes the laser linewidth requirements. For the 3-photon process to be coherent, the three lasers

must be phase-locked. Although the necessary wavelengths potentially span hundreds of nanometers (see Table 5.2), the lasers can be stabilized to each other with a cavity transfer lock, an electromagnetically induced transparency (EIT) lock, or a beatnote lock to an optical frequency comb [299–304].

Here, we investigate the feasibility of the 3-photon scheme by numerically integrating the optical Bloch equations (OBEs) for the 13-level system of bosonic AE atoms (see Figure 5.2). The simulations use linewidths and wavelengths for strontium and ytterbium, but the generic results should apply to calcium as well. We present the numerical results and estimate the effective 3-photon linewidth in Section 5.1.3. Section 5.1.4 describes possible solutions to several experimental challenges, including ways to extend the lifetime of the metastable sample and mitigate inhomogeneous broadening. We summarize our results and discuss future outlook in Section 5.1.5.

5.1.3 3-Photon Dynamics

Figure 5.2 shows the 13 relevant Zeeman sublevels for bosonic AE atoms and the coupling lasers needed for the 3-photon transition. We label the states $|\ell, m_J\rangle$, where $\ell = {}^{2S+1}L_J$ is the term symbol for the state and m_J the projection of the total electronic angular momentum, J , onto the z -axis. The optical field coupling level $|\ell\rangle$ to $|\ell'\rangle$ is given by its electric field magnitude, $E_{\ell,\ell'} = \Omega_{\ell,\ell'} / \langle \ell' || \vec{d} || \ell \rangle$, where $\Omega_{\ell,\ell'}$ is the single-photon Rabi frequency, $\langle \ell' || \vec{d} || \ell \rangle$ is the reduced dipole matrix element, and we have taken $\hbar = 1$. The one-photon laser detuning is Δ_{3P_1} , the two-photon detuning is Δ_{3S_1} , and the 3-photon detuning is either Δ_{3P_2} or Δ_{3P_0} depending on the desired final state. All the detunings, Δ_ℓ , are referenced to the lowest energy Zeeman state of level $|\ell\rangle$. A magnetic field, $\vec{B} = \Omega_B \hat{z} / \mu_B$ with μ_B the Bohr magneton, breaks the degeneracy of the Zeeman states. This splitting allows individual addressing of 3P_0 or the $m_J = \pm 2$ states of 3P_2 . For our calculation, we selected $|{}^3P_2, \pm 2\rangle$ as the target states in 3P_2 based on their large quadrupole moment [283] and favorable Clebsch-Gordan overlap with $|{}^3S_1, \pm 1\rangle$. Other 3P_2 Zeeman

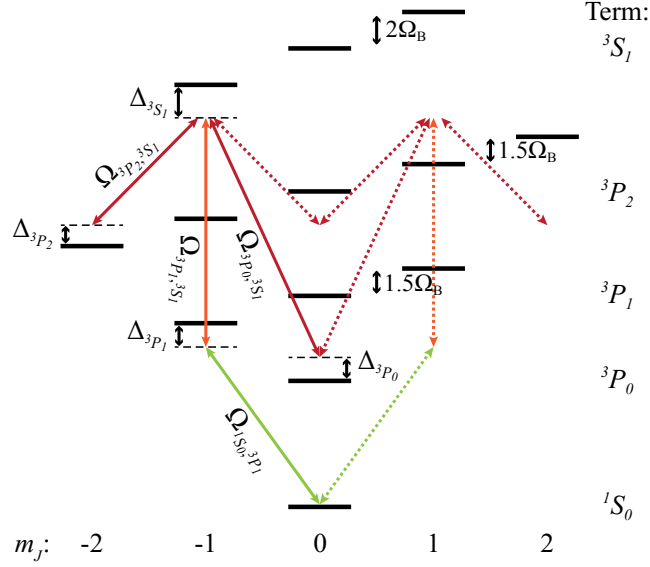


Figure 5.2: The Zeeman level structure of bosonic AE atoms relevant for the 3-photon process. The colored double-headed arrows indicate dipole-allowed transitions for each optical field after projection of its polarization onto the quantization axis. These arrows are solid for the transitions closest to resonance and dotted for transitions that are far off resonance. The polarization projection depends on the angle, $\alpha_{\ell, \ell'}$, between the laser polarization vector and the magnetic field, $\vec{B} = \Omega_B \hat{z} / \mu_B$ (see Figure 5.1), where ℓ (ℓ') is the term symbol of the lower (upper) state of the transition and we have taken $\hbar = 1$. The excitation laser strength is $E_{\ell, \ell'} = \Omega_{\ell, \ell'} / \langle \ell' \| \vec{d} \| \ell \rangle$ with $\langle \ell' \| \vec{d} \| \ell \rangle$ the reduced dipole matrix element. The detuning, Δ_{ℓ} , is referenced to the lowest energy Zeeman state of $|\ell\rangle$. Here, we have depicted a 3-photon transition to either $|^3P_2, -2\rangle$ or $|^3P_0, 0\rangle$, but $|^3P_2, 2\rangle$ can be reached by reversing the magnetic field or detuning each laser to the blue of the highest energy Zeeman state that it addresses. RF transitions from $|^3P_2, \pm 2\rangle$ can prepare other Zeeman states in 3P_2 .

levels can be prepared using RF transitions, as has been demonstrated in [295]. The laser polarizations, Zeeman splittings, and laser detunings must be carefully chosen to suppress dipole-allowed transitions to undesired states (see Figure 5.2). For example, the laser driving the $|^3P_1\rangle \rightarrow |^3S_1\rangle$ transition must be π polarized to prevent unwanted accumulation of atoms in $|^3P_1, \pm 1\rangle$.

In the rotating wave approximation, the Hamiltonian for the system shown in Fig-

ure 5.2 is [256]:

$$\begin{aligned}
\hat{H} = \sum_{\ell} \sum_{m_J=-J}^J \left[(\Delta_{\ell}(-1))^{\delta(\ell, {}^3P_1) + \delta(\ell, {}^3S_1)} + g_J(m_J + J)\Omega_B \right] |\ell, m_J\rangle\langle\ell, m_J| \\
+ \left(\sum_{\substack{\{\ell', m_{J'}\} \\ > \{\ell, m_J\}}} \sum_{\sigma} \frac{\Omega_{\ell, \ell'}}{2} C_{\ell, \ell'}^{\sigma, m_J, m_{J'}} \left(\frac{|\sigma|}{\sqrt{2}} \sin(\alpha_{\ell, \ell'}) e^{-i(\sigma\varphi_{\ell, \ell'} + \pi/2)} \right. \right. \\
\left. \left. + (1 - |\sigma|) \cos(\alpha_{\ell, \ell'}) \right) |\ell', m_{J'}\rangle\langle\ell, m_J| \right) + h.c. \Big]. \quad (5.1)
\end{aligned}$$

The first term in the brackets represents the energy shift of the Zeeman state $|\ell, m_J\rangle$ due to the laser detuning and magnetic field, where g_J is the Landé g -factor and $\delta(\ell, \ell')$ is the Kronecker delta. The second term and its Hermitian conjugate contain the off-diagonal couplings. We denote the photon polarization basis states by $|\sigma\rangle$, with $\sigma \in \{-1, 0, 1\}$. The laser connecting $|\ell\rangle$ to $|\ell'\rangle$ propagates at an angle $\varphi_{\ell, \ell'}$ relative to the x -axis and is linearly polarized at an angle $\alpha_{\ell, \ell'}$ from the z -axis. These two angles control the projection of the laser photon's angular momentum onto the quantization axis and the relative phase of the Rabi frequencies, $\Omega_{\ell, \ell'}$. For a coherent process, these phases are well-defined and we take the $\Omega_{\ell, \ell'}$ to be real valued. The Clebsch-Gordan coefficients, $C_{\ell, \ell'}^{\sigma, m_J, m_{J'}}$, set the relative strength of the drive between different magnetic sublevels of $|\ell\rangle$ and $|\ell'\rangle$.

We incorporate the non-Hermitian component of the 3-photon process using the density matrix formalism. The density matrix for our system is

$$\hat{\rho} = \sum_{\{\ell, m_J\}} \sum_{\{\ell', m_{J'}\}} \rho_{\{\ell, m_J\}, \{\ell', m_{J'}\}} |\ell, m_J\rangle\langle\ell', m_{J'}|. \quad (5.2)$$

Each state's population, $\rho_{\{\ell, m_J\}, \{\ell, m_J\}}$, decreases at a rate given by the sum of the natural decay rates, $\Gamma_{\ell} = \sum_{\ell'} \Gamma_{\ell', \ell}$, connecting it to lower states $|\ell'\rangle$. The coherence, $\rho_{\{\ell, m_J\}, \{\ell', m_{J'}\}}$, between states with distinct term symbols ℓ and ℓ' decays at a rate $\Gamma_{\ell, \ell'}/2$. Coherences between the magnetic sublevels, $|\ell, m_1\rangle$ and $|\ell, m_2\rangle$ of a given $|\ell\rangle$ increase at a rate given by the decay of upper states into $|\ell\rangle$ and the Clebsch-Gordan coefficients governing the

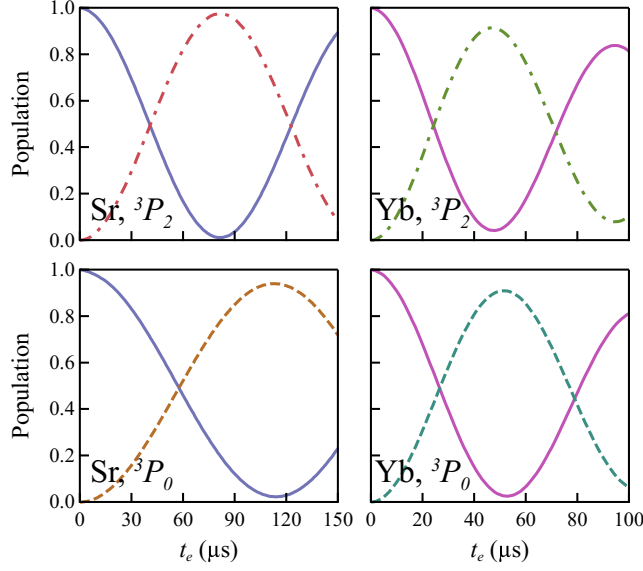


Figure 5.3: Results of the numerical integration of the Optical Bloch Equations (OBEs) for bosonic AE atoms given in equation (5.5). Solid curves show ground state populations while dashed and dash-dotted curves show target state populations ($|^3P_0, 0\rangle$ and $|^3P_2, -2\rangle$, respectively). The populations in other states are negligible and not shown. Each laser turns on instantaneously at time zero and is instantaneously extinguished at time t_e . All the parameters for these simulations can be found in Table 5.1.

branching of those decays into $|\ell, m_1\rangle$ and $|\ell, m_2\rangle$. In order to account for all of these processes, we define

$$\hat{\xi}_{\sigma, \ell, \ell'} = \sum_{m_J, m_{J'}} C_{\ell, \ell'}^{\sigma, m_J, m_{J'}} |\ell, m_J\rangle \langle \ell', m_{J'}|, \quad (5.3)$$

which allows us to construct the Liouville operator between $|\ell\rangle$ and $|\ell'\rangle$,

$$\hat{\mathcal{L}}_{\ell, \ell'} = \frac{\Gamma_{\ell, \ell'}}{2} \sum_{\sigma} [(\hat{\xi}_{\sigma, \ell, \ell'} \hat{\rho} \hat{\xi}_{\sigma, \ell, \ell'}^\dagger - \hat{\xi}_{\sigma, \ell, \ell'}^\dagger \hat{\xi}_{\sigma, \ell, \ell'} \hat{\rho}) + h.c.]. \quad (5.4)$$

By combining equations (5.1) and (5.4), we arrive at the OBEs for the system [256]

$$\frac{d}{dt} \hat{\rho} = -i [\hat{H}, \hat{\rho}] + \sum_{\ell, \ell'} \hat{\mathcal{L}}_{\ell, \ell'}. \quad (5.5)$$

Once we insert the propagation angles, $\varphi_{\ell, \ell'}$, and the polarization angles, $\alpha_{\ell, \ell'}$, for the target

Table 5.1: The input parameters and results for the simulations in Figure 5.3. The peak population in the target state, ρ_π , is reached after an evolution time, t_π . By varying $\Delta_{^3P_{0(2)}}$ in the simulations, we can extract the full width at half maximum of the 3-photon resonance, $\gamma_{3\text{-photon}}$ (see Figure 5.4). We quote detunings in units of the natural decay rate of their associated level.

	Sr, $ ^3P_2, \pm 2\rangle$	Sr, $ ^3P_0, 0\rangle$	Yb, $ ^3P_2, \pm 2\rangle$	Yb, $ ^3P_0, 0\rangle$
$\Delta_{^3P_1}$	$-100 \times \Gamma_{^3P_1}$	$-470 \times \Gamma_{^3P_1}$	$-230 \times \Gamma_{^3P_1}$	$-210 \times \Gamma_{^3P_1}$
$\Delta_{^3S_1}$	$-21.6 \times \Gamma_{^3S_1}$	$-86.4 \times \Gamma_{^3S_1}$	$-38.9 \times \Gamma_{^3S_1}$	$-47.2 \times \Gamma_{^3S_1}$
$\Delta_{^3P_{0(2)}}$	0	0	0	0
$\frac{1}{2\pi}\Omega_{^1S_0, ^3P_1}$	0.25 MHz	0.25 MHz	1.5 MHz	1.5 MHz
$\frac{1}{2\pi}\Omega_{^3P_1, ^3S_1}$	100 MHz	90 MHz	150 MHz	150 MHz
$\frac{1}{2\pi}\Omega_{^3P_{0(2)}, ^3S_1}$	4.0 MHz	3.0 MHz	6.0 MHz	4.1 MHz
$\frac{1}{2\pi}\Omega_B$	10 MHz	10 MHz	10 MHz	10 MHz
$\alpha_{^1S_0, ^3P_1}$	90°	90°	90°	90°
$\alpha_{^3P_1, ^3S_1}$	0°	0°	0°	0°
$\alpha_{^3P_{0(2)}, ^3S_1}$	90°	90°	90°	90°
$\varphi_{^1S_0, ^3P_1}$	-60.9°	-59.6°	-53.8°	-51.5°
$\varphi_{^3P_1, ^3S_1}$	60.8°	59.5°	80.7°	73.3°
ρ_π	97.5%	94.0%	91.5%	91.0%
t_π	81.5 μ s	112.3 μ s	46.9 μ s	51.4 μ s
$\gamma_{3\text{-photon}}$	10.0 kHz	7.2 kHz	17.6 kHz	15.5 kHz

state (either $|^3P_2, \pm 2\rangle$ or $|^3P_0, 0\rangle$, see Table 5.1), the OBEs contain seven free parameters: the detunings ($\Delta_{^3P_1}$, $\Delta_{^3S_1}$, and $\Delta_{^3P_{0(2)}}$), the magnetic field strength (Ω_B), and the three Rabi frequencies ($\Omega_{^1S_0, ^3P_1}$, $\Omega_{^3P_1, ^3S_1}$, and $\Omega_{^3P_{0(2)}, ^3S_1}$). Our objective is to find experimentally reasonable values for the free parameters that produce Rabi dynamics between $|^1S_0, 0\rangle$ and the target state.

We numerically integrate the OBEs and vary the input parameters to optimize the amplitude of Rabi oscillations. The optical fields all turn on instantaneously at time zero, uniformly illuminate the system for an evolution time, t_e , and then are all instantaneously extinguished. For both Sr and Yb, we find values of the detunings and couplings that yield

$\gtrsim 90\%$ peak population transfer. Figure 5.3 shows the evolution of the relevant diagonal elements of the density matrix for these parameter sets. The transfer efficiency is slightly higher for strontium than ytterbium, which is likely due to the reduced linewidth of the $^1S_0 \rightarrow ^3P_1$ line. The coherence of the dynamics allows a degenerate gas to be transferred to a metastable state with minimal heating. We plot the peak excitation fraction of the target state as a function of the 3-photon detuning in Figure 5.4. The width of these curves is a numerical estimate of the 3-photon linewidth, which we extract from a sinc^2 fit to the numerical results. The fit captures the behavior of the central peak, but deviates in the wings because the actual lineshape is a convolution of multiple broadening effects. We find that the full width at half maximum is $\simeq 10$ kHz for Sr and $\simeq 20$ kHz for Yb. We have not simulated the 3-photon dynamics for AE fermions due to the $10\times$ ($6\times$, $2\times$) larger Hilbert space for ^{87}Sr (^{173}Yb , ^{171}Yb). However, the results for bosons suggest that high efficiency transfer of a spin-polarized Fermi degenerate gas to a metastable state is possible.

5.1.4 Experimental Considerations

In Section 5.1.3, we demonstrated that a coherent, 3-photon excitation scheme can in principle transfer a large population fraction from $|^1S_0, 0\rangle$ to $|^3P_0, 0\rangle$ or $|^3P_2, -2\rangle$. However, there are several technical details that must be considered in order to realize the 3-photon process experimentally. For example, the incident laser beams must be carefully aligned to minimize the net momentum transfer to the degenerate gas during excitation. The differential AC Stark shift between the four Zeeman levels involved in the process must also be controlled to avoid inhomogeneous broadening of the 3-photon transition. The elastic and inelastic interactions of the degenerate gas could also broaden the 3-photon transition or affect the utility of the resulting metastable sample.

For the 3-photon process to be successful, it must not excite center-of-mass oscillations or heat the sample excessively. During population transfer, an atom emits a photon

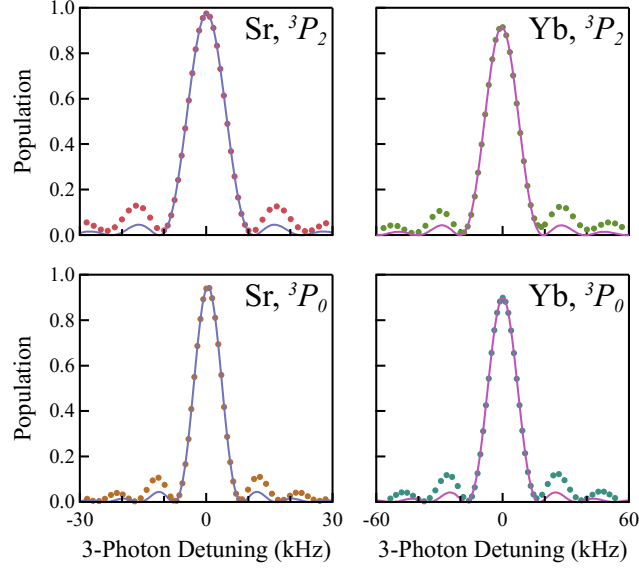


Figure 5.4: The excitation fraction of the target state, $|^3P_{2,\pm 2}\rangle$ ($|^3P_{0,0}\rangle$), at t_π as a function of the 3-photon detuning is shown in the top (bottom) row. The left column shows the results for Sr and the right column shows the results for Yb. Except for the 3-photon detuning, which is varied, the parameters for the simulations are identical to those used in Figure 5.3 and reported in Table 5.1. The sinc^2 fits (solid lines) yield full widths at half maximum for the 3-photon transitions to 3P_2 (3P_0) of 10.0 (7.2) kHz for Sr and of 17.6 (15.5) kHz for Yb. The amplitude mismatch between the wings of the fit and the simulation is likely caused by the convolution of power broadening and the transform limit.

into the laser beam addressing $^3P_{0(2)} \rightarrow ^3S_1$ and absorbs one photon each from the other two lasers. Because three photons are involved in the excitation, we can find angles of incidence, $\varphi_{\ell,\ell'}$, that eliminate net momentum transfer to the degenerate gas even though each photon carries distinct momentum. For the laser configuration in Figure 5.1, the $\varphi_{\ell,\ell'}$ are given by

$$\begin{aligned} k_{1S_0,^3P_1} \cos(\varphi_{1S_0,^3P_1}) + k_{3P_1,^3S_1} \cos(\varphi_{3P_1,^3S_1}) &= k_{3S_1,^3P_{0(2)}} \\ k_{1S_0,^3P_1} \sin(\varphi_{1S_0,^3P_1}) + k_{3P_1,^3S_1} \sin(\varphi_{3P_1,^3S_1}) &= 0, \end{aligned} \quad (5.6)$$

where $k_{\ell,\ell'}$ is the wavenumber for the $|\ell\rangle \rightarrow |\ell'\rangle$ transition. The first equation in (5.6) represents the momentum transfer along \hat{x} and the second is the transfer along \hat{y} (see Figure 5.1). The angles for excitation to $^3P_{0(2)}$ for both Sr and Yb are given in Table 5.1. Misalignment of any of the lasers will lead to heating during the 3-photon transfer. We can

Table 5.2: The wavelengths and linewidths for the transitions involved in the 3-photon process [113, 305]. Except for the $^1S_0 \rightarrow ^3P_1$ transition in Yb, diode lasers can easily generate the requisite wavelengths.

ℓ, ℓ'	Sr		Yb	
	$\lambda_{\ell, \ell'}$	$\gamma_{\ell, \ell'}$	$\lambda_{\ell, \ell'}$	$\gamma_{\ell, \ell'}$
$^1S_0, ^3P_1$	689 nm	7.5 kHz	556 nm	180 kHz
$^3P_0, ^3S_1$	679 nm	1.4 MHz	649 nm	1.5 MHz
$^3P_1, ^3S_1$	688 nm	4.3 MHz	680 nm	4.3 MHz
$^3P_2, ^3S_1$	707 nm	6.7 MHz	770 nm	6.0 MHz

estimate the effect of misalignment by comparing the recoil energy of the net momentum after the 3-photon process (E_r) to the level spacing of the harmonic trapping potential (E_{trap}). If we assume a trap frequency of 50 Hz and a $\pm 1^\circ$ error in either or both of $\varphi_{^1S_0, ^3P_1}$ and $\varphi_{^3P_1, ^3S_1}$, then $E_r/E_{trap} < 0.09$ (0.07) for both target states in Sr (Yb). Each of the lasers could also be misaligned out of the xy -plane. For the worst combination of $\pm 1^\circ$ vertical alignment errors and the same 50 Hz trap frequency, $E_r/E_{trap} < 0.27$ (0.17) for either target state in Sr (Yb). Both types of misalignment result in E_r/E_{trap} being substantially less than unity, so the recoil heating should be insignificant.

The Rabi frequencies $\{\Omega_{^1S_0, ^3P_1}, \Omega_{^3P_1, ^3S_1}, \Omega_{^3P_0, ^3S_1}, \Omega_{^3P_2, ^3S_1}\}$ from Figure 5.3 correspond to saturation parameters, I/I_{sat} , on the order of $\{1000, 1000, 10, 1\}$ (For Yb, the saturation for $\Omega_{^1S_0, ^3P_1}$ is on the order of 100). For the $^3P_1 \rightarrow ^3S_1$ transition, a laser beam can achieve the necessary intensity with approximately 10 mW of power and a $1/e^2$ radius $\simeq 400 \mu\text{m}$. The other transitions only require a beam with $\lesssim 1$ mW of power and a waist $\simeq 3$ mm to reach the appropriate saturation. Diode lasers can easily produce these powers and the requisite waists are much larger than the typical dimensions of a degenerate gas, which will suppress dephasing due to the Gaussian intensity profile of the laser beams.

The three excitation lasers must be phase stabilized to better than the 3-photon linewidth (see Figure 5.4 and Table 5.1) in order to produce coherent dynamics. The lasers for Sr have similar wavelengths (see Table 5.2), and interrogation of the $^1S_0 \rightarrow ^3P_1$

transition in Sr typically requires a high finesse optical cavity to decrease that laser's linewidth. These two observations make a cavity transfer lock an appealing strategy, and cavity mediated stability transfer at the $\lesssim 10$ kHz level has been demonstrated in the context of Sr Rydberg excitation [304]. The excitation wavelengths span a much larger range for Yb, which increases the technical difficulty of a cavity transfer lock. The lasers could instead be locked using a combination of cascade and lambda type EIT [299, 300] or by stabilizing each laser with an optical frequency comb [302, 303].

Ideally, the 3-photon excitation would occur in an optical trap with no differential AC stark shift between any of the coupled levels. However, due to the dipole-allowed transitions between $|^3S_1\rangle$ and the states in the 3P_J manifold, we should expect that no practical wavelength satisfies this condition. Intuition from two-photon Raman processes suggests, and simulations of our system verify, that trap induced shifts to the intermediate detunings (Δ_{3P_1} and Δ_{3S_1}) contribute only weakly to inhomogeneous broadening of the 3-photon transition. Therefore, population transfer can occur in a trap operating at a magic wavelength that eliminates the differential AC Stark shift between the initial and final states. The magic wavelengths for $|^1S_0\rangle$ and $|^3P_0\rangle$ are well known in Sr and Yb because of their application to optical clocks [56–58]. To search for magic wavelengths for $|^3P_{2,\pm 2}\rangle$, we calculate the polarizability (scalar and tensor) for each state involved in the multi-photon transition following the procedure in [53, 256] with lines from [113] and linewidths from [40, 113, 276, 306–309], for Sr, and [113, 305, 310, 311], for Yb. We expect the calculated polarizabilities to predict magic wavelengths with better than ± 10 nm accuracy (the level at which it reproduces known magic wavelengths in Sr) except for the Yb 3P_0 state, for which few matrix elements have been reported in the literature.

Figure 5.5 contains the results of our calculations for trapping lasers polarized parallel and perpendicular to the magnetic field axis. The plots show the differential polarizabilities between $\{|^3P_0, 0\rangle, |^3P_1, \pm 1\rangle, |^3P_2, \pm 2\rangle, |^3S_1, \pm 1\rangle\}$ and the ground state, $|^1S_0, 0\rangle$. In the two upper panels of Figure 5.5, we see two magic wavelengths for $|^1S_0, 0\rangle$ and

$|^3P_{2,\pm 2}\rangle$ near 520 nm and 950 nm. The lower panels in Figure 5.5 indicate that in Yb there is a magic wavelength for these two states near 1100 nm. All of these magic wavelengths can be tuned over a wide range ($\gtrsim 100$ nm for the near-IR wavelengths) by varying the dipole trap polarization angle, θ , between 0° and 90° . In particular, the Yb $|^3P_{2,\pm 2}\rangle$ magic wavelength moves to 1064 nm when $\theta \approx 66^\circ$ and the green magic wavelength in Sr is tunable over the range $\{508, 520\}$ nm. We can also see in Figure 5.5 that the near-IR magic wavelengths for $|^3P_{1,\pm 1}\rangle$ and $|^3P_{2,\pm 2}\rangle$ have opposite angular dependence in both Sr and Yb. This observation suggests the existence of a doubly-magic wavelength, $\lambda_{2\times m}$, that eliminates differential light shifts between $|^3P_{2,\pm 2}\rangle$, $|^3P_{1,\pm 1}\rangle$ and $|^1S_0, 0\rangle$ when the dipole trap is polarized at a magic angle, $\theta_{2\times m}$. By varying θ , we are able to identify one doubly-magic wavelength in Sr and two in Yb (see Table 5.3), which would allow further reduction of the trap-induced inhomogeneous broadening. We note that the optical clock transition magic wavelengths can also be made doubly-magic for both elements by tuning the polarizability of $|^3P_{1,\pm 1}\rangle$.

The remaining AC Stark shift of $|^3S_1\rangle$ or $|^3P_1\rangle$ with respect to the ground state inhomogeneously broadens the 3-photon transition. This inhomogeneous broadening arises due to the different harmonic confinement of $|^3S_1\rangle$ and $|^3P_1\rangle$ compared to the ground state. We estimate the scale of the broadening by taking the difference between the ground-state chemical potential of the degenerate gas, μ_{1S_0} , and the chemical potential it would have in $|^3S_1\rangle$, μ_{3S_1} , or $|^3P_1\rangle$, μ_{3P_1} . Typical degenerate gases have chemical potentials on the order of 1 kHz. The excited-state chemical potential is related to the ground-state chemical potential by the ratio of the polarizabilities of the two states, assuming that the s -wave scattering lengths are equal. For the magic wavelengths under consideration (see Table 5.3), the ratio of the $|^3S_1, \pm 1\rangle$ and $|^1S_0, 0\rangle$ polarizabilities for Sr (Yb) ranges from -0.1 to -10 (-2 to -40), meaning that the inhomogeneous broadening, $\mu_{1S_0} - \mu_{3S_1}$, should be $\lesssim 10$ kHz for Sr and $\lesssim 40$ kHz for Yb. Because the inhomogeneous broadening due to $|^3S_1, \pm 1\rangle$ is substantially smaller than the two-photon detuning, the effect of this

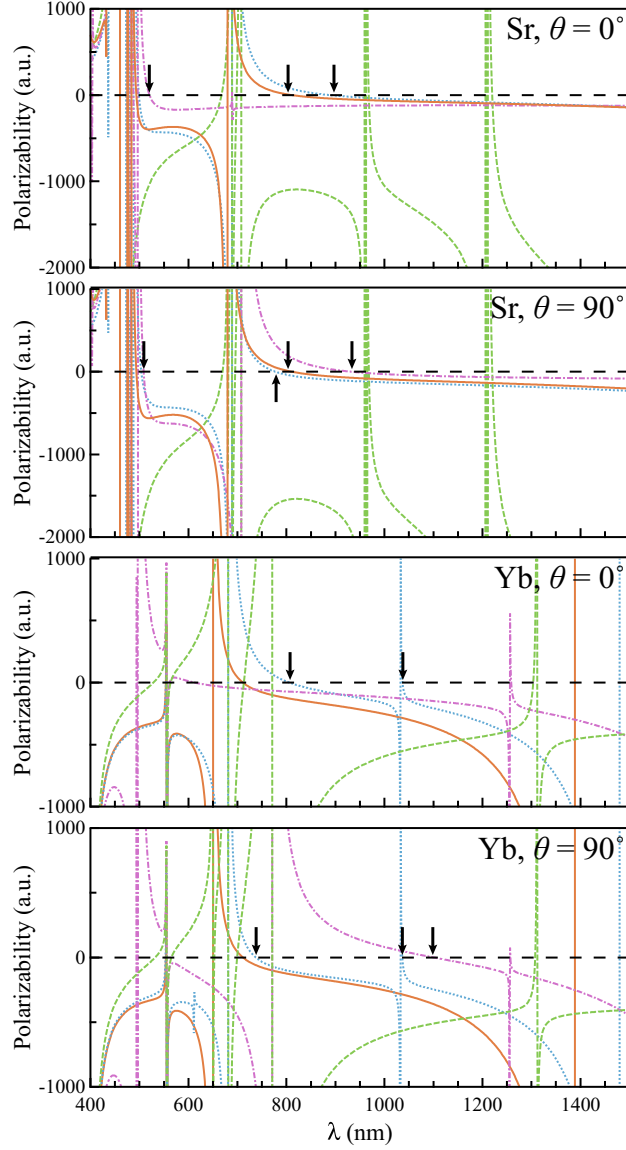


Figure 5.5: The differential AC polarizability between each of the excited states ($|^3P_0, 0\rangle$ (solid orange), $|^3P_1, \pm 1\rangle$ (dotted blue), $|^3P_2, \pm 2\rangle$ (dash-dotted magenta), and $|^3S_1, \pm 1\rangle$ (dashed green)) and the $|^1S_0, 0\rangle$ ground state in atomic units. The top two panels show the polarizability of Sr for ODT light polarized parallel and perpendicular to the quantization axis, respectively. The bottom two panels are the corresponding plots for Yb. Every zero crossing indicates a magic wavelength. We indicate the magic wavelengths of specific interest here using black arrows. For $|^3P_2, \pm 2\rangle$ and $|^3P_1, \pm 1\rangle$, the laser polarization can tune the indicated magic wavelengths over a wide range (see Table 5.3). Note that the position of the $|^3P_0, 0\rangle$ and $|^3P_2, \pm 2\rangle$ magic wavelengths flips with respect to the $|^3P_1, \pm 1\rangle$ magic wavelength in the near-IR as the polarization angle changes from 0° to 90° . This indicates the presence of a double magic wavelength at a particular polarization angle that equalizes the AC Stark shifts of three energy levels.

Table 5.3: Magic wavelengths and magic wavelength ranges for the target states in the 3-photon process. We also list the double magic wavelengths and associated angles that equalize the AC Stark shifts of $|^3S_0, 0\rangle$, $|^3P_1, \pm 1\rangle$, and $|^3P_2, \pm 2\rangle$ or $|^3P_0, 0\rangle$. For $|^3P_0, 0\rangle$, magic wavelengths for fermionic isotopes are taken from [56, 58] and rounded to the nearest nm.

	Sr, $ ^3P_2, \pm 2\rangle$	Sr, $ ^3P_0, 0\rangle$	Yb, $ ^3P_2, \pm 2\rangle$	Yb, $ ^3P_0, 0\rangle$
λ_{magic}	720 – 935 nm 508 – 520 nm	813 nm	780 – 1100 nm	759 nm
$\lambda_{2\times m}$	823 nm	813 nm	802 nm 1036 nm	759 nm
$\theta_{2\times m}$	44°	55°	15° 58°	55°

broadening on the Rabi dynamics should be negligible. Similarly, our reasoning implies that the inhomogeneous broadening from $|^3P_1, \pm 1\rangle$ will be $\lesssim 5$ kHz, which is substantially smaller than the one-photon detunings we consider.

The s -wave scattering length of atoms in the metastable degenerate gas will generally differ from the scattering length of atoms in the ground state. This difference in interaction strength will both shift the resonance frequency and cause inhomogeneous broadening of the 3-photon transition. There have been few measurements or calculations of the scattering lengths of metastable AE atoms [77, 78, 284, 296], so an accurate estimate of this inhomogeneous broadening is not possible. However, it is reasonable to assume that the interaction broadening will be on the order of the ground-state chemical potential, μ_{1S_0} , and thus only weakly perturb the 3-photon dynamics since the intermediate detunings are large. The inelastic collision rate for metastable AE atoms is on the order of 10^{-10} cm³/s to 10^{-11} cm³/s depending on the state and species [269, 290–294], while AE degenerate gases usually have densities $\gtrsim 10^{13}$ cm⁻³ [116, 241]. We would thus expect the lifetime of the metastable degenerate gas to be limited to ≈ 10 ms, severely restricting the experimental timescale. However, several AE atom isotopes (^{40}Ca , ^{86}Sr , ^{168}Yb) have sufficiently strong interactions to allow cooling to degeneracy at relatively low densities ($\approx 10^{12}$ cm⁻³) [121, 124, 126]. These isotopes could also sympathetically cool other isotopes to degeneracy

at low density. Alternatively, recent advances in optical trapping techniques might allow dynamic decompression of the ground state degenerate gas at fixed trap depth [129, 312]. By using either a strongly interacting isotope or a dynamically decompressed trap to generate a low density sample, the lifetime of a metastable degenerate gas could be extended to ≈ 100 ms. This timescale is sufficient for a wide variety of experiments, and for $|^3P_2\rangle$ it could be extended even further using a magnetic Feshbach resonance [284]. The Bose-Einstein or Fermi-Dirac statistics of the degenerate gas will suppress inelastic collisions due to changes in the two-particle correlation function (as has been observed for three-body loss processes in, *e.g.*, [209, 313]), potentially allowing longer sample lifetimes.

5.1.5 Conclusions

We have proposed and studied a coherent 3-photon process for creating quantum degenerate metastable samples of AE atoms. Numerical simulations of the 3-photon Rabi dynamics show that ≈ 90 % population transfer to $^3P_{0(2)}$ can be achieved in Sr and Yb. Similar transfer efficiency should be attainable in Ca as well. The smaller mass of Ca reduces the linewidth of the $^1S_0 \rightarrow ^3P_1$ transition (to ≈ 370 Hz), which will increase the technical challenge of phase-locking the necessary lasers. The Rabi dynamics are fast compared to reasonable trap oscillation frequencies, but slow compared to typical experimental timing resolution. We considered several experimental obstacles to implementation of the transfer scheme. The excitation lasers require moderate laser power ($\lesssim 10$ mW) with reasonable beam waists ($\gtrsim 100$ μm) and can be arranged to cancel the momentum kick during population transfer. An optical dipole trap could operate near a doubly magic wavelength to cancel the differential polarizability between three of the four states involved in the excitation. Even in the worst case, the inhomogeneous broadening due to the remaining state, 3S_1 , is insignificant. The ratio of the detuning from, and linewidth of, the remaining state (3S_1) to the worst case inhomogeneous broadening induced by the trap is large enough to render the broadening insignificant. A similar

argument applies to interaction induced broadening effects. By using an isotope with a large ground state s -wave scattering length or by dynamically changing the trapping potential to decompress the degenerate gas at fixed trap depth, the lifetime of the final metastable sample could be extended to ≈ 100 ms. The Bose or Fermi statistics of the metastable sample suppress inelastic collisions [209, 313] and will increase the lifetime further (potentially to several seconds for spin-polarized Fermi degenerate gases). The 100 ms timescale is long enough to perform useful experiments in the thermodynamically 3-dimensional limit [286] or to adiabatically ramp on an optical lattice to create a Mott insulating state for quantum simulation experiments [283, 285].

The authors thank A. Gorshkov, Z. Smith, V. Vaidya, and S. Eckel for useful discussions. This work was partially supported by ONR, and the NSF through the PFC at the JQI.

5.2 STIRAP

Stimulated Raman adiabatic passage (STIRAP) is a powerful technique for coherently transferring atomic samples between quantum states [314–316]. STIRAP reduces the technical challenge of multiphoton population transfer because it suppresses population in lossy intermediate states and is less sensitive to the precise temporal shape of the laser pulses. Typically, STIRAP is applied to systems with a Λ -shaped level structure. These systems possess a dark state, which can easily be identified when the two coupling lasers are individually tuned to resonance. The level structure of the AE atom system we are considering (see Figure 5.2) is substantially more complex than the standard STIRAP picture. However, there still exists a dark state when all detunings are large enough that we can simplify the level structure by neglecting the off-resonance couplings and decay processes. When all the lasers are on resonance, the Hamiltonian for the reduced level

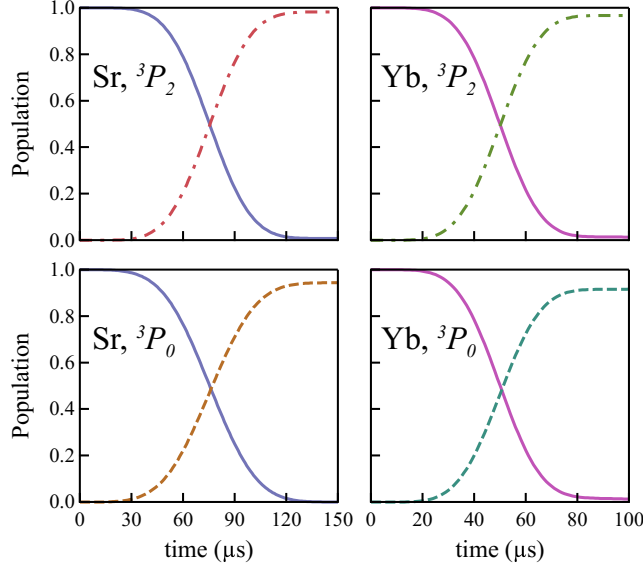


Figure 5.6: Results of the numerical integration of a STIRAP pulse using the Optical Bloch Equations (OBEs), for bosonic AE atoms, given in equation (5.5). Solid curves show ground state populations while dashed and dash-dotted curves show target state populations ($|^3P_0, 0\rangle$ and $|^3P_2, -2\rangle$, respectively). The populations in other states are negligible and not shown. The STIRAP pulse shapes are given by Equation 5.10. All the parameters for these simulations can be found in Table 5.4.

structure in the rotating wave approximation is

$$\begin{aligned}
 \hat{H}_{\text{reduced}} = & \left[\frac{\Omega_{1S_0, 3P_1}}{2\sqrt{2}} C_{1S_0, 3P_1}^{-1,0,-1} \sin(\alpha_{1S_0, 3P_1}) e^{-i(-\varphi_{1S_0, 3P_1} + \pi/2)} |^3P_1, -1\rangle \langle ^1S_0, 0| \right. \\
 & + \frac{\Omega_{3P_1, 3S_1}}{2} C_{3P_1, 3S_1}^{0,-1,-1} \cos(\alpha_{3P_1, 3S_1}) |^3S_1, -1\rangle \langle ^3P_1, -1| \\
 & + \left. \frac{\Omega_{3P_{0(2)}, 3S_1}}{2\sqrt{2}} C_{3P_{0(2)}, 3S_1}^{-1,0(-2), \pm 1} \sin(\alpha_{3P_{0(2)}, 3S_1}) e^{-i(-\varphi_{3P_{0(2)}, 3S_1} + \pi/2)} |^3S_1, -1\rangle \langle ^3P_{0(2)}, 0(-2)| \right] \\
 & + h.c.
 \end{aligned} \tag{5.7}$$

This Hamiltonian has no useful dark state, which initially convinced us that the Hamiltonian of Equation 5.1 did not admit a STIRAP protocol. In the large $\Omega_{3P_1, 3S_1}$ limit, $|^3P_1, -1\rangle$ and $|^3S_1, -1\rangle$ hybridize, so the level structure becomes an effective stacked Λ system. The apparent lack of a dark state is due to interference between excitation along the upper and lower legs of this effective structure. A. Gorshkov pointed out that the

interference can be eliminated by setting the one-photon and two-photon detunings to $\pm \frac{\Omega_{3P_1,3S_1}}{2} C_{3P_1,3S_1}^{0,-1,-1} \cos(\alpha_{3P_1,3S_1}) = \pm \frac{\Omega_{3P_1,3S_1}}{2\sqrt{2}}$. After inputting these detunings and diagonalizing the 2×2 subspace spanned by $|^3S_1, -1\rangle$ and $|^3P_1, -1\rangle$, the Hamiltonian of Equation 5.7 becomes

$$\begin{aligned} \hat{H}_{\text{stirap}} = & \frac{\Omega_{3P_1,3S_1}}{\sqrt{2}} |+\rangle\langle +| \\ & + \left[\frac{\Omega_{1S_0,3P_1}}{4} C_{1S_0,3P_1}^{-1,0,-1} \sin(\alpha_{1S_0,3P_1}) e^{-i(-\varphi_{1S_0,3P_1} + \pi/2)} |+\rangle\langle ^1S_0, 0| \right. \\ & - \frac{\Omega_{1S_0,3P_1}}{4} C_{1S_0,3P_1}^{-1,0,-1} \sin(\alpha_{1S_0,3P_1}) e^{-i(-\varphi_{1S_0,3P_1} + \pi/2)} |-\rangle\langle ^1S_0, 0| \\ & + \frac{\Omega_{3P_{0(2)},3S_1}}{4} C_{3P_{0(2)},3S_1}^{-1,0(-2),\pm 1} \sin(\alpha_{3P_{0(2)},3S_1}) e^{-i(-\varphi_{3P_{0(2)},3S_1} + \pi/2)} |+\rangle\langle ^3P_{0(2)}, 0(-2)| \\ & \left. + \frac{\Omega_{3P_{0(2)},3S_1}}{4} C_{3P_{0(2)},3S_1}^{-1,0(-2),\pm 1} \sin(\alpha_{3P_{0(2)},3S_1}) e^{-i(-\varphi_{3P_{0(2)},3S_1} + \pi/2)} |-\rangle\langle ^3P_{0(2)}, 0(-2)| \right] \\ & + h.c. \end{aligned} \quad (5.8)$$

where $|\pm\rangle = (|^3S_1, -1\rangle \pm |^3P_1, -1\rangle)/\sqrt{2}$. Diagonalization of \hat{H}_{stirap} and simplification, using the Clebsch-Gordan coefficients and the laser polarization angles from Table 5.4, yields the dark state

$$|D\rangle = \frac{e^{i\varphi_{1S_0,3P_1}} \Omega_{1S_0,3P_1} |^3P_{0(2)}, 0(-2)\rangle - C_{3P_{0(2)},3S_1}^{-1,0(-2),\pm 1} \Omega_{3P_{0(2)},3S_1} |^1S_0, 0\rangle}{\Omega_{1S_0,3P_1}^2 + |C_{3P_{0(2)},3S_1}^{-1,0(-2),\pm 1} \Omega_{3P_{0(2)},3S_1}|^2}. \quad (5.9)$$

This result suggests that the full Hamiltonian 5.1 may also have a dark state that can be used to adiabatically transfer a degenerate gas to a metastable state.

I investigated the application of STIRAP to the bosonic AE level structure (Figure 5.2) via numerical simulation of the OBEs (Equation 5.5).¹ To produce STIRAP

¹Note that the full Hamiltonian of Equation 5.1 probably does not have a true dark state.

Table 5.4: The input parameters and results for the simulations in Figure 5.6. The final population in the target state, ρ_{stirap} , is reached after an evolution time, t_{stirap} . By varying $\Delta_{3P_{0(2)}}$ in the simulations, we can extract the full width at half maximum of the STIRAP resonance, γ_{stirap} (see Figure 5.7). I quote detunings in units of $\Omega_{3P_1,^3S_1}$. Note that the $\alpha_{\ell,\ell'}$ and the $\varphi_{\ell,\ell'}$ have the same values as given in Table 5.1.

	Sr, $ ^3P_2, \pm 2\rangle$	Sr, $ ^3P_0, 0\rangle$	Yb, $ ^3P_2, \pm 2\rangle$	Yb, $ ^3P_0, 0\rangle$
Δ_{3P_1}	$-0.009 \times \Omega_{3P_1,^3S_1}$	$-0.61 \times \Omega_{3P_1,^3S_1}$	$-0.097 \times \Omega_{3P_1,^3S_1}$	$-0.88 \times \Omega_{3P_1,^3S_1}$
Δ_{3S_1}	$-1.8 \times \Omega_{3P_1,^3S_1}$	$-7.1 \times \Omega_{3P_1,^3S_1}$	$-2.7 \times \Omega_{3P_1,^3S_1}$	$-1.4 \times \Omega_{3P_1,^3S_1}$
$\Delta_{3P_{0(2)}}$	0	0	0	0
$\frac{1}{2\pi}\Omega_{1S_0,^3P_1}$	0.75 MHz	1.25 MHz	1.5 MHz	2.0 MHz
$\frac{1}{2\pi}\Omega_{3P_1,^3S_1}$	110 MHz	160 MHz	130 MHz	160 MHz
$\frac{1}{2\pi}\Omega_{3P_{0(2)},^3S_1}$	7.0 MHz	4.5 MHz	6.0 MHz	3.5 MHz
$\frac{1}{2\pi}\Omega_B$	25 MHz	25 MHz	25 MHz	25 MHz
$\alpha_{1S_0,^3P_1}$	90°	90°	90°	90°
$\alpha_{3P_1,^3S_1}$	0°	0°	0°	0°
$\alpha_{3P_{0(2)},^3S_1}$	90°	90°	90°	90°
$\varphi_{1S_0,^3P_1}$	-60.9°	-59.6°	-53.8°	-51.5°
$\varphi_{3P_1,^3S_1}$	60.8°	59.5°	80.7°	73.3°
ρ_{stirap}	98.3%	94.4%	96.7%	91.6%
t_{stirap}	150 μs	150 μs	100 μs	100 μs
γ_{stirap}	9.2 kHz	60.2 kHz	13.9 kHz	14.4 kHz

dynamics, I made the replacement

$$\begin{aligned}
\Omega_{1S_0,^3P_1} &\rightarrow \frac{\Omega_{1S_0,^3P_1}}{2} (1 - \cos(\pi t/t_{\text{stirap}})) \\
\Omega_{3P_{0(2)},^3S_1} &\rightarrow \frac{\Omega_{3P_{0(2)},^3S_1}}{2} (1 + \cos(\pi t/t_{\text{stirap}}))
\end{aligned} \tag{5.10}$$

in Equation 5.1. For sufficiently long t_{stirap} , this replacement implements an adiabatic ramp of the Rabi frequencies that appear in $|D\rangle$. Once again, the objective is to find experimentally reasonable values for the Rabi frequencies and detunings that produce significant population transfer to the target metastable state. Iterative optimization of the metastable population at t_{stirap} by varying Δ_{3P_1} , Δ_{3S_1} , $\Omega_{1S_0,^3P_1}$, $\Omega_{3P_1,^3S_1}$, and $\Omega_{3P_{0(2)},^3S_1}$

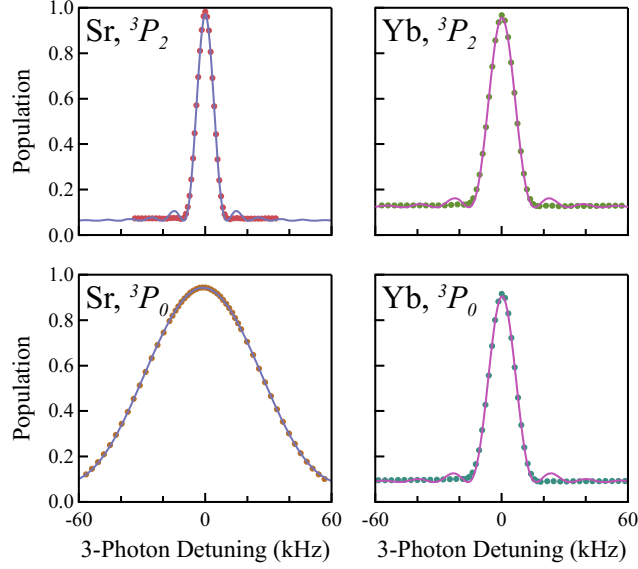


Figure 5.7: The excitation fraction of the target state, $|^3P_{2, \pm 2}\rangle$ ($|^3P_0, 0\rangle$), at t_{stirap} as a function of the three-photon detuning is shown in the top (bottom) row. The left column shows the results for Sr and the right column shows the results for Yb. Except for the three-photon detuning, which is varied, the parameters for the simulations are identical to those used in Figure 5.6 and reported in Table 5.4. The sinc^2 fits (solid lines) yield full widths at half maximum for the three-photon transitions to 3P_2 (3P_0) of 9.2 (60.2) kHz for Sr and of 13.9 (14.4) kHz for Yb. The amplitude mismatch between the wings of the fit and the simulation is likely caused by the convolution of power broadening and the transform limit.

converged to the parameter sets in Table 5.4 after ≈ 1000 runs. These parameter sets transfer $\gtrsim 90\%$ of the population to the target state and produce the dynamics shown in Figure 5.6. Note that the balanced one- and two-photon detunings suggested by analysis of the reduced STIRAP Hamiltonian (Equation 5.8) do not maximize adiabatic transfer under the full OBE evolution. The optimization algorithm does not vary t_{stirap} or Ω_B , but several hundred optimization runs at nearby values for these parameters did not improve the results.

The utility of the STIRAP protocol depends greatly on the spectral width of the STIRAP feature, since this width determines both the technical challenge of realizing the protocol and its sensitivity to realistic perturbations (such as those discussed in Section 5.1.4). There are two methods for extracting the three-photon transition linewidth: numerical estimation using the OBEs or direct computation of the electric susceptibility [257, 317]. The latter approach works best in steady state or in the limit of weak

excitation, neither of which apply here or in Section 5.1.3. In addition, analytical calculations of the susceptibility typically use a non-Hermitian Schrödinger equation technique since it is simpler than a full density matrix calculation [257]. The quantum jump probability,

$$P_{QJ} \simeq \frac{|\Omega_{\ell,\ell'}|^2}{\Delta_{\ell,\ell'}^2} \Gamma_{\ell} t, \quad (5.11)$$

with t the interrogation time, for our parameter sets is large enough to invalidate the non-Hermitian Schrödinger method (see Table 5.1 and Table 5.4). Directly solving the OBEs for the system would yield an expression for $\rho_{\{|^3P_1,-1\rangle,|^1S_0,0\rangle\}}$, which is proportional to the susceptibility [257, 317]. However, even in steady state, solving the OBEs (Equation 5.5) is nontrivial and, more importantly, the resulting analytical form for the susceptibility is likely to be so complicated that it obfuscates the essential physics. For these reasons, both here and in our publication, we prefer numerical methods to estimate the three-photon linewidth. The variation in the final target-state population, ρ_{stirap} , with the three-photon detuning is shown in Figure 5.7. The full width at half maximum of sinc^2 fits to these numerical results is an approximate linewidth, γ_{stirap} , for the STIRAP process (see Table 5.4). For Yb and $|^3P_2, \pm 2\rangle$ in Sr, the STIRAP linewidths are similar to the Rabi process linewidths reported in Section 5.1.3. Interestingly, the three-photon resonance for $|^3P_0, 0\rangle$ in Sr is substantially broader, suggesting that there may be parameter sets that achieve high transfer efficiencies with larger linewidths for the other target states as well. The narrow linewidth of the three-photon transition (or a doubly-forbidden transition) is the primary obstacle to realizing a metastable AE degenerate gas. A larger linewidth reduces sensitivity to many of the technical issues discussed in Section 5.1.4, so a search for these broader linewidth parameter sets should be a priority for anyone attempting to implement the three-photon transfer scheme.

Appendix A: Fermionic Absorption Cross Section

Resonant absorption imaging of ^{87}Sr on the 461-nm transition is complicated by the unresolved hyperfine structure of the 1P_1 state. The splitting between the $F = 11/2$ and $F = 7/2$ ($F = 9/2$) excited states is 43 MHz (−17 MHz). The absorption cross section for the fermionic isotope depends on both the spin state populations and the probe laser polarization. We can use a rate-equation model to compute the optical pumping dynamics during the probe pulse and extract the scattering cross section as a function of pulse duration. The essential pieces of this calculation were initially worked out at Rice University by P. Mickelson and are available in his Ph.D. thesis [181]. In this appendix, I discuss the implementation of the rate equation model for our experiment and our method for combining it with the image analysis techniques of Section 3.2.

A.1 Absorption for Bosonic Isotopes

Bosonic alkaline-earth atoms all have nuclear spin $I = 0$ and so possess no hyperfine structure. This makes conversion between the measured optical depth and the atomic column density straightforward. The absorption cross section for the bosons, including the effects of detuning and saturation, is

$$\sigma(s, \Delta) = \frac{3\lambda_{bl}^2}{2\pi} \frac{1}{1 + s + 4(\Delta/\Gamma_{bl})^2} = \frac{\sigma_{88}}{1 + s + 4(\Delta/\Gamma_{bl})^2}, \quad (\text{A.1})$$

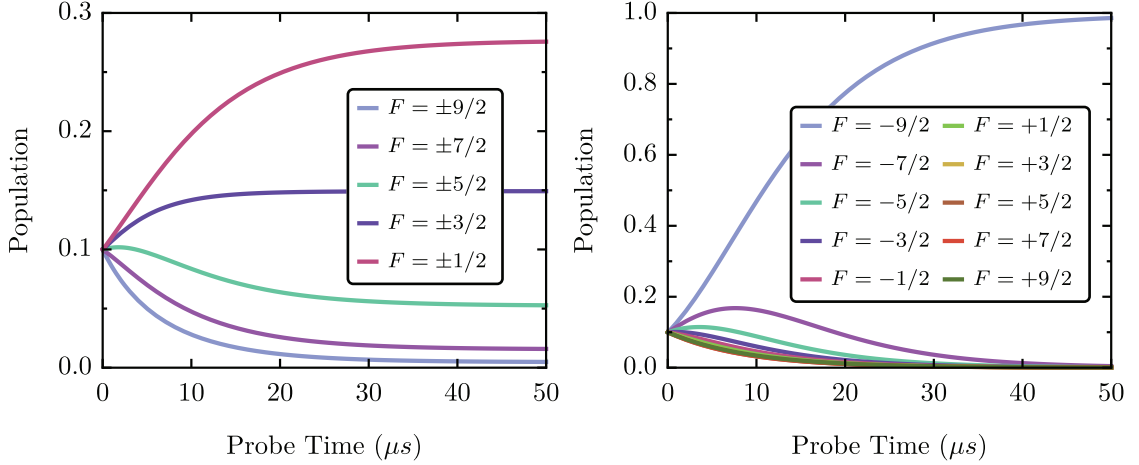


Figure A.1: Rate equation simulation (see Equation A.5) of optical pumping of fermionic samples during the absorption image at saturation parameter $s = 0.01$ for a linearly polarized probe (left) and a circularly polarized probe (right).

where Γ_{bl} is the linewidth, Δ the laser detuning, λ_{bl} is the wavelength, and $s = I/I_{sat}$ is the saturation parameter for the 461-nm transition.¹ The resonant, unsaturated bosonic scattering cross section is $\sigma_{88} = 3\lambda_{bl}^2/2\pi$. In principle, Equation A.1 should contain a Clebsch-Gordan factor, but for the $^1S_0 \rightarrow ^1P_1$ transition in the bosons all Clebsch-Gordan coefficients are identical and equal to 1. Therefore, the atomic column density is

$$\tilde{n}(x, y) = \frac{D_{rs}(x, y)}{\sigma_{88}} = D_m(x, y) \frac{1 + 4(\Delta/\Gamma_{bl})^2 + s(x, y)}{\sigma_{88}}, \quad (\text{A.2})$$

where $D_m(x, y)$ is the measured optical depth and $D_{rs}(x, y)$ is the resonant, unsaturated optical depth (see Section 3.2).

A.2 Relative Cross Section Calculation

The situation for the fermionic isotope is quite different. The 1P_1 state splits into three hyperfine manifolds and none of these manifolds are spectrally resolved. To calculate the absorption cross section accurately, we must take contributions to the photon scattering

¹Of course, with an appropriate change in parameters, Equation A.1 can also be applied to the $^1S_0 \rightarrow ^3P_1$ transition.

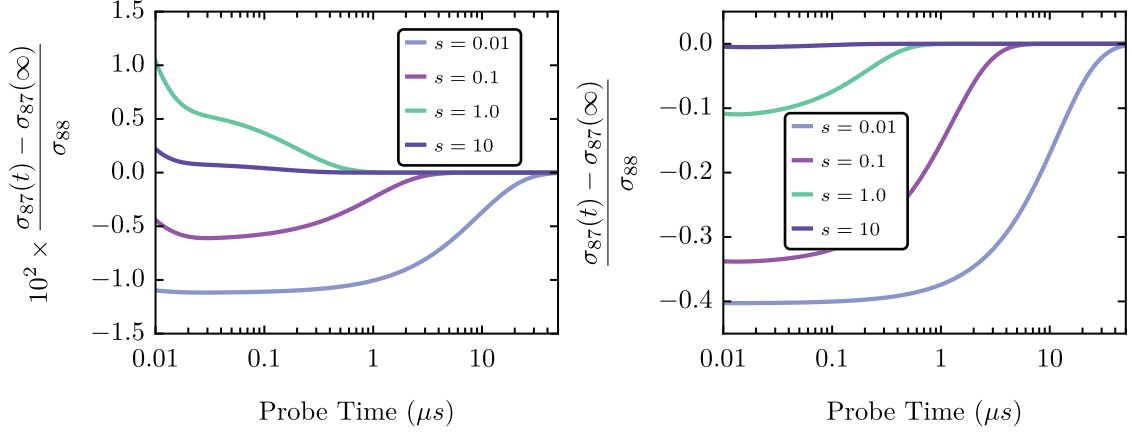


Figure A.2: The fermionic cross section as a function of integration time relative to its steady state value for a linearly polarized probe (left) and a circularly polarized probe (right).

rate from each of these levels into account. Because the size of our ultracold gases is much larger than the optical wavelength and the lifetime of the 1P_1 state ($\tau = 1/\Gamma_{bl} \simeq 5$ ns [62, 63]) is much shorter than the interrogation time (≈ 10 μ s), we are justified in using rate equations to model the optical pumping dynamics during the probe pulse. The model will return the population in each of the Zeeman sublevels of the relevant states and convert these populations into a scattering rate from which we can extract the absorption cross section.

The optical pumping dynamics are governed by laser driven excitation to the 1P_1 state and spontaneous decay that returns population to the ground state. The decay from the state $|e, F_e, m_{F_e}\rangle$ to the state $|g, F_g, m_{F_g}\rangle$, where g and e label the ground and excited states, respectively, is

$$\kappa_{|e, F_e, m_{F_e}\rangle \rightarrow |g, F_g, m_{F_g}; m_\gamma\rangle}^{decay} = \Gamma_{bl} \left| \langle F_g, m_{F_g}; 1, m_\gamma | F_e, m_{F_e} \rangle \right|^2. \quad (\text{A.3})$$

The branching from the excited state into the magnetic sublevels of $|g\rangle$ is governed by a Clebsch-Gordan coefficient, $\langle F_g, m_{F_g}; 1, m_\gamma | F_e, m_{F_e} \rangle$.² Excitation from $|F_g, m_{F_g}\rangle$ to

²There is no 6- J symbol because the ground state has no electronic spin, see [256].

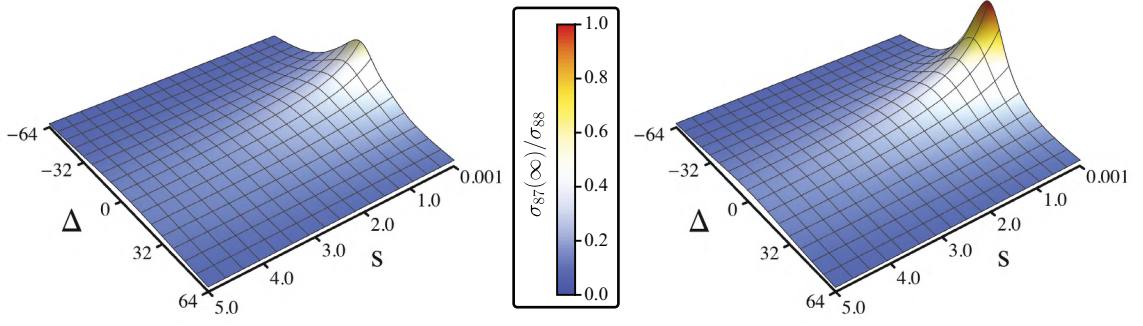


Figure A.3: The steady state fermionic cross section as a function of detuning and saturation for a linearly polarized probe (left) and a circularly polarized probe (right).

$|F_e, m_{F_e}\rangle$, including the effect of saturation and detuning, proceeds at a rate given by

$$\kappa_{|g, F_g, m_{F_g}; m_\gamma \rightarrow |e, F_e, m_{F_e}\rangle}^{exc} = \frac{s \Gamma_{bl} f(m_\gamma) |\langle F_g, m_{F_g}; 1, m_\gamma | F_e, m_{F_e} \rangle|^2}{1 + s + 4(\Delta/\Gamma_{bl})^2}, \quad (\text{A.4})$$

where $f(m_\gamma)$ is the fraction of the incident probe light with polarization projection m_γ . We represent the populations in each Zeeman state with $P_{|g, F_g, m_{F_g}\rangle}$ and $P_{|e, F_e, m_{F_e}\rangle}$. Using Equations A.3 and A.4, we can construct the rate equations for the singlet hyperfine structure of ^{87}Sr ,

$$\begin{aligned} \dot{P}_{|g, F_g, m_{F_g}\rangle} &= \sum_{m_\gamma=-1}^1 \left[-P_{|g, F_g, m_{F_g}\rangle} \left(\sum_{F_e=7/2}^{11/2} \kappa_{|g, F_g, m_{F_g}; m_\gamma \rightarrow |e, F_e, m_{F_g}+m_\gamma\rangle}^{exc} \right) \right. \\ &\quad \left. + \left(\sum_{F_e=7/2}^{11/2} P_{|e, F_e, m_{F_g}+m_\gamma\rangle} \kappa_{|e, F_e, m_{F_g}+m_\gamma\rangle \rightarrow |g, F_g, m_{F_g}; m_\gamma\rangle}^{decay} \right) \right], \\ \dot{P}_{|e, F_e, m_{F_e}\rangle} &= -P_{|e, F_e, m_{F_e}\rangle} \Gamma_{bl} + \sum_{m_\gamma=-1}^1 \left(P_{|g, F_g, m_{F_e}-m_\gamma\rangle} \kappa_{|g, F_g, m_{F_e}-m_\gamma; m_\gamma \rightarrow |e, F_e, m_{F_e}\rangle}^{exc} \right). \end{aligned} \quad (\text{A.5})$$

We numerically solve the rate equations A.5 to see the optical pumping dynamics as a function of probe polarization and saturation. The results of these simulations for a balanced initial spin distribution are shown in Figure A.1. We can use the spin-state populations and the probe-beam parameters to construct an effective cross section. The

power per unit volume scattered out of the probe beam by the atoms is

$$\frac{dI}{dz} = -\hbar\omega \sum_{F_e, m_{F_g}, m_\gamma} (\kappa_{|g, F_g, m_{F_g}; m_\gamma \rangle \rightarrow |e, F_e, m_{F_g} + m_\gamma \rangle}^{exc} n_{m_{F_g}}) = -\sigma_{87}(t)nI, \quad (\text{A.6})$$

where I is the probe intensity, ω is the probe frequency, $n = \sum_{m_{F_g}} n_{m_{F_g}}$, and $n_{m_{F_g}}$ is the density in $|g, F_g, m_{F_g}\rangle$ [50]. From Equation A.6, we can find the fermionic cross section relative to the resonant, unsaturated bosonic cross section,

$$\frac{\sigma_{87}(t)}{\sigma_{88}} = \frac{2}{s\Gamma_{bl}} \sum_{F_e, m_{F_g}, m_\gamma} (\kappa_{|g, F_g, m_{F_g}; m_\gamma \rangle \rightarrow |e, F_e, m_{F_g} + m_\gamma \rangle}^{exc} P_{|g, F_g, m_{F_g}\rangle}). \quad (\text{A.7})$$

In Figure A.2, we compare the fermionic cross section to its steady-state value, assuming an initially unpolarized distribution. The cross section rapidly converges to the steady state for the polarizations and saturation parameters that we use in the experiment. The horizontal probe beam is π -polarized with $s \simeq 0.01$ and the vertical probe beam is σ^- -polarized with $s \simeq 1$. Both imaging systems typically use a 10- μ s integration time. We created lookup tables for the steady state relative cross section, $\sigma_{87}(\infty)/\sigma_{88}$, as a function of s and Δ (Figure A.3). Because the integration time is long compared to the cross section equilibration time for our unpolarized ^{87}Sr samples, the ^{87}Sr column density is

$$\tilde{n}_{87}(x, y) = \frac{D_{rs}(x, y)}{\sigma_{88}} = \frac{D_m(x, y)}{[\frac{\sigma_{87}(\infty)}{\sigma_{88}}(x, y)] \sigma_{88}}. \quad (\text{A.8})$$

We checked the validity of the steady-state approximation of Equation A.8 by adjusting the number of initially populated spin states in the rate equation model. The simulations show that, for a π -polarized probe, the cross section depends only weakly on the spin state (Figure A.4). A σ^- -polarized probe causes much larger spin mixture dependent variations in the cross section at low saturation (Figure A.4), but the effect is reduced to negligible levels at higher saturation (e.g. Figure A.2). Although the simulation data are not shown, we also ran simulations for a $(\sigma^+ + \sigma^-)$ -polarized probe. The dynamics

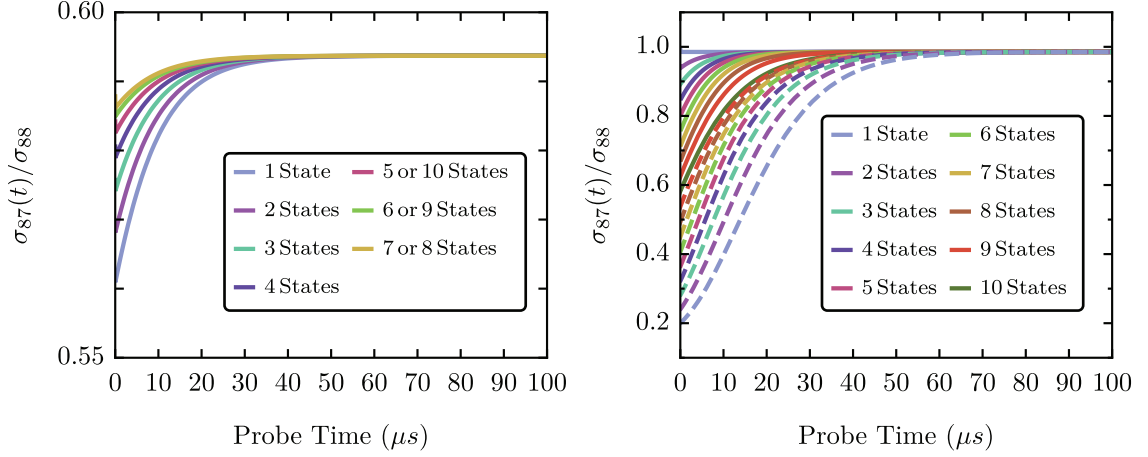


Figure A.4: The fermionic cross section as a function of integration time and number of populated spin states at saturation parameter $s = 0.01$ for a linearly polarized probe (left) and a circularly polarized probe (right). In the right hand graph, solid lines indicate nearly "stretched" spin distributions and dashed lines indicated nearly "anti-stretched" spin distributions. For both plots, spin distributions are an even mixture of the number of Zeeman states specified in the legend.

were nearly identical to those for π -polarized light and $\sigma_{87}(t)$ differed by $\lesssim 1\%$ from the π -polarized value.

We also used the OBEs for the ^{87}Sr hyperfine structure,

$$\frac{d}{dt} \hat{\rho} = -i [\hat{H}, \hat{\rho}] + \sum_{F_e=7/2}^{11/2} \sum_{m_{F_e}=-F_e}^{F_e} \sum_{m_{F_g}=-F_g}^{F_g} \hat{\mathcal{L}}_{F_e, m_{F_e}, m_{F_g}}, \quad (\text{A.9})$$

to confirm that the rate equations produce the correct optical pumping dynamics and cross section. After taking the rotating-wave approximation, the Hamiltonian of the system in a co-rotating frame is [256]

$$\begin{aligned} \hat{H} = & \sum_{F_e=7/2}^{11/2} \sum_{m_{F_e}=-F_e}^{F_e} \sum_{m_{F_g}=-F_g}^{F_g} \left[(-\Delta - \Delta_{9/2} \delta_{F_e}^{9/2} - \Delta_{7/2} \delta_{F_e}^{7/2}) |e, F_e, m_{F_e}\rangle \langle e, F_e, m_{F_e}| \right. \\ & \left. + \sum_{m_\gamma=-1}^1 \left(\frac{\Omega}{2} \langle F_e, m_{F_e} | F_g, m_{F_g}; 1, m_\gamma \rangle |e, F_e, m_{F_e}\rangle \langle g, F_g, m_{F_g}| + h.c. \right) \right], \end{aligned} \quad (\text{A.10})$$

where $\Omega = \Gamma_{bl} \sqrt{s/2}$ and δ_a^b is the Kronecker delta. The hyperfine splittings are $\Delta_{9/2}/2\pi =$

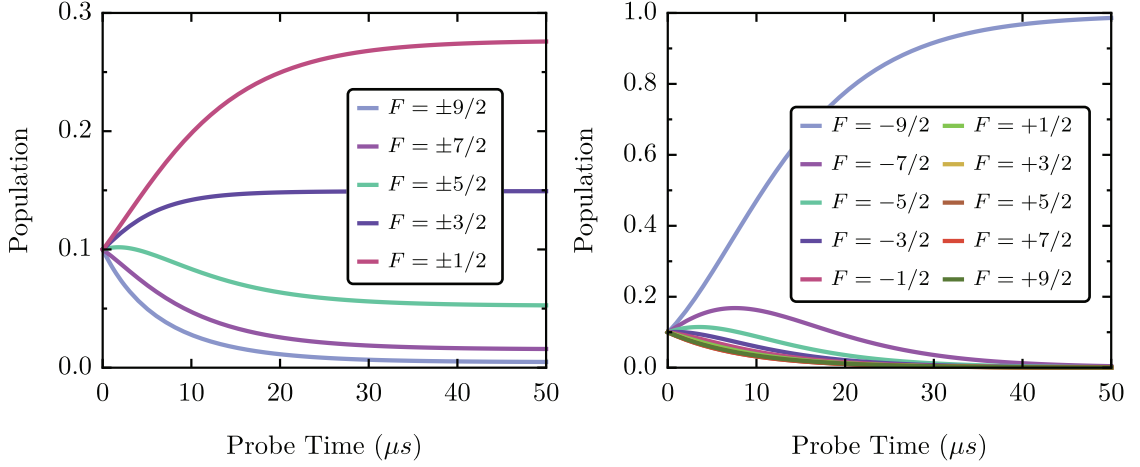


Figure A.5: OBE simulation (see Equation A.5) of optical pumping of fermionic samples during the absorption image at saturation parameter $s = 0.01$ for a linearly polarized probe (left) and a circularly polarized probe (right).

-17 MHz and $\Delta_{7/2}/2\pi = 43$ MHz. The Liouville operator is

$$\begin{aligned} \hat{\mathcal{L}}_{F_e, m_{F_e}, m_{F_g}} = \\ \frac{\Gamma_{bl}}{2} \sum_{m_\gamma=-1}^1 [(\hat{\xi}_{m_\gamma, F_e, m_{F_e}, m_{F_g}} \hat{\rho} \hat{\xi}_{m_\gamma, F_e, m_{F_e}, m_{F_g}}^\dagger - \hat{\xi}_{m_\gamma, F_e, m_{F_e}, m_{F_g}}^\dagger \hat{\xi}_{m_\gamma, F_e, m_{F_e}, m_{F_g}} \hat{\rho}) + h.c.], \end{aligned} \quad (\text{A.11})$$

where we define

$$\hat{\xi}_{m_\gamma, F_e, m_{F_e}, m_{F_g}} = \sum_{m_{F_e}, m_{F_g}} \langle F_g, m_{F_g}; 1, m_\gamma | F_e, m_{F_e} \rangle |g, F_g, m_{F_g}\rangle \langle e, F_e, m_{F_e}|. \quad (\text{A.12})$$

Numerical integration of the OBEs with a Rabi frequency corresponding to $s = 0.01$ produces the optical pumping dynamics of Figure A.5, which are qualitatively indistinguishable from the rate equation dynamics in Figure A.1. In the OBE formalism, the

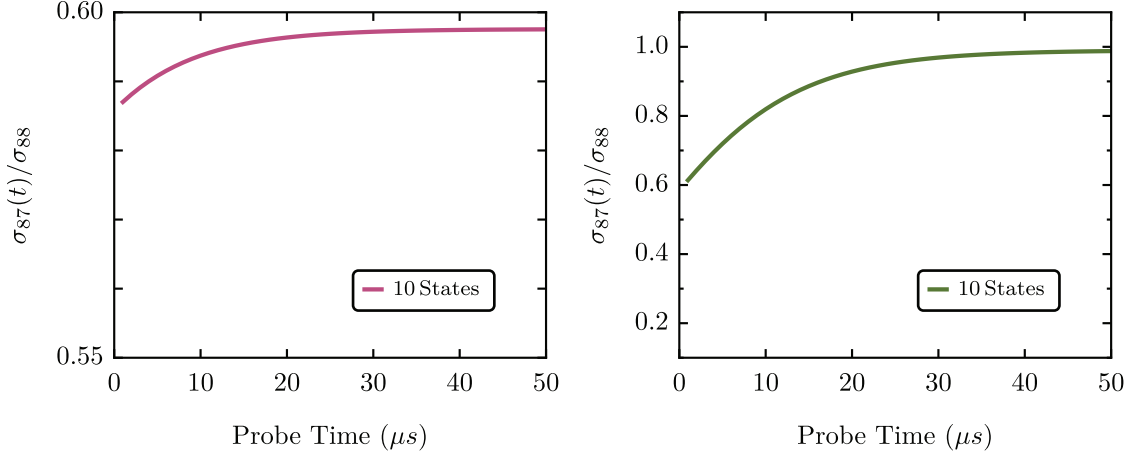


Figure A.6: The fermionic cross section extracted using the OBEs as a function of integration time at saturation parameter $s = 0.01$ for a linearly polarized probe (left) and a circularly polarized probe (right). For both plots, spin distributions are an even mixture of the number of Zeeman states specified in the legend.

power scattered per unit volume is given by [318]

$$\begin{aligned} \frac{dI}{dz} &= -\hbar\omega n \sum_{F_e, m_{F_g}, m_\gamma} \left(\Omega \langle F_g, m_{F_g}; 1, m_\gamma | F_e, m_{F_e} \rangle \text{Im}(\rho_{|g, F_g, m_{F_g}\rangle, |e, F_e, m_{F_e}\rangle}) \right) \\ &= -\sigma_{87}(t) n I, \end{aligned} \quad (\text{A.13})$$

where $\text{Im}(\rho_{|g, F_g, m_{F_g}\rangle, |e, F_e, m_{F_e}\rangle})$ denotes the imaginary piece of $\rho_{|g, F_g, m_{F_g}\rangle, |e, F_e, m_{F_e}\rangle}$. The relative fermionic cross section is then

$$\frac{\sigma_{87}(t)}{\sigma_{88}} = \frac{2}{s\Gamma_{bl}} \sum_{F_e, m_{F_g}, m_\gamma} \left(\Omega \langle F_g, m_{F_g}; 1, m_\gamma | F_e, m_{F_e} \rangle \text{Im}(\rho_{|g, F_g, m_{F_g}\rangle, |e, F_e, m_{F_e}\rangle}) \right). \quad (\text{A.14})$$

Figure A.6 shows the relative cross section calculated by inserting the OBE numerical integration results into Equation A.14. The cross section derived from the OBEs differs from the steady state rate equation cross section by $< 1\%$. This difference is less than the systematic atom number uncertainty for the bosons and the shot-to-shot atom number fluctuations. As such, the lookup tables in Figure A.3 can safely be used to compute the ^{87}Sr atom number.

Bibliography

- [1] William D. Phillips and Harold Metcalf. Laser deceleration of an atomic beam. *Physical Review Letters*, 48(9):596, 1982.
- [2] Steven Chu, L. Hollberg, J. E. Bjorkholm, Alex Cable, and A. Ashkin. Three-Dimensional Viscous Confinement and Cooling of Atoms by Resonance Radiation Pressure. *Physical Review Letters*, 55(1):48, 1985.
- [3] Alan L. Migdall, John V. Prodan, William D. Phillips, Thomas H. Bergeman, and Harold J. Metcalf. First observation of magnetically trapped neutral atoms. *Physical Review Letters*, 54(24):2596, 1985.
- [4] Steven Chu, J. E. Bjorkholm, A. Ashkin, and A. Cable. Experimental Observation of Optically Trapped Atoms. *Physical Review Letters*, 57(3):314, 1986.
- [5] E. L. Raab, M. Prentiss, Alex Cable, Steven Chu, and D. E. Pritchard. Trapping of Neutral Sodium Atoms with Radiation Pressure. *Physical Review Letters*, 59(23):2631, 1987.
- [6] V. S. Bagnato, G. P. Lafyatis, A. G. Martin, E. L. Raab, R. N. Ahmad-Bitar, and D. E. Pritchard. Continuous Stopping and Trapping of Neutral Atoms. *Physical Review Letters*, 58(21):2194, 1987.
- [7] Matthew P. A. Fisher, Peter B. Weichman, G. Grinstein, and Daniel S. Fisher. Boson localization and the superfluid-insulator transition. *Physical Review B*, 40(1):546, 1989.
- [8] S. A. Diddams, J. C. Bergquist, S. R. Jefferts, and C. W. Oates. Standards of Time and Frequency at the Outset of the 21st Century. *Science*, 306:1318, 2004.
- [9] Immanuel Bloch, Jean Dalibard, and Wilhelm Zwerger. Many-body physics with ultracold gases. *Reviews of Modern Physics*, 80(3):885, 2008.
- [10] Alexander D. Cronin, Jörg Schmiedmayer, and David E. Pritchard. Optics and interferometry with atoms and molecules. *Reviews of Modern Physics*, 81(3):1051, 2009.

- [11] Cheng Chin, Rudolf Grimm, Paul Julienne, and Eite Tiesinga. Feshbach resonances in ultracold gases. *Reviews of Modern Physics*, 82(2):1225, 2010.
- [12] M. Saffman, T. G. Walker, and K. Mølmer. Quantum information with Rydberg atoms. *Reviews of Modern Physics*, 82(3):2313, 2010.
- [13] Michael A. Nielsen and Isaac L. Chuang. *Quantum Computation and Quantum Information: 10th Anniversary Edition*. Cambridge University Press, 2011.
- [14] I. M. Georgescu, S. Ashhab, and Franco Nori. Quantum simulation. *Reviews of Modern Physics*, 86(1):153, 2014.
- [15] M. H. Anderson, J. R. Ensher, M. R. Matthews, C. E. Wieman, and E. A. Cornell. Observation of Bose-Einstein Condensation in a Dilute Atomic Vapor. *Science*, 269:198, 1995.
- [16] K. B. Davis, M.-O. Mewes, M. R. Andrews, N. J. van Druten, D. S. Durfee, and D. M. Kurn. Bose-Einstein Condensation in a Gas of Sodium Atoms. *Physical Review Letters*, 75(22):3969, 1995.
- [17] C. C. Bradley, C. A. Sackett, and R. G. Hulet. Bose-Einstein Condensation of Lithium: Observation of Limited Condensate Number. *Physical Review Letters*, 78(6):985, 1997.
- [18] B. DeMarco and D.S. Jin. Onset of Fermi Degeneracy in a Trapped Atomic Gas. *Science*, 285:1703, 1999.
- [19] Andrew G. Truscott, Kevin E. Strecker, William I. McAlexander, Guthrie B. Partridge, and Randall G. Hulet. Observation of Fermi Pressure in a Gas of Trapped Atoms. *Science*, 291:2570, 2001.
- [20] F. Schreck, L. Khaykovich, K. L. Corwin, G. Ferrari, T. Bourdel, J. Cubizolles, and C. Salomon. Quasipure Bose-Einstein Condensate Immersed in a Fermi Sea. *Physical Review Letters*, 87(8):080403, 2001.
- [21] S. R. Granade, M. E. Gehm, K. M. O’Hara, and J. E. Thomas. All-Optical Production of a Degenerate Fermi Gas. *Physical Review Letters*, 88(12):120405, 2002.
- [22] A. Görlitz, J. M. Vogels, A. E. Leanhardt, C. Raman, T. L. Gustavson, J. R. Abo-Shaeer, A. P. Chikkatur, S. Gupta, S. Inouye, T. Rosenband, and W. Ketterle. Realization of Bose-Einstein Condensates in Lower Dimensions. *Physical Review Letters*, 87(13):130402, 2001.
- [23] Markus Greiner, Olaf Mandel, Tilman Esslinger, Theodor W. Hänsch, and Immanuel Bloch. Quantum phase transition from a superfluid to a Mott insulator in a gas of ultracold atoms. *Nature*, 415:39, 2002.
- [24] B. Paredes, A. Widera, V. Murg, O. Mandel, S. Fölling, I. Cirac, G. V. Shlyapnikov, T. W. Hänsch, and I. Bloch. Tonks-Girardeau gas of ultracold atoms in an optical lattice. *Nature*, 429:277, 2004.

- [25] Gregor Thalhammer, Matthias Theis, Klaus Winkler, Rudolf Grimm, and Johannes Hecker Denschlag. Inducing an optical Feshbach resonance via stimulated Raman coupling. *Physical Review A*, 71(3):033403, 2005.
- [26] Zoran Hadzibabic, Peter Krüger, Marc Cheneau, Baptiste Battelier, and Jean Dalibard. Berezinskii-Kosterlitz-Thouless crossover in a trapped atomic gas. *Nature*, 441:1118, 2006.
- [27] Mi Yan, B. J. Desalvo, B. Ramachandhran, H. Pu, and T. C. Killian. Controlling Condensate Collapse and Expansion with an Optical Feshbach Resonance. *Physical Review Letters*, 110(12):123201, 2013.
- [28] T. Kurosu and F. Shimizu. Laser Cooling and Trapping of Calcium and Strontium. *Japanese Journal of Applied Physics*, 29(11):L 2127, 1990.
- [29] Th. Kisters, K. Zeiske, F. Riehle, and J. Helmcke. High-resolution spectroscopy with laser-cooled and trapped calcium atoms. *Applied Physics B*, 59:89, 1994.
- [30] Kurt R. Vogel, Tim P. Dinneen, Alan C. Gallagher, and John L. Hall. Experiments with strontium in a vapor cell magneto-optic trap. In Bryan L. Fearey, editor, *Methods for Ultrasensitive Detection*. SPIE-Intl Soc Optical Eng, May 1998.
- [31] T. P. Dinneen, K. R. Vogel, E. Arimondo, J. L. Hall, and A. Gallagher. Cold collisions of Sr^* -Sr in a magneto-optical trap. *Physical Review A*, 59(2):1216, 1999.
- [32] K. Honda, Y. Takahashi, T. Kuwamoto, M. Fujimoto, K. Toyoda, K. Ishikawa, and T. Yabuzaki. Magneto-optical trapping of Yb atoms and a limit on the branching ratio of the 1P_1 state. *Physical Review A*, 59(2):R934, 1999.
- [33] Hidetoshi Katori, Tetsuya Ido, Yoshitomo Isoya, and Makoto Kuwata-Gonokami. Magneto-Optical Trapping and Cooling of Strontium Atoms down to the Photon Recoil Temperature. *Physical Review Letters*, 82(6):1116, 1999.
- [34] T. Kuwamoto, K. Honda, Y. Takahashi, and T. Yabuzaki. Magneto-optical trapping of Yb atoms using an intercombination transition. *Physical Review A*, 60(2):R745, 1999.
- [35] T. Binnewies, G. Wilpers, U. Sterr, F. Riehle, J. Helmcke, T. E. Mehlstäubler, E. M. Rasel, and W. Ertmer. Doppler Cooling and Trapping on Forbidden Transitions. *Physical Review Letters*, 87(12):123002, 2001.
- [36] Takashi Mukaiyama, Hidetoshi Katori, Tetsuya Ido, Ying Li, and Makoto Kuwata-Gonokami. Recoil-Limited Laser Cooling of ^{87}Sr Atoms near the Fermi Temperature. *Physical Review Letters*, 90(11):113002, 2003.
- [37] R. Maruyama, R. H. Wynar, M. V. Romalis, A. Andalkar, M. D. Swallows, C. E. Pearson, and E. N. Fortson. Investigation of sub-Doppler cooling in an ytterbium magneto-optical trap. *Physical Review A*, 68:011403(R), 2003.

- [38] E. Anne Curtis, Christopher W. Oates, and Leo Hollberg. Quenched narrow-line second- and third-stage laser cooling of ^{40}Ca . *Journal of the Optical Society of America B*, 20(5):977, 2003.
- [39] Hidetoshi Katori, Masao Takamoto, V. G. Pal'chikov, and V. D. Ovsiannikov. Ultrastable Optical Clock with Neutral Atoms in an Engineered Light Shift Trap. *Physical Review Letters*, 91(17):173005, 2003.
- [40] Tetsuya Ido and Hidetoshi Katori. Recoil-Free Spectroscopy of Neutral Sr Atoms in the Lamb-Dicke Regime. *Physical Review Letters*, 91(5):053001, 2003.
- [41] Masao Takamoto and Hidetoshi Katori. Spectroscopy of the 1S_0 - 3P_1 Clock Transition of ^{87}Sr in an Optical Lattice. *Physical Review Letters*, 91(22):223001, 2003.
- [42] S. R. Jefferts, J. Shirley, T. E. Parker, T. P. Heavner, D. M. Meekhof, C. Nelson, F. Levi, G. Costanzo, A. De Marchi, R. Drullinger, L. Hollberg, W. D. Lee, and F. L. Walls. Accuracy evaluation of NIST-F1. *Metrologia*, 39:321, 2003.
- [43] Uwe Sterr, C. Degenhardt, H. Stoeck, Ch. Lisdat, H. Schnatz, J. Helmcke, F. Riehle, G. Wilpers, Ch. Oates, and L. Hollberg. The optical calcium frequency standards of PTB and NIST. *Comptes Rendus Physique*, 5:845, 2004.
- [44] C. W. Hoyt, Z. W. Barber, C. W. Oates, T. M. Fortier, S. A. Diddams, and L. Hollberg. Observation and Absolute Frequency Measurements of the 1S_0 - 3P_0 Optical Clock Transition in Neutral Ytterbium. *Physical Review Letters*, 95(8):083003, 2005.
- [45] S. Bize, P. Laurent, M. Abgrall, H. Marion, I. Maksimovic, L. Cacciapuoti, J. Grunert, C. Vian, F. Pereira dos Santos, P. Rosenbusch, P. Lemonde, G. Santarelli, P. Wolf, A. Clairon, A. Luiten, M. Tobar, and C. Salomon. Cold atom clocks and applications. *Journal of Physics B: Atomic, Molecular and Optical Physics*, 38:S449, 2005.
- [46] T. P. Heavner, S. R. Jefferts, E. A. Donley, J. H. Shirley, and T. E. Parker. NIST-F1: recent improvements and accuracy evaluations. *Metrologia*, 42:411, 2005.
- [47] Thomas P. Heavner, Elizabeth A. Donley, Filippo Levi, Giovanni Costanzo, Thomas E. Parker, Jon H. Shirley, Neil Ashby, Stephan Barlow, and S. R. Jefferts. First accuracy evaluation of NIST-F2. *Metrologia*, 51(3):174, 2014.
- [48] C.J. Foot. *Atomic Physics*. Oxford University Press Inc., New York, 2005.
- [49] J. J. Sakurai and Jim J. Napolitano. *Modern Quantum Mechanics (2nd Edition)*. Pearson, 2010.
- [50] Harold J. Metcalf and Peter van der Straten. *Laser Cooling and Trapping*. Springer New York, 1999.

- [51] A. V. Taichenachev, V. I. Yudin, C. W. Oates, C. W. Hoyt, Z. W. Barber, and L. Hollberg. Magnetic Field-Induced Spectroscopy of Forbidden Optical Transitions with Application to Lattice-Based Optical Atomic Clocks. *Physical Review Letters*, 96(8):083001, 2006.
- [52] Z. W. Barber, C. W. Hoyt, C. W. Oates, L. Hollberg, A. V. Taichenachev, and V. I. Yudin. Direct Excitation of the Forbidden Clock Transition in Neutral ^{174}Yb Atoms Confined to an Optical Lattice. *Physical Review Letters*, 96(8):083002, 2006.
- [53] Martin M. Boyd. *High Precision Spectroscopy of Strontium in an Optical Lattice: Towards a New Standard for Frequency and Time*. PhD thesis, University of Colorado, Boulder, 2007.
- [54] M. M. Boyd, T. Zelevinsky, A. D. Ludlow, S. Blatt, T. Zanon-Willette, S. M. Foreman, and J. Ye. Nuclear spin effects in optical lattice clocks. *Physical Review A*, 76(2):022510, 2007.
- [55] A. Yamaguchi, S. Uetake, S. Kato, H. Ito, and Y. Takahashi. High-resolution laser spectroscopy of a Bose-Einstein condensate using the ultranarrow magnetic quadrupole transition. *New Journal of Physics*, 12:103001, 2010.
- [56] N. Hinkley, J. A. Sherman, N. B. Phillips, M. Schioppo, N. D. Lemke, K. Beloy, M. Pizzocaro, C. W. Oates, and A. D. Ludlow. An Atomic Clock with 10^{-18} Instability. *Science*, 341:1215, 2013.
- [57] B. J. Bloom, T. L. Nicholson, J. R. Williams, S. L. Campbell, M. Bishof, X. Zhang, W. Zhang, S. L. Bromley, and J. Ye. An optical lattice clock with accuracy and stability at the 10^{-18} level. *Nature*, 506:71, 2014.
- [58] T. L. Nicholson, S. L. Campbell, R. B. Hutson, G. E. Marti, B. J. Bloom, R. L. McNally, W. Zhang, M. D. Barrett, M. S. Safronova, G. F. Strouse, W. L. Tew, and J. Ye. Systematic evaluation of an atomic clock at 2×10^{-18} total uncertainty. *Nature Communications*, 6:6896, 2015.
- [59] Piotr Morzynski, Marcin Bober, Dobrosława Bartoszek-Bober, Jerzy Nawrocki, Przemysław Krehlik, Łukasz Sliwczynski, Marcin Lipinski, Piotr Masłowski, Agata Cygan, Piotr Dunst, Michał Garus, Daniel Lisak, Jerzy Zachorowski, Wojciech Gawlik, Czesław Radzewicz, Roman Ciuryło, and Michał Zawada. Absolute measurement of the $^1S_0 - ^3P_0$ clock transition in neutral ^{88}Sr over the 330 km-long stabilized fibre optic link. *Scientific Reports*, 5:17495, 2015.
- [60] Charles W. Bauschlicher Jr, Stephen R. Langhoff, and Harry Partridge. The radiative lifetime of the 1D_2 state of Ca and Sr: a core-valence treatment. *Journal of Physics B: Atomic, Molecular and Optical Physics*, 18:1523, 1985.
- [61] L. R. Hunter, W. A. Walker, and D. S. Weiss. Observation of an Atomic Stark-Electric-Quadrupole Interference. *Physical Review Letters*, 56(8):823, 1986.

- [62] S. B. Nagel, P. G. Mickelson, A. D. Saenz, Y. N. Martinez, Y. C. Chen, T. C. Killian, P. Pellegrini, and R. Côté. Photoassociative Spectroscopy at Long Range in Ultracold Strontium. *Physical Review Letters*, 94(8):083004, 2005.
- [63] Masami Yasuda, Tetsuo Kishimoto, Masao Takamoto, and Hidetoshi Katori. Photoassociation spectroscopy of Sr^{88} : Reconstruction of the wave function near the last node. *Physical Review A*, 73(1):011403(R), 2006.
- [64] J. E. Sansonetti and G. Nave. Wavelengths, Transition Probabilities, and Energy Levels for the Spectrum of Neutral Strontium (Sr I). *Journal of Physical and Chemical Reference Data*, 39(3):033103, 2010.
- [65] Simon Stellmer, Benjamin Pasquiou, Rudolf Grimm, and Florian Schreck. Laser cooling to quantum degeneracy. *Physical Review Letters*, 110(26):263003, 2013.
- [66] K. Enomoto, K. Kasa, M. Kitagawa, and Y. Takahashi. Optical Feshbach Resonance Using the Intercombination Transition. *Physical Review Letters*, 101(20):203201, 2008.
- [67] R. Yamazaki, S. Taie, S. Sugawa, and Y. Takahashi. Submicron Spatial Modulation of an Interatomic Interaction in a Bose-Einstein Condensate. *Physical Review Letters*, 105(5):050405, 2010.
- [68] Rekishu Yamazaki, Shintaro Taie, Seiji Sugawa, Katsunari Enomoto, and Yoshiro Takahashi. Observation of a p-wave optical Feshbach resonance. *Physical Review A*, 87(1):010704, 2013.
- [69] M. Mancini, G. Pagano, G. Cappellini, L. Livi, M. Rider, J. Catani, C. Sias, P. Zoller, M. Inguscio, M. Dalmonte, and L. Fallani. Observation of chiral edge states with neutral fermions in synthetic Hall ribbons. *Science*, 349(6255):1510, 2015.
- [70] G. Reinaudi, C. B. Osborn, M. McDonald, S. Kotochigova, and T. Zelevinsky. Optical Production of Stable Ultracold $^{88}\text{Sr}_2$ Molecules. *Physical Review Letters*, 109(11):115303, 2012.
- [71] Simon Stellmer, Benjamin Pasquiou, Rudolf Grimm, and Florian Schreck. Creation of Ultracold Sr_2 Molecules in the Electronic Ground State. *Physical Review Letters*, 109(11):115302, 2012.
- [72] M. Yan, B. J. Desalvo, Y. Huang, P. Naidon, and T. C. Killian. Rabi Oscillations between Atomic and Molecular Condensates Driven with Coherent One-Color Photoassociation. *Physical Review Letters*, 111(15):150402, 2013.
- [73] Shintaro Taie, Shunsuke Watanabe, Tomohiro Ichinose, and Yoshiro Takahashi. Feshbach-Resonance-Enhanced Coherent Atom-Molecule Conversion with Ultranarrow Photoassociation Resonance. *Physical Review Letters*, 116(4):043202, 2016.

- [74] B. J. Desalvo, J. A. Aman, F. B. Dunning, T. C. Killian, H. R. Sadeghpour, S. Yoshida, and J. Burgdörfer. Ultra-long-range Rydberg molecules in a divalent atomic system. *Physical Review A*, 92(3):031403(R), 2015.
- [75] B. J. DeSalvo, J. A. Aman, C. Gaul, T. Pohl, S. Yoshida, J. Burgdörfer, K. R. A. Hazzard, F. B. Dunning, and T. C. Killian. Rydberg-blockade effects in Autler-Townes spectra of ultracold strontium. *Physical Review A*, 93(2):022709, 2016.
- [76] F. Camargo, J. D. Whalen, R. Ding, H. R. Sadeghpour, S. Yoshida, J. Burgdörfer, F. B. Dunning, and T. C. Killian. Lifetimes of ultra-long-range strontium Rydberg molecules. *Physical Review A*, 93(2):022702, 2016.
- [77] G. Cappellini, M. Mancini, G. Pagano, P. Lombardi, L. Livì, M. Siciliani de Cumis, P. Cancio, M. Pizzocaro, D. Calonico, F. Levi, C. Sias, J. Catani, M. Inguscio, and L. Fallani. Direct Observation of Coherent Interorbital Spin-Exchange Dynamics. *Physical Review Letters*, 113(12):120402, 2014.
- [78] F. Scazza, C. Hofrichter, M. Höfer, P. C. De Groot, I. Bloch, and S. Fölling. Observation of two-orbital spin-exchange interactions with ultracold SU(N)-symmetric fermions. *Nature Physics*, 10:779, 2014.
- [79] D. Jaksch, H.-J. Briegel, J. I. Cirac, C. W. Gardiner, and P. Zoller. Entanglement of Atoms via Cold Controlled Collisions. *Physical Review Letters*, 82(9):1975, 1999.
- [80] Andrew J. Daley, Martin M. Boyd, Jun Ye, and Peter Zoller. Quantum Computing with Alkaline-Earth-Metal Atoms. *Physical Review Letters*, 101(17):170504, 2008.
- [81] A. V. Gorshkov, A. M. Rey, A. J. Daley, M. M. Boyd, J. Ye, P. Zoller, and M. D. Lukin. Alkaline-Earth-Metal Atoms as Few-Qubit Quantum Registers. *Physical Review Letters*, 102(11):110503, 2009.
- [82] A. Dareau, M. Scholl, Q. Beaufils, D. Doring, J. Beugnon, and F. Gerbier. Doppler spectroscopy of an ytterbium Bose-Einstein condensate on the clock transition. *Physical Review A*, 91(2):023626, 2015.
- [83] M. Yamashita, S. Kato, A. Yamaguchi, S. Sugawa, T. Fukuhara, S. Uetake, and Y. Takahashi. Strongly interacting array of Bose-Einstein condensates trapped in a one-dimensional optical lattice. *Physical Review A*, 87(4):041604(R), 2013.
- [84] K. Shibata, R. Yamamoto, Y. Seki, and Y. Takahashi. Optical spectral imaging of a single layer of a quantum gas with an ultranarrow optical transition. *Physical Review A*, 89(3):031601(R), 2014.
- [85] S. Kato, K. Inaba, S. Sugawa, K. Shibata, R. Yamamoto, M. Yamashita, and Y. Takahashi. Laser spectroscopic probing of coexisting superfluid and insulating states of an atomic Bose-Hubbard system. *Nature Communications*, 7:11341, 2016.

- [86] F. Sorrentino, A. Alberti, G. Ferrari, V. V. Ivanov, N. Poli, M. Schioppo, and G. M. Tino. Quantum sensor for atom-surface interactions below $10\text{ }\mu\text{m}$. *Physical Review A*, 79(1):013409, 2009.
- [87] N. Poli, F.-Y. Wang, M. Tarallo, A. Alberti, M. Prevedelli, and G. Tino. Precision Measurement of Gravity with Cold Atoms in an Optical Lattice and Comparison with a Classical Gravimeter. *Physical Review Letters*, 106(3):038501, 2011.
- [88] Alan O. Jamison, Benjamin Plotkin-Swing, and Subhadeep Gupta. Advances in precision contrast interferometry with Yb Bose-Einstein condensates. *Physical Review A*, 90(3):063606, 2014.
- [89] M. G. Tarallo, T. Mazzoni, N. Poli, D. V. Sutyurin, X. Zhang, and G. M. Tino. Test of Einstein Equivalence Principle for 0-Spin and Half-Integer-Spin Atoms: Search for Spin-Gravity Coupling Effects. *Physical Review Letters*, 113(2):023005, 2014.
- [90] A. V. Gorshkov, M. Hermele, V. Gurarie, C. Xu, P. S. Julienne, J. Ye, P. Zoller, E. Demler, M. D. Lukin, and A. M. Rey. Two-orbital $SU(N)$ magnetism with ultracold alkaline-earth atoms. *Nature Physics*, 6(4):289, 2010.
- [91] K. I. Kugel and D. I. Khomskii. Crystal structure and magnetic properties of substances with orbital degeneracy. *Sov. Phys.-JETP*, 37(4):725, 1973.
- [92] B. Sutherland. Model for a multicomponent quantum system. *Physical Review B*, 12(9):3795, 1975.
- [93] M. van den Bossche, F.-C. Zhang, and F. Mila. Plaquette ground state in the two-dimensional $SU(4)$ spin-orbital model. *European Physical Journal B*, 17:367, 2000.
- [94] Y. Tokura and N. Nagaosa. Orbital Physics in Transition Metal Oxides. *Science*, 288:462, 2000.
- [95] P. Coleman. Heavy Fermions: electrons at the edge of magnetism. arXiv:cond-mat/0612006v3.
- [96] S. Pankov, R. Moessner, and S. L. Sondhi. Resonating singlet valence plaquettes. *Physical Review B*, 76(10):104436, 2007.
- [97] M. Greiter and S. Rachel. Valence bond solids for $SU(n)$ spin chains: Exact models, spinon confinement, and the Haldane gap. *Physical Review B*, 75(18):184441, 2007.
- [98] C. Xu and C. Wu. Resonating plaquette phases in $SU(4)$ Heisenberg antiferromagnet. *Physical Review B*, 77(13):134449, 2008.
- [99] C. Hadley and S. Bose. Multilevel multiparty singlets as ground states and their role in entanglement distribution. *Physical Review A*, 77(5):050308(R), 2008.
- [100] F. Wang and A. Vishwanath. Z_2 spin-orbital liquid state in the square lattice Kugel-Khomskii model. *Physical Review B*, 80(6):064413, 2009.

- [101] S. Rachel, R. Thomale, M. Fühlinger, P. Schmitteckert, and M. Greiter. Spinon confinement and the Haldane gap in $SU(n)$ spin chains. *Physical Review B*, 80(18):180420(R), 2009.
- [102] Shintaro Taie, Rekishu Yamazaki, Seiji Sugawa, and Yoshiro Takahashi. An $SU(6)$ Mott insulator of an atomic Fermi gas realized by large-spin Pomeranchuk cooling. *Nature Physics*, 8:825, 2012.
- [103] G. Pagano, M. Mancini, G. Cappellini, P. Lombardi, F. Schäfer, H. Hu, X.-J. Liu, J. Catani, C. Sias, M. Inguscio, and L. Fallani. A one-dimensional liquid of fermions with tunable spin. *Nature Physics*, 10:198, 2014.
- [104] Christian Hofrichter, Luis Riegger, Francesco Scazza, Moritz Höfer, Diogo Rio Fernandes, Immanuel Bloch, and Simon Fölling. Direct Probing of the Mott Crossover in the $SU(N)$ Fermi-Hubbard Model. *Physical Review X*, 6(2):021030, 2016.
- [105] D. Banerjee, M. Bögli, M. Dalmonte, E. Rico, P. Stebler, U.-J. Wiese, and P. Zoller. Atomic Quantum Simulation of $U(N)$ and $SU(N)$ Non-Abelian Lattice Gauge Theories. *Physical Review Letters*, 110(12):125303, 2013.
- [106] U.-J. Wiese. Ultracold quantum gases and lattice systems: quantum simulation of lattice gauge theories. *Annalen der Physik*, 525(10):777, 2013.
- [107] B. Bradlyn and A. Gromov. Supersymmetric waves in Bose-Fermi mixtures. *Physical Review A*, 93(3):033642, 2016.
- [108] F. Vogt, Ch. Grain, T. Nazarova, U. Sterr, F. Riehle, Ch. Lisdat, and E. Tiemann. Determination of the calcium ground state scattering length by photoassociation spectroscopy at large detunings. *European Physical Journal D*, 44:73, 2007.
- [109] Y. N. Martinez de Escobar, P. G. Mickelson, P. Pellegrini, S. B. Nagel, A. Traverso, M. Yan, R. Côté, and T. C. Killian. Two-photon photoassociative spectroscopy of ultracold ^{88}Sr . *Physical Review A*, 78(6):062708, 2008.
- [110] Masaaki Kitagawa, Katsunari Enomoto, Kentaro Kasa, Yoshiro Takahashi, Roman Ciuryło, Pascal Naidon, and Paul S. Julienne. Two-color photoassociation spectroscopy of ytterbium atoms and the precise determinations of s-wave scattering lengths. *Physical Review A*, 77(1):012719, 2008.
- [111] Sebastian Kraft, Felix Vogt, Oliver Appel, Fritz Riehle, and Uwe Sterr. Bose-Einstein Condensation of Alkaline Earth Atoms: ^{40}Ca . *Physical Review Letters*, 103(13):130401, 2009.
- [112] U. Dammalapati, L. Willmann, and S. Knoop. Scattering lengths of calcium and barium isotopes. *Physical Review A*, 84(5):054703, 2011.

- [113] A. Kramida, Yu. Ralchenko, J. Reader, and NIST ASD Team. NIST Atomic Spectra Database (ver. 5.2), [Online]. Available: <http://physics.nist.gov/asd> [2015, July 7]. National Institute of Standards and Technology, Gaithersburg, MD., 2014.
- [114] NIST Database of Atomic Weights and Isotopic Compositions. <http://www.nist.gov/pml/data/comp.cfm>.
- [115] J. R. de Laeter and N. Bukilic. The isotopic composition and atomic weight of ytterbium. *International Journal of Mass Spectrometry*, 252:222, 2006.
- [116] Yosuke Takasu, Kenichi Maki, Kaduki Komori, Tetsushi Takano, Kazuhito Honda, Mitsutaka Kumakura, Tsutomu Yabuzaki, and Yoshiro Takahashi. Spin-Singlet Bose-Einstein Condensation of Two-Electron Atoms. *Physical Review Letters*, 91(4):040404, 2003.
- [117] Simon Stellmer, Meng Khoon Tey, Bo Huang, Rudolf Grimm, and Florian Schreck. Bose-Einstein Condensation of Strontium. *Physical Review Letters*, 103(20):200401, 2009.
- [118] Y. N. Martinez de Escobar, P. G. Mickelson, M. Yan, B. J. DeSalvo, S. B. Nagel, and T. C. Killian. Bose-Einstein Condensation of ^{84}Sr . *Physical Review Letters*, 103(20):200402, 2009.
- [119] Takeshi Fukuhara, Seiji Sugawa, and Yoshiro Takahashi. Bose-Einstein condensation of an ytterbium isotope. *Physical Review A*, 76(5):051604(R), 2007.
- [120] Takeshi Fukuhara, Seiji Sugawa, Yosuke Takasu, and Yoshiro Takahashi. All-optical formation of quantum degenerate mixtures. *Physical Review A*, 79(2):021601, 2009.
- [121] Simon Stellmer, Meng Khoon Tey, Rudolf Grimm, and Florian Schreck. Bose-Einstein condensation of ^{86}Sr . *Physical Review A*, 82(4):041602(R), 2010.
- [122] P. G. Mickelson, Y. N. Martinez de Escobar, M. Yan, B. J. DeSalvo, and T. C. Killian. Bose-Einstein condensation of ^{88}Sr through sympathetic cooling with ^{87}Sr . *Physical Review A*, 81(5):051601(R), 2010.
- [123] B. J. DeSalvo, M. Yan, P. G. Mickelson, Y. N. Martinez de Escobar, and T. C. Killian. Degenerate Fermi Gas of ^{87}Sr . *Physical Review Letters*, 105(3):030402, 2010.
- [124] Seiji Sugawa, Rekishu Yamazaki, Shintaro Taie, and Yoshiro Takahashi. Bose-Einstein condensate in gases of rare atomic species. *Physical Review A*, 84(1):011610(R), 2011.
- [125] A. H. Hansen, A. Khramov, W. H. Dowd, A. O. Jamison, V. V. Ivanov, and S. Gupta. Quantum degenerate mixture of ytterbium and lithium atoms. *Physical Review A*, 84(1):011606(R), 2011.

- [126] Purbasha Halder, Chih-Yun Yang, and Andreas Hemmerich. Alternative route to Bose-Einstein condensation of two-electron atoms. *Physical Review A*, 85(3):031603(R), 2012.
- [127] S. Dörscher, A. Thobe, B. Hundt, A. Kochanke, R. Le Targat, P. Windpassinger, C. Becker, and K. Sengstock. Creation of quantum-degenerate gases of ytterbium in a compact 2D-/3D-magneto-optical trap setup. *Review of Scientific Instruments*, 84(4):043109, 2013.
- [128] V. D. Vaidya, J. Tiamsuphat, S. L. Rolston, and J. V. Porto. Degenerate Bose-Fermi mixtures of rubidium and ytterbium. *Physical Review A*, 92(4):043604, 2015.
- [129] Richard Roy, Alaina Green, Ryan Bowler, and Subhadeep Gupta. Rapid cooling to quantum degeneracy in dynamically shaped atom traps. *Physical Review A*, 93(4):043403, 2016.
- [130] Thomas H. Loftus, Tetsuya Ido, Andrew D. Ludlow, Martin M. Boyd, and Jun Ye. Narrow Line Cooling: Finite Photon Recoil Dynamics. *Physical Review Letters*, 93(7):073003, 2004.
- [131] Simon Stellmer, Rudolf Grimm, and Florian Schreck. Production of quantum-degenerate strontium gases. *Physical Review A*, 87(1):013611, 2013.
- [132] Neil W. Ashcroft and N. David Mermin. *Solid State Physics*. Cengage Learning, 1976.
- [133] Masatoshi Imada, Atsushi Fujimori, and Yoshinori Tokura. Metal-insulator transitions. *Reviews of Modern Physics*, 70(4):1039, 1998.
- [134] R. Staudt, M. Dzierzawa, and A. Muramatsu. Phase diagram of the three-dimensional Hubbard model at half filling. *European Physical Journal B*, 17:411, 2000.
- [135] Patrick A. Lee, Naoto Nagaosa, and Xiao Gang Wen. Doping a Mott insulator: Physics of high-temperature superconductivity. *Reviews of Modern Physics*, 78(1):17, 2006.
- [136] Michael P. Marder. *Condensed Matter Physics*. Wiley, 2015.
- [137] D. Jaksch, C. Bruder, J. I. Cirac, C. W. Gardiner, and P. Zoller. Cold Bosonic Atoms in Optical Lattices. *Physical Review Letters*, 81(15):3108, 1998.
- [138] D. Jaksch and P. Zoller. The cold atom Hubbard toolbox. *Annals of Physics*, 315:52, 2005.
- [139] W. Hofstetter, J. I. Cirac, P. Zoller, E. Demler, and M. D. Lukin. High-Temperature Superfluidity of Fermionic Atoms in Optical Lattices. *Physical Review Letters*, 89(22):220407, 2002.

- [140] A. N. Pasupathy, A. Pushp, K. K. Gomes, C. V. Parker, J. Wen, Z. Xu, G. Gu, S. Ono, Y. Ando, and A. Yazdani. Electronic Origin of the Inhomogeneous Pairing Interaction in the High-Tc Superconductor $\text{Bi}_2\text{Sr}_2\text{CaCu}_2\text{O}_{8+\delta}$. *Science*, 320(5873):196, 2008.
- [141] A. Georges, G. Kotliar, W. Krauth, and M. J. Rozenberg. Dynamical mean-field theory of strongly correlated fermion systems and the limit of infinite dimensions. *Reviews of Modern Physics*, 68(1):13, 1996.
- [142] E. Khatami and M. Rigol. Thermodynamics of strongly interacting fermions in two-dimensional optical lattices. *Physical Review A*, 84(5):053611, 2011.
- [143] M. A. Cazalilla, A. F. Ho, and M. Ueda. Ultracold gases of ytterbium: Ferromagnetism and Mott states in an $\text{SU}(6)$ Fermi system. *New Journal of Physics*, 11:103033, 2009.
- [144] M. Hermele, V. Gurarie, and A. M. Rey. Mott Insulators of Ultracold Fermionic Alkaline Earth Atoms: Underconstrained Magnetism and Chiral Spin Liquid. *Physical Review Letters*, 103(13):135301, 2009.
- [145] C. Xu. Liquids in multiorbital $\text{SU}(N)$ magnets made up of ultracold alkaline-earth atoms. *Physical Review B*, 81(14):144431, 2010.
- [146] Michael Foss-Feig, Michael Hermele, and Ana Maria Rey. Probing the Kondo lattice model with alkaline-earth-metal atoms. *Physical Review A*, 81(5):051603(R), 2010.
- [147] M. Foss-Feig, M. Hermele, V. Gurarie, and A. M. Rey. Heavy fermions in an optical lattice. *Physical Review A*, 82(5):053624, 2010.
- [148] M. Hermele, V. Gurarie, and A. M. Rey. Erratum: Mott Insulators of Ultracold Fermionic Alkaline Earth Atoms: Underconstrained Magnetism and Chiral Spin Liquid [Phys. Rev. Lett. 103, 135301 (2009)]. *Physical Review Letters*, 107(5):059901, 2011.
- [149] Salvatore R. Manmana, Kaden R. A. Hazzard, Gang Chen, Adrian E. Feiguin, and Ana Maria Rey. $\text{SU}(N)$ magnetism in chains of ultracold alkaline-earth-metal atoms: Mott transitions and quantum correlations. *Physical Review A*, 84(4):043601, 2011.
- [150] K. R. A. Hazzard, V. Gurarie, M. Hermele, and A. M. Rey. High-temperature properties of fermionic alkaline-earth-metal atoms in optical lattices. *Physical Review A*, 85(4):041604(R), 2012.
- [151] L. Bonnes, K. R. A. Hazzard, S. R. Manmana, A. M. Rey, and S. Wessel. Adiabatic loading of one-dimensional $\text{SU}(N)$ alkaline-earth-atom fermions in optical lattices. *Physical Review Letters*, 109(20):205305, 2012.
- [152] P. Nataf and F. Mila. Exact Diagonalization of Heisenberg $\text{SU}(N)$ Models. *Physical Review Letters*, 113(12):127204, 2014.

- [153] P. Nataf, M. Lajkó, P. Corboz, A. M. Läuchli, K. Penc, and F. Mila. Plaquette order in the SU(6) Heisenberg model on the honeycomb lattice. *Physical Review B*, 93(20):201113, 2016.
- [154] A. V. Gorshkov, M. Hermele, V. Gurarie, C. Xu, P. S. Julienne, J. Ye, P. Zoller, E. Demler, M. D. Lukin, and A. M. Rey. Two-orbital SU(N) magnetism with ultracold alkaline-earth atoms: supplementary information. *Nature Physics*, 6, 2010.
- [155] Wilhelm Zwerger. Mott-Hubbard transition of cold atoms in optical lattices. *Journal of Optics B*, 5:S9, 2003.
- [156] Ana Maria Rey, Guido Pupillo, Charles W. Clark, and Carl J. Williams. Ultracold atoms confined in an optical lattice plus parabolic potential: A closed-form approach. *Physical Review A*, 72(3):033616, 2005.
- [157] C. J. Pethick and H. Smith. *Bose-Einstein Condensation in Dilute Gases*. Cambridge University Press, 2008.
- [158] D. McKay, M. White, and B. DeMarco. Lattice thermodynamics for ultracold atoms. *Physical Review A*, 79(6):063605, 2009.
- [159] D. Greif, T. Uehlinger, G. Jotzu, L. Tarruell, and T. Esslinger. Short-Range Quantum Magnetism of Ultracold Fermions in an Optical Lattice. *Science*, 340:1307, 2013.
- [160] R. A. Hart, P. M. Duarte, T.-L. Yang, X. Liu, T. Paiva, E. Khatami, R. T. Scalettar, N. Trivedi, D. A. Huse, and R. G. Hulet. Observation of antiferromagnetic correlations in the Hubbard model with ultracold atoms. *Nature*, 519:211, 2015.
- [161] S. Trotzky, P. Cheinet, S. Fölling, M. Feld, U. Schnorrberger, A. M. Rey, A. Polkovnikov, E. A. Demler, M. D. Lukin, and I. Bloch. Time-resolved observation and control of superexchange interactions with ultracold atoms in optical lattices. *Science*, 319:295, 2008.
- [162] T. Fukuhara, P. Schauß, M. Endres, S. Hild, M. Cheneau, I. Bloch, and C. Gross. Microscopic observation of magnon bound states and their dynamics. *Nature*, 502:76, 2013.
- [163] S. Hild, T. Fukuhara, P. Schauß, J. Zeiher, M. Knap, E. Demler, I. Bloch, and C. Gross. Far-from-equilibrium spin transport in heisenberg quantum magnets. *Physical Review Letters*, 113(14):147205, 2014.
- [164] R. C. Brown, R. Wyllie, S. B. Koller, E. A. Goldschmidt, M. Foss-Feig, and J. V. Porto. Two-dimensional superexchange-mediated magnetization dynamics in an optical lattice. *Science*, 348(6234):540, 2015.
- [165] M. E. Beverland, G. Alagic, M. J. Martin, A. P. Koller, A. M. Rey, and A. V. Gorshkov. Realizing exactly solvable SU(N) magnets with thermal atoms. *Physical Review A*, 93(5):051601, 2016.

- [166] A. L. Gaunt, T. F. Schmidutz, I. Gotlibovych, R. P. Smith, and Z. Hadzibabic. Bose-Einstein Condensation of Atoms in a Uniform Potential. *Physical Review Letters*, 110(20):200406, 2013.
- [167] I. Gotlibovych, T. F. Schmidutz, A. L. Gaunt, N. Navon, R. P. Smith, and Z. Hadzibabic. Observing properties of an interacting homogeneous Bose-Einstein condensate: Heisenberg-limited momentum spread, interaction energy, and free-expansion dynamics. *Physical Review A*, 89(6):061604(R), 2014.
- [168] Lauriane Chomaz, Laura Corman, Tom Bienaimé, Rémi Desbuquois, Christof Weitenberg, Sylvain Nascimbène, Jérôme Beugnon, and Jean Dalibard. Emergence of coherence via transverse condensation in a uniform quasi-two-dimensional Bose gas. *Nature Communications*, 6:6162, 2015.
- [169] W. Ketterle, D. S. Durfee, and D. M. Stamper-Kurn. Making, probing and understanding Bose-Einstein condensates. In M. Inguscio, S. Stringari, and C. E. Wieman, editors, *Bose-Einstein condensation in atomic gases, Proceedings of the International School of Physics "Enrico Fermi", Course CXL*, pages 67–176. IOS Press, Amsterdam, 1999.
- [170] L. P. Pitaevskii. Vortex Lines in an imperfect Bose gas. *Soviet Physics JETP*, 13(2):451, 1961.
- [171] E. P. Gross. Structure of a quantized vortex in boson systems. *Il Nuovo Cimento*, 20(3):454, 1961.
- [172] Y. Castin and R. Dum. Bose-Einstein Condensates in Time Dependent Traps. *Physical Review Letters*, 77(27):5315, 1996.
- [173] D. A. Butts and D. S. Rokhsar. Trapped Fermi gases. *Physical Review A*, 55(6):4346, 1997.
- [174] G. M. Bruun and C. W. Clark. Ideal gases in time-dependent traps. *Physical Review A*, 61(6):061601(R), 2000.
- [175] B. Demarco. *Quantum Behavior of an Atomic Fermi Gas*. PhD thesis, University of Colorado, Boulder, 2001.
- [176] Wolfgang Ketterle and Martin W. Zwierlein. Making, probing and understanding ultracold Fermi gases. In M. Inguscio, W. Ketterle, and C. Salomon, editors, *Ultracold Fermi Gases, Proceedings of the International School of Physics "Enrico Fermi", Course CLXIV*, pages 95–287. IOS Press, Amsterdam, 2008, 0801.2500v1.
- [177] Ulrich Schneider. *Interacting Fermionic Atoms in Optical Lattices - A Quantum Simulator for Condensed Matter Physics*. PhD thesis, Johannes Gutenberg-Universität, Mainz, 2010.

- [178] Kurt Richard Vogel. *Laser cooling on a narrow atomic transition and measurement of the two-body cold collision loss rate in a strontium magneto-optical trap*. PhD thesis, University of Colorado, Boulder, 1999.
- [179] Sarah B. Nagel. *Ultracold Collisions in Atomic Strontium*. PhD thesis, Rice University, 2008.
- [180] Andrew D. Ludlow. *The Strontium Optical Lattice Clock: Optical Spectroscopy with Sub-Hertz Accuracy*. PhD thesis, University of Colorado, Boulder, 2008.
- [181] Pascal Gerry Mickelson. *Trapping and Evaporation of ^{87}Sr and ^{88}Sr Mixtures*. PhD thesis, Rice University, 2010.
- [182] Simon Stellmer. *Degenerate quantum gases of strontium*. PhD thesis, University of Innsbruck, 2013.
- [183] Yenny Natali Martinez de Escobar. *Bose-Einstein Condensation of ^{84}Sr* . PhD thesis, Rice University, 2012.
- [184] Nelson Darkwah Oppong. Towards a Degenerate Fermi Gas of Strontium-87 in a 3D Optical Lattice. Master's thesis, University of Colorado, Boulder, 2015.
- [185] Xinye Xu, Thomas H. Loftus, Matthew J. Smith, John L. Hall, Alan Gallagher, and Jun Ye. Dynamics in a two-level atom magneto-optical trap. *Physical Review A*, 66(1):011401(R), 2002.
- [186] Xinye Xu, Thomas H. Loftus, Josh W. Dunn, Chris H. Greene, John L. Hall, Alan Gallagher, and Jun Ye. Single-Stage Sub-Doppler Cooling of Alkaline Earth Atoms. *Physical Review Letters*, 90(19):193002, may 2003.
- [187] Xinye Xu, Thomas H. Loftus, John L. Hall, Alan Gallagher, and Jun Ye. Cooling and trapping of atomic strontium. *Journal of the Optical Society of America B*, 20(5):968, 2003.
- [188] I. Courtillot, A. Quessada, R. P. Kovacich, J. J. Zondy, A. Landragin, A. Clairon, and P. Lemonde. Efficient cooling and trapping of strontium atoms. *Optics Letters*, 28(6):468, 2003.
- [189] H.-Jürgen Kluge and Hatto Sauter. Levelcrossing Experiments in the First Excited 1P_1 States of the Alkaline Earths. *Z. Physik*, 270:295, 1974.
- [190] B. A. Bushaw and W. Nörtershäuser. Resonance ionization spectroscopy of stable strontium isotopes and ^{90}Sr via $5s^2\ ^1S_0 \rightarrow \text{E}\check{S}5s5p\ ^1P_1 \rightarrow \text{E}\check{S}5s5d\ ^1D_2 \rightarrow \text{E}\check{S}5s11f\ ^1F_3 \rightarrow \text{E}\check{S}\text{Sr}^+$. *Spectrochimica Acta, Part B*, 55:1679, 2000.
- [191] Stig Stenholm. The semiclassical theory of laser cooling. *Reviews of Modern Physics*, 58(3):699, 1986.

- [192] Thierry Chanelière, Jean-Louis Meunier, Robin Kaiser, Christian Miniatura, and David Wilkowski. Extra-heating mechanism in Doppler cooling experiments. *Journal of the Optical Society of America B*, 22(9):1819, 2005.
- [193] S. C. Bell, M. Junker, M. Jasperse, L. D. Turner, Y. J. Lin, I. B. Spielman, and R. E. Scholten. A slow atom source using a collimated effusive oven and a single-layer variable pitch coil Zeeman slower. *Review of Scientific Instruments*, 81(1):013105, 2010.
- [194] Björn Ole Kock. *Magneto-Optical Trapping of Strontium for use as a Mobile Frequency Reference*. PhD thesis, University of Birmingham, 2013.
- [195] S. B. Nagel, C. E. Simien, S. Laha, P. Gupta, V. S. Ashoka, and T. C. Killian. Magnetic trapping of metastable 3P_2 atomic strontium. *Physical Review A*, 67(1):011401(R), 2003.
- [196] Gisbert zu Putlitz. Bestimmung des elektrischen Kernquadrupolmomentes des ungeraden stabilen Strontium-87-Kerns. *Zeitschrift für Physik*, 175:543, 1963.
- [197] B. A. Bushaw and B. D. Cannon. Diode laser based resonance ionization mass spectrometric measurement of strontium-90. *Spectrochimica Acta, Part B*, 52:1839, 1997.
- [198] Irène Courtillet. *Première observation de la transition fortement interdite $1S_0-3P_0$ du strontium, pour une horloge optique à atomes piégés*. PhD thesis, Université Pierre et Marie Curie - Paris VI, 2003.
- [199] Y. Castin, H. Wallis, and J. Dalibard. Limit of Doppler cooling. *Journal of the Optical Society of America B*, 6(11):2046, 1989.
- [200] Thomas H. Loftus, Tetsuya Ido, Martin M. Boyd, Andrew D. Ludlow, and Jun Ye. Narrow line cooling and momentum-space crystals. *Physical Review A*, 70(6):063413, 2004.
- [201] T. Chanelière, L. He, R. Kaiser, and D. Wilkowski. Three dimensional cooling and trapping with a narrow line. *European Physical Journal D*, 46:507, 2008.
- [202] Rudolf Grimm, Matthias Weidemüller, and Yurii B. Ovchinnikov. Optical dipole traps for neutral atoms. In *Advances In Atomic, Molecular, and Optical Physics*, pages 95–170. Elsevier BV, 2000.
- [203] Harald F. Hess. Evaporative cooling of magnetically trapped and compressed spin-polarized hydrogen. *Physical Review B*, 34(5):3476, 1986.
- [204] Naoto Masuhara, John M. Doyle, Jon C. Sandberg, Daniel Kleppner, Thomas J. Greytak, Harald F. Hess, and Greg P. Kochanski. Evaporative cooling of spin-polarized atomic hydrogen. *Physical Review Letters*, 61(8):935, 1988.

- [205] M. D. Barrett, J. A. Sauer, and M. S. Chapman. All-Optical Formation of an Atomic Bose-Einstein Condensate. *Physical Review Letters*, 87(1):010404, 2001.
- [206] Tino Weber, Jens Herbig, Michael Mark, Hanns-Christoph Nägerl, and Rudolf Grimm. Bose-Einstein Condensation of Cesium. *Science*, 299:232, 2003.
- [207] Toshiya Kinoshita, Trevor Wenger, and David S. Weiss. All-optical Bose-Einstein condensation using a compressible crossed dipole trap. *Physical Review A*, 71(1):011602(R), 2005.
- [208] O. J. Luiten, M. W. Reynolds, and J. T. M. Walraven. Kinetic theory of the evaporative cooling of a trapped gas. *Physical Review A*, 53(1):381, 1996.
- [209] E. A. Burt, R. W. Ghrist, C. J. Myatt, M. J. Holland, E. A. Cornell, and C. E. Wieman. Coherence, Correlations, and Collisions: What One Learns about Bose-Einstein Condensates from Their Decay. *Physical Review Letters*, 79(3):337, 1997.
- [210] G. Ferrari, R. E. Drullinger, N. Poli, F. Sorrentino, and G. M. Tino. Cooling of Sr to high phase-space density by laser and sympathetic cooling in isotopic mixtures. *Physical Review A*, 73(2):023408, 2006.
- [211] D. Comparat, A. Fioretti, G. Stern, E. Dimova, B. Laburthe Tolra, and P. Pillet. Optimized production of large Bose-Einstein condensates. *Physical Review A*, 73(4):043410, 2006.
- [212] M. Yan, R. Chakraborty, A. Mazurenko, P. G. Mickelson, Y. N. Martinez de Escobar, B. J. DeSalvo, and T. C. Killian. Numerical modeling of collisional dynamics of Sr in an optical dipole trap. *Physical Review A*, 83(3):032705, 2011.
- [213] Abraham J. Olson, Robert J. Niffenegger, and Yong P. Chen. Optimizing the efficiency of evaporative cooling in optical dipole traps. *Physical Review A*, 87(5):053613, 2013.
- [214] S. Friebe, C. D’Andrea, J. Walz, M. Weitz, and T. W. Hänsch. CO₂-laser optical lattice with cold rubidium atoms. *Physical Review A*, 57(1):R20, 1998.
- [215] Ying Huang. A New Optical Trap System for Ultracold Strontium. Master’s thesis, Rice University, 2013.
- [216] M.-O. Mewes, M. R. Andrews, N. J. van Druten, D. M. Kurn, D. S. Durfee, C. G. Townsend, and W. Ketterle. Collective Excitations of a Bose-Einstein Condensate in a Magnetic Trap. *Physical Review Letters*, 77(6):988, 1996.
- [217] D. S. Jin, J. R. Ensher, M. R. Matthews, C. E. Wieman, and E. A. Cornell. Collective Excitations of a Bose-Einstein Condensate in a Dilute Gas. *Physical Review Letters*, 77(3):420, 1996.
- [218] Miroslav Gajdacz, Poul L. Pedersen, Troels Mørch, Andrew J. Hilliard, Jan Arlt, and Jacob F. Sherson. Non-destructive Faraday imaging of dynamically controlled ultracold atoms. *Review of Scientific Instruments*, 84(8):083105, 2013.

- [219] K. M. O'Hara, M. E. Gehm, S. R. Granade, and J. E. Thomas. Scaling laws for evaporative cooling in time-dependent optical traps. *Physical Review A*, 64(5):051403(R), 2001.
- [220] Meng Khoon Tey, Simon Stellmer, Rudolf Grimm, and Florian Schreck. Double-degenerate Bose-Fermi mixture of strontium. *Physical Review A*, 82(1):011608(R), 2010.
- [221] Didier Clamond. Complex dilogarithm. <http://www.mathworks.com/matlabcentral/fileexchange/10186-complex-dilogarithm>, 2006.
- [222] David Wood. The computation of polylogarithms. Technical Report 15-92*, University of Kent, Computing Laboratory, University of Kent, Canterbury, UK, June 1992.
- [223] L. Lewin. *Dilogarithms and Associated Functions*. MacDonald, London, 1958.
- [224] Maximilian Kuhnert. Enhanced computation of polylogarithm aka de jonquieres function. <https://www.mathworks.com/matlabcentral/fileexchange/37229-enhanced-computation-of-polylogarithm-aka-de-jonquieres-function/content/polylog.m>, 2012.
- [225] Vikram Bhagat, Ranjan Bhattacharya, and Dhiranjan Roy. On the evaluation of generalized Bose-Einstein and Fermi-Dirac integrals. *Computer Physics Communications*, 155:7, 2003.
- [226] Igor Gotlibovych. *Degenerate Bose Gases in a Uniform Potential*. PhD thesis, University of Cambridge, 2014.
- [227] NIST Digital Library of Mathematical Functions. <http://dlmf.nist.gov/>, Release 1.0.11 of 2016-06-08. Online companion to [319].
- [228] Yosuke Shimada, Yuko Chida, Nozomi Ohtsubo, Takatoshi Aoki, Makoto Takeuchi, Takahiro Kuga, and Yoshio Torii. A simplified 461-nm laser system using blue laser diodes and a hollow cathode lamp for laser cooling of Sr. *Review of Scientific Instruments*, 84(6):063101, 2013.
- [229] Jürgen Appel, Andrew MacRae, and A. I. Lvovsky. A versatile digital GHz phase lock for external cavity diode lasers. *Measurement Science and Technology*, 20:055302, 2009.
- [230] R. W. P. Drever, J. L. Hall, F. V. Kowalski, J. Hough, G. M. Ford, A. J. Munley, and H. Ward. Laser Phase and Frequency Stabilization Using an Optical Resonator. *Applied Physics B*, 31:97, 1983.
- [231] T. Okoshi, K. Kikuchi, and A. Nakayama. Novel method for high resolution measurement of laser output spectrum. *Electronics Letters*, 16(16):630, 1980.

- [232] Hanne Ludvigsen, Mika Tossavainen, and Matti Kaivola. Laser linewidth measurements using self-homodyne detection with short delay. *Optics Communications*, 155(October):180, 1998.
- [233] P. B. Gallion and G. Debarge. Quantum Phase Noise and Field Correlation in Single Frequency Semiconductor Laser Systems. *IEEE Journal of Quantum Electronics*, QE-20(4):343, 1984.
- [234] L. E. Richter, H. I. Mandelberg, M. S. Kruger, and P. A. McGrath. Linewidth Determination from Self-Heterodyne Measurements with Subcoherence Delay Times. *IEEE Journal of Quantum Electronics*, QE-22(11):2070, 1986.
- [235] Eryn C. Cook, Paul J. Martin, Tobias L. Brown-Heft, Jeffrey C. Garman, and Daniel A. Steck. High passive-stability diode-laser design for use in atomic-physics experiments. *Review of Scientific Instruments*, 83(4):043101, 2012.
- [236] R. W. Fox, L. Hollberg, and A. S. Zibrov. Semiconductor diode lasers. In F. B. Dunning and R. G. Hulet, editors, *Experimental Methods in the Physical Sciences*, volume 29C, chapter 4, pages 77–102. Academic Press, Inc, 1997.
- [237] K. G. Libbrecht and J. L. Hall. A low-noise high-speed diode laser current controller. *Review of Scientific Instruments*, 64(8):2133, 1993.
- [238] Christopher J. Erickson, Marshall Van Zijll, Greg Doermann, and Dallin S. Durfee. An ultrahigh stability, low-noise laser current driver with digital control. *Review of Scientific Instruments*, 79(7):073107, 2008.
- [239] Ian R. Hill, Richard Hobson, William Bowden, Elizabeth M. Bridge, Sean Donnellan, E. Anne Curtis, and Patrick Gill. A low maintenance Sr optical lattice clock. arXiv:1602.05810.
- [240] Simon Stellmer and Florian Schreck. Reservoir spectroscopy of $5s5p\ ^3P_2 - 5snd\ ^3D_{1,2,3}$ transitions in strontium. *Physical Review A*, 90(2):022512, 2014.
- [241] Simon Stellmer, Florian Schreck, and Thomas C. Killian. Degenerate quantum gases of strontium. In K. Madison, K. Bongs, L. D. Carr, A. M. Rey, and H. Zhai, editors, *Annual Review of Cold Atoms and Molecules*, volume 2, chapter 1, pages 1–80. World Scientific Publishing Co., 2014.
- [242] P. G. Mickelson, Y. N. Martinez de Escobar, P. Anzel, B. J. DeSalvo, S. B. Nagel, A. J. Traverso, M. Yan, and T. C. Killian. Repumping and spectroscopy of laser-cooled Sr atoms using the $(5s5p)^3P_2 - (5s4d)^3D_2$ transition. *Journal of Physics B: Atomic, Molecular and Optical Physics*, 42:235001, 2009.
- [243] Stephan M. Heider and Gilbert O. Brink. Hyperfine structure of ^{87}Sr in the 3P_2 metastable state. *Physical Review A*, 16(4):1371, 1977.

- [244] Kilian Singer, Selim Jochim, Marcel Mudrich, Allard Mosk, and Matthias Weidemüller. Low-cost mechanical shutter for light beams. *Review of Scientific Instruments*, 73(12):4402, 2002.
- [245] Alexander Lloyd Gaunt. *Degenerate Bose Gases : Tuning Interactions & Geometry*. PhD thesis, University of Cambridge, 2014.
- [246] Tobias Fabian Schmidutz. *Studies of a Homogeneous Bose Gas*. PhD thesis, University of Cambridge, 2014.
- [247] Robert Ulichney. *Digital Halftoning (MIT Press)*. The MIT Press, 1987.
- [248] L. M. Bennie, P. T. Starkey, M. Jasperse, C. J. Billington, R. P. Anderson, and L. D. Turner. A versatile high resolution objective for imaging quantum gases. *Optics express*, 21(7):9011, 2013.
- [249] M. R. Andrews, M.-O. Mewes, N. J. van Druten, D. S. Durfee, D. M. Kurn, and W. Ketterle. Direct, Nondestructive Observation of a Bose Condensate. *Science*, 273(5271):84, 1996.
- [250] J. E. Lye, J. J. Hope, and J. D. Close. Nondestructive dynamic detectors for Bose-Einstein condensates. *Physical Review A*, 67(4):043609, 2003.
- [251] G. Reinaudi, T. Lahaye, Z. Wang, and D. Guéry-Odelin. Strong saturation absorption imaging of dense clouds of ultracold atoms. *Optics Letters*, 32(21):3143, 2007.
- [252] Anand Ramanathan, Sérgio R. Muniz, Kevin C. Wright, Russell P. Anderson, William D. Phillips, Kristian Helmerson, and Gretchen K. Campbell. Partial-transfer absorption imaging: A versatile technique for optimal imaging of ultracold gases. *Review of Scientific Instruments*, 83(8):083119, 2012.
- [253] Eugene Hecht. *Optics (4th Edition)*. Addison-Wesley, 2002.
- [254] Lord Rayleigh F.R.S. XXXI. investigations in optics, with special reference to the spectroscope. *Philosophical Magazine Series 5*, 8(49):261, 1879.
- [255] C. M. Sparrow. On spectroscopic resolving power. *The Astrophysical Journal*, 44:76, 1916.
- [256] Daniel Adam Steck. Quantum and Atom Optics. available online at <http://steck.us/teaching> (revision 0.10.2, 16 October 2015).
- [257] M. D. Lukin and L. Childress. Modern Atomic and Optical Physics II Lecture Notes. available online at <http://ultracold.jqi.umd.edu/atomic-physics-721/>, 2005.
- [258] Ruwan Senaratne, Shankari V. Rajagopal, Zachary A. Geiger, Kurt M. Fujiwara, Vyacheslav Lebedev, and David M. Weld. Effusive atomic oven nozzle design using an aligned microcapillary array. *Review of Scientific Instruments*, 86(2):023105, 2015.

- [259] J. J. Tollett, C. C. Bradley, C. A. Sackett, and R. G. Hulet. Permanent magnet trap for cold atoms. *Physical Review A*, 51(1):R22, 1995.
- [260] C. C. Bradley, C. A. Sackett, J. J. Tollett, and R. G. Hulet. Evidence of Bose-Einstein condensation in an atomic gas with attractive interactions. *Physical Review Letters*, 75(9):1687, 1995.
- [261] G. Reinaudi, C. B. Osborn, K. Bega, and T. Zelevinsky. Dynamically configurable and optimizable Zeeman slower using permanent magnets and servomotors. *Journal of the Optical Society of America B*, 29(4):729, 2012.
- [262] G. Lamporesi, S. Donadello, S. Serafini, and G. Ferrari. Compact high-flux source of cold sodium atoms. *Review of Scientific Instruments*, 84(6):063102, 2013.
- [263] Ian R. Hill, Yuri B. Ovchinnikov, Elizabeth M. Bridge, E. Anne Curtis, and Patrick Gill. Zeeman slowers for strontium based on permanent magnets. *Journal of Physics B: Atomic, Molecular and Optical Physics*, 47(7):075006, 2014.
- [264] Creston David Herold. *Ultracold Mixtures of Rubidium and Ytterbium for Open Quantum System Engineering*. PhD thesis, University of Maryland, College Park, 2014.
- [265] M. D. White. *Ultracold Atoms in a Disordered Optical Lattice*. PhD thesis, University of Illinois at Urbana-Champaign, 2009.
- [266] Roger Brown. *Nonequilibrium Manybody Dynamics with Ultracold Atoms in Optical Lattices and Selected Problems in Atomic Physics*. PhD thesis, University of Maryland, College Park, 2015.
- [267] D. S. Barker, B. J. Reschovsky, N. C. Pisenti, and G. K. Campbell. Enhanced magnetic trap loading for atomic strontium. *Physical Review A*, 92(4):043418, 2015.
- [268] Tetsuya Ido, Yoshitomo Isoya, and Hidetoshi Katori. Optical-dipole trapping of Sr atoms at a high phase-space density. *Physical Review A*, 61(6):061403(R), 2000.
- [269] A. Traverso, R. Chakraborty, Y. N. Martinez de Escobar, P. G. Mickelson, S. B. Nagel, M. Yan, and T. C. Killian. Inelastic and elastic collision rates for triplet states of ultracold strontium. *Physical Review A*, 79(6):060702(R), 2009.
- [270] Y. N. Martinez de Escobar, P. G. Mickelson, M. Yan, and T. C. Killian. Modification of atom scattering using an intercombination-line optical Feshbach resonance at large detuning. arXiv:0906.1837v1.
- [271] I. Courtillot, A. Quessada-Vial, A. Brusch, D. Kolker, G. D. Rovera, and P. Lemonde. Accurate spectroscopy of Sr atoms. *The European Physical Journal D*, 33:161, 2005.

- [272] Kanhaiya Pandey, K. D. Rathod, Sambit Bikas Pal, and Vasant Natarajan. Magnetic trapping of Yb in the metastable 3P_2 state. *Physical Review A*, 81(3):033424, 2010.
- [273] J. R. Guest, N. D. Scielzo, I. Ahmad, K. Bailey, J. P. Greene, R. J. Holt, Z. T. Lu, T. P. O'Connor, and D. H. Potterveld. Laser trapping of ^{225}Ra and ^{226}Ra with Repumping by Room-Temperature Blackbody Radiation. *Physical Review Letters*, 98:093001, 2007.
- [274] S. De, U. Dammalapati, K. Jungmann, and L. Willmann. Magneto-optical trapping of barium. *Physical Review A*, 79(4):041402(R), 2009.
- [275] Jan Grünert and Andreas Hemmerich. Sub-Doppler magneto-optical trap for calcium. *Physical Review A*, 65(4):041401(R), 2002.
- [276] H. G. C. Werij, C. H. Greene, C. E. Theodosiou, and Alan Gallagher. Oscillator strengths and radiative branching ratios in atomic Sr. *Physical Review A*, 46(3):1248, 1992.
- [277] D. S. Barker, N. C. Pienti, B. J. Reschovsky, and G. K. Campbell. Three-photon process for producing a degenerate gas of metastable alkaline-earth-metal atoms. *Physical Review A*, 93(5):053417, 2016.
- [278] Matthew A. Norcia and James K. Thompson. Cold-Strontium Laser in the Super-radiant Crossover Regime. *Physical Review X*, 6(1):011025, 2016.
- [279] Ryuta Yamamoto, Jun Kobayashi, Takuma Kuno, Kohei Kato, and Yoshiro Takahashi. An ytterbium quantum gas microscope with narrow-line laser cooling. *New Journal of Physics*, 18:023016, 2016.
- [280] Shuta Nakajima, Takafumi Tomita, Shintaro Taie, Tomohiro Ichinose, Hideki Ozawa, Lei Wang, Matthias Troyer, and Yoshiro Takahashi. Topological Thouless pumping of ultracold fermions. *Nature Physics*, 2016.
- [281] B. H. McGuyer, C. B. Osborn, M. McDonald, G. Reinaudi, W. Skomorowski, R. Moszynski, and T. Zelevinsky. Nonadiabatic Effects in Ultracold Molecules via Anomalous Linear and Quadratic Zeeman Shifts. *Physical Review Letters*, 111(24):243003, 2013.
- [282] M. McDonald, B. H. McGuyer, F. Apfelbeck, C.-H. Lee, I. Majewska, R. Moszynski, and T. Zelevinsky. Photodissociation of a diatomic molecule in the quantum regime reveals ultracold chemistry. arXiv:1512.06673.
- [283] S. G. Bhongale, L. Mathey, Erhai Zhao, S. F. Yelin, and Mikhail Lemeshko. Quantum Phases of Quadrupolar Fermi Gases in Optical Lattices. *Physical Review Letters*, 110(15):155301, 2013.
- [284] A. Derevianko, S. G. Porsev, S. Kotochigova, E. Tiesinga, and P. S. Julienne. Ultracold Collision Properties of Metastable Alkaline-Earth Atoms. *Physical Review Letters*, 90(6):063002, 2003.

- [285] M. Lahrz, M. Lemeshko, K. Sengstock, C. Becker, and L. Mathey. Detecting quadrupole interactions in ultracold Fermi gases. *Physical Review A*, 89(4):043616, 2014.
- [286] C. D. Herold, V. D. Vaidya, X. Li, S. L. Rolston, J. V. Porto, and M. S. Safronova. Precision Measurement of Transition Matrix Elements via Light Shift Cancellation. *Physical Review Letters*, 109(24):243003, 2012.
- [287] William F. Holmgren, Raisa Trubko, Ivan Hromada, and Alexander D. Cronin. Measurement of a Wavelength of Light for Which the Energy Shift for an Atom Vanishes. *Physical Review Letters*, 109(24):243004, 2012.
- [288] M. S. Safronova, Z. Zuhrianda, U. I. Safronova, and Charles W. Clark. The magic road to precision. arXiv:1507.06570.
- [289] Michael Foss-Feig, Andrew J. Daley, James K. Thompson, and Ana Maria Rey. Steady-State Many-Body Entanglement of Hot Reactive Fermions. *Physical Review Letters*, 109(23):230501, 2012.
- [290] D. Hansen and A. Hemmerich. Observation of Multichannel Collisions of Cold Metastable Calcium Atoms. *Physical Review Letters*, 96(7):073003, 2006.
- [291] Ch. Lisdat, J. S. R. Vellore Winfred, T. Middelmann, F. Riehle, and U. Sterr. Collisional Losses, Decoherence, and Frequency Shifts in Optical Lattice Clocks with Bosons. *Physical Review Letters*, 103(9):090801, 2009.
- [292] A. Yamaguchi, S. Uetake, D. Hashimoto, J. M. Doyle, and Y. Takahashi. Inelastic Collisions in Optically Trapped Ultracold Metastable Ytterbium. *Physical Review Letters*, 101(23):233002, 2008.
- [293] Satoshi Uetake, Ryo Murakami, John M. Doyle, and Yoshiro Takahashi. Spin-dependent collision of ultracold metastable atoms. *Physical Review A*, 86(3):032712, 2012.
- [294] Purbasha Halder, Hannes Winter, and Andreas Hemmerich. Inelastic collisions of optically trapped metastable calcium atoms. *Physical Review A*, 88(6):063639, 2013.
- [295] Alexander Khramov, Anders Hansen, William Dowd, Richard J. Roy, Constantinos Makrides, Alexander Petrov, Svetlana Kotochigova, and Subhadeep Gupta. Ultracold Heteronuclear Mixture of Ground and Excited State Atoms. *Physical Review Letters*, 112(3):033201, 2014.
- [296] X. Zhang, M. Bishof, S. L. Bromley, C. V. Kraus, , M. S. Safronova, P. Zoller, A. M. Rey, and J. Ye. Spectroscopic observation of SU(N)-symmetric interactions in Sr orbital magnetism. *Science*, 345(6203):1467, 2014.

- [297] Hideaki Hara, Hideki Konishi, Shuta Nakajima, Yosuke Takasu, and Yoshiro Takahashi. A Three-Dimensional Optical Lattice of Ytterbium and Lithium Atomic Gas Mixture. *Journal of the Physical Society of Japan*, 83:014003, 2014.
- [298] Gretchen K. Campbell, Andrew D. Ludlow, Sebastian Blatt, Jan W. Thomsen, Michael J. Martin, Marcio H. G. de Miranda, Tanya Zelevinsky, Martin M. Boyd, Jun Ye, S. A. Diddams, T. P. Heavner, T. E. Parker, and S. R. Jefferts. The absolute frequency of the ^{87}Sr optical clock transition. *Metrologia*, 45:539, 2008.
- [299] S. C. Bell, D. M. Heywood, J. D. White, J. D. Close, and R. E. Scholten. Laser frequency offset locking using electromagnetically induced transparency. *Applied Physics Letters*, 90:171120, 2007.
- [300] R. P. Abel, A. K. Mohapatra, M. G. Bason, J. D. Pritchard, K. J. Weatherill, U. Raitzsch, and C. S. Adams. Laser frequency stabilization to excited state transitions using electromagnetically induced transparency in a cascade system. *Applied Physics Letters*, 94:071107, 2009.
- [301] C. E. Liekhuis-Schmaltz, R. Mantifel, M. Torabifard, I. B. Burgess, and J. D. D. Martin. Injection-locked diode laser current modulation for Pound-Drever-Hall frequency stabilization using transfer cavities. *Journal of the Optical Society of America B*, 29(6):1394, 2012.
- [302] Hajime Inaba, Kazumoto Hosaka, Masami Yasuda, Yoshiaki Nakajima, Kana Iwakuni, Daisuke Akamatsu, Sho Okubo, Takuya Kohno, Atsushi Onae, and Feng-Lei Hong. Spectroscopy of ^{171}Yb in an optical lattice based on laser linewidth transfer using a narrow linewidth frequency comb. *Optics Express*, 21(7):7891, 2013.
- [303] Nils Scharnhorst, Jannes B. Wübbena, Stephan Hannig, Kornelius Jakobsen, Johannes Kramer, Ian D. Leroux, and Piet O. Schmidt. High-bandwidth transfer of phase stability through a fiber frequency comb. *Optics Express*, 23(15):19771, 2015.
- [304] Elizabeth M. Bridge, Niamh C. Keegan, Alistair D. Bounds, Danielle Boddy, Daniel P. Sadler, and Matthew P. A. Jones. A tunable CW UV laser with < 35 kHz absolute frequency instability for precision spectroscopy of Sr Rydberg states. *Optics Express*, 24(3):2281, 2016.
- [305] S. G. Porsev, Yu. G. Rakhlin, and M. G. Kozlov. Electric-dipole amplitudes, lifetimes, and polarizabilities of the low-lying levels of atomic ytterbium. *Physical Review A*, 60(4):2781, 1999.
- [306] P. G. Mickelson, Y. N. Martinez, A. D. Saenz, S. B. Nagel, Y. C. Chen, T. C. Killian, P. Pellegrini, and R. Côté. Spectroscopic Determination of the s -Wave Scattering Lengths of ^{86}Sr and ^{88}Sr . *Physical Review Letters*, 95(22):223002, 2005.

- [307] D. A. Miller, L. You, J. Cooper, and Alan Gallagher. Collisional energy transfer between excited-state strontium and noble-gas atoms. *Physical Review A*, 46(3):1303, 1992.
- [308] H. J. Andra, H.-J. Plohn, W. Wittmann, A. Gaupp, J. O. Stoner Jr., and M. Gaillard. Lifetimes of levels in neutral strontium (Sr I). *Journal of the Optical Society of America*, 65(12):1410, 1975.
- [309] W. H. Parkinson, E. M. Reeves, and F. S. Tomkins. Neutral calcium, strontium and barium: determination of f values of the principal series by the hook method. *Journal of Physics B: Atomic and Molecular Physics*, 9(2):157, 1976.
- [310] Y. Takasu, K. Komori, K. Honda, M. Kumakura, T. Yabuzaki, and Y. Takahashi. Photoassociation Spectroscopy of Laser-Cooled Ytterbium Atoms. *Physical Review Letters*, 93(12):123202, 2004.
- [311] V. A. Dzuba and A. Derevianko. Dynamic polarizabilities and related properties of clock states of the ytterbium atom. *Journal of Physics B: Atomic, Molecular and Optical Physics*, 43:074011, 2010.
- [312] Thomas A. Bell, Jake A. P. Glidden, Leif Humbert, Michael W. J. Bromley, Simon A. Haine, Matthew J. Davis, Tyler W. Neely, Mark A. Baker, and Halina Rubinsztein-Dunlop. Bose-Einstein condensation in large time-averaged optical ring potentials. *New Journal of Physics*, 18:035003, 2016.
- [313] T. B. Ottenstein, T. Lompe, M. Kohnen, A. N. Wenz, and S. Jochim. Collisional Stability of a Three-Component Degenerate Fermi Gas. *Physical Review Letters*, 101(20):203202, 2008.
- [314] U. Gaubatz, P. Rudecki, S. Schiemann, and K. Bergmann. Population transfer between molecular vibrational levels by stimulated Raman scattering with partially overlapping laser fields. A new concept and experimental results. *The Journal of Chemical Physics*, 92(9):5363, 1990.
- [315] K. Bergmann, H. Theuer, and B. W. Shore. Coherent population transfer among quantum states of atoms and molecules. *Rev. Mod. Phys.*, 70(3):1003, 1998.
- [316] Kang-Kuen Ni. *A Quantum Gas of Polar Molecules*. PhD thesis, University of Colorado, Boulder, 2010.
- [317] Tao Hong, Claire Cramer, Warren Nagourney, and E. N. Fortson. Optical Clocks Based on Ultranarrow Three-Photon Resonances in Alkaline Earth Atoms. *Physical Review Letters*, 94(5):050801, 2005.
- [318] Claude Cohen-Tannoudji, Jacques Dupont-Roc, and Gilbert Grynberg. *Atom—Photon Interactions*. Wiley-Blackwell, 1998.

- [319] F. W. J. Olver, D. W. Lozier, R. F. Boisvert, and C. W. Clark, editors. *NIST Handbook of Mathematical Functions*. Cambridge University Press, New York, NY, 2010. Print companion to [\[227\]](#).